

Todo list

neutron methods	118
Need data from simon on these materials	125
Need simulated isotherms from Simon	129
Talk about CO	141
need data from Simon for figure...	144



AIX-MARSEILLE UNIVERSITY

DOCTORAL SCHOOL: Physics and Material Science

PARTENAIRES DE RECHERCHE

Laboratoire MADIREL

Submitted with the view of obtaining the degree of doctor

Discipline: Material Science

Specialty: Characterisation of porous materials

Paul A. Iacomi

Titre de la thèse: sous-titre de la thèse

Defended on JJ/MM/AAAA in front of the following jury:

Prénom NOM	Affiliation	Rapporteur
Prénom NOM	Affiliation	Rapporteur
Prénom NOM	Affiliation	Examinateur
Prénom NOM	Affiliation	Examinateur
Prénom NOM	Affiliation	Examinateur
Prénom NOM	Affiliation	Directeur de thèse

National thesis number: 2017AIXM0001/001ED62



This work falls under the conditions of the Creative Commons Attribution License - No commercial use - No modification 4.0 International.

Abstract

Abstract is here.

Acknowledgements

Acknowledgements go here

Contents

Abstract	iii
Acknowledgements	iv
1. Introduction to this thesis	1
2. Building a framework for isotherm data processing	2
2.1. Introduction	2
2.2. Physical models of adsorption	3
2.2.1. The Gibbs surface excess approach	4
2.2.2. The Henry model	7
2.2.3. Langmuir and multi-site Langmuir model	7
2.2.4. BET model	8
2.2.5. Toth model	10
2.2.6. Temkin model	10
2.2.7. Jensen-Seaton model	11
2.2.8. Quadratic model	11
2.2.9. Virial model	11
2.2.10. Vacancy solution theory models	12
2.3. Characterisation of materials through adsorption	13
2.3.1. Specific surface area and pore volume calculation	13
2.3.2. Assessing porosity	17
2.3.3. Predicting multicomponent adsorption	22
2.4. pyGAPS overview	23
2.4.1. Core structure	24
2.4.2. Creation of an Isotherm	26
2.4.3. Units	28
2.4.4. Workflow	28
2.4.5. Characterisation using pyGAPS	29
2.5. Processing a large adsorption dataset	36
2.5.1. The NIST ISODB dataset	36
2.5.2. A comparison between surface area calculation methods	38
2.5.3. Variability of the dataset	39

2.6. Conclusion	41
Bibliography	43
3. Extending bulk analysis of porous compounds through calorimetry	46
3.1. Introduction	46
3.2. Energetics of adsorption	47
3.2.1. Forces involved in adsorption	47
3.2.2. Thermodynamic quantities of the adsorbed phase	48
3.2.3. Application of differential enthalpy of adsorption to the characterisation of materials	49
3.3. Measuring the enthalpy of adsorption	50
3.3.1. Isosteric enthalpy of adsorption	50
3.3.2. Microcalorimetry	51
3.3.3. Experimental apparatus and accuracy	54
3.4. Case studies for the use of microcalorimetry combined with adsorption experiments .	55
3.4.1. Comparison between enthalpies of adsorption measured through the direct and indirect method	55
3.4.2. An example dataset on a reference material	56
3.4.3. A study on a novel MOF	58
3.5. Conclusion	62
Bibliography	63
4. Exploring the impact of structural defects	66
4.1. Introduction	66
4.2. The defective nature of MOFs	68
4.2.1. Types of crystal defects and their analogues in MOFs	68
4.2.2. Consequences of defects	70
4.2.3. Defect engineering of MOFs	71
4.2.4. The propensity of UiO-66(Zr) for defect generation	71
4.3. Materials and methods	73
4.3.1. Materials	73
4.3.2. Methods for quantifying defects	74
4.4. Results and discussion	76
4.4.1. Crystallinity of leached samples	76
4.4.2. Thermogravimetry results	76
4.4.3. Nitrogen sorption at 77K	79
4.4.4. Characterisation of trends	79
4.4.5. Carbon dioxide isotherms	85
4.5. Conclusion	87
Bibliography	88

5. Exploring the impact of material form on adsorption measurements	93
5.1. Introduction	93
5.2. Shaping in context	94
5.3. Materials, shaping and characterisation methods	96
5.3.1. Materials	96
5.3.2. Shaping Procedure	97
5.3.3. Characterisation of powders and pellets	98
5.3.4. Sample activation for adsorption	98
5.4. Results and discussion	98
5.4.1. Thermal stability	98
5.4.2. Adsorption isotherms at 77K and room temperature	100
5.4.3. Room temperature gas adsorption and microcalorimetry	102
5.4.4. Vapour adsorption	109
5.5. Conclusion	114
Bibliography	115
6. Exploring intrinsic framework phenomena — adsorption induced phase changes	117
6.1. Introduction	117
6.2. Compliance in porous crystals	118
6.2.1. Examining the assumption of an inert adsorbent	118
6.2.2. Flexibility in metal organic frameworks	119
6.2.3. Describing and inducing MOF compliance	120
6.2.4. Consequences and applications of flexible MOFs	122
6.2.5. Unique flexible behaviour of DUT-49	123
6.3. Materials and characterisation methods	124
6.3.1. Materials	124
6.3.2. Characterisation methods	125
6.4. Results and discussion	128
6.4.1. The structural transition leading to NGA in DUT-49	128
6.4.2. Impact of framework structure on transition mechanics	131
6.4.3. An in-depth analysis of the NGA mechanism	138
6.5. Conclusion	147
Bibliography	150
7. Conclusions	155
A. Common characterisation techniques	156
A.1. Thermogravimetry	156
A.2. Bulk density determination	156
A.3. Skeletal density determination	157

A.4. Nitrogen physisorption at 77 K	157
A.5. Vapour physisorption at 298 K	157
A.6. Gravimetric isotherms	158
A.7. High throughput isotherm measuremnt	158
A.8. Powder X-ray diffraction	158
A.9. Nuclear magnetic resonance	158
A.10. Adsorption manometry and calorimetry at 303 K	158
Bibliography	158
B. Synthesis method of referenced materials	159
B.1. Takeda 5A reference carbon	159
B.2. MCM-41 mesoporous silica	159
B.3. Zr fumarate MOF	159
B.4. UiO-66(Zr) for defect study	160
B.5. UiO-66(Zr) for shaping study	160
B.6. MIL-100(Fe) for shaping study	160
B.7. MIL-127(Fe) for shaping study	161
Bibliography	161
C. Calculation of uncertainty in adsorption measurements	162
Bibliography	162
D. Appendix for chapter 3	163
Bibliography	165
E. Appendix for chapter 4	166
E.1. Acid and solvent properties	166
E.2. Powder diffraction patterns	167
E.3. TGA curves	168
E.3.1. DMF leached samples	168
E.3.2. Water leached samples	169
E.3.3. Methanol leached samples	170
E.3.4. DMSO leached samples	171
E.3.5. High resolution curves	172
E.4. Nitrogen sorption isotherms	173
E.4.1. DMF leached samples	173
E.4.2. H ₂ O leached samples	174
E.4.3. MeOH leached samples	176
E.4.4. DMSO leached samples	178
E.5. Characterisation	180

Bibliography	181
F. Appendix for chapter 5	182
F.1. Calorimetry dataset UiO-66(Zr)	183
F.2. Calorimetry MIL-100(Fe)	185
F.3. Calorimetry MIL-127(Fe)	187
G. Appendix for chapter 6	189
G.1. Table of properties for low temperature probes	189
G.2. Ambient temperature calorimetry experiments	190
G.3. Low temperature calorimetry experiments	194

1. Introduction to this thesis

2. Building a framework for isotherm data processing

2.1. Introduction

Historically, the processing of isotherms was done by hand, with large worksheets being used for the calculations. As an example, we point out that one of the initial limitations of the Barrett-Joyner and Halenda method for determining pore size distribution was that each point had to be estimated with an approximation of critical pore radius, resulting in tedious work involved in the calculation.⁽¹⁾

The advent of computers meant that calculations could be performed quickly and reliably and led to the development of more computationally demanding methods for adsorption modelling and isotherm processing, such as the density functional theory (DFT) and grand canonical monte carlo (GCMC) kernel fitting methods for pore size distribution.^(2,3) Commercial adsorption equipment which offers the users a complete software solution for any isotherm calculations is now commonplace, and makes obtaining reports of desired properties for measured materials a matter of seconds.

Given the current ubiquitousness of adsorption as a characterisation method, particularly for investigating surfaces and porous compounds, there is a large pool of data published in the scientific community. Recent efforts have focused on building a database of adsorption isotherms⁽⁴⁾, to offer a searchable pool of standardised behaviours on different materials. This serves as both a useful reference for comparing synthesised compounds, as well as a method for quickly finding suitable materials which have the desired properties for a particular application.

The abundance of data reflects a trend in recent years where, due to the prevalence of digital records and cheap storage, more information is available than ever before. As such, challenges now lie in making sense of the so called “big data”. Key performance indicators (KPI) such as specific surface area, working capacity and pore volume are commonly reported in scientific literature and used as benchmarking tools. Furthermore, several studies have attempted to find a reliable indicator for the suitability of an adsorbent for a specific application⁽⁵⁻⁷⁾ such as pressure swing adsorption.

However, we feel that a critical step in the process has yet to be fully addressed. Transitioning from isotherms published in literature to the calculation of such KPIs requires individual implementation of previously mentioned techniques. As such, not only can errors arise in such implementations,

but a critical survey of the results is tedious and time consuming. In conclusion, a standardised method of high throughput processing of such data would be invaluable not only for reference purposes, but also for in-depth studies of data reliability, structure-property relationships and effect of variables on the adsorption properties of a material.

Chapter summary

In this chapter an open-source software package is presented, which is released under an MIT licence and written in Python, intended to be used for manipulation, storage, visualisation and processing of adsorption isotherms. The software is aimed to give users a powerful yet easy to use package that can perform the kind of processing common to adsorption methodology, but using large datasets of hundreds or thousands of isotherms. The code is then used to process a dataset of 26000 isotherms from the NIST adsorption database in order to highlight the variability of adsorption data reported in literature on MOFs.

Contribution

Paul Iacomi wrote the python code for the pyGAPS framework and is responsible for its publication and maintenance as an open source package. The IAST functionality is a modified version of the pyIAST code, published by Cory Simon. Example data on reference materials was recorded by Paul Iacomi for Takeda 5A and UiO-66(Zr) and by Emily Bloch on MCM-41 and porous silica. The bulk processing example data comes from the NIST Adsorption Database, maintained by Dan Siderius.

2.2. Physical models of adsorption

As the process of characterisation of porous materials relies on mathematical models of adsorption, this section details several concepts essential to the description of the adsorbed phase, as well as several guest-host system archetypes.

Adsorption isotherms can have highly different shapes and features, depending on the system involved. Much effort was put into attempting to describe and categorize the phenomenon of adsorption, with IUPAC recommendations suggesting six types of isotherms, as seen in Figure 2.1. While these isotherm types can be useful for fast classification, there is no “one size fits all” approach. Indeed, the only certain behaviour is that the amount adsorbed is zero at the isotherm start and that the loading increases with increasing pressure, with the latter shown in chapter 6 to not be always true. However, through careful assumptions and a well-defined model, the underlying mechanisms of adsorption can be understood. Unfortunately, the plethora of isotherm features and shapes can only be truly recreated by molecular simulation, a method which requires an exact knowledge of the adsorbent structure and its interaction with the guest molecules.

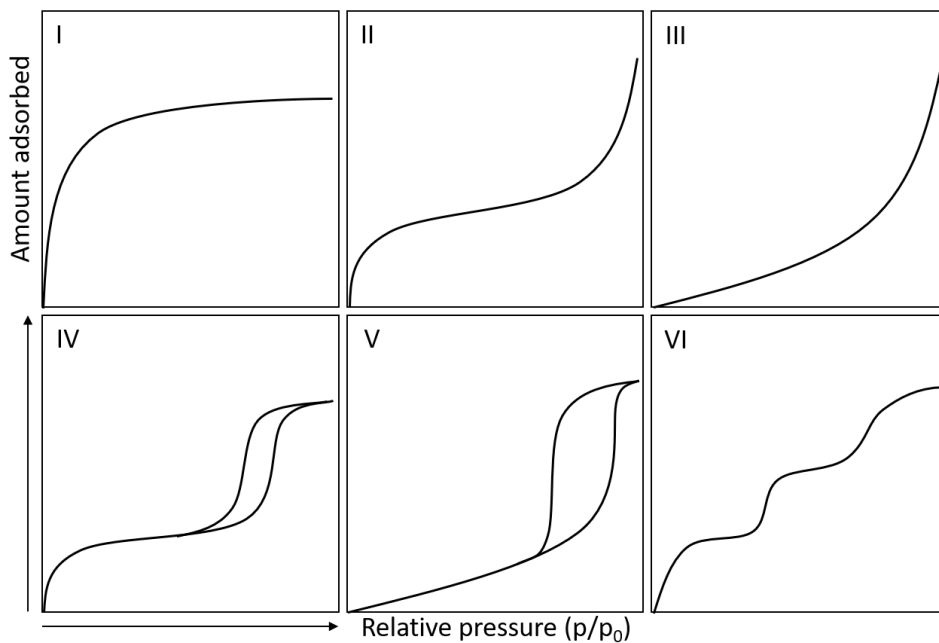


Figure 2.1.: IUPAC isotherm types. Adapted from Rouquerol et al.⁽⁸⁾.

Nevertheless, models derived from a kinetic or thermodynamic view of adsorption can be useful for obtaining simple parameters which are representative of physical factors such as guest-host interaction, surface area, pore size, and total capacity. Thermodynamical models require a coherent definition of the adsorbed phase, often done through the Gibbs surface excess approach. This description allows for an equation relating the bulk and adsorbed phase to be obtained, called the Gibbs isotherm. Models which are derived from this equation include Henry's law, the virial model and vacancy solution theory. Adsorption can also be described from a kinetic standpoint, where the rate of adsorption and desorption of molecules on available sites is mathematically modelled. Equations based on kinetics include the Langmuir model, the BET model, the Temkin model and empirical or semi-empirical derivatives such as the Toth, Quadratic or the Jensen-Seaton model. A page of figures for different models and how the described isotherm varies with different values of their parameters can be seen in Figure 2.2. The following section will describe these equations, together with their assumptions and applicability.

2.2.1. The Gibbs surface excess approach

A description of the adsorbed phase can be made through expressing the change in density or concentration of fluid from the adsorbent surface to the bulk phase. The density has a maxima in the immediate zone close to the surface, and then decreases until it reaches the density of the bulk fluid. However, when defined as such, the boundary between the two phases is difficult to pinpoint. Therefore, in most cases it is useful to employ the concept of the Gibbs dividing surface.

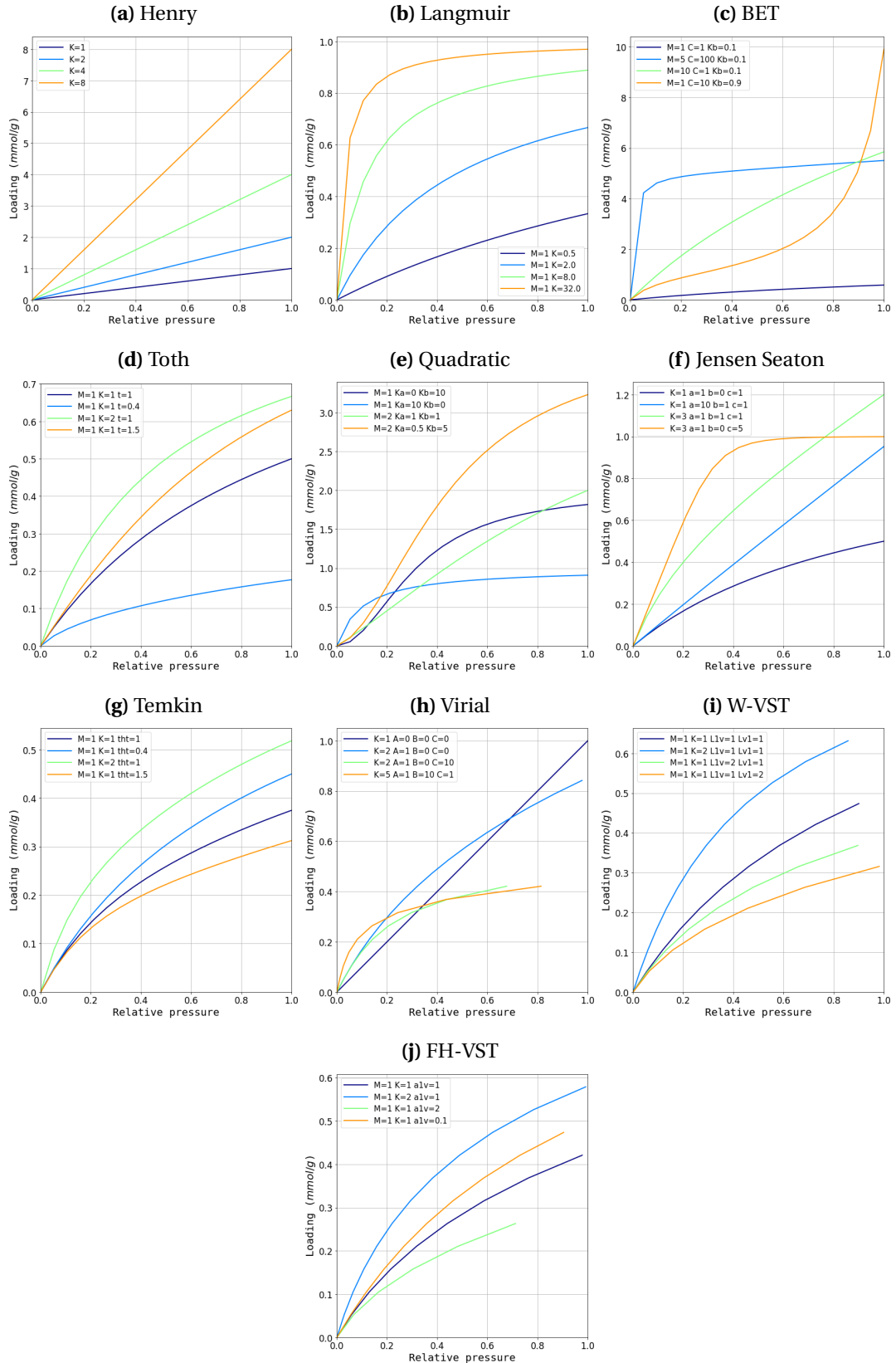


Figure 2.2.: The various adsorption models discussed in this chapter, alongside the influence of their parameters on the resulting isotherm.

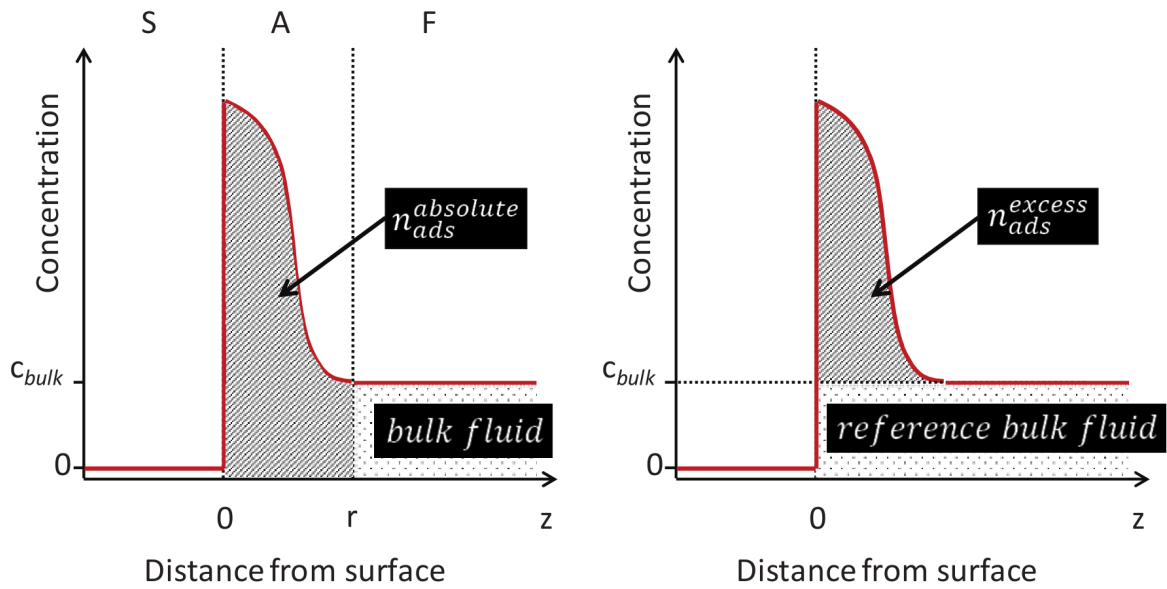


Figure 2.3.: Representation of the adsorbed and bulk phases according to the (left) layer model and the (right) Gibbs dividing surface approach. Adapted from Rouquerol et al.⁽⁸⁾.

This approach describes the adsorbed phase only in terms of an *excess* from the properties of the bulk phase. As represented in Figure 2.3, the total amount adsorbed can be defined as:

$$n_{ads}^a = A \int_0^r c \, dz \quad (2.1)$$

The imaginary Gibbs dividing surface is usually envisaged parallel to the real surface of the adsorbent and in the resulting system, the concentration of the adsorbent in the adsorbed phase are expressed as an excess from the concentration of the bulk fluid. The relationship between the total amount adsorbed and the excess amount adsorbed is then:

$$n_{ads}^\sigma = n_{ads}^a + c_{bulk} \cdot V_{ads} \quad (2.2)$$

As long as the volume of the adsorbed layer V_{ads} can be considered negligible and the concentration of adsorbate in the bulk phase c_{bulk} is low, the total amount adsorbed and the surface excess amount may be considered as approximately equal. This is usually the case for experiments such as nitrogen adsorption at 77 K, or ambient temperature adsorption below 1 bar. At high pressures, or when the difference in concentration between the adsorbed and the bulk phase is low, the total amount adsorbed begins to diverge significantly from the surface excess.

In most cases, isotherms are reported in terms of excess surface amount. From an engineering viewpoint, this representation is often more useful. However, any modelling and simulations of isotherms refers to the total amount adsorbed. If n_t is to be calculated, a value for the volume of the adsorbed phase and the sample is required, for a correction using Equation 2.2. In the case of adsorption in porous materials, the volume of the adsorbed phase may be taken as the total pore

volume. This approach assumes that the volume enclosed by the Gibbs dividing surface is the same as the volume of the sample, which may not be the case if it is determined with a blank measurement of a non-adsorbing gas.

Isotherm models which have a thermodynamical basis are derived from the Gibbs equation (Equation 2.3). The pressure and volume concepts of the bulk phase are replaced by the 2-dimensional analogues of spreading pressure (π) and surface area.

$$\left(\frac{d\pi}{d \ln p} \right) = \frac{n}{A} R_g T \quad (2.3)$$

By substituting spreading pressure with an equation of state for the adsorbed phase, an expression for the amount adsorbed can be obtained as a function of bulk phase pressure.

2.2.2. The Henry model

The simplest method of describing adsorption on a surface is Henry's law. It assumes only interactions with the adsorbate surface and is described by a linear dependence of adsorbed amount with increasing pressure.

$$n_a(p) = K_H p \quad (2.4)$$

It is derived from the Gibbs isotherm, by substituting a two dimensional analogue to the ideal gas law. From a physical standpoint, Henry's law is unrealistic as adsorption sites will saturate at higher pressures. However, the constant K_H , or Henry's constant, can be thought of as a measure of the strength of the interaction of the probe gas with the surface. At very low concentrations of gas there is a thermodynamic requirement for the applicability of Henry's law. Therefore, most models reduce to Equation 2.4 as $\lim_{p \rightarrow 0} n(p)$.

2.2.3. Langmuir and multi-site Langmuir model

The Langmuir theory⁽⁹⁾, proposed at the start of the 20th century, states that adsorption takes place on specific sites on a surface, until all sites are occupied. It was originally derived from a kinetic model of gas adsorption and is based on several assumptions.

- All sites are equivalent and have the same chance of being occupied.
- Each adsorbate molecule can occupy one adsorption site.
- There are no interactions between adsorbed molecules.
- The rates of adsorption and desorption are proportional to the number of sites currently free and currently occupied, respectively.
- Adsorption is complete when all sites are filled.

Using these assumptions we can define rates for both adsorption and desorption. The adsorption rate (Equation 2.5) will be proportional to the number of sites available on the surface, as well as the number of molecules in the gas, which is given by pressure. The desorption rate, on the other hand, will be proportional to the number of occupied sites and the energy of adsorption (Equation 2.6). It is also useful to define $\theta = n_a / n_a^m$ as the fractional surface coverage, the number of sites occupied divided by the total sites. At equilibrium, the rate of adsorption and the rate of desorption are equal, therefore the two equations can be combined. The equation can then be arranged to obtain an expression for the loading called the Langmuir model (Equation 2.9).

$$v_a = k_a p (1 - \theta) \quad (2.5)$$

$$v_d = k_d \theta \exp\left(-\frac{E_{ads}}{RT}\right) \quad (2.6)$$

$$v_a = v_d \quad (2.7)$$

$$k_a p (1 - \theta) = k_d \theta \exp\left(-\frac{E_{ads}}{RT}\right) \quad (2.8)$$

$$n_a(p) = n_a^m \frac{Kp}{1 + Kp} \quad (2.9)$$

The Langmuir constant K is the product of the individual desorption and adsorption constants k_a and k_d and exponentially related to the energy of adsorption E_{ads} .

A common extension to the Langmuir model is to consider the experimental isotherm to be the sum of several Langmuir-type isotherms, each with specific maximum coverage and affinities. The underlying assumption is that the adsorbent has several distinct types of homogeneous adsorption sites and a Langmuir equation is used for each. This is particularly applicable in cases where the structure of the adsorbent suggests that different types of sites are present, such as in crystalline materials of variable chemistry like zeolites and MOFs. The resulting isotherm equation becomes:

$$n_a(p) = \sum_i n_{a,i}^m \frac{K_i p}{1 + K_i p} \quad (2.10)$$

In practice, only up to three adsorption sites are usually considered.

2.2.4. BET model

Like the Langmuir model, The BET model⁽¹⁰⁾ assumes that adsorption is kinetically driven and takes place on adsorption sites at the material surface. However, each adsorbed molecule becomes, in itself, a secondary adsorption site, such that incremental layers are formed. The conditions imagined by the BET model are:

- The surface adsorption sites are equivalent, and therefore the surface is considered homogeneous.
- There are no lateral interactions between adsorbed molecules.

- The adsorption occurs in layers, with adsorbed molecules acting as sites for the next layer.
- The energy of adsorption on subsequent layers after the initial monolayer is equal to the liquefaction energy of the adsorbate.

A percentage of the surface θ_x is occupied with x layers. For each layer at equilibrium, the adsorption and desorption rates must be equal. The Langmuir model is then applied for each of layer as shown in Table 2.1. It is assumed that the adsorption energy of a molecule on the second and higher layers is just the condensation energy of the adsorbent $E_{i>1} = E_L$. Since it follows that all layers beside the first have the same properties, we can also define $g = k_{d_2} k_{a_2} = k_{d_3} k_{a_3} = \dots$.

Table 2.1.: Derivation of the BET method from each adsorbed layer

All layers	Re-arranged
$k_{a_1} p\theta_0 = k_{d_1} \theta_1 \exp\left(-\frac{E_1}{RT}\right)$	$p\theta_0 = \frac{k_{d_1}}{k_{a_1}} \theta_1 \exp\left(-\frac{E_1}{RT}\right)$
$k_{a_2} p\theta_1 = k_{d_2} \theta_2 \exp\left(-\frac{E_2}{RT}\right)$	$p\theta_1 = g\theta_2 \exp\left(-\frac{E_L}{RT}\right)$
$k_{a_2} p\theta_2 = k_{d_3} \theta_3 \exp\left(-\frac{E_3}{RT}\right)$	$p\theta_2 = g\theta_3 \exp\left(-\frac{E_L}{RT}\right)$
\vdots	\vdots
$k_{a_i} p\theta_{i-1} = k_{d_i} \theta_i \exp\left(-\frac{E_i}{RT}\right)$	$p\theta_{i-1} = g\theta_i \exp\left(-\frac{E_L}{RT}\right)$

The coverage for each layer θ can now be expressed in terms of θ_0 .

$$\theta_i = \left[p \frac{k_{a_1}}{k_{d_1}} \exp\left(-\frac{E_1}{RT}\right) \right] x^{i-1} \theta_0 \quad (2.11)$$

where

$$x = \frac{p}{g} \exp\left(-\frac{E_L}{RT}\right) \quad (2.12)$$

A constant C may be defined such that:

$$C = \frac{k_{a_1}}{k_{d_1}} g \exp\left(\frac{E_1 - E_L}{RT}\right) \quad (2.13)$$

$$\theta_i = C x^i \theta_0 \quad (2.14)$$

For all layers N, the equations can be summed:

$$\frac{n}{n_m} = \sum_{i=1}^N i \theta^i = C \sum_{i=1}^N i x^i \theta_0 \quad (2.15)$$

and since

$$\theta_0 = 1 - \sum_1^N \theta_i \sum_{i=1}^N i x^i = \frac{x}{(1-x)^2} \quad (2.16)$$

It is usually assumed that the number of layers tends to infinity $N = \infty$ as the partial pressure increases to 1. In this case, we obtain the BET equation as:

$$n_a(p) = n_a^m \frac{C(p/p_0)}{(1-p/p_0)[1-(p/p_0)+C(p/p_0)]} \quad (2.17)$$

The BET constant C is exponentially proportional to the difference between the surface adsorption energy and the intermolecular attraction and can be seen to influence the “knee” a BET-type isotherm has at low pressure, before statistical monolayer formation.

2.2.5. Toth model

The Toth model is an empirical modification to the Langmuir equation (Equation 2.9) which introduces a power parameter for the denominator leading to the following equation:

$$n_a(p) = n_a^m \frac{Kp}{[1+(Kp)^t]^{1/t}} \quad (2.18)$$

The parameter t is a measure of the system heterogeneity. Thanks to this additional parameter, the Toth equation can accurately describe a large number of adsorbent/adsorbate systems and, due to its correct behaviour in both the low and high pressure limits, is recommended as the fitting isotherms of many adsorbents such as hydrocarbons, carbon oxides, hydrogen sulphide and alcohols on activated carbons and zeolites.

2.2.6. Temkin model

The Temkin adsorption isotherm⁽¹¹⁾, like the Langmuir model, considers a surface with n_a^m identical adsorption sites, but takes into account adsorbate-adsorbate interactions by assuming that the heat of adsorption is a linear function of coverage. The formula in Equation 2.19 is derived using a mean-field argument and uses an asymptotic approximation to obtain an explicit equation for the loading.⁽¹²⁾

$$n_a(p) = n_a^m \frac{Kp}{1+Kp} + n_a^m \theta \left(\frac{Kp}{1+Kp} \right)^2 \left(\frac{Kp}{1+Kp} - 1 \right) \quad (2.19)$$

Here, n_a^m and K have the same physical meaning as in the Langmuir model. The additional parameter θ describes the strength of the adsorbate-adsorbate interactions ($\theta < 0$ for attractions).

2.2.7. Jensen-Seaton model

When modelling supercritical adsorption in micropores, a requirement was highlighted by Jensen and Seaton in 1996⁽¹³⁾ that at sufficiently high pressures the adsorption isotherm should not reach a horizontal plateau corresponding to saturation but that this asymptote should continue to rise due to the compression of the adsorbate in the pores. They developed a semi-empirical equation to describe this phenomenon based on a function that interpolates between two asymptotes: the Henry's law asymptote at low pressure and an asymptote reflecting the compressibility of the adsorbate at high pressure.

$$n(p) = K_H p \left(1 + \frac{K_H p}{[a(1+bp)]^c}\right)^{(-1/c)} \quad (2.20)$$

where K_H is the Henry constant, b is the compressibility of the adsorbed phase and c an empirical constant.

The equation can be used to model both absolute and excess adsorption as the pore volume can be incorporated into the definition of b , although this can lead to negative adsorption slopes for the compressibility asymptote. This equation has been found to provide a better fit for experimental data from microporous solids than the Langmuir or Toth equation, in particular for adsorbent/adsorbate systems with high Henry's constants where the amount adsorbed increases rapidly at relatively low pressures and then slows down dramatically.

2.2.8. Quadratic model

The quadratic adsorption isotherm⁽¹⁴⁾ exhibits an inflection point. The loading is convex at low pressures but changes concavity as it saturates, yielding an S-shape. The S-shape can be explained by adsorbate-adsorbate attractive forces: the initial convexity is due to a cooperative effect of adsorbate-adsorbate attractions aiding in the recruitment of additional adsorbate molecules.

$$n(p) = n_a^m \frac{(K_a + 2K_b p)p}{1 + K_a p + K_b^2 p} \quad (2.21)$$

The parameter K_a can be interpreted as the Langmuir constant; the strength of the adsorbate-adsorbate attractive forces is embedded in K_b . It is often useful in systems where the energy of guest-guest interactions is actually higher than the energy of adsorption, such as when adsorbing water on a hydrophobic surface.

2.2.9. Virial model

A virial isotherm model attempts to fit the measured data to a factorized exponent relationship between loading and pressure.⁽¹⁵⁾

$$p = n \exp(K_1 n^0 + K_2 n^1 + K_3 n^2 + K_4 n^3 + \dots + K_i n^{i-1}) \quad (2.22)$$

It has been applied with success to describe the behaviour of standard as well as supercritical isotherms. The factors are usually empirical, although some relationship with physical properties can be determined: the first constant is related to the Henry constant at zero loading, while the second constant is a measure of the adsorbate-adsorbate interactions.

$$K_1 = -\ln K_{H,0} \quad (2.23)$$

In practice, besides the first constant, only 2–3 factors are used.

2.2.10. Vacancy solution theory models

The vacancy solution theory (VST) family of models, are based on the concept of a “vacancy” species and assume that the adsorbed phase is analogous to a mixture of vacancies and the adsorbate. The main assumptions in the VST models are defined as follows:

- A vacancy is an imaginary entity defined as a vacuum space, which acts as the solvent in both the gas and adsorbed phases.
- The properties of the adsorbed phase are defined through the Gibbs approach, as excess properties in relation to a dividing surface.
- The entire system, including the adsorbent, is at thermal equilibrium. However, only the gas and the adsorbed phases are at thermodynamic equilibrium.
- The equilibrium of the system is maintained by the spreading pressure which arises from a potential field at the surface.

It is possible to derive expressions for the vacancy chemical potential in both the adsorbed phase and the gas phase, which when equated give the following equation of state for the adsorbed phase:

$$\pi = -\frac{R_g T}{\sigma_v} \ln y_\nu x_\nu \quad (2.24)$$

where y_ν is the activity coefficient and x_ν is the mole fraction of the vacancy in the adsorbed phase. This can then be introduced into the Gibbs equation (Equation 2.3) to obtain a general isotherm equation for VST-type models (Equation 2.25) where K_H is the Henry's constant and $f(\theta)$ is a function that describes the non-ideality of the system in terms of activity coefficients of the adsorbate and vacancy species.

$$p = \frac{n_{ads}}{K_H} \frac{\theta}{1-\theta} f(\theta) \quad (2.25)$$

The general VST equation requires an expression for the activity coefficients $f(\theta)$. One option is to use the Wilson⁽¹⁶⁾ approach, which expresses the activity coefficient in terms of the mole fractions

of the two species (adsorbate and vacancy) and two constants Λ_{1v} and Λ_{v1} . The equation then for activity coefficients becomes:

$$f(\theta) = \Lambda_{1v} \frac{1 - (1 - \Lambda_{v1})\theta}{\Lambda_{1v} + (1 - \Lambda_{1v})\theta} \exp\left(-\frac{\Lambda_{v1}(1 - \Lambda_{v1})\theta}{1 - (1 - \Lambda_{v1})\theta} - \frac{(1 - \Lambda_{1v})\theta}{\Lambda_{1v} + (1 - \Lambda_{1v})\theta}\right) \quad (2.26)$$

A simpler alternative was introduced by Cochran.⁽¹⁷⁾ The result is a three parameter equation based on the Flory–Huggins equation for the activity coefficient. $f(\theta)$ is represented as

$$f(\theta) = \exp \frac{\alpha_{1v}^2 \theta}{1 + \alpha_{1v} \theta} \quad \text{where} \quad \alpha_{1v} = \frac{\alpha_1}{\alpha_v} - 1 \quad (2.27)$$

where α_1 and α_v are the molar areas of the adsorbate and the vacancy respectively. Both the Wilson and Flory–Huggins expressions for the vacancy-adsorbate interactions can be directly inserted in the general VST model (Equation 2.25).

2.3. Characterisation of materials through adsorption

Adsorption is a powerful tool for characterisation of materials. As it can give insight into the surface properties of solids, it is most often used for the investigation of porous or finely divided materials where the surface area to volume ratio is high enough for adsorption to be detected with common laboratory measurement techniques such as manometry and gravimetry (see Appendix A). The most common properties which can be obtained through adsorption methods are probe accessible surface area, pore volume and pore size distribution. Other characteristics such as surface chemistry or material response can be probed through adsorption. Finally, pure component adsorption isotherms can be used to predict multicomponent adsorption through computational models such as IAST. The following section will go into detail on how such methods are applied.

2.3.1. Specific surface area and pore volume calculation

BET surface area

The BET method⁽¹⁰⁾ for determining surface area is the recommended IUPAC method⁽¹⁸⁾ to calculate the surface area of a porous material. It is generally applied on isotherms obtained through N₂ adsorption at 77 K, although other adsorbates (Ar at 77 K or 87 K, Kr at 77 K, CO₂ at 293 K) have been used. In principle, any probe with an adsorption isotherm which can be described through the BET equation in the low pressure regime can be used.

As previously mentioned, subsection 2.2.4 the BET model assumes that adsorption takes place in incremental layers on the material surface. Even if the adsorbent is porous, the initial amount adsorbed (usually between 0.05–0.4 p/p_0) can be described through the equation written in its linear

form:

$$\frac{p/p_0}{n_{ads}(1-p/p_0)} = \frac{1}{n_m C} + \frac{C-1}{n_m C}(p/p_0) \quad (2.28)$$

If a plot of the isotherm points as $(p/p_0)/n_{ads}(1-p/p_0)$ versus p/p_0 is generated, a linear region can usually be found. The slope and intercept of this line can then be used to calculate n_m , the amount adsorbed at the statistical monolayer, as well as C , the BET constant.

$$n_m = \frac{1}{s+i} \quad C = \frac{s}{i} + 1 \quad (2.29)$$

From the BET monolayer capacity, the specific surface area can be calculated if the area taken up by one of the adsorbate molecules on the surface is known. The calculation uses the following equation together with Avogadro's number:

$$a_{BET} = n_m A_N \sigma \quad (2.30)$$

While commonly used for surface area determination, the BET area should be used with care, as the assumptions made in its calculation may not hold. To augment the validity of the BET method, Rouquerol⁽⁸⁾ proposed several checks to ensure that the selected BET region is valid:

- The BET (C) obtained should be positive;
- In the corresponding Rouquerol plot where $n_{ads}(1-p/p_0)$ is plotted with respect to p/p_0 , the points chosen for BET analysis should be strictly increasing;
- The loading at the statistical monolayer should be situated within the limits of the BET region.

Regardless, the BET surface area should still be interpreted carefully. Since adsorption takes place on the pore surface, microporous materials which have pores of similar or smaller size as the probe molecule used will not give a realistic surface area. In the micropore range it is difficult to separate pore condensation behaviour from multilayer adsorption. Furthermore, the cross-sectional area of the molecule on the surface cannot be guaranteed. For example, nitrogen has been known to adopt a different conformation on the surface of some materials due to inter-molecular forces, which effectively lowers its cross-sectional area⁽⁸⁾ from 0.168 nm to 0.138 nm.

Langmuir surface area

The Langmuir equation (Equation 2.9) can be also be expressed in a linear form by rearranging it as:

$$\frac{p}{n} = \frac{1}{Kn_m} + \frac{p}{n_m} \quad (2.31)$$

Assuming the data can be fitted with a Langmuir model, by plotting p/n against pressure, a straight line will be obtained. The slope and intercept of this line can then be used to calculate n_m , the amount adsorbed at the monolayer capacity, as well as K , the Langmuir constant.

$$n_m = \frac{1}{s} \quad K = \frac{1}{i * n_m} \quad (2.32)$$

The surface area can then be calculated by using the monolayer capacity in a manner analogous to the BET surface area method.

$$a_{Langmuir} = n_m A_N \sigma \quad (2.33)$$

The Langmuir method for determining surface area assumes that adsorption takes place until all active sites on the material surface are occupied, or until monolayer formation in the case of complete surface coverage. Most adsorption processes (except chemisorption) don't follow this behaviour, although high temperature isotherms can often be estimated through this model. Therefore it is important to regard the Langmuir surface area as an estimate.

Ideal isotherms or thickness functions

The initial part of an isotherm (the Henry regime) can be seen to be very dependent on the interactions between the adsorbate and the surface. However, subsequent layers are less influenced by the material and can often be assumed, like in the BET model, to have an energy of adsorption identical to the enthalpy of liquefaction of the bulk liquid. Therefore, their formation will essentially depend only on partial pressure.

With this assumption, several studies have been focused on obtaining an “ideal” isotherm of adsorption on a non-porous material which can then, if the cross-sectional area of the molecule is known, be transformed in a function capable of predicting the thickness of the adsorbed layer as a function of pressure. This kind of empirical function, also referred to as a *thickness function* or *t-curve*, can be used as an alternative method for surface area determination, as explained in the following section. These curves are also used in the classical methods for calculating mesoporous size distribution. It is important to clarify that the function is only applicable for a single adsorbent and temperature.

For example, two common thickness functions applicable for nitrogen at 77 K are the Halsey⁽¹⁹⁾ (Equation 2.34) and the Harkins and Jura⁽²⁰⁾ (Equation 2.35) curves.

$$t_{Halsey} = 0.354 \left(\frac{-5}{\log(p/p_0)} \right)^{1/3} \quad (2.34)$$

$$t_{Harkins\&Jura} = \left(\frac{0.1399}{0.034 - \log_{10}(p/p_0)} \right)^{1/2} \quad (2.35)$$

t-plot method

The t-plot method is an empirical method developed as a tool to determine the surface area of porous materials, which can also be used for other calculations, such as external surface area and pore volume.⁽²¹⁾ A plot is constructed, where the isotherm loading data is plotted versus the ideal thickness of the adsorbate layer, obtained through a t-curve (section 2.3.1). It stands to reason that, in the case when the experimentally measured isotherm conforms to the model, a straight line will be obtained with its intercept through the origin. However, as in most cases there are differences between adsorption in pores and surface multilayer adsorption, the t-plot will deviate and reveal features which can be analysed to obtain material characteristics. For example, a sharp vertical deviation will indicate condensation in a type of mesopore while a gradual slope will indicate adsorption on a specific surface.

The slope of a linear section can be used to calculate the area where adsorption is taking place. If the linear region occurs at low loadings, it will represent the total surface area of the material. If at the end of the curve, it will instead represent adsorption on external surface area. The formula to calculate an area starting from the t-plot slope is presented in Equation 2.36, where ρ_l is the liquid density of the adsorbate at experimental conditions.

$$a_{surface} = \frac{sM_m}{\rho_l} \quad (2.36)$$

If the linear region selected is after a vertical deviation, the intercept of the calculated line will no longer pass through the origin. This intercept can be used to calculate the volume of the filled pore through the following equation:

$$V_{ads} = \frac{iM_m}{\rho_l} \quad (2.37)$$

As the t-plot method compares the experimental isotherm with an ideal model, care must be taken to ensure that the t-curve is an accurate representation of the thickness of the adsorbate layer. Since there is no such thing as a universal thickness curve, a reliable model which is applicable to both material and adsorbate should be chosen. It should also be noted that, features on the t-plot found at loadings lower than the monolayer thickness may not have any physical meaning.

α_s Method

In order to extend the t-plot analysis with other adsorbents and non-standard thickness curves, the α_s method was devised.⁽²²⁾ Instead of attempting to find an ideal isotherm that describes the thickness of the adsorbed layer, a reference isotherm is used. This isotherm is measured on a non-porous version of the same material, which is assumed to have identical surface characteristics. The dimensionless α_s values are obtained from this isotherm by dividing the loading values by the

amount adsorbed at a specific relative pressure, usually taken as $p/p_0 = 0.4$ since nitrogen hysteresis loops theoretically close at this point.

$$\alpha_s = \frac{n_a}{n_{0.4}} \quad (2.38)$$

The analysis then proceeds as in the t-plot method, with the same explanation for observed features. The only difference is that the surface area calculation from linear regions observed uses the known specific area of the reference material.

$$A = \frac{sA_{ref}}{(n_{ref})_{0.4}} \quad (2.39)$$

The reference isotherm chosen for the α_s method must be a description of adsorption on a completely non-porous sample of the same material. It is often impossible to obtain such a version. Furthermore, an adsorption isotherm on a non-porous solid may be a challenging endeavour, due to the small ratio of surface area to volume.

2.3.2. Assessing porosity

Characterization of pore sizes and their distribution in a porous material is often the main goal when performing adsorption experiments. When it comes to such materials, three kinds of pore sizes can be defined, based on their lengthscale: micropores (<2 nm), mesopores (2 nm to 50 nm), and macropores (>50 nm).

Macropores are generally unable to be characterised through adsorption, with methods such as mercury intrusion porosimetry as the standard for pore size determination at this lengthscale, although other alternatives have been suggested⁽²³⁾ due to the high toxicity of mercury.

In the mesopore range, “classical” methods are often used, which are based on the application of Kelvin’s equation pertaining to capillary condensation. This equation calculates the critical pressure at which the fluid completely files a pore of a specific diameter. It is applicable to a range of geometries is used in multiple approaches such as the Barrett-Joyner-Halenda (BJH) method or the Dollimore-Heal (DH) method.

For microporous materials, the Kelvin equation, with its assumption of continuous fluid properties and comparable density of the adsorbed state to bulk liquid density breaks down. An atomistic approach is required, addressing the interaction between solid-fluid and fluid-fluid through potential functions. The Horvath-Kawazoe or HK method is often used, alongside the older Dubinin-Radushkevich model.

Finally, computational methods based on Grand Canonical Monte Carlo (GCMC) and density functional theory (DFT) together with its derivations such as non-local DFT (NLDFT) and quenched solid state DFT (QSDFT) should be mentioned, as they can be used for multiscale (micropore and

mesopore) characterisation. These methods rely on *in-silico* simulation of isotherms on a range of pore sizes, which can then be collated in a so-called *kernel*, able to be used to deconvolute an experimental isotherm to obtain a pore size distribution.

It should be noted that all methods here described require knowledge of the pore geometry and depend on the material having pores which conform to a well-defined shape. Real adsorbents usually have interconnected networks of irregular pores, which the ideal pores used in these models merely approximate.

Mesoporous size distribution

The Kelvin equation Since the Kelvin equation is the basis of most mesoporous PSD calculations, such as the BJH and DH methods, it will be described first. The original form of the equation (Equation 2.40) gives the dependence of pressure on the radius of curvature of a meniscus in a pore r by means of surface tension γ , molar liquid volume, here expressed as $v_l = M_m / \rho_l$ and the fluid contact angle with the surface θ . The fluid is often assumed to be fully wetting, with $\theta = 0$ and $\cos\theta = 1$.

$$\ln\left(\frac{p}{p_0}\right) = -\frac{\gamma M_m}{\rho_l RT} \frac{2\cos\theta}{r} \quad (2.40)$$

To apply the Kelvin equation to different types of pore systems, the generalized form presented in Equation 2.41 is used. It replaces the meniscus radius by a mean radius of curvature r_m .

$$\ln\left(\frac{p}{p_0}\right) = -\frac{\gamma M_m}{\rho_l RT} \frac{2}{r_m} \quad (2.41)$$

The mean radius of curvature is defined through the two principal radii of the curved interface.

$$\frac{1}{r_m} = \frac{1}{2} \left(\frac{1}{r_1} + \frac{1}{r_2} \right) \quad (2.42)$$

The relationship of the Kelvin radius r_m to the actual pore radius is more subtle, as it depends on pore geometry and the filling state of the pore.⁽²⁴⁾ If considering a cylindrical pore open at both ends, the radius reduces to the original Kelvin equation during the desorption phase, and takes other values with different combinations of parameters as can be seen in Table 2.2.

According to Rouquerol⁽⁸⁾, in adopting this approach, it is assumed that:

- The Kelvin equation is applicable over the pore range (mesopores). Therefore in pores which are below a certain size (around 2.5 nm), the granularity of the liquid-vapour interface becomes too large for classical bulk methods to be applied.
- The meniscus curvature is controlled by pore size and shape. Ideal shapes for the curvature are assumed.

Table 2.2.: Assumed relationship between pore geometry and meniscus geometry during adsorption and desorption

Pore geometry	Assumed meniscus geometry	
	Adsorption	Desorption
infinite slit	infinite radius cylindrical	concave
open-ended cylinder	cylindrical	spherical
sphere	spherical	spherical

- Pores are rigid and of well defined shape. Their geometry is considered to be invariant across the entire adsorbate.
- The filling/emptying of each pore does not depend on its location.
- Adsorption on the pore walls is not different from surface adsorption.

The Barrett, Joyner and Halenda (BJH) method The BJH method for calculating pore size distribution is based on a classical description of the adsorbate behaviour in the adsorbent pores.⁽¹⁾ Under this method, the guest is adsorbing on the pore walls following an ideal model, and decreasing the apparent pore volume until condensation takes place, filling the entire pore. The critical radius is a sum of two radii, the adsorbed layer thickness, which can be modelled by a thickness model (such as Halsey, Harkins & Jura or similar as presented in section 2.3.1) and a critical radius model for condensation/evaporation, based on a form of the Kelvin equation.

$$r_p = t + r_k \quad (2.43)$$

The original model uses the desorption curve as a basis for calculating pore size distribution. Between two points of the curve, the volume desorbed can be described as the volume contribution from pore evaporation and the volume from layer thickness decrease as per Equation 2.43. The computation is done cumulatively, starting from the filled pores and calculating the volume adsorbed in a pore for each point using the following equation:

$$V_p = \left(\frac{\bar{r}_p}{\bar{r}_k + \Delta t_n} \right)^2 \left(\Delta V_n - \Delta t_n \sum_{i=1}^{n-1} \Delta A_p + \Delta t_n \bar{t}_n \sum_{i=1}^{n-1} \frac{\Delta A_p}{\bar{r}_p} \right) \quad (2.44)$$

where

$$A = 2\Delta V_p / r_p \quad (2.45)$$

In the BJH equation:

- ΔA_p is the area of the pores
- ΔV_p is the adsorbed volume change between two points

- \bar{r}_p is the average pore radius calculated as a sum of the Kelvin radius and layer thickness of the pores at pressure p between two measurement points
- \bar{r}_k is the average Kelvin radius between two measurement points
- \bar{t}_n is the average layer thickness between two measurement points
- Δt_n is the average change in layer thickness between two measurement points

Then, by plotting $\Delta V/(2 * \Delta r_p)$ versus the width of the pores calculated for each point, the pore size distribution can be obtained.

The Dollimore-Heal (DH) method The DH or Dollimore-Heal method⁽²⁵⁾ is an extension of the BJH method which takes into account the geometry of the pores by introducing a length component. Like the BJH method, it is based on a classical description of the adsorbate behaviour in the adsorbent pores and uses the same assumptions. The modified equation becomes:

$$V_p = \left(\frac{\bar{r}_p}{\bar{r}_k + \Delta t_n} \right)^2 \left(\Delta V_n - \Delta t_n \sum_{i=1}^{n-1} \Delta A_p + 2\pi \Delta t_n \bar{t}_n \sum_{i=1}^{n-1} L_p \right) \quad (2.46)$$

$$A = 2\Delta V_p / r_p \quad (2.47)$$

$$L = \Delta A_p / 2\pi r_p \quad (2.48)$$

The meaning of each symbol is the same as in the BJH equation. As before, a plot of $\Delta V/(2 * \Delta r_p)$ versus the width of the pores calculated for each point yields the pore size distribution. The Dollimore-Heal method is used on the desorption branch, of the isotherm but often also applied on the adsorption branch.

Microporous size distribution

When it comes to micropores (width <2 nm), classical fluid methods stop being viable. Adsorption of molecules in these pores of comparable scale is highly dependent on the surface properties and on guest-host interaction and leads to adsorbate phase densities which are often very different than those in the bulk liquid state. In order to model adsorption in such pores, a good description of both solid-fluid and fluid-fluid potential functions is required.

The Horvath-Kawazoe (HK) method The H-K method attempts to describe the adsorption within pores by calculation of the average potential energy for a pore.⁽²⁶⁾ The method starts by assuming the relationship between the gas phase as being:

$$R_g T \ln \left(\frac{p}{p_0} \right) = U_0 + P_a \quad (2.49)$$

Here U_0 is the potential function describing the surface to adsorbent interactions and P_a is the potential function describing guest-guest interactions. This equation is derived from the equation

of the free energy of adsorption at constant temperature where the term $T\Delta S^{tr}(w/w_\infty)$ is assumed to be negligible.

If it is assumed that a Lennard-Jones-type potential function can accurately describe the interactions between adsorbate and surface molecules, then the two contributions to the total potential can be replaced by the extended function in Equation 2.50.

$$RT \ln(p/p_0) = N_A \frac{n_a A_a + n_A A_A}{2\sigma^4(l-d)} \times \int_{d/l_2}^{1-d/l_2} \left[-\left(\frac{\sigma}{r}\right)^4 + \left(\frac{\sigma}{r}\right)^{10} - \left(\frac{\sigma}{l-r}\right)^4 + \left(\frac{\sigma}{l-r}\right)^4 \right] dx \quad (2.50)$$

Here l is the width of the pore, d defined as $d = d_a + d_A$ is the sum of the diameters of the adsorbate and adsorbent molecules, n_a is number of molecules of adsorbent and A_a and A_A the Lennard-Jones potential constant of the fluid molecule and solid molecule respectively. They are defined as:

$$A_a = \frac{6mc^2\alpha_a\alpha_A}{\alpha_a/\kappa_a + \alpha_A/\kappa_A} \quad (2.51)$$

and

$$A_a = \frac{3mc^2\alpha_A\kappa_A}{2} \quad (2.52)$$

where m is the mass of an electron, α_a and α_A are the polarizability of the adsorbate and adsorbate molecule and κ_a and κ_A the magnetic susceptibility of the adsorbate molecule and adsorbent molecule, respectively.

The HK method is applicable to slit pores, and it can be extended through modification to cylindrical and spherical pores. It is worth noting that there are several assumptions which limit its applicability.

- The HK method is reliant on knowledge of the properties of the surface atoms. This assumption is true only if the material surface is homogenous. Furthermore, longer range interactions with multiple surface layers are not considered.
- Each pore is modelled as uniform and of infinite length. Materials with varying pore shapes or highly interconnected networks may not give realistic results.
- Only dispersive forces are accounted for. If the adsorbate-adsorbent interactions have other specific contributions, as is the case for dipole-dipole or *pi*-backbonding interactions, the Lennard-Jones potential function will not be an accurate description.
- The model does not have a description of capillary condensation. This means that the pore size distribution can only be considered accurate up to a maximum of 3 nm to 5 nm.

Multiscale computational methods

DFT theory emerged as a rigorous description of molecular adsorption in pores.⁽²⁾ It calculates the properties of the fluid directly from the forces acting between constituent molecules through a sta-

tistical mechanical approach. Latter developments, like non-local DFT (NLDFT)⁽³⁾, which makes an account for short range molecule correlation and therefore for the changes in the density profile around the pore walls, and quenched solid state DFT (QSDFT)⁽²⁷⁾, which allows for heterogeneity of pore walls to be incorporated in the model, have improved the accuracy of the method.

The density functional theory approach can therefore simulate adsorption isotherms on pores of different geometries and sizes. By defining a pore geometry and running the simulation with a range of pore radii, a collection of isotherms is obtained. If an experimental isotherm is thought of as a sum of adsorption isotherms in different size pores, then it stands to reason that the preponderence of those pores can be calculated through deconvolution.

Since the DFT method can model adsorbate condensation behaviour, as well as micropore filling and multilayer adsorption, it can be used for multiscale pore size distribution. The downside is that DFT kernels are temperature, probe, pore-geometry and adsorbent specific and as such are not universally applicable.

2.3.3. Predicting multicomponent adsorption

Until now, we have only referred to isotherms pertaining to the adsorption of a single adsorbate. However, besides gas storage, most if not all industrial applications of adsorbents involve multiple chemical species undergoing competitive adsorption. Experiments involving several adsorbents are generally difficult and time consuming. There is therefore a need to predict such multicomponent systems in order to rapidly screen for potentially interesting separations starting from pure component data.

To this end, several methods have been devised, with perhaps the most common approach as considering the adsorbed phase as an analogue to a fluid mixture, in a manner analogous to the vacancy solution theory presented in subsection 2.2.10. This method, also known as ideal adsorbed solution theory (IAST) will be presented here. Other multicomponent theories such as real adsorbed solution theory (RAST) or the Nitta model exist, but usually require more information such as specific surface binary activity coefficients, and are therefore less suited to a general approach. Furthermore, the IAST method has been proven^(28,29) to be successful in the prediction of multicomponent adsorption even when considering adsorption in microporous materials such as MOFs.

Originally derived by Myers and Prausnitz⁽³⁰⁾, the IAST model is based on three main assumptions. First, that the same surface area is available for all components. Then it is assumed that the mixture behaves like an ideal solution at constant spreading pressure and temperature. This means the spreading pressure of each component is the same as the surface potential of the mixture π and therefore the mean strength of interaction is equal between all molecules of solution. Finally the surface adsorbed phase is assumed to be at equilibrium with the gas phase. Equation 2.53 can then be written, where $p_{i,g}$ is the partial pressure of the component in the gas phase, $p_i^0(\pi)$ the pressure

of that component which will give the same spreading pressure on the surface and x_i is its fraction in the adsorbed phase.

$$p_{i,g} = p_i^0(\pi) x_i \quad (2.53)$$

$$\frac{\pi A}{R_g T} = \int_0^{P_i^0} n_{ads,i} d\ln(p_i) \quad (2.54)$$

$$\sum_{i=1}^N x_i = 1 \quad (2.55)$$

In order to account for non-ideality of the gas phase fugacity can be used instead of pressure, with a suitable equation of state required to relate it to bulk pressure. The pressure and spreading pressure are then related through the integrated Gibbs isotherm (Equation 2.54). As the sum of all fractions in the adsorbed phase is equal to unity (Equation 2.55), the equations can be solved for a given pressure and gas composition to give the fractions of each component in the adsorbed phase at the hypothetical pressure P_i^0 . The total amount adsorbed can then be calculated.

$$\frac{1}{n_{ads,t}} = \sum_{i=1}^N \frac{x_i}{n_{ads,i}^0} \quad (2.56)$$

Finally, the number of moles adsorbed for each component is given by multiplying the total amount adsorbed by the fraction of each component.

$$n_{ads,i} = x_i n_{ads,t} \quad (2.57)$$

In order to calculate the spreading pressure, an adsorption model such as the ones presented in section 2.2 is required. By substituting the amount adsorbed (n_{ads}) in Equation 2.53 and calculation of the resulting integral, an expression for spreading pressure can be determined. The integral can only be evaluated analytically in the case of a few models, for example in the previously mentioned Henry, Langmuir and multi-site Langmuir, BET, Quadratic and Temkin models. In other cases, a numerical approach must be used for its calculation. An alternative to using a model is to use an interpolation method between recorded experimental points to approximate the amount adsorbed at a pressure p . Numerical quadrature is then used to evaluate the integral and obtain the spreading pressure.

2.4. pyGAPS overview

After a description of adsorption and its application to porous material characterisation and prediction of mixture adsorption, the code which was developed to tackle this type of processing can be presented.

The software was imagined for use in two types of scenario. First, as a command line interface, in common data science environments such as IPython and Jupyter. The typical user working in

these environments is likely to be processing a small batch of results at a time, and is interested in obtaining the results in graphical form. For this type of application, the framework should provide an unobtrusive way of importing the user data, as well as present an API which does not require extensive knowledge of processing methods. Finally, a graphing environment is required which will allow the user to visualise their dataset and results.

The second envisaged application is related to bulk data processing. Requirements here shift towards parameter control, scripting and extensibility. The framework API should offer the option to change implicit parameters, select calculation limits and return the results in a numerical form for further processing. This type of application is also likely to require storage of isotherms in a database or under other types of data files.

2.4.1. Core structure

In order to offer a clear structuring of functionality, pyGAPS introduces several classes which abstract data and concepts for facile interaction (Figure 2.4). The classes are intuitively named: Isotherm, Sample and Adsorbent.

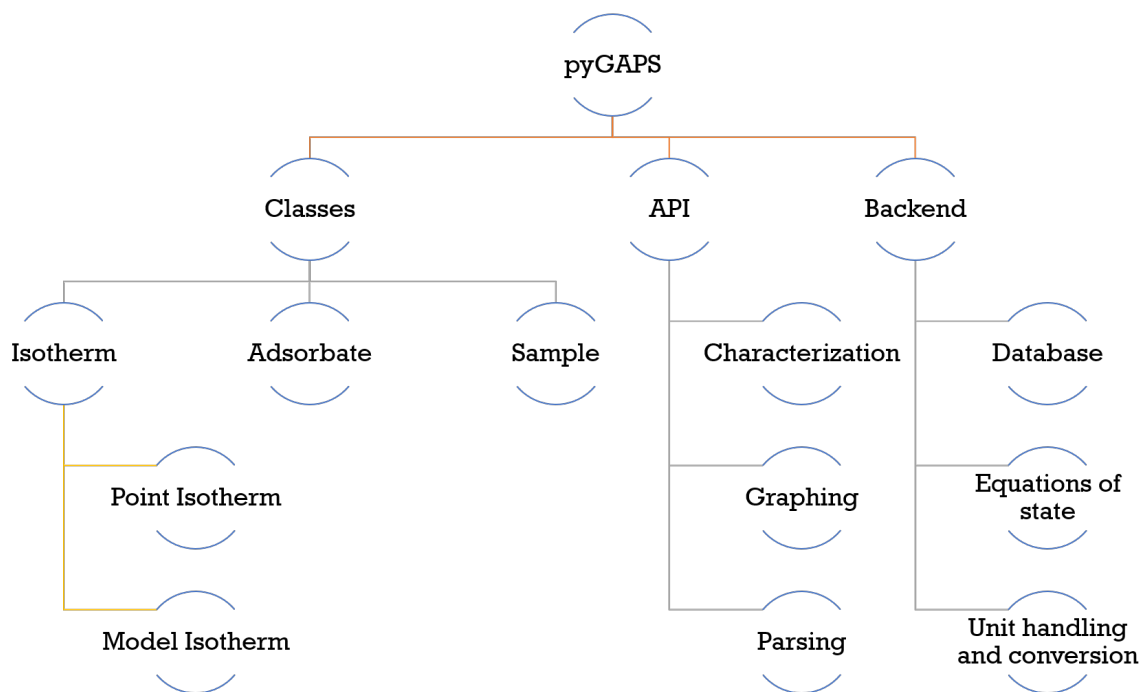


Figure 2.4.: An overview of the package structure

The Isotherm class

The Isotherm class is a representation of an adsorption isotherm i.e. a function of the amount adsorbed, or loading, with pressure at a fixed temperature. The class also contains other information relating to the isotherm, such as the material name and batch it describes, the adsorbate used and other user-defined properties.

This relationship can be defined in two ways:

- individual pressure-loading pairs of points which have been recorded as part of a measurement or
- as a mathematical function describing the relationship between the two properties.

As such, the Isotherm class is used as a parent class for two subclasses: the PointIsotherm which contains datapoints and the ModelIsotherm, containing a model such as Henry, Langmuir etc. The two classes are interchangeable as they share most methods and properties. Once an instance of an Isotherm class is created, it can then be used for the processing, conversion and graphing capabilities of pyGAPS.

The Sample class

The isotherm classes contain the name and batch of the sample they are measured on in a string format. The user might want to specify other information about the material, such as the date of synthesis or the material's density, as well as store this information in the database. For this case, pyGAPS provides the Sample class. The framework uses the string values in the isotherm to connect an Isotherm instance to a specific Sample. If sample-related properties are needed for processing, such as conversion of an isotherm from a mass basis to a volume basis, this class will be checked for the required data.

The Adsorbate class

Finally, in order for many of the calculations included in pyGAPS to be performed, properties of the adsorbate used are needed e.g. liquid density, vapour pressure etc. The Adsorbate class is provided for this purpose, which is connected to an Isotherm class in an identical manner as the Sample class. The physical properties are calculated automatically through an equation of state, either the open source CoolProp library⁽³¹⁾ or the NIST-made REFPROP⁽³²⁾, if available on the user's computer. The properties can also be retrieved from the internal database or specified by the user.

2.4.2. Creation of an Isotherm

An Isotherm can be created either from the command line directly or through an import from a supported format. For direct creation, the code takes two kinds of inputs: the data itself, in the form of a pandas .DataFrame, and the isotherm parameters describing it. Only four parameters are strictly required: the material name, the material batch, the adsorbate used and the experimental temperature. Other parameters can be passed as well and will be stored in the isotherm class. An example code can be seen in Listing 2.1.

The DataFrame must contain a column containing the pressure points and one containing the corresponding loading points of the isotherm. Other columns can also be passed, when secondary data such as enthalpy of adsorption is present at each measurement point. These columns will be saved in the case of the PointIsotherm class and can be plotted afterwards. The framework can automatically attempt to determine the adsorption and desorption branches, by analysing the input data. Alternatively, the user can manually specify which points belong to each branch.

If no unit data is specified in the constructor, the framework will assume that the isotherm is in units of mmol g^{-1} loading as a function of bar. Both the units and the basis can be specified, as it is explained in a latter section.

Finally, the data is saved in the newly created class or used to generate parameters for a model such as BET, Langmuir, etc., in the case of a PointIsotherm and ModelIsotherm respectively. The creation of Sample and Adsorbate instances is similar.

Alternatively, the isotherm can be imported from a file containing a format that is recognised by pyGAPS. Parsing from suitably structured JSON, CSV and Excel files is supported.

Both PointIsotherms and ModelIsotherm can be created from an instance of the other, by using the available functions. As an example, a model is automatically generated from the previous isotherm using the function in Listing 2.2, which fits all available models and selects the one with the lowest residuals between the fitted function and the real data.

Listing 2.2: Guessing the best model

```
1 model = pygaps.ModelIsotherm.from_pointisotherm(iso, guess_model=True)
```

```
Attempting to model using Henry
Model Henry success, rmse is 7.42
Attempting to model using Jensen-Seaton
Modelling using Jensen-Seaton failed
.....
Best model fit is Quadratic
```

Listing 2.1: Creating the PointIsotherm

```

1 point_isotherm = pygaps.PointIsotherm(
2
3     # First the pandas.DataFrame with the points
4     # and the keys to what the columns represent.
5
6     pandas.DataFrame({
7         'pressure' : [1, 2, 3, 4, 5, 3, 2],
8         'loading' : [1, 2, 3, 4, 5, 3, 2],
9         'enthalpy' : [15, 15, 15, 15, 15, 15, 15],
10        'xrd_peak_1' : [0, 0, 1, 2, 2, 1, 0],
11    }),
12
13    loading_key='loading',           # The loading column
14    pressure_key='pressure',        # The pressure column
15    other_keys=['enthalpy',
16                'xrd_peak_1'],      # The columns containing other data
17
18    # Some of the unit parameters can be
19    # specified if desired.
20
21    pressure_mode='absolute',       # absolute pressure
22    pressure_unit='bar',           # with units of bar
23    adsorbent_basis='mass',         # adsorbent mass basis
24    adsorbent_unit='kg',           # with units of kg
25    loading_basis='mass',          # loading mass basis
26    loading_unit='g',              # with units of g
27
28    # Finally the isotherm description
29    # parameters are passed.
30
31    'sample_name' : 'carbon',       # Required
32    'sample_batch' : 'X1',          # Required
33    'adsorbate' : 'nitrogen',       # Required
34    't_exp' : 77,                  # Required
35    't_act' : 150,                 # Recognised / named
36    'user' : 'Username',           # Recognised / named
37    'DOI' : '10.000/mydoi',        # Unknown / user specific
38 )

```

2.4.3. Units

When computers work with physical data, units are often a matter that introduces confusion. Here we explain how pyGAPS handles units and other physical world concepts such as relative pressure and mass or volume basis.

The following dimensions can be specified for an Isotherm: the measurement *pressure*, the quantity of guest adsorbed or *loading* and the amount of adsorbent material the loading is reported on, or *adsorbent*.

Pressure can be reported either in an absolute value, in several common units such as bar, torr, Pa, or as *relative pressure*, absolute pressure divided by the saturation vapour pressure of the adsorbate at the respective measurement temperature. Conversions between the two modes are automatic and handled internally.

Both the *loading* and *adsorbent* can be reported in three different bases: a molar basis, a mass basis or a volume basis. Within each basis different units are recognised and can be easily converted. The conversions between bases can also easily performed if the required conversion factors (i.e. molar mass and density) are available. For *loading*, these factors are automatically calculated internally using the available equation of state, while for the *adsorbent* they should be provided by the user in the respective Sample class.

2.4.4. Workflow

Once an isotherm object is created, it will be used for all further processing. The class contains methods which can be used to inspect the data visually, or retrieve parts of the isotherm such as the adsorption or desorption branches with user-chosen limits or units. Singular values of pressure or loading can be calculated, either through interpolation in the case of a PointIsotherm or by evaluation of the internal model in the ModelIsotherm. For an isotherm with datapoints, these can also be converted into different units or modes.

Characterisation functions take an isotherm object as their first parameter. This is the case for the BET area, Langmuir area, t-plot, α_s plot, and pore size distribution methods. These characterisation functions attempt to automate as much of the process as possible. For example, the BET area limits are automatically calculated using the Rouquerol⁽⁸⁾ method, with all the checks implemented into the code. In another example the straight line sections of the t-plot are determined automatically through a calculation of the second derivative of the transformed isotherm. For detailed control, there are available options for each individual method, such as manual BET limits, different thickness functions for the t-plot or Kelvin-based mesoporous pore distribution methods, custom parameters for the Horvath-Kawazoe microporous pore distribution, custom DFT or NLDFT kernels and more. The results are returned in a numerical form for further processing, or can be directly displayed if the verbose parameter is passed.

2.4.5. Characterisation using pyGAPS

BET and Langmuir surface area

pyGAPS comes with several common methods used to determine surface area, some with theoretical basis like the IUPAC-recommended BET method and some empirical, such as the t-plot method.

Starting from an isotherm object, it is easy to calculate the nitrogen BET area of a sample of UiO-66(Zr) MOF by using the code in Listing 2.3. The framework automatically applies the methodology described in section 2.3.1 to find the optimum pressure range. The `verbose=True` option prints a short text with all the calculation variables as well as graphing the BET and Rouquerol plots (Figure 2.5). The user can override automatic pressure range selection by using the range parameter (`limits=(0.05, 0.3)`).

Listing 2.3: Calculating a BET area

```
area_dict = pygaps.area_BET(isotherm, verbose=True)
```

```
BET surface area: a = 1277 m2/g
Minimum pressure point chosen is 0.005 and maximum is 0.034
The slope of the BET fit: s = 76.344
The intercept of the BET fit: i = 0.052
BET constant: C = 1463
Amount for a monolayer: n = 0.01309 mol/g
```

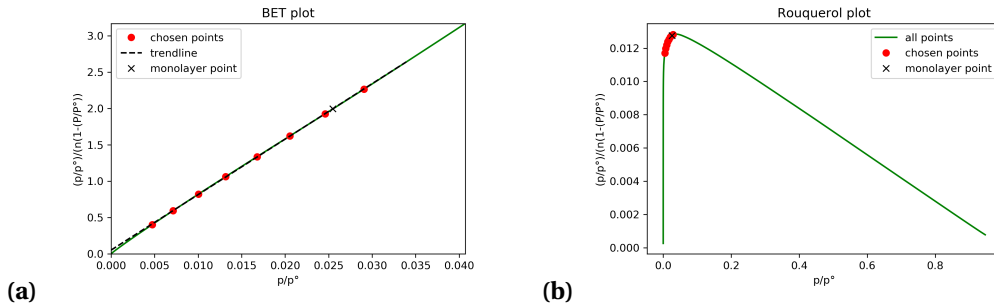


Figure 2.5.: Output from the BET area function (a) the BET plot showing the selected points for fitting the equation, as well as the location of the statistical monolayer and (b) the Rouquerol plot for this calculation.

Similarly to the BET area, the Langmuir area is calculated by using the code in Listing 2.4. The framework will alert the user if the correlation is not linear in the selected range. In this example, the surface area of a nitrogen isotherm measured on a MCM-41 sample is calculated. Here the `verbose=True` option prints a short text with all the calculation results, as well as generating the Langmuir plot as seen in Figure 2.6a. If desired the user can override automatic pressure range selection as seen in the second example in Listing 2.4.

Listing 2.4: Calculating a Langmuir area

```
1 area_dict = pygaps.area_langmuir(isotherm, verbose=True)
```

| WARINING The correlation is not linear!

```
1 area_dict = pygaps.area_langmuir(isotherm,
2                                     limits=(0.05, 0.3),
3                                     verbose=True)
```

```
Langmuir surface area: a = 415 m2/g
Minimum pressure point chosen is 0.0 and maximum is 0.194
The slope of the Langmuir line: s = 234.968
The intercept of the Langmuir line: i = 1.607
The Langmuir constant is: K = 146
Amount for a monolayer: n = 0.00426 mol/g
```

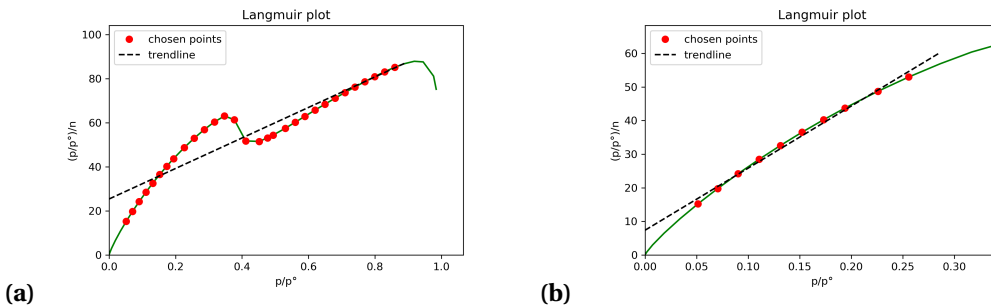


Figure 2.6: Output from the Langmuir area function (a) the Langmuir plot showing the automatic fitting attempt which generates a warning and (b) a manually selected pressure range for the Langmuir plot.

The t-plot Method and α_s Method

The t-plot method requires a model for the thickness of the adsorbed layer, as described in section 2.3.1. The two equations presented there have been implemented in pyGAPS. These t-curves are selected by name as parameters in the functions that use them. The user can also define their own t-curve as a function and pass it as a parameter.

When the t-plot function is called without any parameters except an isotherm, the framework will attempt to find plateaus in the data and automatically fit them with a straight line, returning a dictionary with the slope, intercept, calculated pore volume and specific area for each linear region found. The same MCM-41 nitrogen isotherm analysed in the previous section is used in Listing 2.5. The first command will generate the graph in Figure 2.7a.

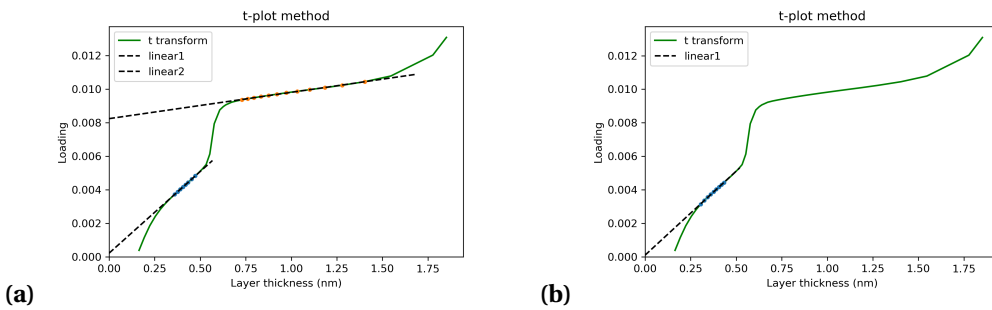
The first linear region in Figure 2.7a can be attributed to adsorption on the mesopore surface, while the second one represents adsorption on the available surface after mesopore filling. Therefore, the surface area values calculated for the first and second region correspond to the area of

Listing 2.5: Generating a t-plot

```

1 # using automatic region detection
2 pygaps.t_plot(isotherm, verbose=True)
3
4 # specifying a manual region
5 pygaps.t_plot(isotherm, limits=(0.3,0.44), verbose=True)
6
7 # using the Halsey thickness curve
8 pygaps.t_plot(isotherm, thickness_model='Halsey', verbose=True)
9
10 # defining a custom t-curve to use in the t-plot
11 def carbon_model(relative_p):
12     return 0.88*(relative_p**2) + 6.45*relative_p + 2.98
13
14 pygaps.t_plot(isotherm, thickness_model=carbon_model, verbose=True)

```

**Figure 2.7.:** Output from the t-plot method function (a) an automatically obtained t-plot with the calculated fit regions and (b) a manually selected range for the t-plot.

the mesopores and the external particle area, respectively. As only one pore filling event occurs, the pore volume calculated for the second region gives us the mesopore volume. We can obtain a more accurate result for the surface area by fitting the first linear region to a zero intercept through manual region selection, as shown in the second example in Listing 2.5.

Finally, the framework allows for the thickness model to be substituted with an user-provided function which will be used for the t-plot. Usage of a carbon black-type thickness curve is presented in the last example in Listing 2.5.

To generate an α_s -plot in pyGAPS, both an analysis isotherm and a reference isotherm must be supplied as shown in Listing 2.6, using the same isotherm as for the t-plot. In this example, the reference isotherm is measured on non-porous silica. The reference material area can be specified by using the `reference_area` parameter. If not specified, it is automatically calculated by applying the BET method to the reference isotherm.

Listing 2.6: Generating an α_s -plot

```

1 pygaps.alpha_s(isotherm,
2                     reference_isotherm=isotherm_r,
3                     verbose=True)

```

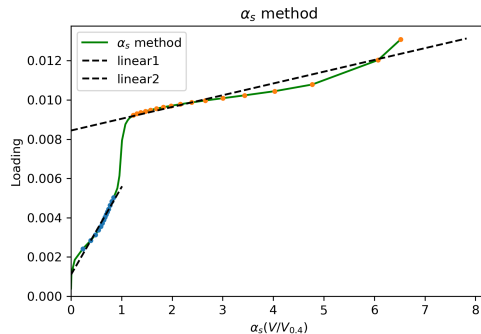


Figure 2.8.: Output from the α_s -plot function showing two automatically fit regions.

Pore size distribution calculations

Both mesoporous, microporous and DFT fitting routines can be used to calculate a pore size distribution in pyGAPS. While the generation of DFT kernels is outside the scope of the framework, it is able to use user-provided kernels to fit adsorption isotherms, and comes with a basic kernel applicable for N₂ adsorption at 77 K on carbon slit pores.

The MCM-41 sample is a mesoporous material, which is expected to have a well-defined pore size in the range of 2.5 nm to 5 nm. The BJH method can be readily applied on the desorption branch of the measured isotherm, through the code in Listing 2.7. The Harkins and Jura thickness function is automatically selected, while the default cylindrical pore geometry is used.

Listing 2.7: PSD using the BJH method

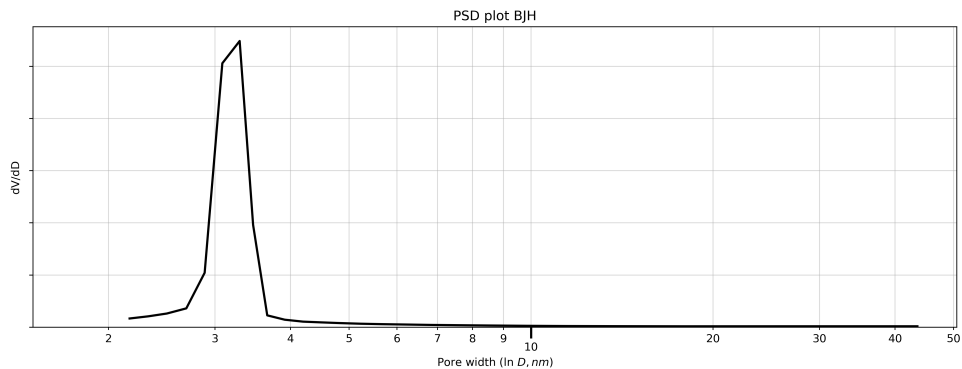
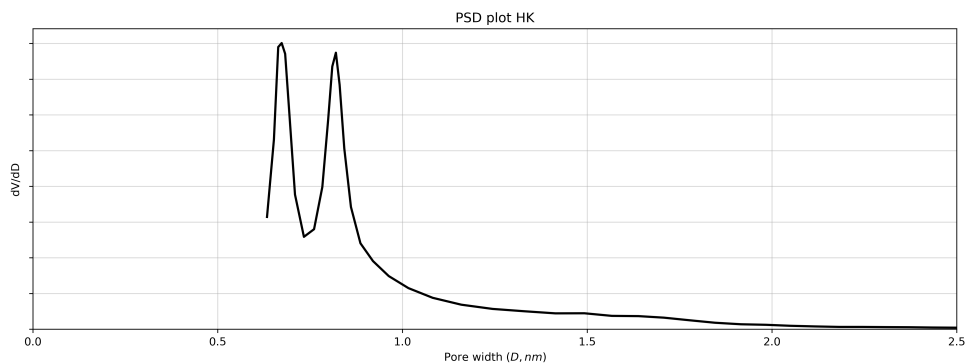
```

1 result_dict = pygaps.mesopore_size_distribution(
2     charact_iso,
3     psd_model='BJH',
4     verbose=True
5 )

```

The resulting pore size distribution in Figure 2.9, confirms the analysis, with a single sharp pore distribution at 3 nm.

A microporous analysis cannot be performed on MCM-41, since it does not contain any pores under 2.5 nm, where such methods are applicable. Instead, the UiO-66(Zr) isotherm is used. This MOF has two micropores, a tetrahedral and octahedral one which are accessible through an 0.8 nm window. The HK method is used for calculating the pore size distribution, as displayed in Listing 2.8.

**Figure 2.9.:** BJH pore size distribution**Figure 2.10.:** Pore size distribution calculated through the Horvath-Kawazoe method on the UIO-66(Zr) sample

The pyGAPS framework contains the required physical properties for the most commonly used adsorbates in its database, as well as properties from literature for several materials: the original parameters developed by Horvath and Kawazoe for a carbon surface⁽²⁶⁾ and the oxide surface parameters published by Saito and Foley.⁽³³⁾ The user can also provide a custom dictionary for these parameters when calling the function as can be seen in the second example in Listing 2.8.

Finally, to determine a pore size distribution using DFT kernel fitting, the `dft_size_distribution` function is used. The function takes an `Isotherm` object and a path to a CSV representation of the DFT kernel. The code then loads the kernel either from disk or memory and applies a minimization function on the sum of squared differences of the sum of all individual kernel isotherms to generate the contribution of each as per the following equation:

$$f(x) = \sum_{p=p_0}^{p=p_x} \left(n_{p,\text{exp}} - \sum_{w=w_0}^{w=w_y} n_{p,\text{kernel}} X_w \right)^2 \quad (2.58)$$

The user can specify their own kernel in a CSV format or, alternatively, use the internal kernel included with the framework. This kernel is only applicable on N₂ adsorption at 77 K on carbon

Listing 2.8: Using the HK method for PSD

```

1 # Calling the HK micropore method with the
2 # Saito-Foley oxide surface parameters
3 result_dict = pygaps.micropore_size_distribution(
4     isotherm,
5     psd_model='HK',
6     adsorbent_model='OxideIon(SF)',
7     verbose=True
8 )
9 # Defining a custom adsorbate parameter dictionary
10 # and using it in the HK method
11 adsorbate_params = {
12     'magnetic_susceptibility': 3.6e-35,
13     'molecular_diameter': 0.3,
14     'polarizability': 1.76e-30,
15     'surface_density': 6.71e+18
16 }
17 result_dict = pygaps.micropore_size_distribution(
18     isotherm,
19     psd_model='HK',
20     adsorbent_model='OxideIon(SF)',
21     adsorbate_model=adsorbate_params,
22     verbose=True
23 )

```

slit-like pores in the range of 0.4 nm to 10 nm.

The isotherm measured on the microporous carbon Takeda 5A is used as an input for the DFT fitting routine (Listing 2.9), using the available internal kernel. The resulting PSD shows that the material is not completely microporous, with a wide mesopore component present.

Listing 2.9: DFT size distribution in pyGAPS

```

1 result_dict = pygaps.dft_size_distribution(
2     charact_iso,
3     'internal',
4     verbose=True
5 )

```

Multicomponent adsorption modelling

The pyGAPS framework includes a modified version of the pyIAST code⁽³⁴⁾ which has been adapted to work with the Isotherm classes. Both model isotherms and real data can be used for IAST, with spreading pressure being calculated through the underlying isotherm model or through interpola-

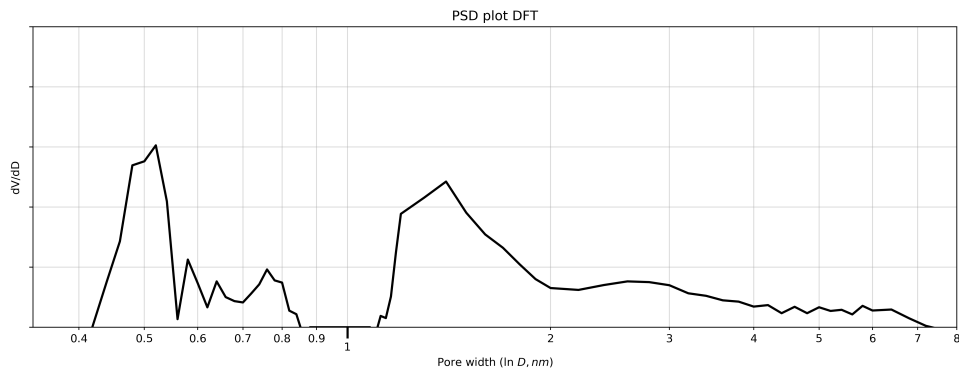


Figure 2.11.: Pore size distribution calculated through the DFT fitting on the Takeda 5A carbon

tion, respectively as detailed in subsection 2.3.3.

As an example, two common case studies will be examined: the capture of CO₂ from N₂ and separation of propane and propylene. Models of isotherms recorded on a Takeda 5A microporous carbon are generated using the automatic fitting functionality. The original isotherms and the best-fitting models are displayed in Figure 2.12a for the CO₂-N₂ pair and in Figure 2.13a for the C₃H₈-C₃H₆ pair.

For the carbon dioxide separation, all equilibrium points for the adsorbed and gaseous phases are simulated at different proportions of the two gases, with a total pressure of 1 bar. To do this we use the `pygaps.iast_vle()` function which produces an analogue of a vapour-liquid equilibrium at a specified pressure for a binary mixture. The resulting graph can be seen in Figure 2.13b. As expected, the predicted adsorbed mixture is rich in carbon dioxide. Selectivity can also be calculated in a single point, with the value at a concentration analogous to flue gas of 15% CO₂ being 16.5.

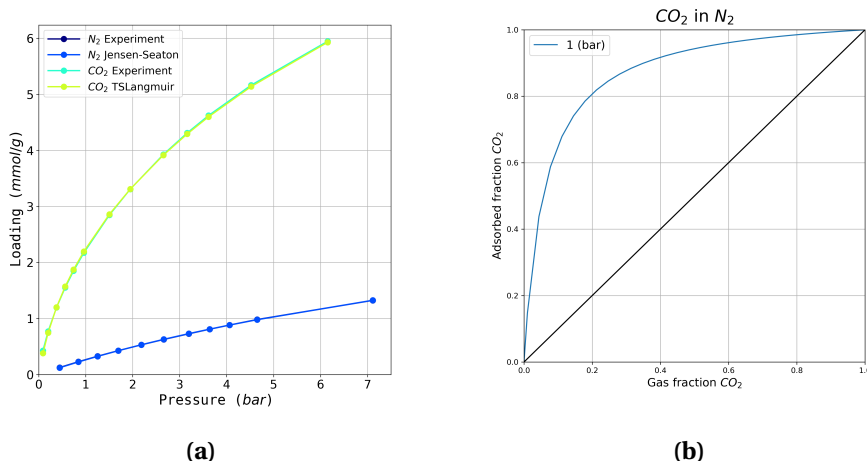


Figure 2.12.: Modelling binary adsorption of CO₂ and N₂: (a) the pure component isotherms and their best fit models and (b) the predicted composition of the gaseous and adsorbed phase for different fractions of CO₂ at 1 bar

For the propane-propylene separation, the selectivity for propane in an equimolar mixture of the two gases is simulated within a pressure range of 0.1 bar to 5 bar. It can be seen that there is little or no preference for the unsaturated molecule, though the selectivity increases slightly at pressures above 1 bar.

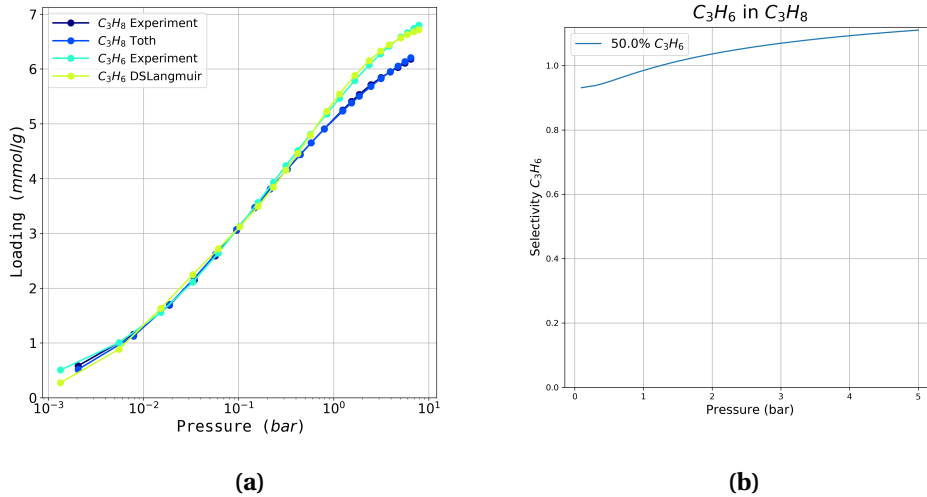


Figure 2.13.: Modelling binary adsorption of a propane-propylene mixture: (a) the pure-component isotherms and their best fit models and (b) the predicted selectivity of propane adsorption of a 50–50% mixture in a range of pressure from 0.1 to 7 bar

2.5. Processing a large adsorption dataset

With the capability for fast processing afforded by pyGAPS, we now turn to using it on an available database of adsorption isotherms. The goal is to test the speed and accuracy of the calculations, as well as to obtain a description of the dataset. Further insights may be obtained from benchmarking of different KPIs, or assessing the reliability of the available data.

2.5.1. The NIST ISODB dataset

The NIST/ARPA-E database of adsorbent materials (ISODB) is a comprehensive set of adsorption isotherms which have been systematically collected from peer-reviewed literature. The data includes measurements on a wide range of materials, from carbon, zeolite, and silica to MOFs and other such PCPs. This resource is a useful tool for reference purposes, as it contains isotherms with many probes at various temperatures. Furthermore, due to the availability of an application programming interface (API), isotherm data can be easily accessed. As such, this database is a great source of data for the kind of large-scale processing which pyGAPS is designed for.

The entire dataset in the NIST adsorption database was downloaded using the publicly available API. This yielded ≈ 26000 isotherms. In order to narrow down the dataset and ensure comparability the following sorting was performed.

- Only isotherms measured with an adsorbate that is available in the pyGAPS database were selected, to allow for calculations using the internal equation of state.
- Isotherms which could not be converted to mmol g^{-1} were discarded outright. This includes data reported on a volume basis of material (as the material density is unknown), simulation data which is reported in units such as molecules per unit cage and fractional coverage isotherms. All remaining isotherms were then converted into mmol g^{-1} using the pyGAPS conversion functionality to ensure a consistent unit set.
- No isotherms with less than 6 measurement points were considered, as it was considered to be the bare minimum required for characterisation.
- Possible outliers were removed from the data by selecting only isotherms recorded under 100 bar, with maximum capacities under 100 mmol and with a temperature of under 443 K. Any such isotherms are likely errors in the data collection process and have little to no physical meaning.

The process of data collation reduced the number of isotherms to ≈ 15800 . A distribution of the isotherms as a function of adsorbate and temperature can be found in Figure 2.14a. We can see that most isotherms are recorded at either 77 K, 273 K or 298 K as these temperatures are readily available through immersion in liquid nitrogen, water-ice mixture, or a thermally controlled water bath respectively. In total, isotherms measured with all 20 probe gasses available in pyGAPS are found in the database, including four common vapours and all linear saturated hydrocarbons up to a carbon number of four.

For an initial round of data processing with pyGAPS, only isotherms recorded with nitrogen at 77 K were selected. These make up ≈ 3500 datapoints, recorded on more than 2200 materials. The BET surface area was then computed for each isotherm, with a distribution as seen in Figure 2.14b. Unfortunately, as many isotherms do not have enough points in the low pressure region, computing a well-defined BET surface area is impossible. In total, only around a third of the isotherms had enough data for this purpose. Several materials are seen to be essentially non-porous with around 80 isotherms recorded having a BET area of less than $100 \text{ m}^2/\text{g}$. As expected, a decrease in number of samples is seen with increasing surface area reflecting the lower preponderence of highly porous materials due to the challenges involved in their creation. Overall, while this initial calculation does not impart any further insights, it serves as an useful overview of the ISODB dataset.

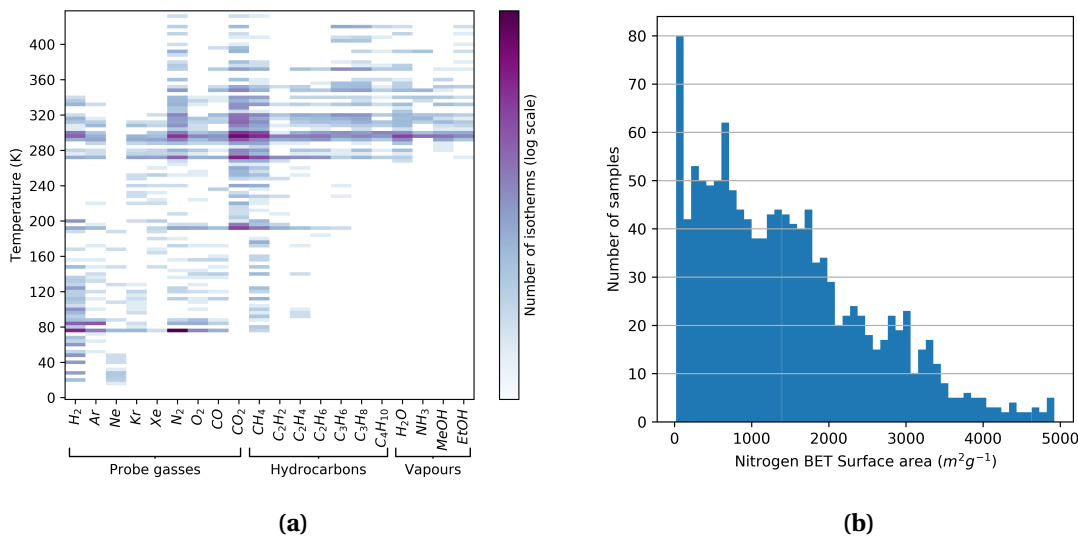


Figure 2.14.: A graphical description of the NIST ISODB dataset. (a) The selected 15800 isotherms presented per adsorbate used and temperature at which the measurement took place. (b) Calculated BET surface area with nitrogen at 77 K for all available isotherms.

2.5.2. A comparison between surface area calculation methods

The Langmuir surface area is an often-reported alternative to the, now standard, BET method area. With such a large dataset at our disposal, we can take the opportunity to observe the differences between results obtained with the two methods. If the Langmuir area is calculated with implicit parameters, by taking the entire available isotherm for the fitting routine, the correlation between the two methods looks like Figure 2.15a. The two results do not agree well, with the Langmuir surface area usually higher than the BET value for the same isotherm. This is a consequence of the Langmuir model assuming adsorption up to a single monolayer with other characteristic phenomena such as multilayer adsorption, pore condensation or multiple types of adsorption types unable to be accounted for. It is for this reason that the Langmuir *should not be used* in adsorption regimes such as nitrogen at 77 K.

If the partial pressure range is narrowed, by only using points up to $0.15 p/p_0$, the correlation improves dramatically, with near-overlap when the area is below $2000 \text{ m}^2/\text{g}$. In this case the selection corresponds to a region below the “knee” of an ideal BET isotherm, before the statistical monolayer is filled.

In truth, the choice of neither model is strictly applicable to determine the accessible area of microporous materials, due to adsorption in such samples being dominated by pore filling mechanisms rather than monolayer formation. However, as detailed by Rouquerol et al.⁽³⁵⁾ and then also shown through comparing simulated and experimental data by Walton and Snurr⁽³⁶⁾, the results produced by judicious application of such models can relate well to the actual surface areas of

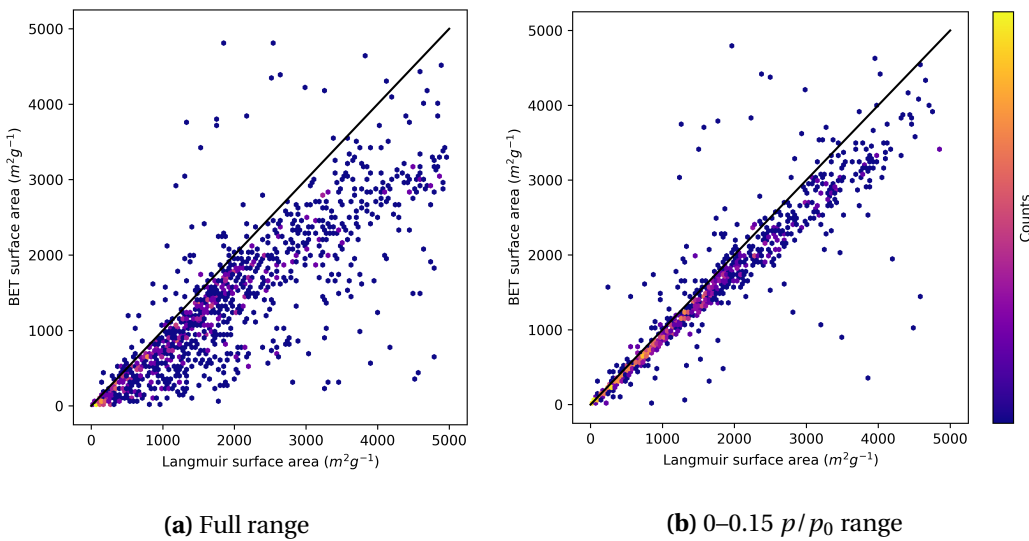


Figure 2.15. Correlation between Langmuir-calculated and BET-calculated surface areas. The black line is a guide for the eye at $S_{Lang} = S_{BET}$.

MOFs.

2.5.3. Variability of the dataset

Before a deeper dive into attempting to relate adsorption isotherm derived parameters to structural properties, an analysis of the reliability of the data from the NIST ISODB should be performed.

The material with the most recorded isotherms is CuBTC, with 122 datapoints. A spread of the calculated BET surface areas, together with the “ideal” area of this MOF as obtained through simulations⁽³⁷⁾ is presented in Figure 2.16. To verify if the variability is due to uncertainty in the surface area calculation a secondary metric, namely the capacity at 0.5 p/p_0 has been calculated and its distribution plotted alongside that of the BET area. The identical trends in both parameters show that there is an inherent uncertainty in the dataset. The results not only have a large standard deviation, but also do not have a typical normal distribution one would expect from repeated sampling of a physical property.

Instead, three normal distributions appear to

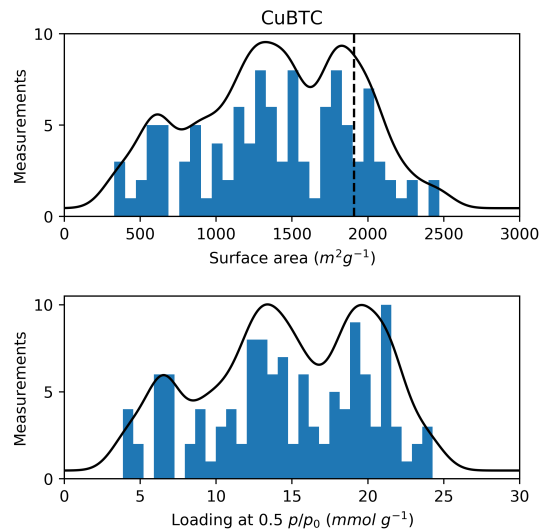


Figure 2.16. A histogram and estimate of the probability density function for (top) BET surface area and (bottom) loading at half saturation pressure for CuBTC. The black dotted line is the simulated surface area of this MOF.

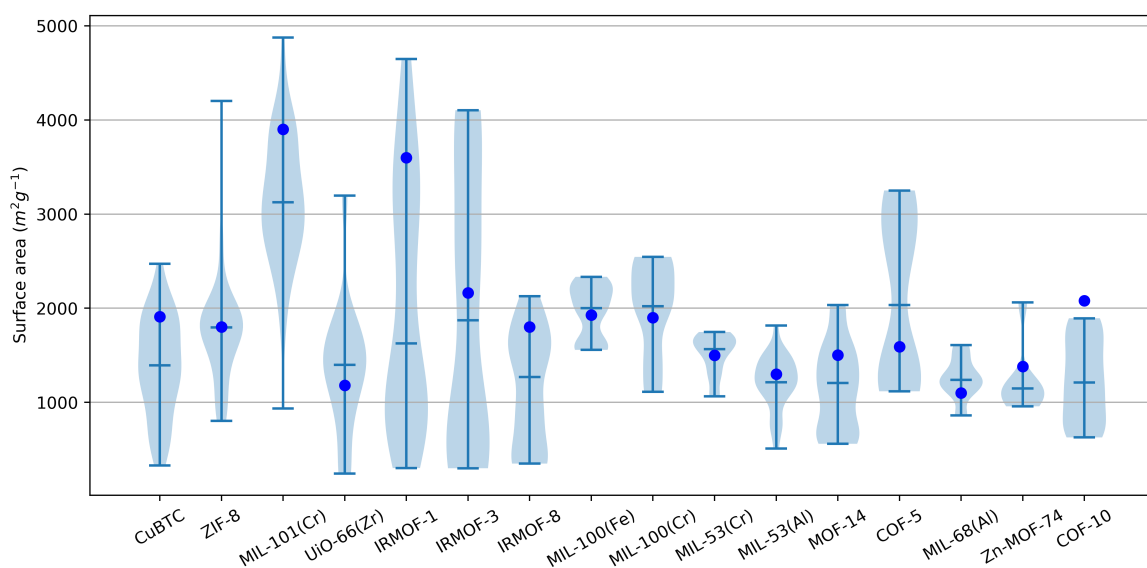


Figure 2.17.: A violin plot of the calculated surface areas for all available nitrogen isotherms on the top 16 MOFs. The top and bottom lines in each plot are the limits for the surface area values. The shaded area is a kernel-density estimate of the probability density function using Gaussian kernels. The median of each dataset is displayed as the horizontal line between the two limits. Finally, the round blue point is the BET surface area of the material as reported in literature through simulation or optimised synthesis.

emerge, one with a median around $500 \text{ m}^2/\text{g}$, a second around $1300 \text{ m}^2/\text{g}$ and a third with a median around $1900 \text{ m}^2/\text{g}$ which also corresponds to the nitrogen accessible surface area determined through simulation. As the NIST data also records the DOI for each isotherm, each measurement can be traced to the publication it originated in. By cherry-picking several studies from each normal distribution we can find that the low surface areas correspond to data measured on modified versions of CuBTC, such as shaped samples ($640 \text{ m}^2/\text{g}$)⁽³⁸⁾, hollow nanoparticles ($450 \text{ m}^2/\text{g}$)⁽³⁹⁾ or nanoplates ($803 \text{ m}^2/\text{g}$).⁽⁴⁰⁾ Studies selected from materials with higher surface area showed no consistent underlying cause for the variability, although some can be accounted for through synthesis method such as mechanochemical synthesis ($1700 \text{ m}^2/\text{g}$)⁽⁴¹⁾, or structural defects ($2050 \text{ m}^2/\text{g}$).⁽⁴²⁾

To extend the analysis to other materials, MOFs with at least 8 recorded nitrogen isotherms were selected, resulting in 16 materials. A violin plot with the results of the calculation for these data-points is presented in Figure 2.17. The blue points mark the surface area of the material as obtained from literature or simulated values or, if not available, the original synthesis paper of the MOF in question. It is obvious that, in most cases, there is a large spread in the calculated values, with some samples such as IRMOF-1, IRMOF-3 and MIL-101(Cr) having a surface area anywhere between $200 \text{ m}^2/\text{g}$ to $5000 \text{ m}^2/\text{g}$. Other materials, such as ZIF-8, the MIL-53 family and MIL-100(Fe) have less variability in their surface areas, although can still be shifted by 200 to $500 \text{ m}^2/\text{g}$.

Similar concerns have been raised for H₂⁽⁴³⁾ and CO₂⁽⁴⁴⁾ measurements. Recently, Sholl and co-workers⁽³⁷⁾ have published a report putting into question the reproducibility of adsorption isotherms, using CO₂ adsorption data from the NIST adsorption database. Their findings highlight a large variability inherent to reported isotherms as on average “one in five CO₂ isotherms [...] cannot be used to provide information that is qualitatively reliable about the properties of the material”. However, in their paper they do not explore the reasons behind the origin of such large variations.

The underlying cause for the poor reproducibility of adsorption isotherms, particularly those measured on metal organic frameworks, is not easy to pinpoint. A large contribution to this divergence is likely accounted for through the variation introduced by the sample preparation method and adsorption apparatus. For example, a recent NIST interlaboratory study in which CO₂ isotherms were recorded on a reference material⁽⁴⁵⁾, received six out of thirteen initial datasets outside the uncertainty range. Errors were determined to arise from sample mass measurement, insufficient activation conditions or improper choice of an equation of state. Other method-specific sources of error exist, such as the lack of a buoyancy correction when using a gravimetric system or a void volume correction when using a volumetric system, both of which can be made if an accurate determination of sample skeletal density is performed. Finally, small differences in thermal gradients, pressure transducer readings, and even the altitude at which the measurement takes place (if a phase change bath is used to control temperature) can also impact the final isotherm.

Such variation is likely minimised when using state-of-the-art adsorption equipment, which eliminates many of the concerns associated with adsorption methodology. *In situ* activation, internal consistency checks for pressure transducers, automatic measurement of skeletal density and associated corrections, reference cells for saturation pressure determination and many other sanity checks are implemented in these machines.

However, it is often the case that the most important factor in the repeatability of MOF adsorption isotherms is not the measurement procedure, but rather the material itself. As evidenced by the closer look at the CuBTC dataset, synthesis method, crystallinity, material form, particle size and contribution of defects all have an impact on the resulting adsorption behaviour of the material. Furthermore, IRMOF-3, the sample with the highest variability in the dataset is known to possess structural flexibility, with the activation procedure responsible for any number of states from a completely open to a completely closed framework.⁽⁴⁶⁾ In this sense, such an analysis of a large MOF dataset can point out which materials tend to be resistant (or susceptible) to the aforementioned sources of variability and can lend themselves to use as standard or reference materials.

2.6. Conclusion

In this chapter, a framework for adsorption data processing is presented, which focuses on standardisation of porous material characterisation through adsorption methods and large-scale pro-

cessing of isotherms. Prediction of multicomponent adsorption is also made possible through IAST calculations.

Analysis of isotherms available in the NIST ISODB, which are collated from literature, shows a comprehensive set of data. A brief comparison between two ways of calculating surface area (BET and Langmuir) as applied to nitrogen isotherms confirms long-standing recommendations of their applicability and use. However, further analysis reveals a large variability present in the measured isotherms on metal-organic frameworks. It was initially hoped to use this dataset as a basis for discovering structure-property relationships pertaining to metal-organic frameworks. However, the uncertainty present in the database and consequently, in the scientific literature, precludes its use for such a purpose. It is therefore essential to rely on carefully recorded lab data if a focus on a particular variable is required, as where systematic errors can be greatly reduced. It should be pointed out that the NIST adsorption dataset can reveal important insight into areas such as inherently repeatable MOFs that have the potential to be used as reference materials or the existence of multiple phases of the same structure.

The other chapters in this thesis will explore the origin of some of this variability, such as inherent defects in the material (chapter 4), changes introduced by shaping (chapter 5) and of course, through unique behaviours of MOFs such as flexibility arising from its building blocks (chapter 6).

Bibliography

- [1] Elliott P. Barrett, Leslie G. Joyner, and Paul P. Halenda. The Determination of Pore Volume and Area Distributions in Porous Substances. I. Computations from Nitrogen Isotherms. *Journal of the American Chemical Society*, 73(1): 373–380, January 1951. ISSN 0002-7863. doi: 10.1021/ja01145a126.
- [2] N.A. Seaton, J.P.R.B. Walton, and N. Quirke. A new analysis method for the determination of the pore size distribution of porous carbons from nitrogen adsorption measurements. *Carbon*, 27(6):853–861, 1989. ISSN 00086223. doi: 10.1016/0008-6223(89)90035-3.
- [3] P. Tarazona, U. Marini Bettolo Marconi, and R. Evans. Phase equilibria of fluid interfaces and confined fluids: Non-local versus local density functionals. *Molecular Physics*, 60(3):573–595, February 1987. ISSN 0026-8976, 1362-3028. doi: 10.1080/00268978700100381.
- [4] Dan Siderius, Vincent Shen, and Russell Johnson. NIST / ARPA-E Database of Novel and Emerging Adsorbent Materials, NIST Standard Reference Database 205, 2015.
- [5] Salil U. Rege and Ralph T. Yang. A simple parameter for selecting an adsorbent for gas separation by pressure swing adsorption. *Separation science and technology*, 36(15):3355–3365, 2001.
- [6] M.W. Ackley, A.B. Stewart, G.W. Henzler, F.W. Leavitt, F. Notaro, and M.S. Kane. PSA apparatus and process using adsorbent mixtures, February 2000. US Patent 6,027,548.
- [7] Andrew D. Wiersum, Jong-San Chang, Christian Serre, and Philip L. Llewellyn. An Adsorbent Performance Indicator as a First Step Evaluation of Novel Sorbents for Gas Separations: Application to Metal–Organic Frameworks. *Langmuir*, 29(10):3301–3309, March 2013. ISSN 0743-7463, 1520-5827. doi: 10.1021/la3044329.
- [8] Jean Rouquerol, Françoise Rouquerol, Philip L. Llewellyn, Guillaume Maurin, and Kenneth Sing. *Adsorption by Powders and Porous Solids : Principles, Methodology and Applications*. 2013. ISBN 978-0-08-097035-6.
- [9] Irving Langmuir. The Adsorption of Gases on Plane Surfaces of Glass, Mica and Platinum. *Journal of the American Chemical Society*, 40(9):1361–1403, September 1918. ISSN 0002-7863, 1520-5126. doi: 10.1021/ja02242a004.
- [10] Stephen Brunauer, P. H. Emmett, and Edward Teller. Adsorption of Gases in Multimolecular Layers. *Journal of the American Chemical Society*, 60(2):309–319, February 1938. ISSN 0002-7863, 1520-5126. doi: 10.1021/ja01269a023.
- [11] Mikhail Temkin. Kinetics of ammonia synthesis on promoted iron catalyst. *Acta Phys. Chim. USSR*, 12:327–356, 1940.
- [12] Cory M. Simon, Jihan Kim, Li-Chiang Lin, Richard L. Martin, Maciej Haranczyk, and Berend Smit. Optimizing nanoporous materials for gas storage. *Physical Chemistry Chemical Physics*, 16(12):5499, 2014. ISSN 1463-9076, 1463-9084. doi: 10.1039/c3cp55039g.
- [13] C. R. C. Jensen and N. A. Seaton. An isotherm equation for adsorption to high pressures in microporous adsorbents. *Langmuir*, 12(11):2866–2867, 1996.
- [14] Terrell L. Hill. *An Introduction to Statistical Thermodynamics*. Dover Publications, New York, 1986. ISBN 978-0-486-65242-9.
- [15] Alan L. Myers. Thermodynamics of adsorption in porous materials. *AICHE Journal*, 48(1):145–160, January 2002. ISSN 00011541. doi: 10.1002/aic.690480115.
- [16] Solot Suwanayuen and Ronald P. Danner. A gas adsorption isotherm equation based on vacancy solution theory. *AICHE Journal*, 26(1):68–76, January 1980. ISSN 00011541. doi: 10.1002/aic.690260112.
- [17] T. W. Cochran, R. L. Kabel, and R. P. Danner. Vacancy solution theory of adsorption using Flory-Huggins activity coefficient equations. *AICHE Journal*, 31(2):268–277, February 1985. ISSN 0001-1541, 1547-5905. doi: 10.1002/aic.690310214.
- [18] Matthias Thommes, Katsumi Kaneko, Alexander V. Neimark, James P. Olivier, Francisco Rodriguez-Reinoso, Jean Rouquerol, and Kenneth S W Sing. Physisorption of gases, with special reference to the evaluation of surface area and pore size distribution (IUPAC Technical Report). *Pure and Applied Chemistry*, 87(9-10):1051–1069, 2015. ISSN 13653075. doi: 10.1515/pac-2014-1117.

- [19] George Halsey. Physical Adsorption on Non-Uniform Surfaces. *The Journal of Chemical Physics*, 16(10):931–937, October 1948. ISSN 0021-9606, 1089-7690. doi: 10.1063/1.1746689.
- [20] William D. Harkins and George Jura. Surfaces of Solids. XIII. A Vapor Adsorption Method for the Determination of the Area of a Solid without the Assumption of a Molecular Area, and the Areas Occupied by Nitrogen and Other Molecules on the Surface of a Solid. *Journal of the American Chemical Society*, 66(8):1366–1373, August 1944. ISSN 0002-7863, 1520-5126. doi: 10.1021/ja01236a048.
- [21] B Lippens. Studies on pore systems in catalysts V. The t method. *Journal of Catalysis*, 4(3):319–323, June 1965. ISSN 00219517. doi: 10.1016/0021-9517(65)90307-6.
- [22] D. Atkinson, A.I. McLeod, and K. S. W. Sing. Adsorptive properties of microporous carbons: Primary and secondary micropore filling. *Journal de Chimie Physique*, 81:791–794, 1984. ISSN 0021-7689. doi: 10.1051/jcp/1984810791.
- [23] Jean Rouquerol, Gino V. Baron, Renaud Denoyel, Herbert Giesche, Johan Groen, Peter Klobes, Pierre Levitz, Alexander V. Neimark, Sean Rigby, Romas Skudas, Kenneth Sing, Matthias Thommes, and Klaus Unger. The characterization of macroporous solids: An overview of the methodology. *Microporous and Mesoporous Materials*, 154:2–6, May 2012. ISSN 13871811. doi: 10.1016/j.micromeso.2011.09.031.
- [24] Duong D Do. *Adsorption Analysis: Equilibria and Kinetics: (With CD Containing Computer Matlab Programs)*, volume 2 of *Series on Chemical Engineering*. Imperial College Press, September 1998. ISBN 978-1-86094-130-6 978-1-78326-224-3. doi: 10.1142/p111.
- [25] D. Dollimore and G.R R. Heal. Pore-size distribution in typical adsorbent systems. *Journal of Colloid and Interface Science*, 33(4):508–519, August 1970. ISSN 00219797. doi: 10.1016/0021-9797(70)90002-0.
- [26] Geza Horvath and Kunitaro Kawazoe. Method for the calculation of effective pore size distribution in molecular sieve carbon. *Journal of Chemical Engineering of Japan*, 16(6):470–475, 1983. ISSN 1881-1299. doi: 10.1252/jcej.16.470.
- [27] Alexander V. Neimark, Yangzheng Lin, Peter I. Ravikovich, and Matthias Thommes. Quenched solid density functional theory and pore size analysis of micro-mesoporous carbons. *Carbon*, 47(7):1617–1628, June 2009. ISSN 00086223. doi: 10.1016/j.carbon.2009.01.050.
- [28] Naomi F Cessford, Nigel A. Seaton, and Tina Düren. Evaluation of Ideal Adsorbed Solution Theory as a Tool for the Design of Metal–Organic Framework Materials. *Industrial & Engineering Chemistry Research*, 51(13):4911–4921, April 2012. ISSN 0888-5885, 1520-5045. doi: 10.1021/ie202219w.
- [29] Timothy Van Heest, Stephanie L. Teich-McGoldrick, Jeffery A. Greathouse, Mark D. Allendorf, and David S. Sholl. Identification of Metal–Organic Framework Materials for Adsorption Separation of Rare Gases: Applicability of Ideal Adsorbed Solution Theory (IAST) and Effects of Inaccessible Framework Regions. *The Journal of Physical Chemistry C*, 116(24):13183–13195, June 2012. ISSN 1932-7447, 1932-7455. doi: 10.1021/jp302808j.
- [30] A. L. Myers and J. M. Prausnitz. Thermodynamics of mixed-gas adsorption. *AIChE Journal*, 11(1):121–127, January 1965. ISSN 0001-1541, 1547-5905. doi: 10.1002/aic.690110125.
- [31] Ian H. Bell, Jorrit Wronski, Sylvain Quoilin, and Vincent Lemort. Pure and Pseudo-pure Fluid Thermophysical Property Evaluation and the Open-Source Thermophysical Property Library CoolProp. *Industrial & Engineering Chemistry Research*, 53(6):2498–2508, February 2014. ISSN 0888-5885, 1520-5045. doi: 10.1021/ie4033999.
- [32] Eric Lemmon. NIST Reference Fluid Thermodynamic and Transport Properties Database: Version 9.0, NIST Standard Reference Database 23, 1989.
- [33] A. Saito and H. C. Foley. Curvature and parametric sensitivity in models for adsorption in micropores. *AIChE Journal*, 37(3):429–436, March 1991. ISSN 0001-1541. doi: 10.1002/aic.690370312.
- [34] Cory M. Simon, Berend Smit, and Maciej Haranczyk. PyIAST: Ideal adsorbed solution theory (IAST) Python package. *Computer Physics Communications*, 200:364–380, 2016. ISSN 00104655. doi: 10.1016/j.cpc.2015.11.016.
- [35] J. Rouquerol, P. Llewellyn, and F. Rouquerol. Is the bet equation applicable to microporous adsorbents? In *Studies in Surface Science and Catalysis*, volume 160, pages 49–56. Elsevier, 2007. ISBN 978-0-444-52022-7. doi: 10.1016/S0167-2991(07)80008-5.

- [36] Krista S. Walton and Randall Q. Snurr. Applicability of the BET Method for Determining Surface Areas of Microporous Metal–Organic Frameworks. *Journal of the American Chemical Society*, 129(27):8552–8556, July 2007. ISSN 0002-7863, 1520-5126. doi: 10.1021/ja071174k.
- [37] Jongwoo Park, Joshua D. Howe, and David S. Sholl. How Reproducible Are Isotherm Measurements in Metal–Organic Frameworks? *Chemistry of Materials*, 29(24):10487–10495, December 2017. ISSN 0897-4756, 1520-5002. doi: 10.1021/acs.chemmater.7b04287.
- [38] Junmin Li, Jiangfeng Yang, Libo Li, and Jinping Li. Separation of CO₂/CH₄ and CH₄/N₂ mixtures using MOF-5 and Cu₃(BTC)2. *Journal of Energy Chemistry*, 23(4):453–460, July 2014. ISSN 20954956. doi: 10.1016/S2095-4956(14)60171-6.
- [39] Ai-Ling Li, Fei Ke, Ling-Guang Qiu, Xia Jiang, Yi-Min Wang, and Xing-You Tian. Controllable synthesis of metal–organic framework hollow nanospheres by a versatile step-by-step assembly strategy. *CrystEngComm*, 15(18):3554, 2013. ISSN 1466-8033. doi: 10.1039/c2ce26636a.
- [40] Li Peng, Jianling Zhang, Jianshen Li, Buxing Han, Zhimin Xue, and Guanying Yang. Surfactant-directed assembly of mesoporous metal–organic framework nanoplates in ionic liquids. *Chemical Communications*, 48(69):8688, 2012. ISSN 1359-7345, 1364-548X. doi: 10.1039/c2cc34416e.
- [41] Maria Klimakow, Peter Klobes, Andreas F Thünemann, Klaus Rademann, and Franziska Emmerling. Mechanochemical Synthesis of Metal–Organic Frameworks: A Fast and Facile Approach toward Quantitative Yields and High Specific Surface Areas. *Chemistry of Materials*, 22(18):5216–5221, September 2010. ISSN 0897-4756, 1520-5002. doi: 10.1021/cm1012119.
- [42] Gokhan Barin, Vaiva Krungleviciute, Oleksii Gutov, Joseph T. Hupp, Taner Yildirim, and Omar K. Farha. Defect Creation by Linker Fragmentation in Metal–Organic Frameworks and Its Effects on Gas Uptake Properties. *Inorganic Chemistry*, 53(13):6914–6919, July 2014. ISSN 0020-1669, 1520-510X. doi: 10.1021/ic500722n.
- [43] D. P. Broom and M. Hirscher. Irreproducibility in hydrogen storage material research. *Energy & Environmental Science*, 9(11):3368–3380, 2016. ISSN 1754-5692, 1754-5706. doi: 10.1039/C6EE01435F.
- [44] Laura Espinal, Dianne L. Poster, Winnie Wong-Ng, Andrew J. Allen, and Martin L. Green. Measurement, Standards, and Data Needs for CO₂ Capture Materials: A Critical Review. *Environmental Science & Technology*, 47(21):11960–11975, November 2013. ISSN 0013-936X, 1520-5851. doi: 10.1021/es402622q.
- [45] H. G. T. Nguyen, L. Espinal, R. D. van Zee, M. Thommes, B. Toman, M. S. L. Hudson, E. Mangano, S. Brandani, D. P. Broom, M. J. Benham, K. Cybosz, P. Bertier, F. Yang, B. M. Krooss, R. L. Siegelman, M. Hakuman, K. Nakai, A. D. Ebner, L. Erden, J. A. Ritter, A. Moran, O. Talu, Y. Huang, K. S. Walton, P. Billemont, and G. De Weireld. A reference high-pressure CO₂ adsorption isotherm for ammonium ZSM-5 zeolite: Results of an interlaboratory study. *Adsorption*, July 2018. ISSN 0929-5607, 1572-8757. doi: 10.1007/s10450-018-9958-x.
- [46] Andrew P. Nelson, Omar K. Farha, Karen L. Mulfort, and Joseph T. Hupp. Supercritical Processing as a Route to High Internal Surface Areas and Permanent Microporosity in Metal–Organic Framework Materials. *Journal of the American Chemical Society*, 131(2):458–460, January 2009. ISSN 0002-7863, 1520-5126. doi: 10.1021/ja808853q.

3. Extending bulk analysis of porous compounds through calorimetry

3.1. Introduction

While the previous chapter focused on a physical description of adsorption and its use for the characterisation of metal organic frameworks and other porous materials, it was found that a large variation in surface areas exists in scientific literature. A requirement for more rigorous characterisation of adsorption data is highlighted, which can be achieved through the use of calorimetry to simultaneously gain data regarding the interactions in the studied system. An understanding of the energetic aspects of adsorption allows for one of the most powerful applications of adsorption methodology, namely a representation of the kinds of physical and chemical processes occurring during adsorption. Through a direct or indirect measurement of the **differential** enthalpy of adsorption ($\Delta_{ads}\dot{h}$), information about surface composition, the strength of adsorbate-guest and guest-guest interactions, phase change phenomena and, in some cases, transitions in the adsorbing material itself can be obtained. This makes it a good parameter for fundamental characterisation.

Furthermore, the enthalpy of adsorption is a crucial parameter in an industrial setting. Owing to the exothermic nature of adsorption in combination with the strong influence of temperature on the performance of adsorbent materials, the total or **integral** enthalpy of adsorption ($\Delta_{ads}H$) is often regarded as one of the most important parameter in the design of beds and columns, alongside working capacity and adsorption/catalytic selectivity. The integral enthalpy of adsorption is also a measure of the sum of all guest-host interactions, which have to be overcome for material regeneration. As such, it represents an important metric of the energy efficiency of the process.

As such the insight afforded through measurement of the energetic components of adsorption can prove invaluable for investigating subtle changes in adsorbent materials which lead to the kind of variability encountered in chapter 2. The thoroughness and suitability of the activation procedure, presence of surface functionalisations, defect formation such as inclusion of counterions and vacancies and activation-driven phenomena such as gate opening, state switching or flexibility can be qualitatively and, with careful methodology, even quantitatively analysed.

Chapter summary

First, an overview of the theoretical aspects underpinning the energetics of adsorption is presented. The methods section will go into detail in the available methodology to study the enthalpy of adsorption on surfaces and in pores. The final part of the chapter will explore the use of combined adsorption and calorimetric measurements as a way of extending characterisation of porous materials.

Contributions

All calorimetric measurements and data processing were performed by Paul Iacomi in the Madirel Laboratory, Marseille. The sample of Zr Fumarate MOF was synthesised in the group of Prof. Peter Behrens, from the University of Hannover, Germany. Gravimetric isotherms referenced in this chapter were recorded by Andrew Wiersum during his thesis.

3.2. Energetics of adsorption

3.2.1. Forces involved in adsorption

From a classical molecular point of view, we can define the guest-host and guest-guest interactions as a sum of several components with distinct physical meaning.

$$\Phi_t = \Phi_R + \Phi_D + \Phi_C + \Phi_I \quad (3.1)$$

The first two types of interaction, namely short range electrostatic repulsion between the electron clouds of neighbouring atoms Φ_R and long range dispersion Φ_D arising from incidental short-lived partial charges are common to all atoms, and can therefore be called “*non-specific*”. Such interactions are commonly modelled through the use of a Lennard-Jones type potential function.⁽¹⁾

$$V_{\text{LJ}} = 4\epsilon \left[\left(\frac{\sigma}{r} \right)^{12} - \left(\frac{\sigma}{r} \right)^6 \right] \quad (3.2)$$

The latter two types, Coulombic interactions Φ_C and induction interactions Φ_I arise from permanent charges and multipoles in the system. Coulombic interactions are attraction and repulsion interactions between charges such as molecular ions, permanent dipoles and quadrupoles. Induction, also known as polarization or Debye forces, is the interaction between a charged particle or a multipole with the induced multipole in a non-charged system. These interactions can be referred to as “*specific*”.

The ease with which a charge can induce such an interaction in a molecule is termed polarizability. The polarisation of the adsorbate by the pore wall is, in particular, a type of interaction which has historically been sometimes included in the non-specific⁽²⁾ and other times in specific category.⁽³⁾

They can be regarded as specific, as they are influenced by the charge distribution on the surface. However, all surfaces possess an electric field due to bond orientation and random fluctuations, therefore they could be rationalised to occur in all host guest systems.

In the standard definition of adsorption, only Van-der-Waals forces are said to account for the interactions between the guest and the host. However, depending on the systems involved, other types of interactions such as hydrogen bonding, electron sharing, stacking or π interactions may also play a role in the overall strength of the guest-host attraction.

The total interactions can also be broken down as contributions from adsorbate-adsorbent interactions and guest-guest interactions. If changes in the adsorbent occur as a result of adsorption, a host-host or self-potential interaction should be considered. The guest-host interaction can be assumed constant for a homogeneous surface or a function of coverage, in the case of a heterogeneous surface.

3.2.2. Thermodynamic quantities of the adsorbed phase

As mentioned in the previous section, adsorption is a consequence of intermolecular attraction between the material surface and the molecules of the fluid. The sum of all interactions accounts for the depth of the potential well and therefore for the energy corresponding to the process. As this energy is net positive, adsorption is an overall exothermic phenomenon.

However, in order to make the transition from a molecular viewpoint to a macroscale bulk fluid representation of adsorption, a thermodynamic description of the adsorbed phase of the process must be performed. This is usually done in terms of the surface excess quantities, which have been first introduced in subsection 2.2.1. A complete thermodynamic theory can then developed for a surface excess phase which is in equilibrium with a gas phase⁽⁴⁾, with only a brief summary to be presented here.

The surface excess may be considered a distinct thermodynamic phase, characterised by an area A , a two-dimensional analogue of pressure named spreading pressure π and a surface excess concentration corresponding to the amount adsorbed per unit area or $\Gamma = n^\sigma / A$.

The differential energy of adsorption can be described as the change in the internal energy of the system upon the transition of an infinitesimal amount of adsorbate from the bulk phase to the surface excess phase. It can be measured directly, through calorimetric methods.

In an adsorption process, a closed system of constant volume V and temperature T can be considered. No mass of material crosses the system boundary, therefore the total change in chemical potential is also zero $d\mu = 0$. Through a derivation⁽⁴⁾ of the gas and adsorbed phase/adsorbent energies we may obtain a Gibbs-Duhem type equation:

$$d\mu^\sigma = -\frac{S^\sigma}{n^\sigma} dT + \frac{A}{n^\sigma} d\pi \quad (3.3)$$

from which the Gibbs adsorption isotherm (Equation 2.3) may be derived, as well as

$$\ln p = \frac{\dot{u}_{T,\Gamma}^\sigma - u_T^g - RT}{RT} - \frac{\dot{s}_{T,\Gamma}^\sigma - s_0^g}{R} = \frac{\Delta_{ads}\dot{h}_{T,\Gamma}}{RT} - \frac{\Delta_{ads}\dot{s}_{T,\Gamma}}{R} \quad (3.4)$$

an expression relating the differential enthalpy of adsorption $\Delta_{ads}\dot{h}_{T,\Gamma}$ and the differential entropy of adsorption $\Delta_{ads}\dot{s}_{T,\Gamma}$ to the pressure of an ideal gas. The relationship between the differential enthalpy and the differential energy of the adsorbed phase is therefore given by:

$$\Delta_{ads}\dot{h}_{T,\Gamma} = \Delta_{ads}\dot{u}_{T,\Gamma} - RT \quad (3.5)$$

The differential enthalpy of adsorption is the quantity which can be calculated indirectly through the isosteric method.

3.2.3. Application of differential enthalpy of adsorption to the characterisation of materials

As the differential enthalpy of adsorption is a measure of the interaction taking place during adsorption, it is often used in conjunction with the isotherm to study the properties of adsorbent materials. Unfortunately, only the total sum of individual interactions is measurable through direct methods. Therefore, the absolute contribution of each component presented in subsection 3.2.1 cannot be determined. However, with careful choice of experiments and interpretation of results, specific factors may be compared.

When adsorbing in microporous materials, the filling of the different types of pores may be followed, as the confinement energy for each pore is specific to its size, assuming identical surface composition. Effect of the material structure and surface chemistry on guest-host interactions can be gauged through alteration of a single property. For example through changing the Si/Al ratio in a series of MFI zeolites⁽⁵⁾, the impact of the adsorbent on the initial adsorption behaviour may be studied. Other examples include the role of compensation cations in an ion-exchanged X-faujasite^(6,7) or the influence of open metal sites⁽⁸⁾ and their distribution.⁽⁹⁾ The contribution of non-specific effects such as π backbonding in porous coordination compounds⁽¹⁰⁾ can be examined by the choice of a suitable probe pair, such as a saturated and unsaturated version of a hydrocarbon (ethane/ethylene/acetylene). Guest-guest interactions during adsorption may also be monitored with cooperative effects such as 2-dimensional analogues of phase changes⁽¹¹⁾ visible as peaks in the enthalpy curve. If the adsorbate itself undergoes structural deformation during adsorption, as is the case in soft materials, the measured enthalpy of adsorption can be a clear indication of such changes.⁽¹²⁾ The net enthalpy of adsorption in such a system is often lowered through the energetic contribution of the state change of the adsorbate, and may be of use for a reduction in the thermal load to be dissipated for adsorption or required to recover the adsorbed material.⁽¹³⁾

The differential enthalpy of adsorption is often represented as a function of partial coverage. In Figure 3.1, isotherm types as defined by IUPAC⁽¹⁴⁾ are presented together with a typical differen-

tial enthalpy curve.⁽¹⁵⁾ Type I isotherms often have an initial plateau, corresponding to adsorption in micropores until a sharp decrease at complete pore filling occurs. If the surface of the pores is heterogeneous, higher energy sites will be occupied first, resulting in a sharp slope at low loadings. Multilayer adsorption in non-porous or mesoporous materials (II and IV) yields a slowly decreasing enthalpy curve, as the solid-guest interactions drop off with increasing layers adsorbed. Finally, cooperative adsorption on non-interacting surfaces (such as water adsorption in hydrophobic porous materials) as seen in a type III isotherm, often gives rise to initial enthalpies of adsorption which are below the enthalpy of vaporisation. Finally, distinct peaks often accompany multilayer adsorption (Type VI) which are an indication of epitaxial phase changes at completion of each layer.^(5,11,16)

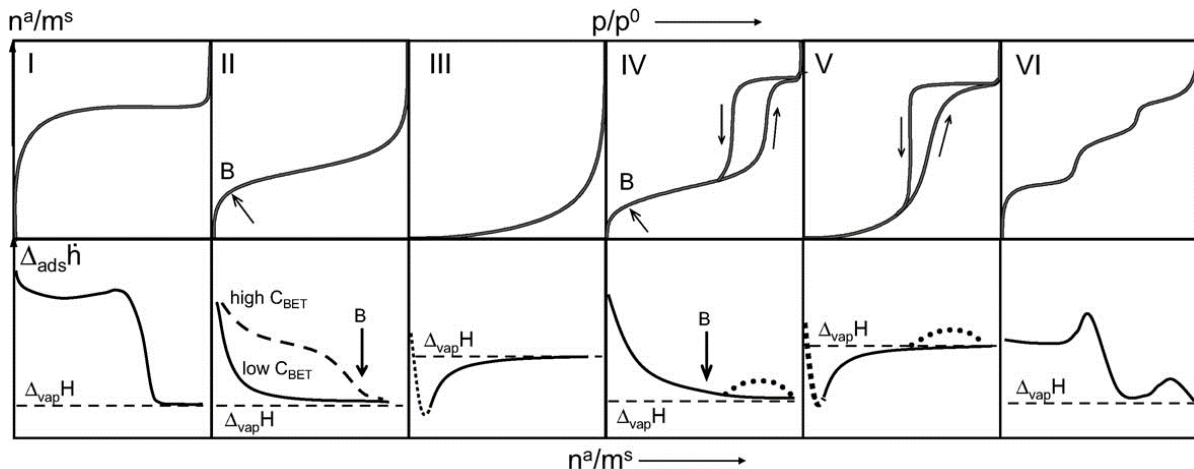


Figure 3.1.: Generalized curves of differential enthalpy of adsorption with respect to coverage corresponding to different IUPAC-defined isotherm types. Adapted from Llewellyn and Maurin⁽¹⁵⁾.

3.3. Measuring the enthalpy of adsorption

Experimentally, two methods are widely used for determining the enthalpy of adsorption. The first relies on measurement of two or more isotherms at different temperatures and the use of a Clausius-Clapeyron-type equation for indirect calculation, while the second is a direct measurement of the evolved heat during adsorption using calorimetry.

A value for the enthalpy of adsorption in a particular system may also be obtained from computer simulation methods. The accuracy of these procedures depends on the accuracy of the chosen model of interaction between simulated species.

3.3.1. Isosteric enthalpy of adsorption

If the differential enthalpy of adsorption is assumed to be independent of temperature, Equation 3.4 can be differentiated with respect to temperature keeping the surface adsorbed amount constant to

obtain an equation analogous to the Clausius-Clapeyron equation:

$$\left(\frac{\partial \ln p}{\partial T} \right)_{n_a} = -\frac{\Delta_{ads}\dot{h}_{T,\Gamma}}{RT^2} \quad (3.6)$$

The equation can be rearranged to calculate the differential enthalpy:

$$\Delta_{ads}\dot{h}_{T,\Gamma} = R \left(\frac{\partial \ln p}{\partial 1/T} \right)_\Gamma \quad (3.7)$$

where $\Delta_{ads}\dot{h}_{T,\Gamma}$ is the often termed the isosteric enthalpy of adsorption.

In order to approximate the partial differential, two or more isotherms are measured at different temperatures. The temperature range chosen is usually small, to maintain the assumption of invariance of isosteric enthalpy with temperature while still obtaining good separation between the two isotherms. Afterwards the isosteric enthalpy of adsorption can be calculated by using the pressures at which the loading is identical using the rearranged equation. By plotting the values of $\ln p$ against $1/T$ we should obtain a straight line with a slope of $-\Delta_{ads}\dot{h}_{T,\Gamma}/R$.

As experimental isotherms do not necessarily have points spaced at equal loading intervals, interpolation is usually used to obtain data at the desired points. Alternatively, a model may be used to first fit the isotherm, which is then used for the calculation.

The isosteric enthalpy is sensitive to differences in pressure between the two isotherms. If the isotherms measured are too close together, the error margin will increase. The method also assumes that isosteric enthalpy does not vary with temperature. If the variation is large for the system in question, the calculation will lead to unrealistic values. Another requirement is that no phase changes in either guest or host occur during adsorption. Thus, the isosteric method is not suited to soft materials, where the structural changes are often in themselves temperature dependent.

Even with carefully measured experimental data, there are several assumptions used in applying Equation 3.7 to a real system: an ideal bulk gas phase and a negligible adsorbed phase molar volume. These have a significant effect on the calculated isosteric enthalpy of adsorption, especially at high relative pressures and for heavy adsorbates.

3.3.2. Microcalorimetry

A direct measurement of the enthalpy of adsorption is possible using calorimetric methods. An isothermal calorimeter is most often used for this purpose, to best approximate a reversible exchange of heat between the system under investigation and the surrounding heat sink. To allow for a complete integration of evolved heat, with minimal losses, a 3D Tian-Calvet thermopile⁽¹⁷⁾ can be used. In order to limit variations in environment, differential mounting is employed, in which the signal is the difference in voltage between a reference and experimental thermopile. In order to ensure the “isothermicity” of the calorimeter, a suitable heat sink must be used, leading to two types of design. Ambient temperature calorimeters use resistance heating to maintain the internal

temperature, while utilising the environment as its heat sink. At low temperature, the environment acts as a heat source and therefore the heat sink must be provided, often in the form of a constant-temperature bath undergoing a phase change (e.g. liquid N₂, Ar) or through a cryostat. Sketches of an ambient and a low temperature differential Tian-Calvet calorimeter can be seen in Figure 3.2.

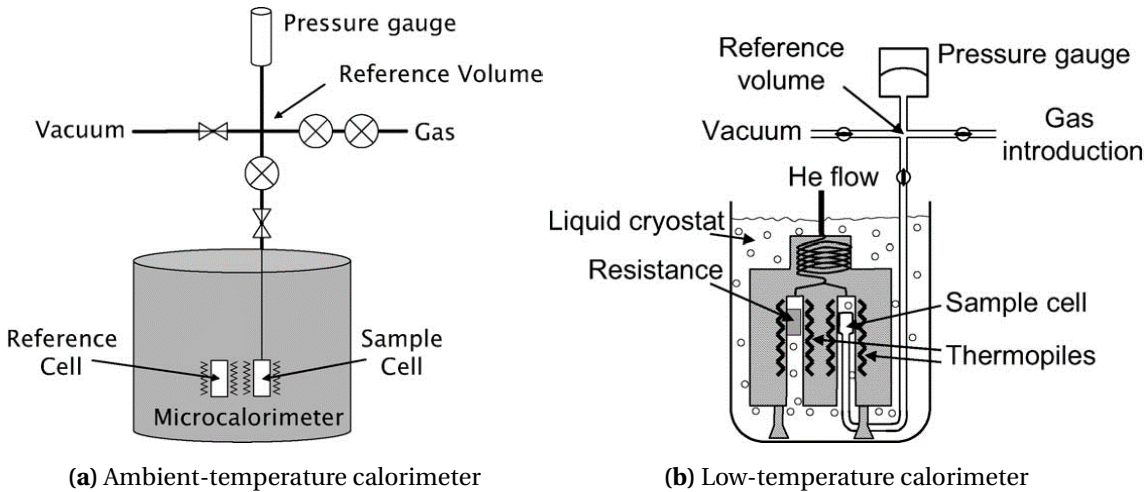


Figure 3.2: Two types of isothermal Tian-Calvet calorimeters for adsorption measurements, specialized for different temperature ranges. Adapted from Llewellyn and Maurin⁽¹⁵⁾.

Care must be taken to ensure that the recorded heat through such an experiment can be related directly to adsorption enthalpy and not to other heat effects. The adsorbate and gas residing inside a calorimeter is best represented by an open system, where the introduction of adsorbate is done through steps that are small enough to consider a reversible process.⁽¹⁸⁾ The accepted convention is that the adsorbate itself is inert and therefore does not contribute to the variation of any state function. Under these conditions, the change in internal energy of the adsorbate can be written as:

$$dU = dQ_{rev} + dW_{rev} + u_T^g dn \quad (3.8)$$

where dQ_{rev} is the reversibly exchanged heat which is measured by the calorimeter. dW_{rev} is the reversible work done by the gas against the external pressure. In the cell volume measured by the calorimeter (V_C), this work may be expressed as

$$dW_{rev} = RTdn^\sigma + V_C dp \quad (3.9)$$

If the previous two equations are combined and differentiated with respect to the amount adsorbed n^σ , then we obtain the equation for the differential heat of adsorption.

$$\frac{dQ_{rev}}{dn^\sigma} + V_C \frac{dp}{dn^\sigma} = \frac{dU^\sigma}{dn^\sigma} - u_T^g - RT = \Delta_{ads} h_{T,\Gamma} \quad (3.10)$$

Two options exist regarding the method of introduction of adsorbate: the continuous and the discontinuous or point-by-point method. In the point-by-point method, discrete insertion steps are

made. A reference volume is filled with gas at a pressure p , which is allowed to equilibrate before a valve between the reference volume and the cell containing the adsorbate is opened, letting the gas adsorb onto the material. With small enough steps, the assumption of a reversible system can be approximated. The peak in the calorimetric signal is integrated over time to give the total energy released during this adsorption step.

In the other method, the flow of adsorbate is continuous, usually kept constant by a restriction in the pipe diameter which is severe enough to allow the gas to enter via sonic flow regimes. At this point, the flowrate is no longer influenced by a pressure differential, instead becoming a function only of upstream pressure and environment temperature. The heat evolved during adsorption (or required during desorption) is therefore measured either as discrete peaks, corresponding to each introduction event or as a continuous heat curve. An example of such a signal for each method presented in Figure 3.3.

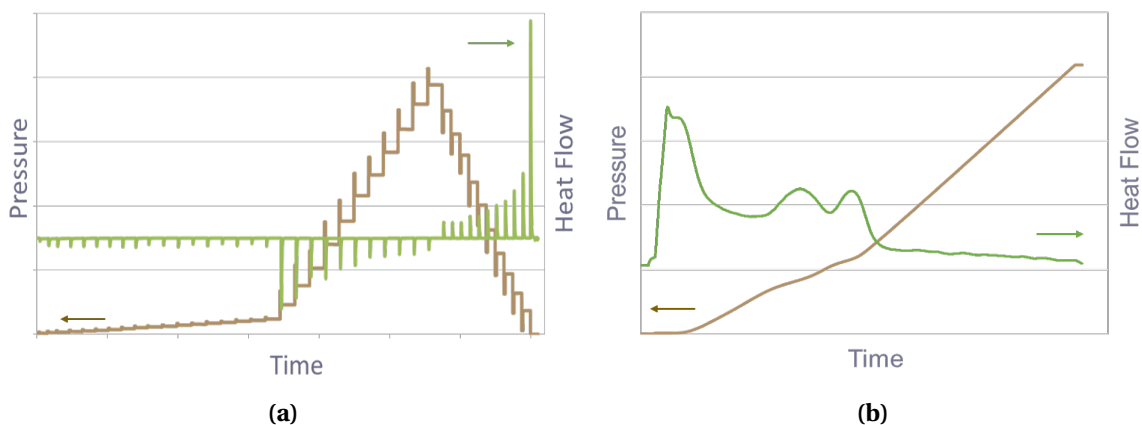


Figure 3.3.: Typical pressure and calorimeter signals for the two available methods of introducing adsorbate into the measurement cell (a) discontinuous and (b) continuous.

The point-by-point method has a lower resolution than continuous introduction, as the measured heat is necessarily a cumulative value of instantaneous differential enthalpy for the coverage range of each adsorbed point. However, it has the advantage of ensuring complete equilibrium at each step, by observing the return to the baseline of the calorimetry signal or a stable pressure signal. On the other hand, the continuous method allows for subtle changes in the differential enthalpy of adsorption, such as those corresponding to adsorbed phase changes, to be seen experimentally. Additionally, the time-resolved data can be used to investigate transient phenomena. Equilibrium between the adsorbed phase and gas phase is no longer guaranteed, and must be tested for by performing multiple experiments at different adsorbate flowrates. Alternatively, the experiment can be stopped to observe that the time for the heat signal to return to its baseline does not diverge from the dead time of the calorimeter.

3.3.3. Experimental apparatus and accuracy

In this thesis, combined isotherms and enthalpy of adsorption measurements were made experimentally using a Tian-Calvet type microcalorimeter coupled with a home-made manometric gas dosing system.⁽¹⁵⁾ Two calorimeter designs were used, one for ambient temperature and one for low temperature adsorption, as displayed in Figure 3.2.

The method of adsorbate introduction can be chosen either as continuous or discontinuous. For routine measurements, the point-by-point method is preferred, as it is guaranteed to achieve equilibrium between the material and the adsorbate removing the influence of diffusion effects. For each injection of gas, equilibrium was assumed to have been reached after 90 min to 250 min, depending on the sample and adsorbate used. This was confirmed by the return of the calorimetric signal to its baseline ($<5\text{ }\mu\text{W}$). For the continuous method, a sonic nozzle was used to maintain the flowrate between $0.5\text{ }\mu\text{mol min}^{-1}$ to $2\text{ }\mu\text{mol min}^{-1}$, low enough that the system can be considered at equilibrium. The assumption of equilibrium is routinely verified by multiple experiments at different upstream pressures.

As the isotherms are recorded through the manometric method, the accuracy in the adsorbed amount depends on the reliability of measuring individual state variables (temperature, pressure, volume) and the equation of state relating them to adsorbate loading. Characteristic to this method, the pressure recorded for a point is measured in relation to the previous one. Therefore, the error is cumulative with each successive measurement point, and is the largest contribution to the total error. The uncertainty can be lowered dramatically by increasing the available surface area inside the calorimeter. Between 50 mg to 200 mg of sample is used in each experiment, such that the specific surface area inside the calorimeter cell is larger than $50\text{ m}^2/\text{g}$. Finally, the REFPROP equation of state is used⁽¹⁹⁾, currently the most accurate available. Overall, error in isotherms measured in this way can be reduced to less than 5%.

The error in the differential enthalpy of adsorption has a contribution from both the heat signal of the calorimeter and the accuracy in the amount adsorbed. At low coverage the error in the calorimetric signal can be estimated to around $\pm 0.2\text{ kJ mol}^{-1}$. This uncertainty is orders of magnitude lower than the contribution from loading, and is therefore omitted in the error calculation. As the value obtained from integration of the signal peaks must be divided by the change in adsorbed amount Δn , the error is largest in flat sections of the isotherm, where the amount adsorbed is low. Thus, uncertainty varies from 0.5–5% in the beginning of the isotherm to over 100% when an isotherm plateau is reached.

A complete error analysis for the resulting isotherms and enthalpy curves can be found in Appendix C. Also, a direct comparison between calorimetry and gravimetry isotherms is presented in the following section.

3.4. Case studies for the use of microcalorimetry combined with adsorption experiments

3.4.1. Comparison between enthalpies of adsorption measured through the direct and indirect method

In order to ascertain the strengths and weaknesses of the isosteric and calorimetric method of measuring the enthalpy of adsorption, a sample of UiO-66(Zr) previously used for a study of carbon dioxide⁽²⁰⁾ adsorption was also measured using microcalorimetry. Two previous isotherms were recorded through gravimetry at 303 K and 323 K respectively and the new isotherm was measured in the calorimeter at 303 K. The complete set of isotherms can be found in Figure 3.4a. The two isotherms measured at 303 K are nearly identical, ensuring that the both adsorption apparatus are working as intended. The isosteric enthalpy of adsorption is calculated from the two isotherms at different temperatures, either using an interpolation method, or through initial fitting of a virial model (subsection 2.2.9). The values are then adjusted according to Equation 3.5. Calculated and measured values for the enthalpy of adsorption are overlaid in Figure 3.4b as a function of amount adsorbed.

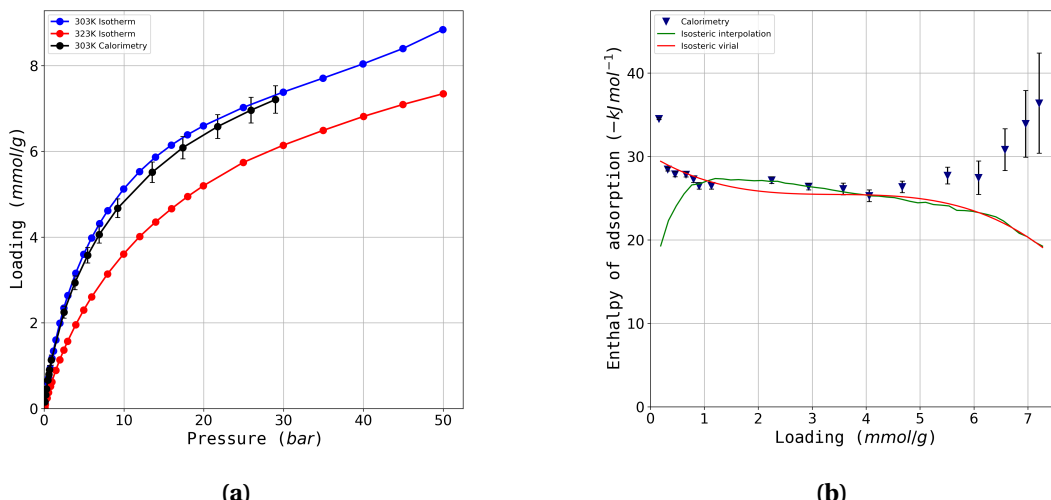


Figure 3.4: (a) The gravimetric isotherms (red and blue) used for isosteric enthalpy calculation and the manometric isotherm measured in the calorimeter (black). (b) Calculated isosteric enthalpy using an interpolation (blue line) and a virial fit (red line) of the gravimetric isotherms together with the directly measured differential enthalpy of adsorption (blue triangles)

When comparing the differential enthalpy of adsorption measured through calorimetry to the isosteric enthalpy obtained through interpolation, a good overlap can be seen for the most part, but the two values diverge at low loadings and near complete coverage. At low loading the small errors in pressure measurement introduce large errors in the isosteric enthalpy. By using the model-

fitted isotherms instead, a better agreement can be achieved. However, the virial model still cannot account for the presence of active sites in the MOF, as seen in the discrepancy of the first adsorption point. The calorimetric measurement is therefore more suited to the low pressure range. At higher loadings, where the isotherm reaches a plateau and the change in adsorbed amount is small between each adsorbate insertion, errors are introduced in the enthalpy of adsorption calculation from the small adsorbed amounts, as can be seen from the extent of the error bars in Figure 3.4b. Here, the indirect calculation provides the more accurate results. As such, the two techniques can be thought of as complementary.

3.4.2. An example dataset on a reference material

A sample of microporous carbon, Takeda 5A (section B.1) was used as a reference material to exemplify the type of information that can be obtained through the combined manometric and calorimetric method. Pure gas adsorption data has been recorded at 303 K using N₂, CO, CO₂, CH₄, C₂H₆, C₃H₆ and C₃H₈ as probes. The complete dataset can be seen in Figure 3.5a, with the corresponding differential enthalpy curves presented in Figure 3.5b.

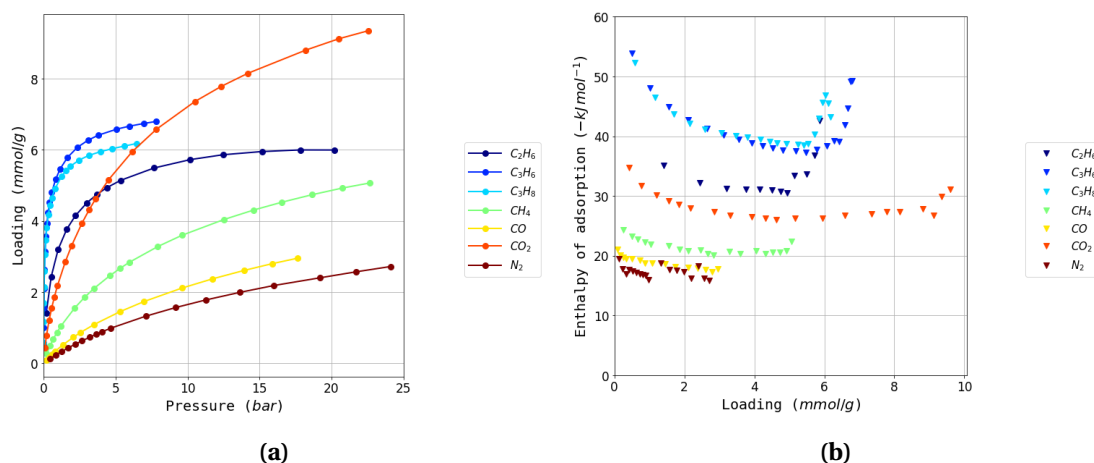


Figure 3.5.: Recorded data on the Takeda 5A sample, (a) the experimental dataset all recorded gases and (b) corresponding differential enthalpy.

It should first be highlighted that the isotherms can be split into two adsorption regimes: subcritical, as is the case for carbon dioxide and all hydrocarbons except methane, and supercritical, as is the case for nitrogen, carbon monoxide and methane. Supercritical gasses do not have any distinction between the gaseous and liquid phase, therefore the density of the adsorbed phase cannot be likened to that of a corresponding liquid. The enthalpy of vaporisation of such a fluid in this regime is necessarily 0. However, in-depth studies of supercritical isotherms⁽²¹⁾ have shown that the density of the adsorbed phase is highly dependent on the surface area of the material. As the interactions in this regime are essentially restricted to guest-host interactions, the density can approach that of a liquid in highly microporous and strong pore field gradient materials.

Nitrogen and carbon monoxide are similar in their adsorption behaviour, with a nearly linear isotherm and low capacities. The enthalpy curves are also an indication of non-specific interactions with the surface, as the enthalpy of adsorption is nearly constant throughout the entire loading range. Carbon dioxide has the highest loading capacity of the entire dataset, likely due to a combination of a small molecule size and interactions with the carbon pore walls. The enthalpy curve shows a higher energy of adsorption at low loading by 5 kJ mol^{-1} to 10 kJ mol^{-1} , corresponding to adsorption on a slightly heterogeneous surface. The adsorption of hydrocarbons takes place in accordance to their size, with both the initial slope and the enthalpy of adsorption increasing linearly as a function of the carbon number. Each methyl group is seen to contribute, on average, with around 10 kJ mol^{-1} to 15 kJ mol^{-1} to the mean enthalpy of adsorption.⁽²²⁾ When it comes to saturated versus unsaturated hydrocarbons, propylene is seen to have a higher capacity than propane. As the enthalpy of adsorption is identical at low loading, specific interactions with the π electrons of the double bond are unlikely, with packing effects from the smaller kinetic diameter of propylene as a more plausible explanation.

Two parameters can be useful in characterising the local pore environment before guest-guest interactions come into effect: the Henry constant at low loadings as well as the initial differential enthalpy of adsorption. Here, the initial Henry's constant is calculated by fitting a virial model to the isotherm, then taking the limit of the function at zero loading.

The initial enthalpy of adsorption can be determined from calorimetric methods simply by taking the value of the first measured point. However, this procedure is susceptible to large errors, particularly if the isotherm has no points in the low coverage region. An alternative is to take an average of all recorded points, a method which assumes a homogenous surface. Myers⁽²³⁾, has suggested that the enthalpy curve follows a polynomial model, similar to a virial isotherm. In this work, an empirical method is used where the enthalpy curve is treated as a compound contribution from guest-host interaction, guest-guest attraction and repulsion, the factors of which are determined using a minimization algorithm. Adsorbate-adsorbate interaction is represented as a logistic function, which can account for both a heterogeneous surface and a micropore filling step. Power functions are used for both attraction and repulsion factors. An example of an enthalpy curve fitted with this method can be seen in Figure 3.6a

A useful method of displaying the two parameters can be to plot them as a function of the polarizability of the probe, as in Figure 3.6b. Both parameters follow a linear trend, which suggests that the interactions between those guests and the pore walls are mostly due to non-specific interactions with the field gradient of the pore. Carbon dioxide has a higher enthalpy of adsorption than the baseline, which can be ascribed to the contribution from its quadrupole moment. There is almost a complete overlap between propane and propylene, confirming that the unsaturated double bond does not interact in a specific way with the carbon surface.

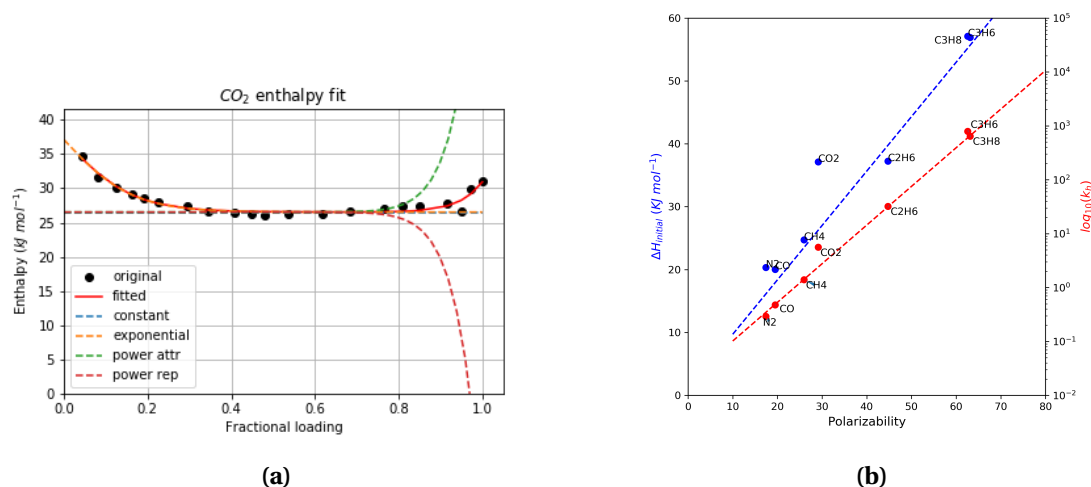


Figure 3.6.: Takeda 5A dataset processing: (a) an example of the empirical enthalpy fit model and (b) the calculated trends for initial heat of adsorption and Henry's constant

3.4.3. A study on a novel MOF

With the methods of characterisation through calorimetry outlined on a reference material, a similar study on a MOF sample can be performed. The aim is to screen for potentially interesting features for use in gas storage and separation.

Material

Zr Fumarate, also known as MOF-801, is a fumaric acid analogue of the well-known UiO-66(Zr) framework.⁽²⁴⁾ Its structure is similar to that of UiO-66, although the smaller non-linear linker leads to a lowering of symmetry and a slight tilting in the Zr-O clusters, as depicted in Figure 3.7. The MOF is synthesised using the modulated synthesis method and formic acid as the modulator to increase the crystallinity of the material. Indeed, when not using this approach, the resulting material is nearly amorphous.⁽²⁵⁾ In this study the sample was synthesised according to the procedure detailed in section B.3.

Zr Fumarate has recently been the subject of interest due to its high water stability⁽²⁶⁾, as well as its potential to be synthesised through green synthesis routes⁽²⁷⁾ or direct monolith formation with a gel approach.⁽²⁸⁾

Furthermore, the material has a remarkably steep water adsorption behaviour at low pressure⁽²⁹⁾, which has led to its possible application as a water scavenger membrane⁽³⁰⁾ or in a water harvesting device which would capture water from air in low relative humidity environments such as the desert. While initial attempts⁽³¹⁾ were criticised for overpromising performance, more recent modifications to such a system have addressed some of these concerns.⁽³²⁾

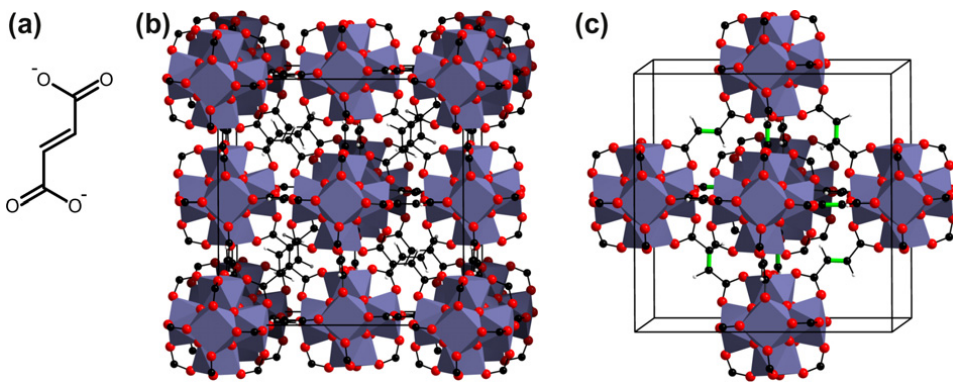


Figure 3.7.: (a) The fumarate linker used in the Zr Fumarate MOF, an ionic form of *trans*-butenedioic acid and (b) and (c) the structural model of the MOF. Illustration adapted from Wißmann et al.⁽²⁴⁾.

The low relative pressure of water adsorption has highlighted the contribution of defects⁽³³⁾ in shifting the adsorption isotherm, an effect arising from cooperative interactions and initial clustering of water molecules on defect sites.⁽³⁴⁾

As the properties of the MOF diverge from the ideal properties indicated by the structure, an experimental study to test for the adsorption or separation of other molecules may reveal unexpected applications.

Results

Adsorption isotherms of nine probe gasses were recorded at 303 K through combined manometry and microcalorimetry as described in subsection 3.3.2. The complete dataset can be seen in Figure 3.8. The results are remarkably similar to the Takeda 5A carbon, with very similar trends visible. All isotherms are somewhat shifted downwards, which suggests less interaction with the pore walls and a lower total pore volume. The enthalpies of adsorption are on average lower by 5 kJ mol⁻¹ to 7 kJ mol⁻¹, confirming that the guest-host attraction is overall lower than in the carbon. Argon, oxygen and nitrogen isotherms are essentially following Henry's law in the measured pressure range, with nearly constant enthalpies of adsorption. Carbon dioxide adsorption enthalpy is seen to take place on specific sites at the start of the isotherm, then decreasing until around 25 kJ/mol. Cooperative interactions take over afterwards, slowly increasing the enthalpy of adsorption.

The propane and propylene isotherms also show a higher total loading for propylene at the plateau. However, the enthalpy curve suggests a higher adsorption enthalpy of propane at lower loading. A similar plot for initial Henry's constant and enthalpy of adsorption at zero loading, in Figure 3.9a, confirms this trend, with propylene showing a decreased value in both parameters. As propane still lies on the trendline generated by unsaturated hydrocarbons, it does not seem that it possesses any increased specific interactions with the MOF surface. Instead, the expected values for propylene are lower than those of its saturated counterpart. It should be pointed out that the slope of the trendline

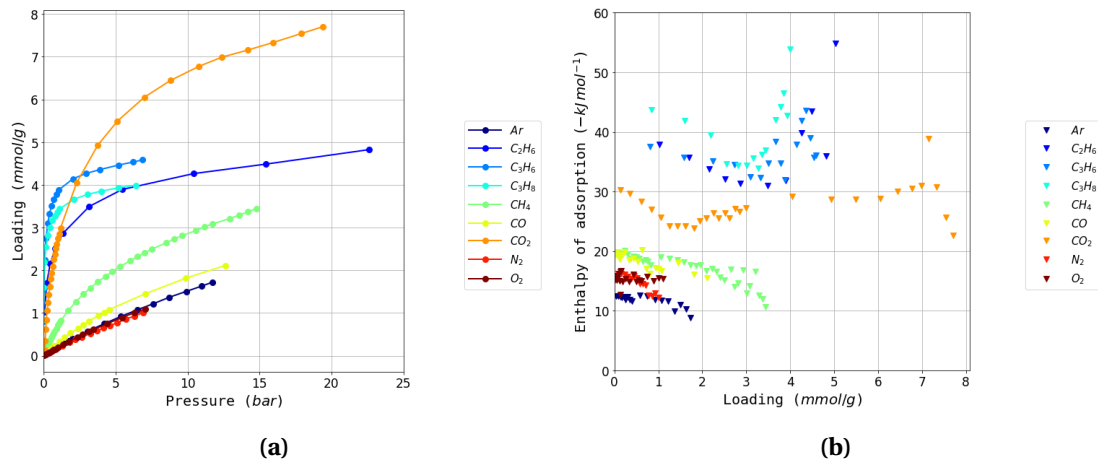


Figure 3.8.: (a) The experimental isotherms of all recorded gases and **(b)** the corresponding enthalpy curves.

is lower than that of the Takeda 5A. This slope can be thought of as a measure of the non-specific interaction strength of the adsorbate surface and described through a field gradient, influenced by the chemistry and size of the pore.

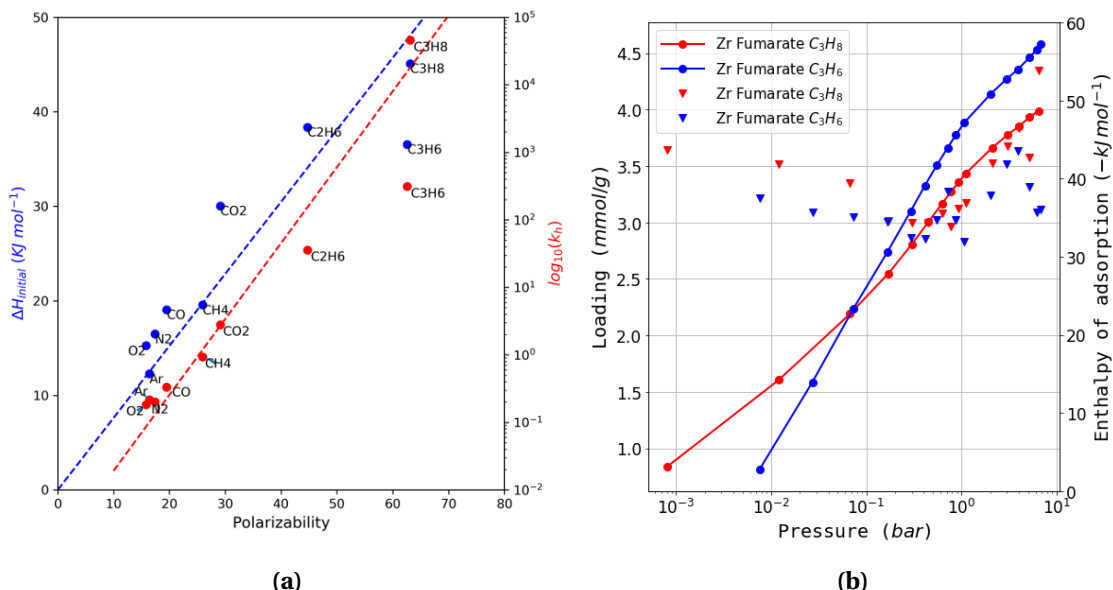


Figure 3.9.: (a) Calculated trends for initial heat of adsorption (red) and Henry's constant (blue) as a function of polarizability for Zr Fumarate. The dotted lines are best fit lines to the series of unsaturated hydrocarbons. **(b)** Logarithmic form of the propane and propylene isotherms.

When examining the low pressure region of the two isotherms (Figure 3.9b) a preference for propane over propylene can be observed, which is the source of the anomaly in the polarizability graph. The isotherms then “cross over” at higher pressures. This behaviour has been reproduced by measuring the same isotherms with a commercial apparatus, which can be found in Appendix D. A higher

selectivity for propylene adsorption is not uncommon in materials with open metal sites which can interact with the π electrons of the molecule.⁽¹⁰⁾ Furthermore, MOFs with pore sizes perfectly tuned for kinetically selective adsorption of propylene over propane have been shown to exist.⁽³⁵⁾ However, the preference for propane in this material is surprising. The effect itself is unlikely to arise from simple diffusion effects⁽³⁶⁾, although it has been shown⁽³⁷⁾ that pore windows can dominate diffusion behaviour. A contribution from framework defects is also be likely, as the crystal structure calculated pore volume is 40% of the total volume as determined from the propane adsorption isotherm. Thermogravimetry and water adsorption experiments, available in Appendix D, both confirm the presence of defects in the material structure.

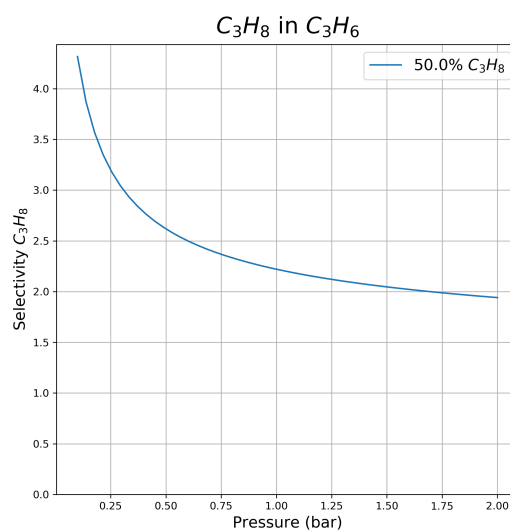


Figure 3.10.: IAST simulation of an equimolar mixture of propane and propylene on Zr Fumarate

To observe the impact on separation efficiency, the two isotherms are fitted with the best conforming model, in this case double site Langmuir, and IAST simulations of an equimolar mixture of propane and propylene are carried out as seen in Figure 3.10. A selectivity of 4–2 for propane is predicted by IAST, which may be of interest in large-scale processes, as even a small separation factor improvement may yield large energy savings.

In this case, direct measurement of the differential enthalpy of adsorption has highlighted several behaviours unique to this MOF. However, in order to understand the source and mechanism of this effect, further study is recommended. Molecular simulation of adsorption isotherms can reveal whether the process is kinetic or thermodynamically controlled, as well as give an indication of the contribution of defect sites to the guest-host molecular interactions. Concomitantly, breakthrough experiments in an adsorbent column of the MOF or binary adsorption experiments can confirm whether the effect holds when a mixture of the two hydrocarbons is present.

3.5. Conclusion

Having previously detailed the kind of information that isotherm processing affords, this chapter extends the type of characterisation of porous materials through a measurement of the enthalpy of adsorption.

This characterisation can be performed either directly, using a highly sensitive microcalorimetric setup, or indirectly, through the application of the isosteric method on isotherms recorded at different temperatures. A short analysis on the applicability and agreement of each method is performed, noting that they are complementary with respect to different adsorption regimes and conditions. Calorimetric methods are shown to be particularly suitable to low coverage adsorption regarding non-specific interactions. Furthermore, the continuous method of adsorbate introduction is seen to be extremely sensitive to minute changes in the measured system due to its high resolution.

An example analysis of a reference microporous carbon is used to benchmark useful methods of data processing. The enthalpy of adsorption at zero loading and initial Henry's constant are two parameters which are shown to be a good indicator of the interaction of the material with the adsorbed molecules.

Finally, the same methods are applied to a metal-organic framework of recent interest and used to highlight a potentially interesting separation of propylene and propane. The material is seen to be more selective for propane at low pressures, a desirable feature for industrial processes. A further study on the viability of such a separation is recommended, combining simulations of ideal isotherms and diffusivity and experimental break-through curves.

With the in-depth characterisation afforded by combined adsorption measurements and microcalorimetry, the following chapters attempt to delve deeper into some of the sources of variability in metal organic framework isotherms.

Bibliography

- [1] J. E. Jones. On the Determination of Molecular Fields. II. From the Equation of State of a Gas. *Proceedings of the Royal Society A: Mathematical, Physical and Engineering Sciences*, 106(738):463–477, October 1924. ISSN 1364-5021, 1471-2946. doi: 10.1098/rspa.1924.0082.
- [2] R. M. Barrer. *Zeolites and Clay Minerals as Sorbents and Molecular Sieves*. Academic Press, London ; New York, 1978. ISBN 978-0-12-079350-1.
- [3] François-Xavier Coudert and Alain H. Fuchs. Computational characterization and prediction of metal–organic framework properties. *Coordination Chemistry Reviews*, 307:211–236, January 2016. ISSN 00108545. doi: 10.1016/j.ccr.2015.08.001.
- [4] Jean Rouquerol, Françoise Rouquerol, Philip L. Llewellyn, Guillaume Maurin, and Kenneth Sing. *Adsorption by Powders and Porous Solids : Principles, Methodology and Applications*. 2013. ISBN 978-0-08-097035-6.
- [5] P. L. Llewellyn, J. P. Coulomb, Y. Grillet, J. Patarin, G. Andre, and J. Rouquerol. Adsorption by MFI-type zeolites examined by isothermal microcalorimetry and neutron diffraction. 2. Nitrogen and carbon monoxide. *Langmuir*, 9 (7):1852–1856, July 1993. ISSN 0743-7463, 1520-5827. doi: 10.1021/la00031a037.
- [6] G. Maurin, P.L. Llewellyn, Th. Poyet, and B. Kuchta. Adsorption of argon and nitrogen in X-faujasites: Relationships for understanding the interactions with monovalent and divalent cations. *Microporous and Mesoporous Materials*, 79(1-3):53–59, April 2005. ISSN 13871811. doi: 10.1016/j.micromeso.2004.10.017.
- [7] G. Maurin, Ph. Llewellyn, Th. Poyet, and B. Kuchta. Influence of Extra-Framework Cations on the Adsorption Properties of X-Faujasite Systems: Microcalorimetry and Molecular Simulations. *The Journal of Physical Chemistry B*, 109(1):125–129, January 2005. ISSN 1520-6106, 1520-5207. doi: 10.1021/jp0461753.
- [8] Lukáš Grajciar, Andrew D. Wiersum, Philip L. Llewellyn, Jong-San Chang, and Petr Nachtigall. Understanding CO₂ Adsorption in CuBTC MOF: Comparing Combined DFT–ab Initio Calculations with Microcalorimetry Experiments. *The Journal of Physical Chemistry C*, 115(36):17925–17933, September 2011. ISSN 1932-7447. doi: 10.1021/jp206002d.
- [9] Ji Woong Yoon, You-Kyung Seo, Young Kyu Hwang, Jong-San Chang, Hervé Leclerc, Stefan Wuttke, Philippe Bazin, Alexandre Vimont, Marco Daturi, Emily Bloch, Philip L. Llewellyn, Christian Serre, Patricia Horcajada, Jean-Marc Grenèche, Alirio E. Rodrigues, and Gérard Férey. Controlled Reducibility of a Metal-Organic Framework with Coordinatively Unsaturated Sites for Preferential Gas Sorption. *Angewandte Chemie International Edition*, 49(34):5949–5952, August 2010. ISSN 14337851. doi: 10.1002/anie.201001230.
- [10] Miroslav Rubeš, Andrew D. Wiersum, Philip L. Llewellyn, Lukáš Grajciar, Ota Bludský, Petr Nachtigall, Miroslav Rubes, Andrew D. Wiersum, Philip L. Llewellyn, Lukáš Grajciar, Ota Bludský, and Petr Nachtigall. Adsorption of propane and propylene on CuBTC metal-organic framework: Combined theoretical and experimental investigation. *Journal of Physical Chemistry C*, 117(21):11159–11167, May 2013. ISSN 19327447. doi: 10.1021/jp401600v.
- [11] Jean Rouquerol, Stanislas Partyka, and Françoise Rouquerol. Calorimetric evidence for a bidimensional phase change in the monolayer of nitrogen or argon adsorbed on graphite at 77 K. *Journal of the Chemical Society, Faraday Transactions 1: Physical Chemistry in Condensed Phases*, 73:306, 1977. ISSN 0300-9599. doi: 10.1039/f19777300306.
- [12] Sandrine Bourrelly, Philip L. Llewellyn, Christian Serre, Franck Millange, Thierry Loiseau, and Gérard Férey. Different Adsorption Behaviors of Methane and Carbon Dioxide in the Isotypic Nanoporous Metal Terephthalates MIL-53 and MIL-47. *Journal of the American Chemical Society*, 127(39):13519–13521, October 2005. ISSN 0002-7863. doi: 10.1021/ja054668v.
- [13] Jarad A. Mason, Julia Oktawiec, Mercedes K. Taylor, Matthew R. Hudson, Julien Rodriguez, Jonathan E. Bachman, Miguel I. Gonzalez, Antonio Cervellino, Antonietta Guagliardi, Craig M. Brown, Philip L. Llewellyn, Norberto Masciocchi, and Jeffrey R. Long. Methane storage in flexible metal–organic frameworks with intrinsic thermal management. *Nature*, 527(7578):357–361, October 2015. ISSN 0028-0836, 1476-4687. doi: 10.1038/nature15732.
- [14] Matthias Thommes, Katsumi Kaneko, Alexander V. Neimark, James P. Olivier, Francisco Rodriguez-Reinoso, Jean Rouquerol, and Kenneth S W Sing. Physisorption of gases, with special reference to the evaluation of surface area

- and pore size distribution (IUPAC Technical Report). *Pure and Applied Chemistry*, 87(9-10):1051–1069, 2015. ISSN 13653075. doi: 10.1515/pac-2014-1117.
- [15] Philip L. Llewellyn and Guillaume Maurin. Gas adsorption microcalorimetry and modelling to characterise zeolites and related materials. *Comptes Rendus Chimie*, 8(3-4):283–302, March 2005. ISSN 16310748. doi: 10.1016/j.crci.2004.11.004.
- [16] P. L. Llewellyn, J. P. Coulomb, Y. Grillet, J. Patarin, H. Lauter, H. Reichert, and J. Rouquerol. Adsorption by MFI-type zeolites examined by isothermal microcalorimetry and neutron diffraction. 1. Argon, krypton, and methane. *Langmuir*, 9(7):1846–1851, July 1993. ISSN 0743-7463, 1520-5827. doi: 10.1021/la00031a036.
- [17] E Calvet and H Prat. *Recent Progress in Microcalorimetry*. 1963. OCLC: 893676446.
- [18] Françoise Rouquerol, Jean Rouquerol, and Douglas H. Everett. Gas—solid interactions. General derivation of reaction enthalpies from the data of isothermal microcalorimetry. *Thermochimica Acta*, 41(3):311–322, November 1980. ISSN 00406031. doi: 10.1016/0040-6031(80)87207-8.
- [19] Eric Lemmon. NIST Reference Fluid Thermodynamic and Transport Properties Database: Version 9.0, NIST Standard Reference Database 23, 1989.
- [20] Andrew D. Wiersum, Estelle Soubeyrand-Lenoir, Qingyuan Yang, Beatrice Moulin, Vincent Guillerm, Mouna Ben Yahia, Sandrine Bourrelly, Alexandre Vimont, Stuart Miller, Christelle Vagner, Marco Daturi, Guillaume Clet, Christian Serre, Guillaume Maurin, and Philip L. Llewellyn. An Evaluation of UiO-66 for Gas-Based Applications. *Chemistry - An Asian Journal*, 6(12):3270–3280, December 2011. ISSN 18614728. doi: 10.1002/asia.201100201.
- [21] D.D Do and H.D Do. Adsorption of supercritical fluids in non-porous and porous carbons: Analysis of adsorbed phase volume and density. *Carbon*, 41(9):1777–1791, 2003. ISSN 00086223. doi: 10.1016/S0008-6223(03)00152-0.
- [22] Joeri F Denayer, Gino V Baron, Johan a Martens, and Pierre a Jacobs. Chromatographic Study of Adsorption of n-Alkanes on Zeolites at High Temperatures. *J. Phys. Chem. B*, 102(97):3077–3081, 1998. ISSN 1520-6106. doi: 10.1021/jp972328t.
- [23] Alan L. Myers. Thermodynamics of adsorption in porous materials. *AIChE Journal*, 48(1):145–160, January 2002. ISSN 00011541. doi: 10.1002/aic.690480115.
- [24] Gesa Wißmann, Andreas Schaate, Sebastian Lilienthal, Imke Bremer, Andreas M. Schneider, and Peter Behrens. Modulated synthesis of Zr-fumarate MOF. *Microporous and Mesoporous Materials*, 152:64–70, April 2012. ISSN 13871811. doi: 10.1016/j.micromeso.2011.12.010.
- [25] Gesa Zahn, Philip Zerner, Jann Lippke, Fabian L. Kempf, Sebastian Lilenthal, Christian A. Schröder, Andreas M. Schneider, and Peter Behrens. Insight into the mechanism of modulated syntheses: *In Situ* synchrotron diffraction studies on the formation of Zr-fumarate MOF. *CrystEngComm*, 16(39):9198–9207, 2014. ISSN 1466-8033. doi: 10.1039/C4CE01095G.
- [26] Gesa Zahn, Hendrik Albert Schulze, Jann Lippke, Sandra König, Uta Sazama, Michael Fröba, and Peter Behrens. A water-born Zr-based porous coordination polymer: Modulated synthesis of Zr-fumarate MOF. *Microporous and Mesoporous Materials*, 203:186–194, February 2015. ISSN 13871811. doi: 10.1016/j.micromeso.2014.10.034.
- [27] Helge Reinsch, Steve Waitschat, Sachin M. Chavan, Karl Petter Lillerud, and Norbert Stock. A Facile “Green” Route for Scalable Batch Production and Continuous Synthesis of Zirconium MOFs: A Facile “Green” Route for Scalable Batch Production and Continuous Synthesis of Zirconium MOFs. *European Journal of Inorganic Chemistry*, 2016 (27):4490–4498, September 2016. ISSN 14341948. doi: 10.1002/ejic.201600295.
- [28] Bart Bueken, Niels Van Velthoven, Tom Willhammar, Timothée Stassin, Ivo Stassen, David A. Keen, Gino V. Baron, Joeri F. M. Denayer, Rob Ameloot, Sara Bals, Dirk De Vos, and Thomas D. Bennett. Gel-based morphological design of zirconium metal-organic frameworks. *Chemical Science*, 8(5):3939–3948, 2017. ISSN 2041-6520, 2041-6539. doi: 10.1039/C6SC05602D.
- [29] Hiroyasu Furukawa, Felipe Gándara, Yue-Biao Zhang, Juncong Jiang, Wendy L. Queen, Matthew R. Hudson, and Omar M. Yaghi. Water Adsorption in Porous Metal–Organic Frameworks and Related Materials. *Journal of the American Chemical Society*, 136(11):4369–4381, 2014. ISSN 0002-7863. doi: 10.1021/ja500330a.

- [30] Youn Jue Bae, Eun Seon Cho, Fen Qiu, Daniel T. Sun, Teresa E. Williams, Jeffrey J. Urban, and Wendy L. Queen. Transparent Metal–Organic Framework/Polymer Mixed Matrix Membranes as Water Vapor Barriers. *ACS Applied Materials & Interfaces*, 8(16):10098–10103, April 2016. ISSN 1944-8244, 1944-8252. doi: 10.1021/acsmami.6b01299.
- [31] Hyunho Kim, Sungwoo Yang, Sameer R Rao, Shankar Narayanan, Eugene A Kapustin, Hiroyasu Furukawa, Ari S Umans, Omar M Yaghi, and Evelyn N Wang. Water harvesting from air with metal-organic frameworks powered by natural sunlight. *Science*, 356(6336):430–434, April 2017. ISSN 0036-8075. doi: 10.1126/science.aam8743.
- [32] Hyunho Kim, Sameer R. Rao, Eugene A. Kapustin, Lin Zhao, Sungwoo Yang, Omar M. Yaghi, and Evelyn N. Wang. Adsorption-based atmospheric water harvesting device for arid climates. *Nature Communications*, 9(1), December 2018. ISSN 2041-1723. doi: 10.1038/s41467-018-03162-7.
- [33] Jongwon Choi, Li-Chiang Lin, and Jeffrey C. Grossman. Role of Structural Defects in the Water Adsorption Properties of MOF-801. *The Journal of Physical Chemistry C*, 122(10):5545–5552, March 2018. ISSN 1932-7447, 1932-7455. doi: 10.1021/acs.jpcc.8b00014.
- [34] M. Vandichel, J. Hajek, A. Ghysels, A. De Vos, M. Waroquier, and V. Van Speybroeck. Water coordination and dehydration processes in defective UiO-66 type metal organic frameworks. *CrystEngComm*, 18(37):7056–7069, 2016. ISSN 1466-8033. doi: 10.1039/C6CE01027J.
- [35] Chang Yeon Lee, Youn-Sang Bae, Nak Cheon Jeong, Omar K. Farha, Amy A. Sarjeant, Charlotte L. Stern, Peter Nickias, Randall Q. Snurr, Joseph T. Hupp, and SonBinh T. Nguyen. Kinetic Separation of Propene and Propane in Metal-Organic Frameworks: Controlling Diffusion Rates in Plate-Shaped Crystals via Tuning of Pore Apertures and Crys-tallite Aspect Ratios. *Journal of the American Chemical Society*, 133(14):5228–5231, April 2011. ISSN 0002-7863, 1520-5126. doi: 10.1021/ja200553m.
- [36] Miguel A. Granato, Miguel Jorge, Thijs J.H. Vlugt, and Alírio E. Rodrigues. Diffusion of propane, propylene and isobutane in 13X zeolite by molecular dynamics. *Chemical Engineering Science*, 65(9):2656–2663, May 2010. ISSN 00092509. doi: 10.1016/j.ces.2009.12.044.
- [37] Aldo F. Combariza, German Sastre, and Avelino Corma. Propane/Propylene Diffusion in Zeolites: Framework Dynamics. *The Journal of Physical Chemistry C*, 113(26):11246–11253, July 2009. ISSN 1932-7447, 1932-7455. doi: 10.1021/jp903245j.

4. Exploring the impact of structural defects

4.1. Introduction

Ideality is a rarely encountered phenomenon in nature. In fact, experience has shown that deliberate and concerted efforts must be made in order to obtain states of matter that have all the properties described by an “ideal state”. Often the divergence is small and can be approximated away, as is the case when using the ideal equation of state for noble gasses or ascribing the thermal radiation emitted by an object to a black-body spectrum. It is, however, in non-ideality where the fascinating complexity of the world asserts itself and where advances in our understanding can be made.

When considering crystals, the ideal description of an infinite periodic repetition of building blocks in three dimensional space is not applicable in the real world. From the necessary existence of crystal boundaries to the possible presence of other structural irregularities, these so called crystal “defects” can have varying effects on the bulk properties of the material. Their presence is not necessarily a fault as they often impart the material with beneficial characteristics on multiple length scales. An understanding of the interplay of defects in the lattices of alloys is an art in itself. Crystal grain size and presence of additives such as carbon and nickel can completely change the hardness, ductility, tensile strength and corrosion resistance of steel.⁽¹⁾ Various other forms of disorder can introduce completely new behaviours altogether. The insertion of foreign elements into the crystal structure of semiconductor materials, such as silicon, can alter its electronic properties and is responsible for the ubiquitousness of computing devices based on the transistor.⁽²⁾ This application of defects can be said to have ushered in the modern digital age, just as the creation of steel led to the industrial revolution. Other such emergent properties exist such as high temperature superconductivity⁽³⁾ or thermoelectric behaviour⁽⁴⁾ which are influenced by defect-related spin effects or defect-mediated charge transfer. As such, the kind of heterogeneity afforded by defects is a key attribute in condensed matter physics and a target for material design. The scientific foray in their control, either through generation or by inhibition can be termed “defect engineering”.

As porous coordination polymers (PCPs) and their subclasses, metal organic frameworks (MOFs) and covalent organic frameworks (COFs), became prominent topics of study in the field of porous materials, the presence and desirability of defects in their ordered crystal structures has been put into question. Investigation of the propensity of these compounds to form defects has suggested potential benefits in the fields of catalysis⁽⁵⁾, gas storage and separation^(6–8), and has even alluded

to applications in sensing and optoelectronics.⁽⁹⁾ Furthermore, MOFs such as UiO-66 and similar oxo-Zr coordination compounds have been shown to have intrinsically defective structures, where clustering and correlation of defects is in fact inevitable.⁽¹⁰⁾ The engineering of defects in PCPs is currently the focus of many initiatives as it is seen as a highly desirable method of tuning their properties through judicious design.^(5,11,12)

From the point of view of describing adsorption in such materials, the presence of defects introduces a conundrum. If a MOF can be defective, and is often intrinsically so, a slight change in synthesis conditions can introduce a large variability in its properties, and obtaining a “standard” isotherm may be a challenge. A large scale meta analysis of the correlation between material structure and its adsorption performance cannot be achieved unless the contribution of defects is assessed for each material.

Chapter summary

In this chapter we explore the kind of changes in adsorption behaviour introduced through defect engineering with the high throughput processing tools presented in chapter 2. First, the range of crystal defects that can be found in MOFs is presented. A summary of the known methods for controlling defects in such materials is discussed, as well as the known impact on different properties. Particular focus is placed on the zirconium variant of UiO-66, due to its remarkable stability to the presence of defects in its structure. An alternative approach to defect generation in this MOF is explored, through induced leaching of linkers in a solvent solution of monotopic acids which have been shown to induce defect formation when present during synthesis. The influence on defect type and preponderence of the acid, its concentration and the solvent itself is investigated, through the changes in adsorption behaviour.

Contributions

This work was in done in collaboration with the DEFNET project partner at the Centre for Surface Chemistry and Catalysis in KU Leuven. The study was designed by Paul Iacomi and João Marreiros during the secondment undertaken in COK as part of this project. Two PWI master students, Giel Arnauts and Wouter Arts helped with the synthesis, leaching and characterisation of the first trial batch. João Marreiros conducted the synthesis, leaching, XRD and NMR of further batches in Leuven. Paul Iacomi performed characterisation through TGA and all physisorption measurements in Marseille. Prof. Philip Llewellyn and Prof. Rob Ameloot provided critical input in the direction of the study and the significance of the results.

4.2. The defective nature of MOFs

4.2.1. Types of crystal defects and their analogues in MOFs

From a crystallographic point of view, defects can be described as features which suspend the order of components in an ideally regular lattice. The building blocks in the case of MOFs can be either individual atoms, molecules or other higher order structure building units (SBUs). Any change with leads to local breaking of symmetry with respect to that original structure can be viewed as a defect.

With respect to dimensionality, defects can be described as point defects, line defects (such as edge dislocations), plane defects (such as grain boundaries or stacking faults) and bulk defects (macroscopic voids, phase coexistence). When it comes to point defects, we can broadly refer to several types: **substitutional defects**, where an existing building unit is replaced or transformed into another, **inclusion or interstitial defects**, where a foreign component or building block is included in the framework and **vacancy defects** where one of the lattice sites is unoccupied. In the context of MOFs, the same general categories of defects apply. However, due to the higher degrees of freedom available in these compounds, a greater variety of potential crystal defects can exist.

Vacancy defects are encountered through missing linker and missing cluster defects. These analogues to Schottky defects arise from the removal of one or several topological nodes or vertices. In most cases, the charge neutrality of the framework is maintained through coordination of available counterions or solvent molecules, though changes in the oxidation state of the metal atoms may also occur.

Substitution point defects are also highly common in MOFs, as the usual requirement for framework connectivity is the existence of “click groups” on metal nodes and linkers. Any molecule which fulfils the connectivity and size requirements may be used, a property which has been exploited in the topological approach to creating new MOFs.^(13–15) It also allows for MOFs in which nodes or vertices are only partly replaced with analogues to be created. This strategy has been successfully employed to create mixed-linker or mixed-metal structures.^(16,17) It should be noted that if the distribution of the substitutions takes a homogenous pattern throughout the lattice, the structure may no longer fall under the definition of a defect.

A special case of substitutional defects which are present in MOFs are mixed valence defects. When metals with multiple stable oxidation states, such as Cu (I–II), Fe (II–III) etc. are part of the framework, a change in their oxidation state can occur. This has been shown to be an integral part of copper paddlewheel and iron trimesate containing MOFs⁽¹⁸⁾ and can even be seen with the naked eye, as such defects have been shown to give HKUST-1 its common blue colour.⁽¹⁹⁾

Inclusion-type point defects are loosely applied to MOFs. As the definition describes an interstitial defect to be an atom occupying an usually vacant space, all foreign bodies occupying the available porosity of the MOF, including aforementioned counterions and solvents could be considered

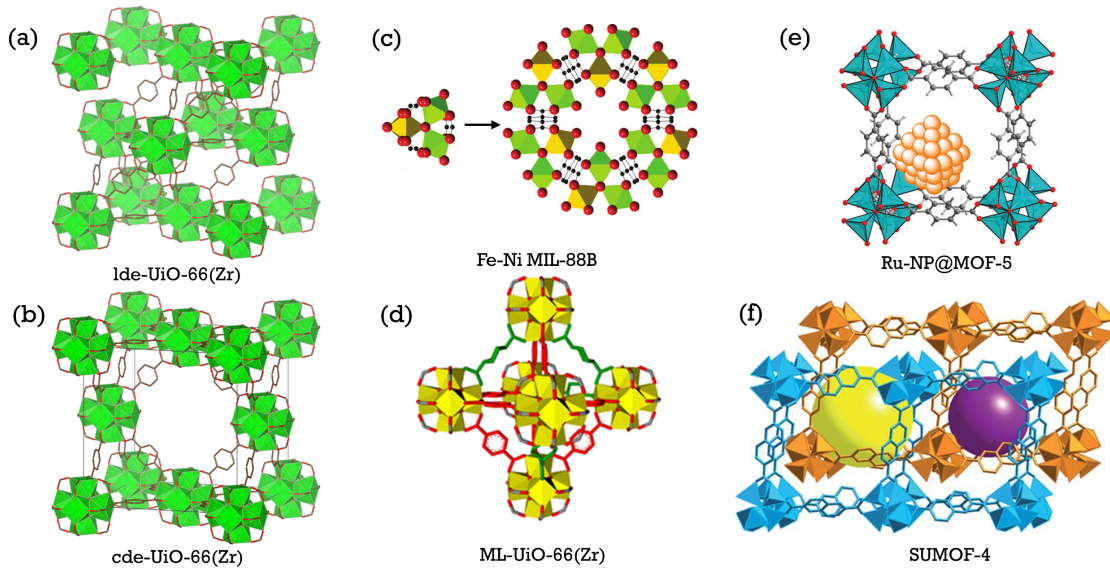


Figure 4.1.: Different types of defects as seen in MOFs: vacancy defects in the form of (a) missing linker and (b) missing cluster substitutional defects such as (c) mixed linker⁽¹⁶⁾ and (d) mixed metal⁽²²⁾ MOFs or defects as created through (e) nanoparticles⁽²¹⁾ or (f) interpenetration⁽²³⁾

as defects in the traditional crystallographic sense. Introduction of nanoparticles such as metals or metal oxides inside the pores is a more traditional view of such defects. These have been shown to have beneficial effects in catalytical applications.^(20,21)

A common feature of structured high porosity compounds is interpenetration. While not a defect in the classical sense, it has important effects on their properties.⁽²⁴⁾ With a large enough pore size, a secondary lattice can form in the pore voids of the primary one. This imposes a limit on the common design strategy of isoreticular synthesis, but can introduce new features such as better adsorption through confinement, increase in active site count and even flexibility.

Finally, the surface of the MOF can also be regarded as a boundary or plane defect. The nature of the surface plays a role in intra-particle interactions, important when considering the agglomeration behaviour or inclusion of crystals in a membrane.⁽²⁵⁾ The surface properties play a crucial role in MOFs which are synthesised as thin films^(26,27), where the nearly 2D materials are better defined by interfacial characteristics than through bulk properties. Crystal size effects on MOF properties such as flexibility can also be through of as a consequence of surface characteristics, more specifically of surface-to-volume ratio. When considering such soft materials^(28,29), it has been shown that the flexible behaviour is highly influenced by entropy barriers introduced by the surface.

4.2.2. Consequences of defects

The introduction of defects in the regular crystal lattice of metal organic frameworks can have a dramatic impact on their properties. In general, the following may occur:

- the porosity of the structured is altered, increasing in the case of vacancy defects and decreasing when bulky substitutions or inclusions are made;
- interactions with adsorbed molecules change, through the different pore environment encountered or through the generation of coordinatively unsaturated sites (CUS);
- the stability of the resulting structure is lower than that of the parent MOF influencing bulk mechanical and thermal properties.
- electronic properties can be changed which may affect the optical electric or magnetic behaviour of the material.

From a purely geometric point of view, the introduction of missing linker or missing cluster defects leads to more voids in the structure, increasing its porosity. It often results in a larger specific surface area and pore volume and thus useful for applications such as gas storage which depend only on the available surface or capacity. Macro-scale void networks can also be desirable, as the better developed pore network has a large impact on the transport properties of the compound, increasing diffusion rates.

The inclusion of defects also changes the landscape of the pore walls leading to different interactions with adsorbed molecules. Charge balancing counterions, molecules capping defect sites, functionalisations of substituted linkers or CUS can change the chemistry of the pore, with specific interactions towards certain adsorbates.⁽³⁰⁾ For example, adsorption of water on oxo-Zr MOFs, has been seen to be dominated by the percentage of defects. The pore filling step can shift from high partial pressure ($0.6 \text{ } p/p_0$) to much lower pressures as seen in UiO-66⁽⁷⁾ and MOF-801.⁽⁶⁾ Defect site adsorbed molecules can also lead to cooperative phenomena, such as the beneficial effect of defect-adsorbed water on the catalysis of Fischer esterification.⁽³¹⁾ or the CO₂ capture on amine-grafted metal centers.⁽³²⁾ Another example can be seen in MOFs containing Fe trimers, such as MIL-127(Fe) or MIL-100(Fe) where heating or acid treatment can induce a reduction of one of the iron atoms, generating additional Lewis sites for catalysis⁽¹⁸⁾ or providing CUS for cooperative binding of carbon monoxide through a spin transition mechanism.⁽³³⁾

Of course, defects are also problematic. Most metal organic frameworks synthesised to date suffer from poor stability. Even if the material is crystalline when solvated, the framework may not have enough structural stability to be able to sustain itself when fully evacuated. The activation process itself can lead to framework collapse, due to the forces encountered in guest removal, necessitating complex activation processes, such as supercritical drying or preliminary solvent exchange. After activation, the metal-ligand bond is susceptible to attack by adsorbed species. Here, defects in the

framework have been shown to play a major role in its stability (or lack thereof).⁽³⁴⁾ Copper paddle-wheel containing structures are particularly vulnerable to such attack.⁽³⁵⁾

Finally, several completely different phenomena may emerge through the introduction of defects. Optical properties such as colour centers and induced luminescence⁽¹⁹⁾, changes in thermal conductivity or induced magnetic properties such as ferromagnetism⁽³⁶⁾ have been shown to be a consequence of the presence of defects.

4.2.3. Defect engineering of MOFs

Since defects introduce another degree of freedom for controlling the properties of metal organic frameworks, the study of their formation can lead to new methods of tuning a material towards a desired application. There are two major pathways of introducing defects, through control of the structure during synthesis or through post-synthetic methods.⁽³⁷⁾

For defect generation during synthesis, the so called “solid solution” approach is to mix several types of building blocks together, be it multiple linkers or metallic nodes. Mixing functionalised versions of linkers leads to the creation of partially-substituted MOFs. Mixed valency frameworks can also be synthesised through this method, as can be seen in the replacement of up to 32% of the linker in the framework in the ruthenium HKUST-1 analogue with a defect-generating linker.⁽³⁸⁾ The commonly used method of improving crystallinity and particle size of modulator-assisted synthesis⁽³⁹⁾ has been shown by Shearer et al. to be a reliable method of introducing defects.⁽⁴⁰⁾ The modulators act as capping agents and occupy metal coordination sites.

Post-synthetic methods are also widely employed for defect generation. Through acid treatment of the previously mentioned MIL-100(Fe), cleavage of one of the Fe–O bonds can be induced, with a protonation of the carboxylic linker and the generation of a CUS.⁽⁴¹⁾ Thermal treatment can achieve the same results, with weakly coordinated molecules removed to expose metal CUS or even *in situ* linker decomposition.⁽⁴²⁾ Ligand exchange has also been shown to be achievable post-synthetically,⁽⁴³⁾ through the replacement of existing linkers, capping agents or even induce structural “healing”. Finally, the linkers are still available for organic reactions which can transform a part of them into functionalised versions, as seen in the nitration of the terephthalate linker in MIL-101.⁽⁴⁴⁾

4.2.4. The propensity of UiO-66(Zr) for defect generation

The UiO-66(Zr) MOF and its derivatives are well known due to their thermal and chemical stability.⁽⁴⁵⁾ It is composed of $[Zr_6O_4(OH)_4]^{12+}$ clusters (seen in Figure 4.2a) which are connected via benzene dicarboxilate (BDC) linkers to form a face-centred cubic framework. Due to its exceptional stability among MOFs, it has been the focus of much research, where it has shown promise⁽⁴⁶⁾ in use for gas adsorption and catalytic applications.

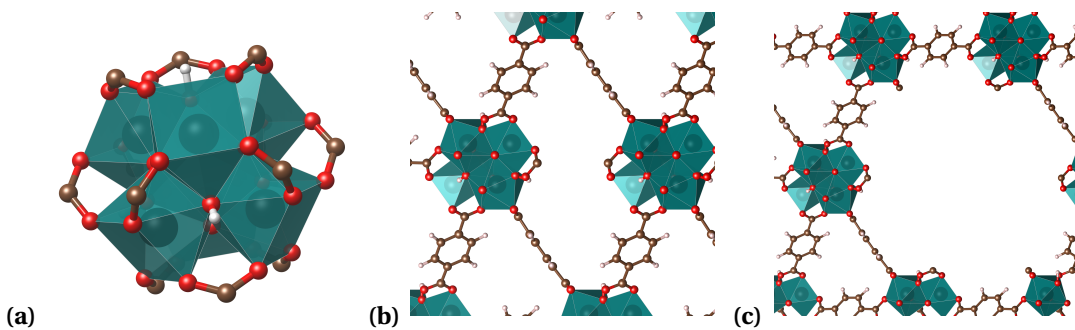


Figure 4.2: (a) The 12-coordinated Zr cluster in UiO-66(Zr) which connects with benzene dicarboxilate (BDC) linkers. Two prototypical defect types are shown (b) a missing linker defect and (c) a missing cluster defect. Zirconium octahedra are represented in turquoise, oxygen in red, carbon in brown and hydrogen in white.

The synthesis of many functional derivatives of UiO-66, through the use of different struts of nodes has been a stepping stone towards obtaining mixed-linker and mixed-metal materials, either thorough the solid solution or post-synthesis modification approach.⁽⁴⁷⁾ It has also been used as a support for nanoparticles, such as palladium⁽⁴⁸⁾ or platinum.⁽⁴⁹⁾

However, UiO-66 is particularly adept in its ability to support vacancy defects. Due to the stability of the metal-oxygen bond, and the high linker to metal ratio, the UiO family of MOFs can tolerate a high degree of defectivity in their structure, which manifests through either missing linker (Figure 4.2b) or missing cluster (Figure 4.2c) defects. Ever since the discovery of a number of defects in the pristine material through neutron powder diffraction methods⁽⁵⁰⁾ and the theoretical basis laid down by Cliffe et al.⁽¹⁰⁾ for the existence of correlated defective nanodomains where the existence of a vacancy induces defect formation in neighbouring sites, this MOF became a prototypical framework for the study of such defects. The modulated synthesis approach, initially used as a means of creating novel topologies and controlling crystal size⁽⁵¹⁾ has been remarkably successful in obtaining defective versions of UiO-66(Zr).⁽⁴⁰⁾ Post-synthetic methods such as ligand exchange⁽⁴³⁾, temperature-induced dehydroxilation of the zirconium cluster⁽⁵²⁾ and thermal removal of one of the linkers in a mixed-linker variant⁽¹⁶⁾ have been similarly adept in obtaining voids in the structure. More recently, the interplay between the defective nature of UiO-66 and the mechanism of post-synthesis linker exchange⁽⁵³⁾ has been put into the limelight.

In these defects, the metal sites are almost always capped, with monoacids such as formate and acetate, water, hydroxyl groups or other counterions being able to assume the role of capping agent. It has been shown by Thornton et al. that the influence of such defects on the adsorption properties depend not only on their position, but also on these capping agents.⁽⁵⁴⁾

Such vacancy defects prove to be useful for generating Lewis sites for catalytic application, as can be seen in the 4-fold increase in conversion in citronellar cyclization or the increase in 4-tert-butylcyclohexanone reduction from 5–7% to almost 90%.⁽⁵⁵⁾ They are also useful for gas separation, as they can increase the interaction towards a component of the mixture, seen for example on the

increased efficiency of CO₂ / N₂ separation.⁽⁵⁴⁾

It can therefore be concluded that vacancy defects are a fundamental characteristic of this MOF, with wide-ranging effects in its properties. As such, it is desirable to have methods to generate and control them. In the following pages, we examine a tertiary method for vacancy defect generation: leaching in solvent solution, a method which has been previously shown to be applicable to other MOFs.⁽⁵⁶⁾

4.3. Materials and methods

4.3.1. Materials

The UiO-66(Zr) MOF used in this study was synthesised according to the procedure described in section B.4, which was adapted from Shearer et al.⁽⁵⁷⁾. This particular method was chosen to ensure that a structure with a minimal number of intrinsic defects would be obtained.

The resulting parent MOF was activated for 8 h at 200 °C to ensure that all solvent was removed. 200 mg aliquots of material were prepared and placed in vials, alongside the monotopic acid dissolved in 20 ml of the respective solvent. The quantities of acid correspond to molar quantities of the framework. The samples were then gestated over a 24 h period at 80 °C in a temperature controlled oven. Pressure resistant Schott sealed bottles were used to ensure that solvents with a lower boiling point do not evaporate. After leaching, samples were collected and washed in ethanol for 4 h, a procedure repeated 4 times. Finally, all samples were dried at 120 °C.

To generate a comprehensive map of the influence of different variables on defect concentration, a number of leaching conditions have been selected. The same monotopic acids which have been successfully used as modulators in the synthesis of defective UiO-66 (formic acid (FA), acetic acid (AA), trifluoroacetic acid (TFA) and benzoic acid (BA)) were used in various concentration ranges, from 1 to 100 molar equivalents with respect to the framework. In order to verify the contribution of the solvent N,N'-dimethylformamide (DMF), deionized water, ethanol and dimethyl sulfoxide (DMSO) were used as the leaching medium. Two parent materials have been synthesised, PWI-C which formed the basis of the initial DMF test trial, and JM237 which was made in bulk to be used for subsequent solvent batches. The DMF dataset does not include any trifluoroacetic acid leached samples, as it was only used in the latter sample sets. Furthermore, no benzoic acid samples could be generated when using water as a solvent, due to its poor solubility. Finally, at high acid concentrations, several of the samples were completely dissolved during leaching conditions. The mass loss during leaching was found to be between 10 and 60%, depending on the acid and solvent used. When using 10 equivalents of TFA in DMSO, only 18% of the original sample could be recovered. A summary of all generated materials can be found in Table 4.1. Some properties of the acids and solvents used, such as acidity, solubility, etc. are found in Table E.2 and Table E.1 in Appendix E

respectively.

4.3.2. Methods for quantifying defects

Determining the abundance of missing linker and missing cluster defects and characterising their distribution is a major challenge, as the components of the framework do not change, only their local order.

If the distribution of defects can introduce changes in the long-range order and topology of their parent framework, such as by the introduction of phase changes, additional peaks can be observed through regular powder diffraction techniques. As Cliffe et al.⁽¹⁰⁾ has shown, the UiO-66 defect-free face-centred unit (**fcu**) net can be transformed through missing cluster defects into a (**reo**) net. Short-range correlations of such domains form nanoregions inside the parent structure and generate diffuse scattering peaks observable at low angles in powder X-ray (pXRD) diffraction patterns, corresponding to “forbidden” reflections in a primitive cubic superstructure. As such, these pXRD peaks can be used to verify the existence of missing cluster defects, but only when their abundance allows for nanodomains of (**reo**) nets to be formed. In this study, pXRD measurements were performed as described in section A.8 as quick screening for a large degree of defectivity.

One of the most accessible way of assessing the defectivity of a MOF is thermogravimetry (TGA). Through heating in an oxygen-rich atmosphere, the MOF is normally reduced to its metal oxide and a stoichiometric analysis of the TGA curve can allow for the percentage of missing linkers to be determined. TGA curves for this study were measured under an air atmosphere using the method described in section A.1. A heating rate of $5\text{ }^{\circ}\text{C min}^{-1}$ was used. The curves are then normalized with respect to the weight at $600\text{ }^{\circ}\text{C}$, which corresponds to pure ZrO_2 . The maximum possible mass loss of a solvent-free structure is calculated from the ratio of the fully-substituted, but dehydroxilated, metallic cluster $\text{Zr}_6\text{O}_6(\text{C}_6\text{H}_4(\text{COO})_2)_6$. The plateau of the TGA curve between $400\text{ }^{\circ}\text{C}$ to $500\text{ }^{\circ}\text{C}$, in the range where it is assumed that the molecules included in the framework are completely evacuated, is used as a measure of the number of terephthalate linkers which are missing.

In order to check for the inclusion of a modulator in the framework, the MOF can be digested with the help of a hydrofluoric acid and the resulting solution can be analysed through proton nuclear magnetic resonance (^1H NMR) or high performance liquid chromatography (HPLC). In this study, ^1H NMR was used through the procedure detailed in section A.9 to qualitatively and quantitatively assess the presence of the capping agents in the UiO-66(Zr) samples.

Finally, both nitrogen adsorption at 77 K and CO_2 adsorption at 303 K can be used to describe the surface characteristics and porosity of the samples. The methods for obtaining the isotherms are presented in detail in section A.4 and section A.7 for N_2 and CO_2 respectively.

Table 4.1.: Samples used in the UiO-66(Zr) linker leaching study

Sample name	Solvent	Modulator	Concentration	Observations
PWI-C	None	None	None	Parent material
FA1	DMF	FA	1:1	—
FA5	DMF	FA	1:5	—
FA10	DMF	FA	1:10	—
FA20	DMF	FA	1:20	—
FA100	DMF	FA	1:100	—
AA1	DMF	AA	1:1	—
AA5	DMF	AA	1:5	—
AA10	DMF	AA	1:10	—
AA20	DMF	AA	1:20	—
AA100	DMF	AA	1:100	—
BA1	DMF	BA	1:1	—
BA5	DMF	BA	1:5	—
BA10	DMF	BA	1:10	—
BA20	DMF	BA	1:20	—
BA100	DMF	BA	1:100	Completely dissolved
JM237	None	None	None	Parent material
JM328	H ₂ O	FA	1:10	—
JM329	H ₂ O	FA	1:100	—
JM330	H ₂ O	AA	1:10	—
JM331	H ₂ O	AA	1:100	—
JM332	H ₂ O	BA	1:10	—
JM333	H ₂ O	BA	1:100	—
JM334	H ₂ O	TFA	1:10	—
JM335	H ₂ O	TFA	1:100	—
JM351	MeOH	FA	1:10	—
JM352	MeOH	FA	1:100	—
JM353	MeOH	AA	1:10	—
JM354	MeOH	AA	1:100	—
JM355	MeOH	BA	1:10	—
JM356	MeOH	BA	1:100	—
JM357	MeOH	TFA	1:10	—
JM358	MeOH	TFA	1:100	—
JM359	MeOH	None	0	Control
JM360	DMSO	FA	1:10	—
JM361	DMSO	FA	1:100	—
JM362	DMSO	AA	1:10	—
JM363	DMSO	AA	1:100	—
JM364	DMSO	BA	1:10	—
JM365	DMSO	BA	1:100	—
JM366	DMSO	TFA	1:10	—
JM367	DMSO	TFA	1:100	Completely dissolved
JM368	DMSO	None	0	Control

4.4. Results and discussion

4.4.1. Crystallinity of leached samples

The crystallinity of the leached samples is verified through XRD. The results in section E.2 confirm that all resulting materials retain the same peaks in their powder diffraction patterns.

A closer look at the low angle scattering (Figure 4.3) reveals the appearance of diffuse peaks, which are marked in the figure by black arrows, which correspond to forbidden reflections of the (**reo**) phase. They confirm that the leached samples begin to exhibit phase coexistence of the original UiO-66(Zr) unit cell and the missing cluster (**reo**) net. These peaks have the highest intensity in the TFA treated materials, suggesting that it has the highest capability of introducing missing cluster defects.

4.4.2. Thermogravimetry results

A typical TGA curve, as measured on a pristine material is characterised by three main mass losses: a loss at low temperature, usually until 100 °C, which is indicative of adsorbed water from the environment; a secondary mass loss in the 100 °C to 200 °C range, corresponding to the evacuation of residual solvent from the pores and finally, a large step which is a sign of sample degradation as the linker is oxidized.

A selection of TGA curves measured on the leached samples can be seen in Figure 4.4. The complete set of data can be found in Appendix E, section E.3.

There are four types of differences that can arise between curves on different samples:

- the aforementioned change in overall height, which indicates the presence of missing linker defects;
- differences in the solvent removal step, as they have different boiling points and interactions with the framework;
- in case the defects are capped by an agent such as the modulator molecule used, it may introduce a new mass loss step between solvent removal and complete structure breakdown;
- finally, a highly defective structure loses part of its thermal resistance altering both the onset of mass loss and the final decomposition temperature.

From the TGA curve of the pristine UiO-66 material, it is immediately obvious that there are some defects already present in the sample. By using the normalized mass at 420 °C a linker-to-cluster

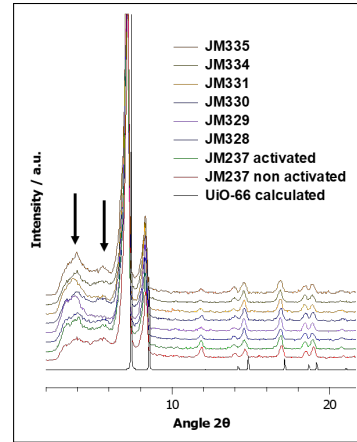


Figure 4.3.: Diffuse scattering peaks in the H₂O leached samples, highlighted by black arrows.

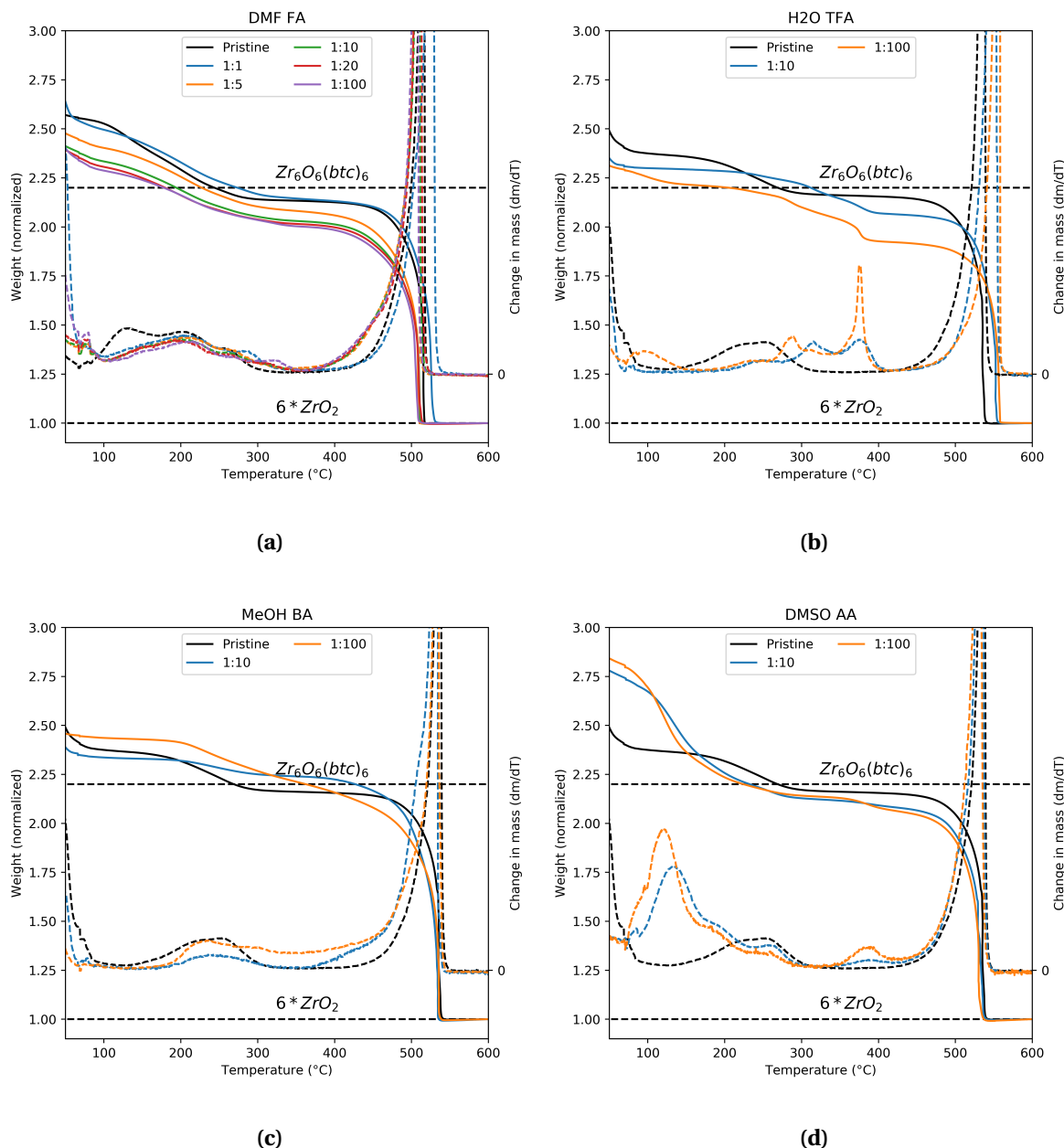
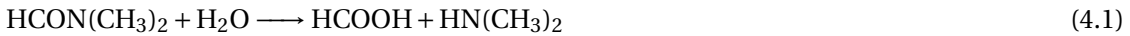


Figure 4.4: A selection of the TGA curves as measured on the leached samples: (a) formic acid in DMF, (b) trifluoroacetic acid in water, (c) benzoic acid in methanol and (d) acetic acid in DMSO. The curve for the parent material is in black. Dotted lines correspond to the secondary y axis as a semilogarithm of the first derivative of mass loss with respect to temperature.

ratio of around 11.6:1 can be calculated. This shows that there are still intrinsic defects in the as-synthesised structure. These defects are most likely capped by formate moieties, which have been generated during the solvothermal synthesis in DMF through solvent self-hydrolysis (Equation 4.1), as commercially available solvent has a small percentage of residual water.⁽⁴⁰⁾



It follows that the mass loss step around 250 °C is the evacuation of formate capping agents from the structure, to generate an open metal site. The same step can be found in the samples which have been leached with formic acid.

In leached samples where other acids were used, it is likely that the original formate capping the defects has been replaced with an acid molecule from solution, either because it is thermodynamically favourable, or simply through kinetic means due to the large excess present. As evidenced in Figure 4.4, the mass loss corresponding to the formate is reduced, or no longer seen. Acetic acid (Figure 4.4d) leaves the structure at a higher temperature, as a new peak is present at 390 °C. Strongly bound capping agents at defect sites have been shown to require a higher activation temperatures to be fully removed.⁽⁵⁸⁾ Benzoic acid (Figure 4.4c) introduces a progressive mass loss near the total decomposition temperature of 550 °C. As it is similar to the BTC linker, its higher stability is not surprising. Finally, the samples leached with TFA have a more complicated curve, with two or even three peaks in the first derivative with respect to temperature. This kind of degradation suggests the existence of different types of capping sites, some more strongly bound than others. A slight difference is also observed in their thermal stability, with all TFA samples having a 20 °C to 30 °C increase in decomposition temperature. Since defects normally have a negative impact on the thermal and mechanical resistance of a MOF, high resolution TGA experiments were carried out to eliminate possible influences of heating rate. The resulting curves (Figure E.5) still display the same behaviour. The effect is likely due to the electron-withdrawing effect of the TFA molecule on the Zr node, which induces a stronger Zr-carboxilate bond. A similar paradoxical increase in mechanical stability has been shown by Van de Voorde et al.⁽⁵⁹⁾ on TFA modulated defective UiO-66 materials.

The solvent used can be removed in all cases before 200 °C. DMSO has the highest preponderence in the leached samples (Figure 4.4d) and is the most difficult to remove, likely due to its higher boiling point.

It is also clearly visible that the leaching procedure led to the generation of defects. The curves of the leached samples fall below that of the original material in normalized weight, indicative of a lower linker-to-node ratio. These trends are analysed in subsection 4.4.4.

4.4.3. Nitrogen sorption at 77K

Isotherms have been recorded on samples activated at both 200 °C and 320 °C. It is important to note that, as seen from the TGA curves, not all capping agents leave the structure when thermally treating at a lower temperature. The moieties which are still coordinated to the Zr cluster will likely influence the adsorption behaviour. At a high temperature, the dehydroxilation of the metal center also occurs⁽⁵²⁾, which may also affect the interaction with physisorbed probes. Several example isotherms can be found in Figure 4.5, with the complete dataset present in Appendix E, section E.4.

There are a few isotherm features which can be analysed to assess the type of modifications introduced in the structure and their preponderence.

- The slope of the isotherm at low p/p_0 is representative of the first interactions with the pore surface, which can be quantified using the initial Henry constant. It will be influenced by any changes in pore environment such as CUS or functionalised defect sites.
- Missing linker defects will lead to an increase of the apparent surface area and perhaps to a more extensive pore network.
- The pore size distribution and total pore volume give indications on the presence of missing cluster defects and/or of the formation of mesoporous voids within the structure.
- A steep step at high p/p_0 is indicative of intercrystal condensation and suggests particle aggregation due to lower average crystal size.

It is immediately apparent that the leaching process had an influence on the adsorption characteristics of UiO-66. Isotherms of acid treated samples diverge from the parent material, often at different pressures. In general, the total molar capacity at full loading is seen to increase, a telltale sign of an increase in pore volume through defect generation. On the other hand, other particularities exist, such as the benzoic acid samples in methanol and DMSO where the low and high concentration has opposite effect on the total loading. Predictors of defects and trends will be analysed in the following section.

4.4.4. Characterisation of trends

The graphs in Figure 4.6 summarize the trends in missing linker defects as calculated through the TGA plateau at 420 °C. The DMF leached samples, due to the multiple datapoints with different acid concentrations show the clearest influence of this variable on defect generation. Even small amounts of modulator lead to the decrease of the linker-to-node ratio, but the increase in concentration stops having an effect at around 20:1 equivalents. It is likely that the trends are similar with other solvents, even if less datapoints are available.

In the case of benzoic acid the data bears careful interpretation. Thermogravimetric methods

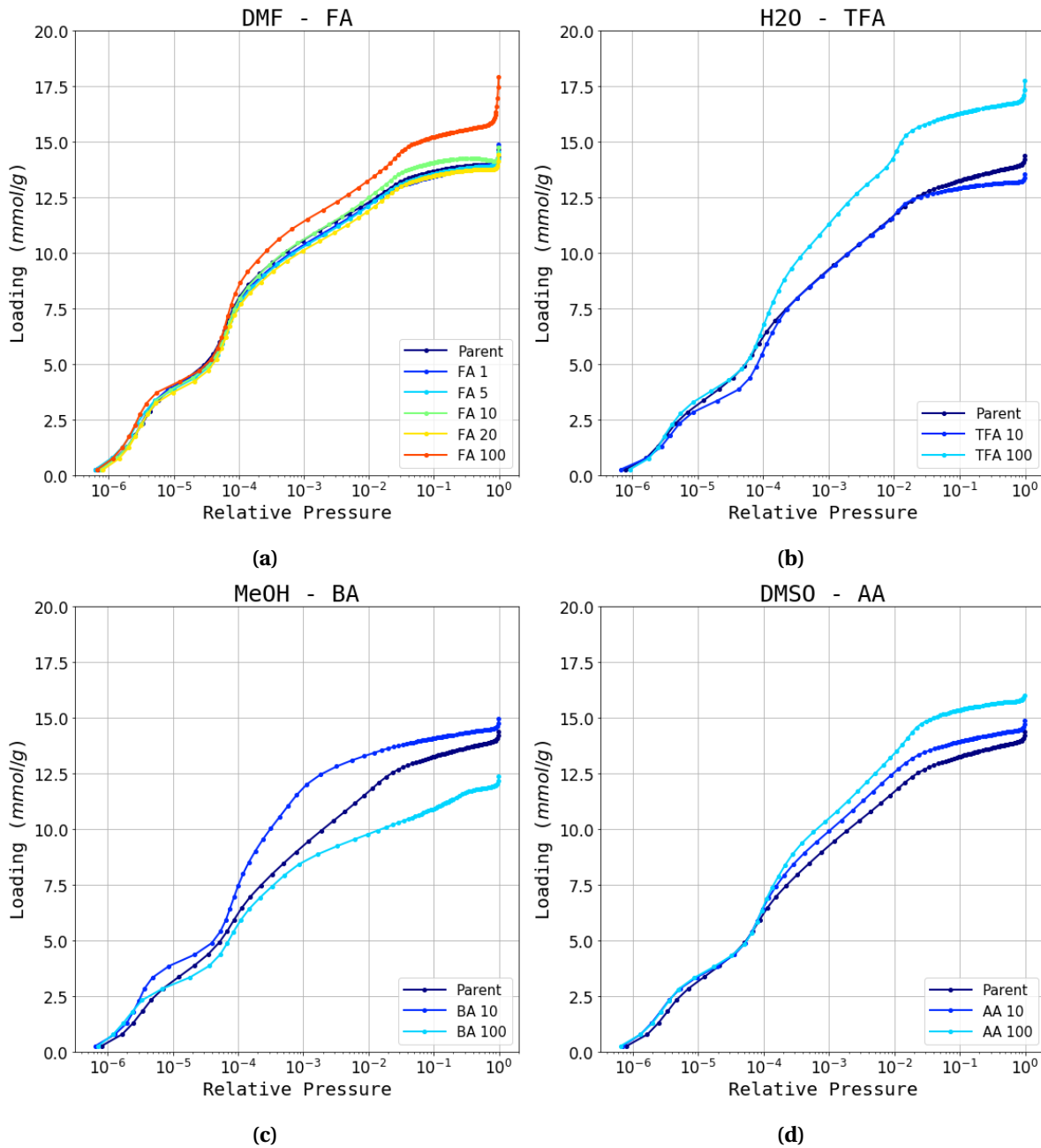


Figure 4.5.: A selection of nitrogen sorption isotherms as measured on the leached samples at 200 °C: (a) formic acid in DMF, (b) trifluoroacetic acid in water, (c) benzoic acid in methanol and (d) acetic acid in DMSO. The curve for the parent material is in dark blue. The x axis is logarithmic for clarity of low pressure points.

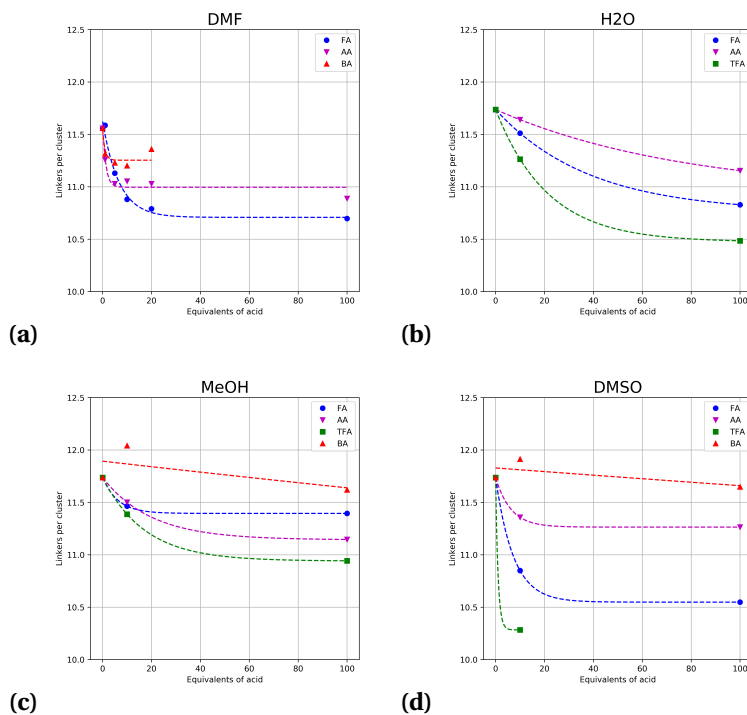


Figure 4.6.: Calculated linker-to-node ratio from the TGA curve normalized mass at 420 °C for (a) DMF (b) H₂O, (c) MeOH and (d) DMSO leached samples. A ratio of 12 to 1 corresponds to a completely defect-free structure. An exponential decay trendline is fitted to each set of points.

may not be suitable for assessing the resulting defects. The comparatively large molecule, high boiling point and similarity to the terephthalate linker make the removal of benzoic acid capping open metal sites harder, and as such, the plateau is not an accurate indication of defectivity. Indeed, the calculated linker ratio is seen to actually increase in the case of methanol and DMSO. It is here proposed that in benzoic acid leached samples defect generation occurs through the coordination of two benzoic molecules (or one, in the case of a “dangling” linker), as seen in Figure 4.7, with the increased amount of organic material effectively compensating for any defects that could be seen in the TGA curve.

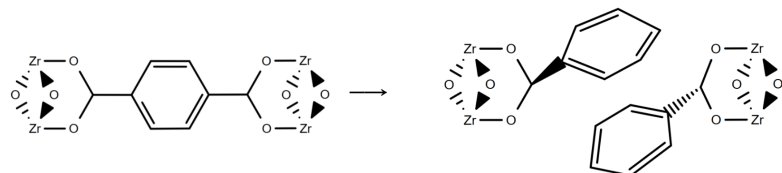


Figure 4.7.: A defect site created through benzoic acid.

For the nitrogen adsorption dataset, the predictors described in the previous section have been calculated using the pyGAPS framework (methods are described in chapter 2). The Henry constant

is determined through the initial slope method, with a linear section found below $10^{-4} p/p_0$. Total pore volume is taken as the liquid density of the amount adsorbed at 0.8 p/p_0 , assuming that nitrogen is in a liquid-like state in the MOF pores. The pore size distribution was calculated through the Horvath-Kawazoe method for micropores, the Dollimore-Heal method for mesopores and DFT kernel fitting for a multiscale distribution. While the applicability of these methods for determination of absolute pore size of the UiO-66 framework may be put into question, they can be readily used to compare between different samples of the same material. In general, the leaching process has a positive effect on surface area and pore volume, both of which increase with a higher concentration of acid used. The strength of the initial interaction of the nitrogen probe with the pore walls is changed as well, with more defective samples likely to have a more pronounced interaction, either through the introduction of CUS or modification of pore environment.

The influence of the acid on the linker-to-node ratio appears to be constant throughout the solvents used, with an overall trend of TFA > FA > AA > BA. The order is similar to the acidic character of the compounds, except for benzoic acid which has a lower pKa (4.2) than acetic acid (4.7). The result is in accordance to the trend published by Shearer et al. when analysing the influence of these acids as used during modulated synthesis on the defectivity of the resulting material.⁽⁴⁰⁾

When examining the influence of the solvent, another trend appears to emerge, with samples leached in DMSO having the largest propensity for defect generation, followed by DMF, water and methanol. In fact, a sample with a high concentration of TFA cannot be obtained, as the framework simply dissolves in the solution. The contribution of the solvent is not as easy to determine due to the complex interplay of multiple factors. The polarity of the solvent molecule has been linked to the rate of post synthetic ligand exchange from pristine UiO-66(Zr).⁽⁴⁷⁾ The leaching results do not, however, conform to the same trend, as water having a relative polarity of 1.0 introduces more defects than methanol (0.7) while DMF (0.38) is less effective than DMSO (0.44). The solubility of terephthalic acid in the solvent of choice may likely be a limiting factor driving its removal from the framework. Water, which has the lowest solubility for BTC, is one of the better solvents for defect generation, likely due to the high temperature of the reaction. As a strong acid is added, the equilibrium shifts even more towards the left, which may explain the worse performance of low equivalents of TFA in water as seen from adsorption predictors. At high concentrations, it is likely that the rate constant for the protonation of the metal-oxygen bond starts to dominate the leaching process. The viscosity of the solvent may also play a role in the mass transport of compounds through the porous media. However, the liquid with the highest kinematic viscosity, DMSO is actually the top performer during leaching, indicating that mass transfer may not be a factor.

The calculated pore sizes with both the HK method and the DFT method show two sharp peaks corresponding to the octahedral and tetrahedral pores in the UiO-66 structure. In Figure 4.9, the pore size distribution for the DMSO dataset is depicted, for both low temperature and high temperature activated variants. The appearance of a tertiary pore is visible in the leached samples with formic, acetic and trifluoroacetic acid. This pore size likely corresponds to the increased pore vol-

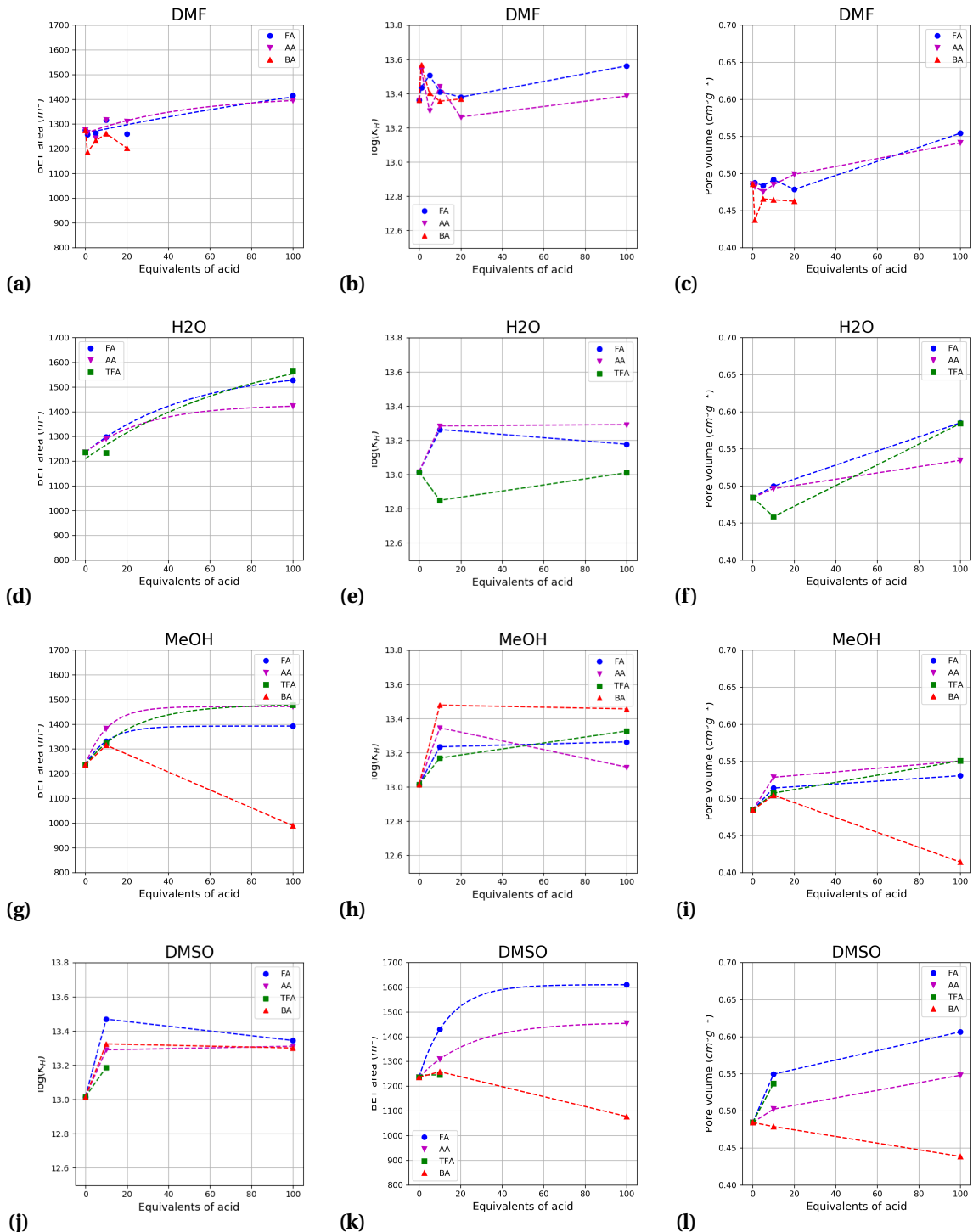


Figure 4.8: Characterisation of all samples through predictors obtained through processing of the nitrogen physisorption data at 200 °C. The figure shows BET surface area (a-d), the logarithm of the initial Henry constant (e-h), and calculated pore volume (i-l) for DMF, H₂O, MeOH and DMSO leached materials, respectively.

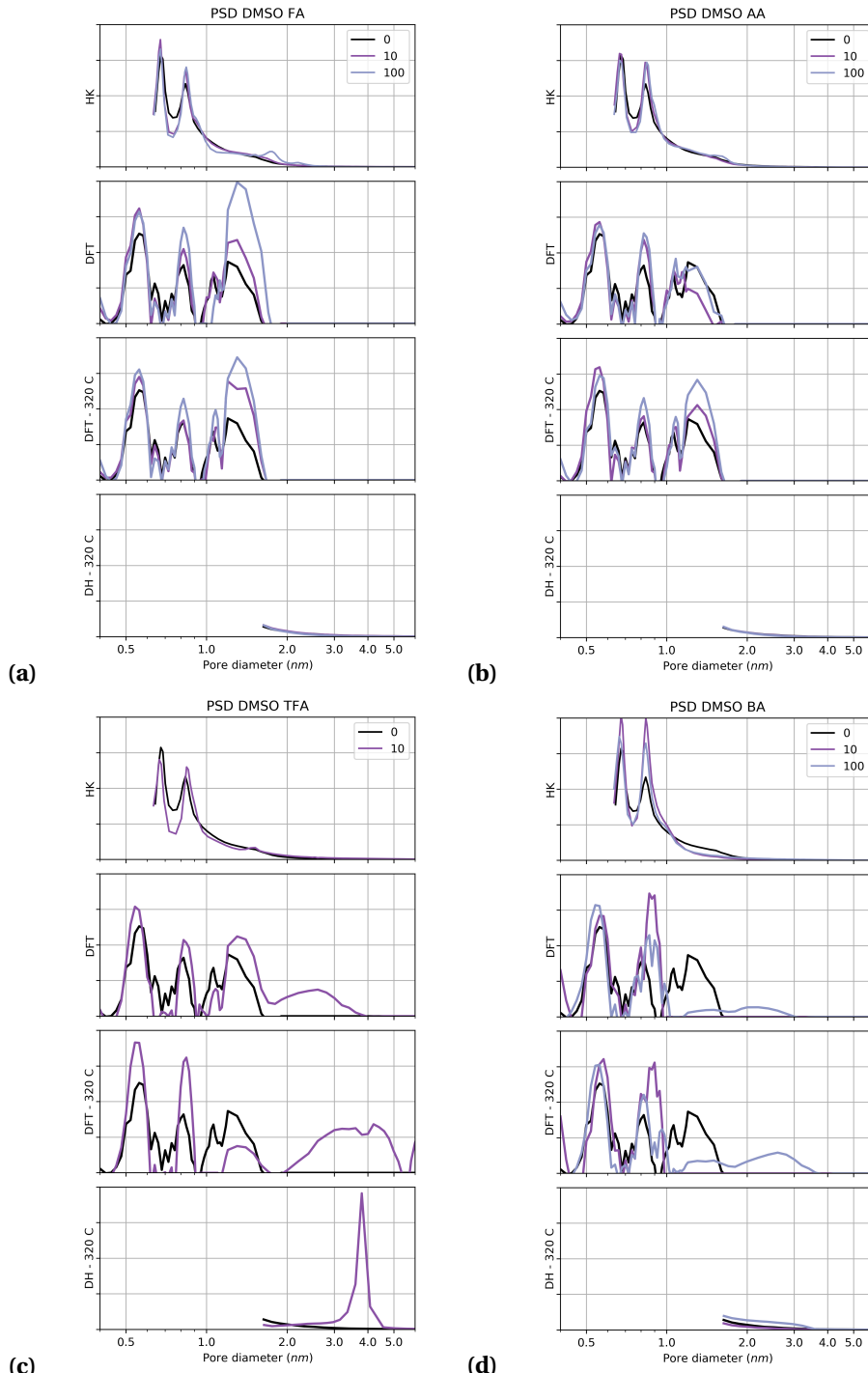


Figure 4.9.: Pore size distribution for the DMSO-leached samples as resulting from the HK (top), DFT (middle) and DH (bottom) methods on (a) formic acid, (b) acetic acid, (c) TFA and (d) BA. The top and bottom two distributions are calculated on the low and high temperature activated material respectively. The parent material is depicted in black.

ume introduced by missing linker-type defects. The calculated diameter of this tertiary pore is inversely proportional to the molecular size of the leaching compound used, which is a clear indication of the presence of the acid molecules in the structure as capping agents. On the samples which have been activated to 320 °C, the pore width shifts to a single value as the coordinated acids are evacuated.

The pore size distribution calculated in the benzoic acid leached samples shows the disappearance of peaks larger than around 1 nm, as the compound replaces formate as the capping agent for the initial defects in the structure. Due to the similarity of the terephthalate linker with benzoate, the structure becomes more “ideal” than the pristine material. At high concentrations of benzoic acid, an overall decrease in porosity may be seen, as two benzoate molecules may act as capping agents in adjacent sites (Figure 4.7), effectively lowering the available pore volume. The effect is corroborated by trends in the linker-to-node ratio, surface area and total pore volume in both methanol, DMSO and to a lesser extent DMF.

At very high concentrations of TFA and BA, a fourth pore size begins to be appear in the DFT calculated pore distribution. This is likely evidence that missing cluster defects can be introduced at these concentrations. It should be noted that if such large-scale modifications of the structure are possible, complete structural breakdown is not far away. Indeed, samples with higher concentrations of acid could not be obtained with TFA in DMSO, with sample subjected to these conditions ending up completely dissolved. The appearance of this type of porosity in the samples treated with benzoic acid is counterintuitive, as the TGA linker ratio does not allude to any changes in coordination. In this case, it could be that missing cluster defects are still generated forming a **re-*o*-benz** phase⁽⁶⁰⁾ while the excess of “dangling” benzoate moieties in the framework account for the decrease in surface area and capacity.

No hysteresis curve is observable on any samples activated at 200 °C. When activating at higher temperature, a hysteresis curve appears in the high concentration leached TFA samples (Figure 4.10), which corresponds to a pore size of around 4 nm in both DFT and DH calculated pore distribution. The shape of the hysteresis loop is also reminiscent of condensation in ink bottle-like pores, suggesting the existence of voids within the crystal matrix which are not directly accessible. This further confirms how effective highly acidic solutions can be at defect generation.

4.4.5. Carbon dioxide isotherms

The adsorption of carbon dioxide has been shown to be a good predictor for the presence of defects from comprehensive simulations by Thornton et al.⁽⁵⁴⁾. In their work they have shown that in

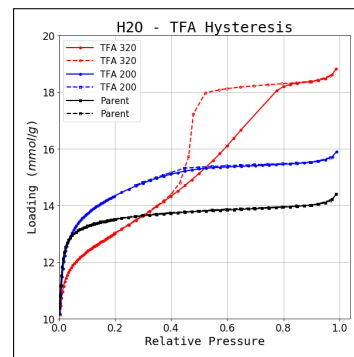


Figure 4.10.: Hysteresis loop in high temperature activated TFA treated UiO-66(Zr)

formate-capped defects, a shift of the CO₂ isotherm towards higher loading is seen at pressures over 5 bar, accompanied by a lower capacity at low pressures. Thus, in order to characterise the leached materials with a secondary probe molecule, carbon dioxide at 303 K was selected. Isotherms on the DMSO sample set are shown in Figure 4.11. The highest available acid ratio materials were selected, as the consequences of defects are likely to be more noticeable. It should be noted that, since activation was performed at 200 °C, complete removal of some capping agents did not take place.

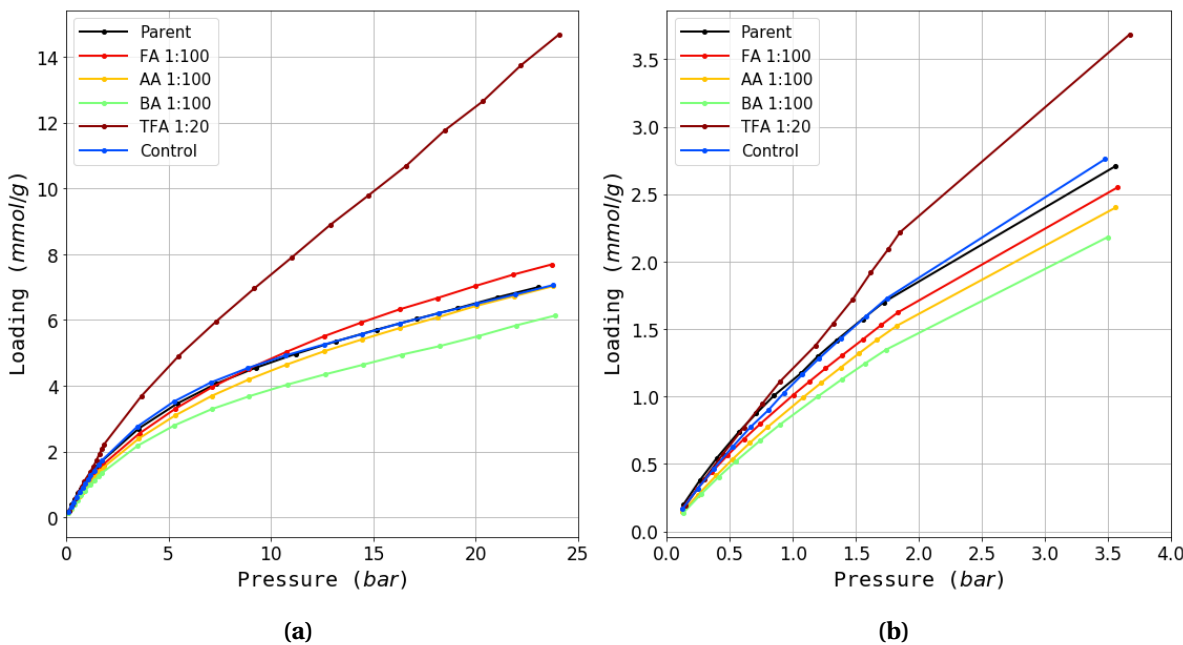


Figure 4.11.: CO₂ adsorption isotherms at 303 K on different materials leached in DMSO in the (a) 0 bar to 25 bar range and the (b) 0 bar to 4 bar range. All materials were activated at 200 °C.

Isotherms follow similar trends as observed with nitrogen sorption and TGA analysis. A large increase in amount adsorbed can be seen on the TFA leached sample, with almost a doubling in the capacity at high pressure ranges. These values can only be obtained if a missing cluster *re o* net is the dominant phase of the material. Combined with the increased interactions with the framework at low loadings due to the fluorine moieties, this variant shows an astounding increase in adsorption capacity. The formate leached sample exhibits a cross-over of the parent material isotherm, highly similar to the simulated missing linker isotherms with around 11 linkers per metal node. A similar pattern may be present in the acetic acid isotherm, but with the intersection point at around 20 bar. The benzoic acid isotherm is shifted downwards throughout the entire pressure range, a further indication that this modulator has a counterproductive effect for obtaining defective materials through leaching. Finally, the control and parent materials have nearly identical isotherms, which confirms that the solvent does not act alone to generate defects in the structure.

4.5. Conclusion

In summary, a new method of generating missing linker and missing cluster type defects in a UiO-66(Zr) framework has been presented. This type of post-synthetic modification is an alternative to modulated synthesis, and can be useful when crystal growth is not desirable. It also introduces new possibilities of framework functionalisation, through sequential rounds of leaching and defect healing. It does, however, come at a cost, as it also partially dissolves the material.

A few trends emerge in regards to the capacity of different solvents and acids to induce defect formation.

- The impact of the monotopic acid is mainly due to its acidity, with pKa a being a good predictor of the resulting defectivity.
- DMSO and water stand out as the most effective solvents for defect generation.
- In general, the leached samples have a larger surface area and pore volume, due to both missing linker and cluster defects. Benzoic acid is a special case where due to its large molecule, may instead result in a loss of available pore space.
- High concentrations of acids may induce mesoporosity through large-scale defect generation. These conditions also make the material susceptible to complete structural breakdown through attack at the crystal surface.
- The resulting defective structures may have different bulk properties such as thermal and mechanical resistance due to the influence of the defect capping agents.
- The coordinated acids can also have an impact on the adsorption properties through changes to the pore environment.

These results also show the vast influence that defects have on the adsorption properties of MOFs. From different interactions with the material surface to vastly different capacities and, in some cases, even changing the sizes of pores or introducing new porosity. When attempting to determine the adsorption performance and behaviour of a compound it is important to consider whether the material in question is representative of its stoichiometric composition or, as is more often the case, a complex interplay of ideal and non-ideal domains.

Bibliography

- [1] Robert E. Reed-Hill and R. Abbaschian. *Physical Metallurgy Principles*. The PWS-Kent series in engineering. PWS-Kent Pub, Boston, 3rd ed edition, 1992. ISBN 978-0-534-92173-6.
- [2] Roland A. Levy and North Atlantic Treaty Organization, editors. *Microelectronic Materials and Processes: Proceedings of the NATO Advanced Study Institute on Microelectronic Materials and Processes, Il Ciocco, Castelvecchio Pascoli, Italy, June 30-July 11, 1986*. Number vol. 164 in NATO ASI series. Series E, Applied sciences. Kluwer Academic, Dordrecht ; Boston, 1989. ISBN 978-0-7923-0147-9 978-0-7923-0154-7.
- [3] Anthony J. Leggett. What DO we know about high T c? *Nature Physics*, 2(3):134–136, March 2006. ISSN 1745-2473, 1745-2481. doi: 10.1038/nphys254.
- [4] Yanzhong Pei, Heng Wang, and G. J. Snyder. Band Engineering of Thermoelectric Materials. *Advanced Materials*, 24(46):6125–6135, December 2012. ISSN 09359648. doi: 10.1002/adma.201202919.
- [5] David S. Sholl and Ryan P. Lively. Defects in Metal–Organic Frameworks: Challenge or Opportunity? *The Journal of Physical Chemistry Letters*, 6(17):3437–3444, September 2015. ISSN 1948-7185. doi: 10.1021/acs.jpcllett.5b01135.
- [6] Jongwon Choi, Li-Chiang Lin, and Jeffrey C. Grossman. Role of Structural Defects in the Water Adsorption Properties of MOF-801. *The Journal of Physical Chemistry C*, 122(10):5545–5552, March 2018. ISSN 1932-7447, 1932-7455. doi: 10.1021/acs.jpcc.8b00014.
- [7] Pritha Ghosh, Yamil J. Colón, and Randall Q. Snurr. Water adsorption in UiO-66: The importance of defects. *Chem. Commun.*, 50(77):11329–11331, 2014. ISSN 1359-7345, 1364-548X. doi: 10.1039/C4CC04945D.
- [8] Jian-Rong Li, Ryan J Kuppler, and Hong-Cai Zhou. Selective gas adsorption and separation in metal–organic frameworks. *Chemical Society Reviews*, 38(5):1477, 2009. ISSN 0306-0012. doi: 10.1039/b802426j.
- [9] Matthew J. Cliffe, Elizabeth Castillo-Martínez, Yue Wu, Jeongjae Lee, Alexander C. Forse, Francesca C. N. Firth, Peyman Z. Moghadam, David Fairén-Jiménez, Michael W. Gaultois, Joshua A. Hill, Oxana V. Magdysyuk, Ben Slater, Andrew L. Goodwin, and Clare P. Grey. Metal–Organic Nanosheets Formed via Defect-Mediated Transformation of a Hafnium Metal–Organic Framework. *Journal of the American Chemical Society*, 139(15):5397–5404, April 2017. ISSN 0002-7863, 1520-5126. doi: 10.1021/jacs.7b00106.
- [10] Matthew J Cliffe, Wei Wan, Xiaodong Zou, Philip a Chater, Annette K Kleppe, Matthew G Tucker, Heribert Wilhelm, Nicholas P Funnell, François-Xavier Coudert, and Andrew L Goodwin. Correlated defect nanoregions in a metal–organic framework. *Nature communications*, 5(May):4176, 2014. ISSN 2041-1723. doi: 10.1038/ncomms5176.
- [11] Thomas D. Bennett, Anthony K. Cheetham, Alain H. Fuchs, and François-Xavier Coudert. Interplay between defects, disorder and flexibility in metal–organic frameworks. *Nature Chemistry*, 9(1):11–16, December 2016. ISSN 1755-4330. doi: 10.1038/nchem.2691.
- [12] Weibin Liang, Lin Li, Jingwei Hou, Nicholas D. Shepherd, Thomas D. Bennett, Deanna M. D’Alessandro, and Vicki Chen. Linking defects, hierarchical porosity generation and desalination performance in metal–organic frameworks. *Chemical Science*, 9(14):3508–3516, 2018. ISSN 2041-6520, 2041-6539. doi: 10.1039/C7SC05175A.
- [13] Brandon J. Burnett, Paul M. Barron, and Wonyoung Choe. Recent advances in porphyrinic metal–organic frameworks: Materials design, synthetic strategies, and emerging applications. *CrystEngComm*, 14(11):3839, 2012. ISSN 1466-8033. doi: 10.1039/c2ce06692k.
- [14] Mian Li, Dan Li, Michael O’Keeffe, and Omar M. Yaghi. Topological Analysis of Metal–Organic Frameworks with Polytopic Linkers and/or Multiple Building Units and the Minimal Transitivity Principle. *Chemical Reviews*, 114(2): 1343–1370, January 2014. ISSN 0009-2665, 1520-6890. doi: 10.1021/cr400392k.
- [15] Norbert Stock and Shyam Biswas. Synthesis of Metal–Organic Frameworks (MOFs): Routes to Various MOF Topologies, Morphologies, and Composites. *Chemical Reviews*, 112(2):933–969, February 2012. ISSN 0009-2665, 1520-6890. doi: 10.1021/cr200304e.
- [16] Bart Bueken, Niels Van Velthoven, Andraž Krajnc, Simon Smolders, Francis Taulelle, Caroline Mellot-Draznieks, Gregor Mali, Thomas D. Bennett, and Dirk De Vos. Tackling the Defect Conundrum in UiO-66: A Mixed-Linker Approach

- to Engineering Missing Linker Defects. *Chemistry of Materials*, 29(24):10478–10486, December 2017. ISSN 0897-4756, 1520-5002. doi: 10.1021/acs.chemmater.7b04128.
- [17] Amarajothi Dhakshinamoorthy, Abdullah M. Asiri, and Hermenegildo Garcia. Mixed-metal or mixed-linker metal organic frameworks as heterogeneous catalysts. *Catalysis Science & Technology*, 6(14):5238–5261, 2016. ISSN 2044-4753, 2044-4761. doi: 10.1039/C6CY00695G.
- [18] Ji Woong Yoon, You-Kyong Seo, Young Kyu Hwang, Jong-San Chang, Hervé Leclerc, Stefan Wuttke, Philippe Bazin, Alexandre Vimont, Marco Daturi, Emily Bloch, Philip L. Llewellyn, Christian Serre, Patricia Horcajada, Jean-Marc Grenèche, Alirio E. Rodrigues, and Gérard Férey. Controlled Reducibility of a Metal-Organic Framework with Coordinatively Unsaturated Sites for Preferential Gas Sorption. *Angewandte Chemie International Edition*, 49(34):5949–5952, August 2010. ISSN 14337851. doi: 10.1002/anie.201001230.
- [19] Kai Müller, Karin Fink, Ludger Schöttner, Meike Koenig, Lars Heinke, and Christof Wöll. Defects as Color Centers: The Apparent Color of Metal–Organic Frameworks Containing Cu²⁺-Based Paddle-Wheel Units. *ACS Applied Materials & Interfaces*, 9(42):37463–37467, October 2017. ISSN 1944-8244, 1944-8252. doi: 10.1021/acsami.7b12045.
- [20] Paolo Falcaro, Raffaele Ricco, Amirali Yazdi, Inhar Imaz, Shuhei Furukawa, Daniel Maspoch, Rob Ameloot, Jack D. Evans, and Christian J. Doonan. Application of metal and metal oxide nanoparticles@MOFs. *Coordination Chemistry Reviews*, 307:237–254, January 2016. ISSN 00108545. doi: 10.1016/j.ccr.2015.08.002.
- [21] Felicitas Schröder, Daniel Esken, Mirza Cokoja, Maurits W. E. van den Berg, Oleg I. Lebedev, Gustaaf Van Tendeloo, Bernadeta Walaszek, Gerd Buntkowsky, Hans-Heinrich Limbach, Bruno Chaudret, and Roland A. Fischer. Ruthenium Nanoparticles inside Porous [Zn₄O(bdc)₃] by Hydrogenolysis of Adsorbed [Ru(cod)(cot)]: A Solid-State Reference System for Surfactant-Stabilized Ruthenium Colloids. *Journal of the American Chemical Society*, 130(19):6119–6130, May 2008. ISSN 0002-7863, 1520-5126. doi: 10.1021/ja078231u.
- [22] Gia-Thanh Vuong, Minh-Hao Pham, and Trong-On Do. Synthesis and engineering porosity of a mixed metal Fe₂Ni MIL-88B metal–organic framework. *Dalton Trans.*, 42(2):550–557, 2013. ISSN 1477-9226, 1477-9234. doi: 10.1039/C2DT32073H.
- [23] Qingxia Yao, Jie Su, Ocean Cheung, Qingling Liu, Niklas Hedin, and Xiaodong Zou. Interpenetrated metal–organic frameworks and their uptake of CO₂ at relatively low pressures. *Journal of Materials Chemistry*, 22(20):10345, 2012. ISSN 0959-9428, 1364-5501. doi: 10.1039/c2jm15933c.
- [24] Ritesh Haldar, Nivedita Sikdar, and Tapas Kumar Maji. Interpenetration in coordination polymers: Structural diversities toward porous functional materials. *Materials Today*, 18(2):97–116, March 2015. ISSN 13697021. doi: 10.1016/j.mattod.2014.10.038.
- [25] Rocio Semino, Naseem A. Ramsahye, Aziz Ghoufi, and Guillaume Maurin. Microscopic Model of the Metal–Organic Framework/Polymer Interface: A First Step toward Understanding the Compatibility in Mixed Matrix Membranes. *ACS Applied Materials & Interfaces*, 8(1):809–819, January 2016. ISSN 1944-8244, 1944-8252. doi: 10.1021/acsami.5b10150.
- [26] Hartmut Gliemann and Christof Wöll. Epitaxially grown metal–organic frameworks. *Materials Today*, 15(3):110–116, March 2012. ISSN 13697021. doi: 10.1016/S1369-7021(12)70046-9.
- [27] Ivo Stassen, Nicholas Burtch, Alec Talin, Paolo Falcaro, Mark Allendorf, and Rob Ameloot. An updated roadmap for the integration of metal–organic frameworks with electronic devices and chemical sensors. *Chemical Society Reviews*, 46(11):3185–3241, 2017. ISSN 0306-0012. doi: 10.1039/C7CS00122C.
- [28] Simon Krause, Volodymyr Bon, Irena Senkovska, Daniel M. Többens, Dirk Wallacher, Renjith S. Pillai, Guillaume Maurin, and Stefan Kaskel. The effect of crystallite size on pressure amplification in switchable porous solids. *Nature Communications*, 9(1), December 2018. ISSN 2041-1723. doi: 10.1038/s41467-018-03979-2.
- [29] L. Vanduyfhuys, S. M. J. Rogge, J. Wieme, S. Vandenbrande, G. Maurin, M. Waroquier, and V. Van Speybroeck. Thermodynamic insight into stimuli-responsive behaviour of soft porous crystals. *Nature Communications*, 9(1), December 2018. ISSN 2041-1723. doi: 10.1038/s41467-017-02666-y.
- [30] Stefano Dissegna, Rifan Hardian, Konstantin Epp, Gregor Kieslich, Marie-Vanessa Coulet, Philip Llewellyn, and

- Roland A. Fischer. Using water adsorption measurements to access the chemistry of defects in the metal–organic framework UiO-66. *CrystEngComm*, pages 1–8, 2017. ISSN 1466-8033. doi: 10.1039/C7CE00224F.
- [31] Chiara Caratelli, Julianna Hajek, Francisco G. Cirujano, Michel Waroquier, Francesc X. Llabrés i Xamena, and Veronique Van Speybroeck. Nature of active sites on UiO-66 and beneficial influence of water in the catalysis of Fischer esterification. *Journal of Catalysis*, 352:401–414, August 2017. ISSN 00219517. doi: 10.1016/j.jcat.2017.06.014.
- [32] Thomas M. McDonald, Jarad A. Mason, Xueqian Kong, Eric D. Bloch, David Gygi, Alessandro Dani, Valentina Crocellà, Filippo Giordanino, Samuel O. Odoh, Walter S. Drisdell, Bess Vlaisavljevich, Allison L. Dzubak, Roberta Poloni, Sondre K. Schnell, Nora Planas, Kyuho Lee, Tod Pascal, Liwen F. Wan, David Prendergast, Jeffrey B. Neaton, Berend Smit, Jeffrey B. Kortright, Laura Gagliardi, Silvia Bordiga, Jeffrey A. Reimer, and Jeffrey R. Long. Cooperative insertion of CO₂ in diamine-appended metal-organic frameworks. *Nature*, 519:303, March 2015.
- [33] Douglas A. Reed, Benjamin K. Keitz, Julia Oktawiec, Jarad A. Mason, Tomče Runčevski, Dianne J. Xiao, Lucy E. Darago, Valentina Crocellà, Silvia Bordiga, and Jeffrey R. Long. A spin transition mechanism for cooperative adsorption in metal–organic frameworks. *Nature*, September 2017. ISSN 0028-0836, 1476-4687. doi: 10.1038/nature23674.
- [34] Nicholas C. Burch, Himanshu Jasuja, and Krista S. Walton. Water Stability and Adsorption in Metal–Organic Frameworks. *Chemical Reviews*, 114(20):10575–10612, October 2014. ISSN 0009-2665, 1520-6890. doi: 10.1021/cr5002589.
- [35] J. Raziel Álvarez, Elí Sánchez-González, Eric Pérez, Emilia Schneider-Revueltas, Ana Martínez, Adriana Tejeda-Cruz, Alejandro Islas-Jácome, Eduardo González-Zamora, and Illich A. Ibarra. Structure stability of HKUST-1 towards water and ethanol and their effect on its CO₂ capture properties. *Dalton Transactions*, 46(28):9192–9200, 2017. ISSN 1477-9226, 1477-9234. doi: 10.1039/C7DT01845B.
- [36] Lei Shen, Shuo-Wang Yang, Shengchang Xiang, Tao Liu, Bangchuan Zhao, Man-Fai Ng, Jörg Göettlicher, Jiabao Yi, Sean Li, Lan Wang, Jun Ding, Banglin Chen, Su-Huai Wei, and Yuan Ping Feng. Origin of Long-Range Ferromagnetic Ordering in Metal–Organic Frameworks with Antiferromagnetic Dimeric-Cu(II) Building Units. *Journal of the American Chemical Society*, 134(41):17286–17290, October 2012. ISSN 0002-7863, 1520-5126. doi: 10.1021/ja3077654.
- [37] Zhenlan Fang, Bart Bueken, Dirk E. De Vos, and Roland A. Fischer. Defect-Engineered Metal-Organic Frameworks. *Angewandte Chemie International Edition*, 54(25):7234–7254, June 2015. ISSN 14337851. doi: 10.1002/anie.201411540.
- [38] Wenhua Zhang, Max Kauer, Olesia Halbherr, Konstantin Epp, Penghu Guo, Miguel I. Gonzalez, Dianne J. Xiao, Christian Wiktor, Francesc X. Llabrés i Xamena, Christof Wöll, Yuemin Wang, Martin Muhler, and Roland A. Fischer. Ruthenium Metal-Organic Frameworks with Different Defect Types: Influence on Porosity, Sorption, and Catalytic Properties. *Chemistry - A European Journal*, 22(40):14297–14307, September 2016. ISSN 09476539. doi: 10.1002/chem.201602641.
- [39] Andreas Schaate, Pascal Roy, Adelheid Godt, Jann Lippke, Florian Waltz, Michael Wiebcke, and Peter Behrens. Modulated Synthesis of Zr-Based Metal-Organic Frameworks: From Nano to Single Crystals. *Chemistry - A European Journal*, 17(24):6643–6651, June 2011. ISSN 09476539. doi: 10.1002/chem.201003211.
- [40] Greig C. Shearer, Sachin Chavan, Silvia Bordiga, Stian Svelle, Unni Olsbye, and Karl Petter Lillerud. Defect Engineering: Tuning the Porosity and Composition of the Metal-Organic Framework UiO-66 via Modulated Synthesis. *Chemistry of Materials*, 28(11):3749–3761, 2016. ISSN 15205002. doi: 10.1021/acs.chemmater.6b00602.
- [41] Frederik Vermoortele, Rob Ameloot, Luc Alaerts, Roman Mattheessen, Bert Carlier, Enrique V. Ramos Fernandez, Jorge Gascon, Freek Kapteijn, and Dirk E. De Vos. Tuning the catalytic performance of metal–organic frameworks in fine chemistry by active site engineering. *Journal of Materials Chemistry*, 22(20):10313, 2012. ISSN 0959-9428, 1364-5501. doi: 10.1039/c2jm16030g.
- [42] Srinivas Gadipelli and Zhengxiao Guo. Postsynthesis Annealing of MOF-5 Remarkably Enhances the Framework Structural Stability and CO₂ Uptake. *Chemistry of Materials*, 26(22):6333–6338, November 2014. ISSN 0897-4756, 1520-5002. doi: 10.1021/cm502399q.
- [43] Greig C. Shearer, Jenny G. Vitillo, Silvia Bordiga, Stian Svelle, Unni Olsbye, and Karl Petter Lillerud. Functionalizing the Defects: Postsynthetic Ligand Exchange in the Metal Organic Framework UiO-66. *Chemistry of Materials*, 28(20): 7190–7193, October 2016. ISSN 0897-4756. doi: 10.1021/acs.chemmater.6b02749.

- [44] Stephan Bernt, Vincent Guillerm, Christian Serre, and Norbert Stock. Direct covalent post-synthetic chemical modification of Cr-MIL-101 using nitrating acid. *Chemical Communications*, 47(10):2838, 2011. ISSN 1359-7345, 1364-548X. doi: 10.1039/c0cc04526h.
- [45] Jasmina Hafizovic Cavka, Søren Jakobsen, Unni Olsbye, Nathalie Guillou, Carlo Lamberti, Silvia Bordiga, and Karl Petter Lillerud. A New Zirconium Inorganic Building Brick Forming Metal Organic Frameworks with Exceptional Stability. *Journal of the American Chemical Society*, 130(42):13850–13851, October 2008. ISSN 0002-7863. doi: 10.1021/ja8057953.
- [46] Andrew D. Wiersum, Estelle Soubeyrand-Lenoir, Qingyuan Yang, Beatrice Moulin, Vincent Guillerm, Mouna Ben Yahia, Sandrine Bourrelly, Alexandre Vimont, Stuart Miller, Christelle Vagner, Marco Daturi, Guillaume Clet, Christian Serre, Guillaume Maurin, and Philip L. Llewellyn. An Evaluation of UiO-66 for Gas-Based Applications. *Chemistry - An Asian Journal*, 6(12):3270–3280, December 2011. ISSN 18614728. doi: 10.1002/asia.201100201.
- [47] Min Kim, John F Cahill, Yongxuan Su, Kimberly A. Prather, and Seth M Cohen. Postsynthetic ligand exchange as a route to functionalization of ‘inert’ metal–organic frameworks. *Chem. Sci.*, 3(1):126–130, 2012. ISSN 2041-6520. doi: 10.1039/c1sc00394a.
- [48] Lijuan Shen, Weiming Wu, Ruowen Liang, Rui Lin, and Ling Wu. Highly dispersed palladium nanoparticles anchored on UiO-66(NH₂) metal-organic framework as a reusable and dual functional visible-light-driven photocatalyst. *Nanoscale*, 5(19):9374, 2013. ISSN 2040-3364, 2040-3372. doi: 10.1039/c3nr03153e.
- [49] Sigurd Øien, Giovanni Agostini, Stian Svelle, Elisa Borfecchia, Kirill A. Lomachenko, Lorenzo Mino, Erik Gallo, Silvia Bordiga, Unni Olsbye, Karl Petter Lillerud, and Carlo Lamberti. Probing Reactive Platinum Sites in UiO-67 Zirconium Metal–Organic Frameworks. *Chemistry of Materials*, 27(3):1042–1056, February 2015. ISSN 0897-4756, 1520-5002. doi: 10.1021/cm504362j.
- [50] Hui Wu, Yong Shen Chua, Vaiva Krungleviciute, Madhusudan Tyagi, Ping Chen, Taner Yildirim, and Wei Zhou. Unusual and highly tunable missing-linker defects in zirconium metal-organic framework UiO-66 and their important effects on gas adsorption. *Journal of the American Chemical Society*, 135(28):10525–10532, July 2013. ISSN 00027863. doi: 10.1021/ja404514r.
- [51] Vincent Guillerm, Silvia Gross, Christian Serre, Thomas Devic, Matthias Bauer, and Gérard Férey. A zirconium methacrylate oxocluster as precursor for the low-temperature synthesis of porous zirconium(IV) dicarboxylates. *Chem. Commun.*, 46(5):767–769, 2010. ISSN 1359-7345, 1364-548X. doi: 10.1039/B914919H.
- [52] Loredana Valenzano, Bartolomeo Civalleri, Sachin Chavan, Silvia Bordiga, Merete H. Nilsen, Søren Jakobsen, Karl Petter Lillerud, and Carlo Lamberti. Disclosing the Complex Structure of UiO-66 Metal Organic Framework: A Synergic Combination of Experiment and Theory. *Chemistry of Materials*, 23(7):1700–1718, April 2011. ISSN 0897-4756. doi: 10.1021/cm1022882.
- [53] Marco Taddei, Russell Jon Wakeham, Athanasios Koutsianos, Enrico Andreoli, and Andrew Ross Barron. Postsynthetic ligand exchange in zirconium-based metal-organic frameworks: Beware of the defects! *Angewandte Chemie International Edition*, July 2018. ISSN 14337851. doi: 10.1002/anie.201806910.
- [54] A. W. Thornton, R. Babarao, A. Jain, F. Trousselle, and F.-X. Couder. Defects in metal-organic frameworks: A compromise between adsorption and stability? *Dalton Trans.*, 45(10):4352–4359, 2016. ISSN 1477-9226, 1477-9234. doi: 10.1039/C5DT04330A.
- [55] Frederik Vermoortele, Bart Bueken, Gaëlle Le Bars, Ben Van de Voorde, Matthias Vandichel, Kristof Houthoofd, Alexandre Vimont, Marco Daturi, Michel Waroquier, Veronique Van Speybroeck, Christine Kirschhock, and Dirk E. De Vos. Synthesis Modulation as a Tool To Increase the Catalytic Activity of Metal–Organic Frameworks: The Unique Case of UiO-66(Zr). *Journal of the American Chemical Society*, 135(31):11465–11468, August 2013. ISSN 0002-7863, 1520-5126. doi: 10.1021/ja405078u.
- [56] Binbin Tu, Qingqing Pang, Doufeng Wu, Yuna Song, Linhong Weng, and Qiaowei Li. Ordered Vacancies and Their Chemistry in Metal–Organic Frameworks. *Journal of the American Chemical Society*, 136(41):14465–14471, October 2014. ISSN 0002-7863, 1520-5126. doi: 10.1021/ja5063423.

- [57] Greig C. Shearer, Sachin Chavan, Jayashree Ethiraj, Jenny G. Vitillo, Stian Svelle, Unni Olsbye, Carlo Lamberti, Silvia Bordiga, and Karl Petter Lillerud. Tuned to Perfection: Ironing Out the Defects in Metal–Organic Framework UiO-66. *Chemistry of Materials*, 26(14):4068–4071, July 2014. ISSN 0897-4756, 1520-5002. doi: 10.1021/cm501859p.
- [58] Yang Jiao, Yang Liu, Guanghui Zhu, Julian T. Hungerford, Souryadeep Bhattacharyya, Ryan P. Lively, David S. Sholl, and Krista S. Walton. Heat-Treatment of Defective UiO-66 from Modulated Synthesis: Adsorption and Stability Studies. *The Journal of Physical Chemistry C*, 121(42):23471–23479, October 2017. ISSN 1932-7447, 1932-7455. doi: 10.1021/acs.jpcc.7b07772.
- [59] Ben Van de Voorde, Ivo Stassen, Bart Bueken, Frederik Vermoortele, Dirk De Vos, Rob Ameloot, Jin-Chong Tan, and Thomas D. Bennett. Improving the mechanical stability of zirconium-based metal–organic frameworks by incorporation of acidic modulators. *Journal of Materials Chemistry A*, 3(4):1737–1742, 2015. ISSN 2050-7488, 2050-7496. doi: 10.1039/C4TA06396A.
- [60] Cesare Atzori, Greig C. Shearer, Lorenzo Maschio, Bartolomeo Civalleri, Francesca Bonino, Carlo Lamberti, Stian Svelle, Karl Petter Lillerud, and Silvia Bordiga. Effect of Benzoic Acid as a Modulator in the Structure of UiO-66: An Experimental and Computational Study. *The Journal of Physical Chemistry C*, 121(17):9312–9324, May 2017. ISSN 1932-7447, 1932-7455. doi: 10.1021/acs.jpcc.7b00483.

5. Exploring the impact of material form on adsorption measurements

5.1. Introduction

An adsorbent cannot be used in an industrial process in its raw powder form. The small crystals which are normally obtained during synthesis are not suited for direct use. Therefore, in order to use a material in a setting such as in beds or columns common in catalysis, PSA (pressure swing adsorption) and TSA (temperature swing adsorption), a structuring into a hierarchically porous structure form is needed.⁽¹⁾

To this end adsorbents are usually shaped into pellets, a process which introduces a range of benefits, such as improved flow regimes, better thermal management and material containment. The shaping process is needed not just for stabilisation of small particles, but also to impart the resulting pellet with a high enough mechanical resistance to withstand the stresses imposed by the high flow encountered in an industrial bed. Ideally, forming would have limited effects on the properties of the material. However, this is often not the case, as shaping can change adsorption performance dramatically.

Shaping is therefore a crucial step towards the large-scale use of an adsorbent material. Even for commonplace adsorbents such as carbons and zeolites, the optimum binding additives and the shaping process itself are the subject of extensive research. Often, the procedure is tailored for an individual material and application.

As metal organic frameworks with properties that make them suited for industrial applications emerge, a push towards obtaining shaped versions of the best-performing materials is desired, first for pilot studies and perhaps large scale use.

Due to the wide range of materials, potential shaping methods, binders and effects introduced through the process itself, a high-throughput methodology is often the kind of approach that is best suited to exhaustively explore the resulting space. The data processing methodologies discussed in chapter 2 combined with calorimetric methods presented in chapter 3 are put to use in a study on the shaping performance of MOFs.

Chapter summary

After a short introduction to shaping, this chapter explores the variability introduced by an ρ -alumina binder in three topical MOFs: UiO-66(Zr), MIL-100(Fe) and MIL-127(Fe). These MOFs have been selected for their known chemical and thermal stability and well-studied adsorption behaviour. The alumina shaped variant of these MOFs is compared to the original powder material with regard to the adsorption of a series of common gasses and vapours. Microcalorimetry in conjunction with 8 gas probes has been used to get an in-depth picture of the change in surface energetics. Finally, a previous study on the same materials shaped with a poly-vinyl alcohol (PVA) binder is extended to vapour adsorption and the entire dataset is processed to obtain an overview of the impact of a hydrophobic and a hydrophilic binder on adsorption performance.

Contributions

Both MOF synthesis and shaping through granulation was performed in the group of Jong-San Chang from the Research Group for Nanocatalysts, Korea Research Institute of Chemical Technology (KRICT). Calorimetry, thermogravimetry, nitrogen and vapour adsorption were carried out by Paul Iacomi. Nicolas Chanut was of great help in interpretation of results.

5.2. Shaping in context

In order to understand the requirement for material forming, we should first examine adsorption from a kinetic, thermal and mechanical standpoint. Until now, in this thesis the isotherms were measured in systems that achieved complete equilibrium between each step, without a mention of experimental duration. However, this parameter is crucial when working with time-dependent systems operating in a flow mode, as columns and beds rarely operate at equilibrium conditions.

The rate of adsorption on the surface of the pore is theoretically immediate, with the controlling step being diffusion of guest molecules between particles (interparticle) and through the pore network (intraparticle).⁽²⁾ Diffusion is dominated by different phenomena depending on the length-scale involved, from molecular diffusion or Knudsen diffusion in large pores, to concentration gradients and steric effects in micropores. Forced flow regimes dramatically improve interparticle and particle surface diffusion at the cost of the energy required to impose the pressure drop. A balance must be struck to obtain a high overall diffusion coefficient while maintaining a large surface area to volume ratio and a reasonable pressure drop across the column or bed.⁽³⁾

As mentioned in chapter 3, adsorption is an exothermic process, with high amounts of heat being released. Since rates and capacity are dictated by an Arrhenius an increase in temperature leads to lower capacities and is rarely desired. As with diffusion, fast thermal transfer is therefore needed to prevent a loss in efficiency or, with some materials, a degradation of the adsorbent itself.

Finally, the mechanical resistance of the material used in a bed or column should be considered. The pressure drops used to improve diffusion and heat transfer through high flow regimes may lead to attrition and breakage of the adsorbent structure. Often in tall columns, the weight of the material itself can be a factor that leads to structural collapse.

The requirements discussed above, lead to the necessity of adsorbent forming or shaping. The forming process generates a hierarchical pore size distribution which helps with reducing pressure drop, as can be seen in Figure 5.1. The addition of binders or other additives improves the mechanical and thermal properties of the final shaped material. Depending on the application, many types of shaped materials exist, from simple granules and pellets, to extruded rods, monoliths and membranes. The process itself consists of extrusion of the particle-binder slurry and then hardening either through temperature, cross-linking or chemical treatment. Other methods, such as spray-drying or granulation can similarly be used.⁽⁴⁾ While the basic steps are the same: the mixing of the powder with any additives, the shaping in their required form and curing of the final structure, many variations are possible in each step.

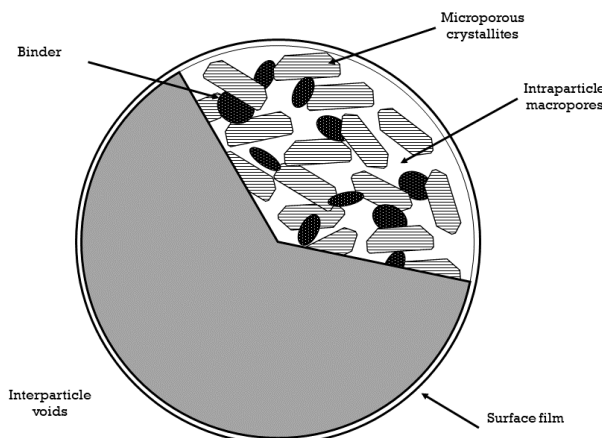


Figure 5.1.: An schematic representation of the possible structure of a shaped sphere.

The binders, as their name imply, serve to hold crystals together during and after the shaping process. For carbons, binders such as pitch, polymers (CMC, PVA) or even non-porous carbon black are commonly used.⁽⁵⁾ For zeolites, inorganic binders are more prevalent, with silica, alumina and clay binders common in industry. Often, a combination of additives is used, each with a different role during the pelletization process⁽⁶⁾ such as improving rheological behaviour. It has been shown^(7,8) that the choice of binder can introduce large property variations, ranging from loss of porosity and structure to the enhancement of the desired reactivity and selectivity through changes in the acid site density or ion migration.

Overall, during shaping the capacity per mass of pellet is expected to decrease due to the addition

of a non-porous component, but the difference should be small and should not arise due to effects such as pore blocking or pore filling with the binder material. Furthermore, a densification effect is expected, leading to better performance on a volume basis. Finally, binder addition should not influence the chemical properties of the adsorbent, and preserve the original interactions with the adsorbate. With a judicious choice of binding material, the resulting pellet may even outperform the powder.

When it comes to MOFs, shaping has been attempted with a wide range of binders and methods. Methods such as granulation, spray-drying or extrusion have all been successfully employed to create MOF pellets.⁽⁹⁾ Monoliths have also been shown to be an effective way for shaping purposes, either through impregnation⁽¹⁰⁾ or through support on alumina.⁽¹¹⁾ Surprisingly, compression⁽¹²⁾ or even simple air drying of MOF slurries⁽¹³⁾ have also shown good results. Note that the monolith prepared through the latter method had a three times larger volumetric specific surface area than the conventional powder.

The connection between MOF and binder is also of crucial importance. The MOF-polymer interface has been shown⁽¹⁴⁾ to be subject to a complex interplay of interactions between the organic chains and the crystal surfaces. These effects can be striking enough to warrant further research into MOF-polymer hybrids⁽¹⁵⁾, with the aim of combining the unique attributes of both materials.

Previous work from MADIREL⁽¹⁶⁾ has analysed the impact of polyvinyl alcohol (PVA) shaping on a series of MOFs. It was shown that the binder did introduce some specific effects, such as a protection effect on the reduction of Fe^{3+} to Fe^{2+} in MIL-127(Fe), as well as a curious gating effect seen on butane adsorption on MIL-100(Fe), likely due to polymer chains covering pore entrances. Otherwise, the shaping imparted good performance to the shaped samples, with almost no capacity loss on a mass basis. Unfortunately, the use of a polymer limited the activation temperature of the samples to a maximum of 150 °C.

5.3. Materials, shaping and characterisation methods

5.3.1. Materials

In this chapter the same series of “topical” MOFs was selected and used to investigate the influence of a different shaping method, namely the use of alumina binder, on their adsorption properties.

The UiO-66(Zr) MOF and its derivatives are well known due to their stability, both in regards to temperature and chemical compounds⁽¹⁷⁾ and has been discussed in detail in chapter 4. It is composed of Zr6-oxo clusters which are connected with benzene dicarboxilate (BDC) linkers to form a face-centered cubic framework. It has shown promise⁽¹⁸⁾ in use for gas adsorption applications. It contains a three-dimensional arrangement of micropores with each centric octahedral cage surrounded by eight corner tetrahedral cages (diameters of approximately 1.1 nm and 2.8 nm respec-

tively) and connected through narrow triangular windows of approximately 0.6 nm.

MIL-100(Fe) is a MOF which uses the benzene tricarboxilate (BTC) linker in conjunction with trimeric iron (III) octahedral clusters.^(19,20) The framework assembles in hybrid supertetrahedra which leads to very large pores: a 2.5 nm cage and a larger, 2.9 nm cage. These pore cages are accessible through windows of 0.55 nm and 0.86 nm respectively. The iron trimers are coordinated with anions and have shown a propensity to partially reduce to a divalent Fe²⁺ state, exposing a naked metal site in the process.⁽²¹⁾

The last material, MIL-127(Fe), originally reported by Liu et al.⁽²²⁾ is a MOF built from the same metal (III) octahedra trimers as MIL-100(Fe), but using the 3,3',5,5'-azobzenenetetracarboxylate (TazBz) linker, to produce a framework with the **soc** topology. This material has shown promise⁽²³⁾ for large scale synthesis. Furthermore, due to its alternating hydrophobic/hydrophilic microporous system, it has been shown to be of interest for multiple applications such as catalysis or CO₂ capture.⁽²⁴⁾

The UiO-66(Zr) and MIL-100(Fe) powders have been synthesised at the Korea Research Institute of Chemical Technology (KRICT). The MIL-127(Fe) MOF was made in the group of Christian Serre, in the Lavoisier Institute in Versailles. Complete details of the synthesis method can be found in the related publication⁽²⁵⁾ and in Appendix B. The structures of the three materials can be seen in Figure 5.2.

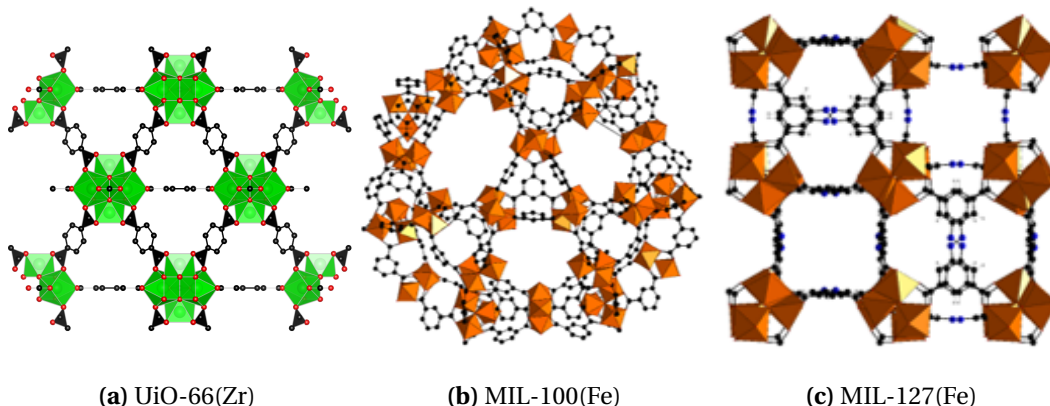


Figure 5.2.: The unit structures of the investigated MOFs. The colour coding is as follows: Zr polyhedra in green, Fe octahedra in brown, C in black, O in red, N in blue. Hydrogen atoms are omitted for clarity.

5.3.2. Shaping Procedure

The shaping of the samples also took place at KRICT and was performed using a wet granulation method. In the case of the alumina binder, the MOF powder was mixed with the previously prepared mesoporous ρ -alumina with water added as the dispersing medium. For the PVA binder, the MOF powder was instead added to a solution of ethanol solution containing a polymer mixture of

polyvinyl groups such as polyvinyl alcohol and polyvinyl butyral. The resulting mixture was shaped into beads using a hand-made pan granulator. During the process, the spheres were sprayed with the respective solvent in order to achieve desired size. The beads were then sieved and rolled using a roller machine to enhance their spherical shape. Finally, the prepared samples were dried at 303 K for 12 h to remove all residual solvent. The resulting beads were near spherical in shape, with a diameter between 2 mm to 2.5 mm.

5.3.3. Characterisation of powders and pellets

The primary interest of the study was observing differences in adsorption properties between the powder and the shaped materials.

Thermogravimetric analysis was used to verify that the binder did not change the thermal stability of the materials and, in the case of the PVA variant, to ensure that the activation temperature chosen did not induce polymer decomposition. The TGA method is described in detail in Appendix A.1.

The bulk and skeletal density of the powder and pellets were measured to allow isotherms to be presented on a volume basis, as well as to check the level of densification afforded through the shaping process. The procedure is described in Appendix A.2 and Appendix A.3.

Specific surface area and pore volume were determined through nitrogen adsorption at 77 K. These measurements were recorded according to the method in Appendix A.4. For inspecting changes in surface hydrophobicity, water and methanol adsorption isotherms were measured according to the method presented in Appendix A.5.

Finally, all calorimetry data was recorded using a high sensitivity Tian-Calvet calorimeter coupled with adsorption manometry, as introduced in chapter 3.

5.3.4. Sample activation for adsorption

The materials were pre-treated before all adsorption experiments by activation at high temperature under secondary vacuum for 16 hours. The activation temperature was specific to each solid: 200 °C for UiO-66(Zr), 150 °C for MIL-100(Fe) and 150 °C for MIL-127(Fe).

5.4. Results and discussion

5.4.1. Thermal stability

In order to check if the shaped samples have not undergone bulk structural changes, as well as find a suitable activation temperature, the powder and shaped samples underwent thermogravimetric analysis under an argon atmosphere.

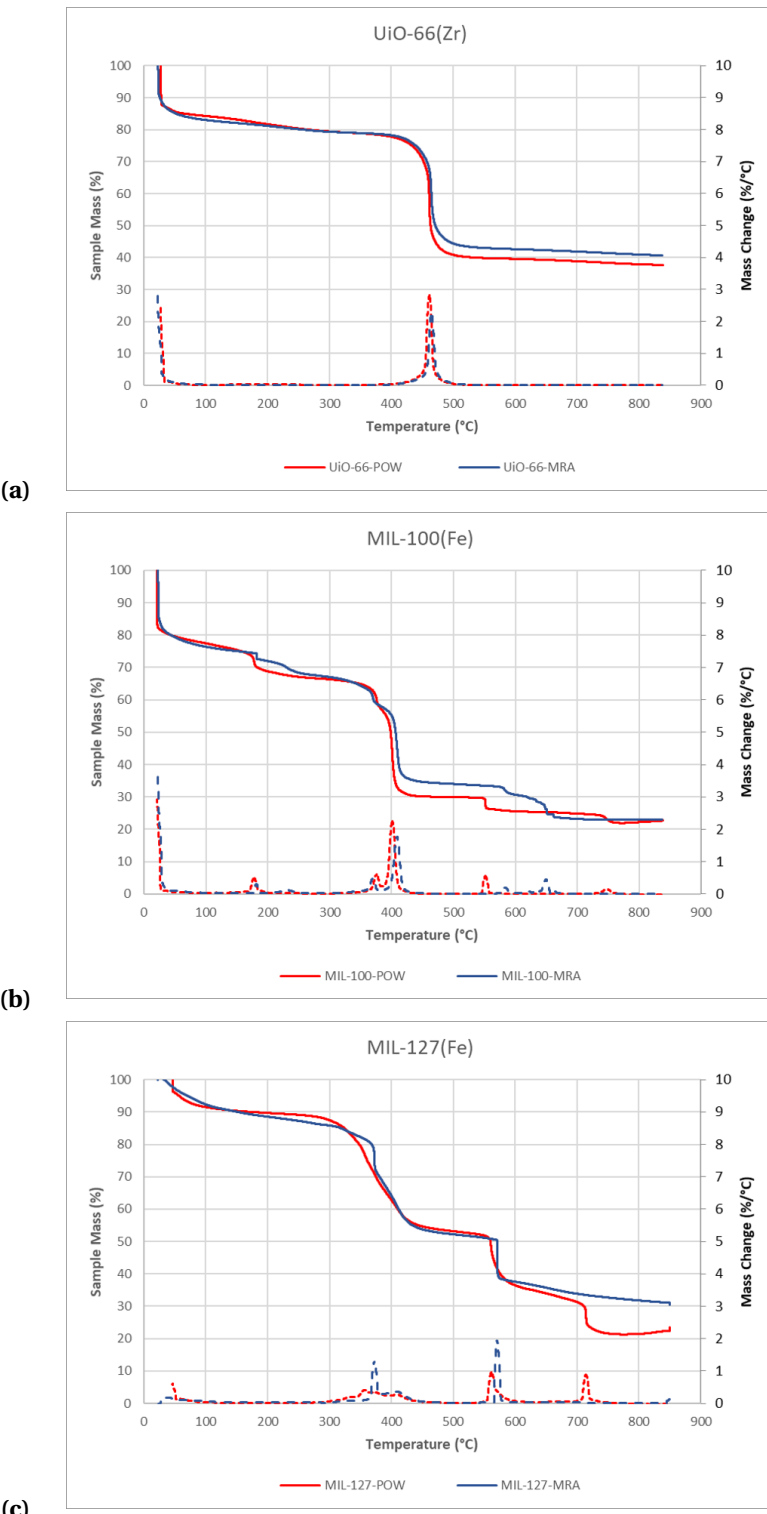


Figure 5.3.: High resolution TGA curves recorded under argon on (a) UiO-66(Zr), (b) MIL-100(Fe) and (c) MIL-127(Fe). The original powders are depicted in red and the shaped material in blue.

The process of shaping did not have any impact on the thermal stability of the investigated MOFs, as evidenced by the TGA curves in Figure 5.3. The primary mass loss occurs in a 10 K range for all powder-pellet pairs. Shaped samples are also seen to have a smaller mass loss at high temperatures. This is expected, as after the addition of temperature inert alumina, the MOF makes up a lower percentage of the material.

5.4.2. Adsorption isotherms at 77K and room temperature

Nitrogen sorption isotherms measured at 77 K have been measured on both powder and ρ -alumina pellets, with the isotherms presented in Figure 5.4. Observation of the physisorption curves sheds light on the impact of the alumina binder on the materials chosen. The shapes of all isotherms are visually similar, with the pellet curves shifted downwards due to the aforementioned structure degradation. In both powders and pellets, the increased uptake after $0.9 p/p^0$ is a sign of condensation in very large pores or voids, which can be attributed to intra-pellet spaces and crystal agglomeration. In the MIL-127(Fe) pellets, a narrow hysteresis curve is seen, which closes at a p/p^0 of 0.5. This curve corresponds to capillary condensation in a pore size of around 4 nm. This pore width is identical to the average pore size of the alumina binder. However, as this feature is present in both the pellet and powder isotherms, it cannot correspond to the binder and is therefore a consequence of particle agglomeration.

Since no other significant features are visible on the isotherms themselves, we use pyGAPS to further process them and obtain properties such as specific surface area, calculated through the BET method and pore volume, calculated as the volume of nitrogen adsorbed at a p/p^0 of 0.2. As the surface area of the binder is lower than the one of the MOF, a drop in both these properties is expected. The calculated values are shown in Table 5.1.

Table 5.1.: Properties of the studied powders and pellets

MOF	form	BET surface area (m^2/g)	Pore volume (cm^3/g)	Bulk density (kg/m^3)
UiO-66(Zr)	powder	903	0.38	0.319
	ρ -alumina	619	0.24	0.472
MIL-100(Fe)	powder	1928	0.78	0.216
	ρ -alumina	1451	0.60	0.351
MIL-127(Fe)	powder	1413	0.76	0.412
	ρ -alumina	1266	0.56	0.526

As predicted, the specific surface area of the shaped samples is decreased compared to the corresponding powder. While in the case of MIL-127(Fe) the BET area is only 10% lower, for the MIL-100(Fe) and UiO-66(Zr) materials a larger drop is seen, of 25% and 31%, respectively. A similar de-

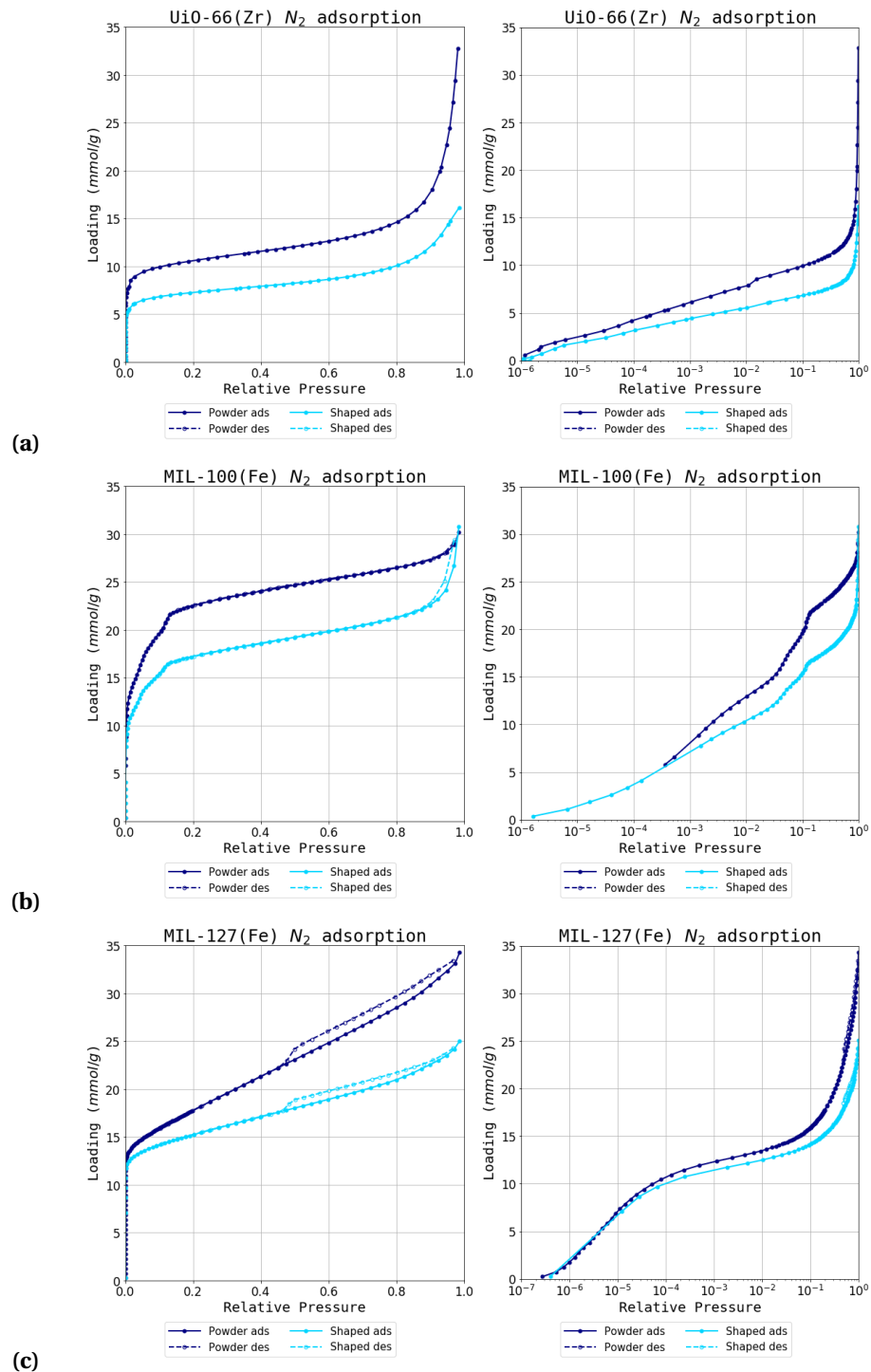


Figure 5.4.: Nitrogen isotherms at 77K for (a) UiO-66(Zr), (b) MIL-100(Fe) and (c) MIL-127(Fe). The powder sample is in light blue while the ρ -alumina sample in dark blue. Logarithmic graphs of the isotherms are on the right for clarity of the low pressure region.

crease can be seen in total pore volume, with a 36%, 23% and 26% loss seen in UiO-66(Zr), MIL-100(Fe) and MIL-127(Fe) respectively. The decrease in both surface area and micropore volume is too large for it to be a consequence of the presence of non-porous binder. It is therefore theorised that some structure degradation must have occurred during the pelletisation process. Despite a loss in surface area, the bulk density of the material has increased, due to crystal aggregation.

5.4.3. Room temperature gas adsorption and microcalorimetry

As previously shown in chapter 3, combining microcalorimetry with adsorption manometry can give an insight into the energetics of the adsorption process by directly measuring differential enthalpy. Even though the different contributions to the overall enthalpy curve cannot be decoupled from the individual sources, such as guest-host interactions or fluid-fluid interactions, it can be successfully applied to observing the effect of a process or treatment such as shaping on the properties of a MOF.

Eight probe gasses have been chosen for adsorption at 303 K: N₂, CO, CO₂, CH₄, C₂H₆, C₃H₆, C₃H₈ and C₄H₁₀. The range of adsorbates chosen allows different effects to be investigated. The adsorption of saturated hydrocarbons with an increasing carbon number (C1-C4) can be assumed to be driven strictly by Van-der-Waals forces, due to the shielding effects of the hydrogen atoms. Differences in the maximum uptakes of these gasses will point to loss of porosity or crystallinity. A capacity loss with an increasing carbon number will point to size exclusion effects induced by the binder, such as particle coating, pore filling or pore obstruction. The other probes have been chosen for their properties which can shine light on other specific interaction types present during the adsorption. Carbon monoxide is a slightly dipolar molecule which has the ability to interact with other charges in the pores. It also can highlight CUS (coordinatively unsaturated sites) generated through defects, reduction or open metal sites due to its propensity for π backbonding coordination. This electron transfer process can also result in complexation with molecular orbitals in systems with π bonds such as alkenes and alkynes. Propylene is used as an unsaturated hydrocarbon probe gas for this purpose. Carbon dioxide is a highly quadrupolar molecule which will be strongly adsorbed in polar pore environments. Changes in the adsorption behaviour of CO₂ will shed light on such surface changes and can even be used as a predictor of hydrophobicity.⁽²⁴⁾ Finally, N₂ is a staple adsorptive for material characterisation when used at 77 K. The molecule is a slight quadrupole and has also been shown to chelate to some transitional metals in an analogue fashion to CO.

To eliminate the influence of kinetic and diffusion effects on the experiments, care has been taken to allow time for complete equilibration of both pressure and calorimeter signal. The complete dataset of adsorption isotherms, on the basis of both mass and volume can be found in Appendix F.

After collecting the combined isotherm and enthalpy data, three indicators have been chosen to best represent the effects of shaping: initial enthalpy of adsorption, initial Henry constant and maximum capacity. These numeric performance indicators have been calculated using the available

functionality in pyGAPS.

The initial enthalpy of adsorption extrapolated at zero coverage is a measure of the interaction with highest energetic sites on the MOF surface. Conversely, the initial Henry constant (K_{Hi}), here obtained through fitting the virial adsorption model as laid out in subsection 2.2.9, is also an indication of adsorption in the pores before any layering or adsorbate-adsorbate interaction comes into effect. The last indicator, maximum capacity, was taken as the loading attained when the isotherm reached a plateau. In the case of probes where the plateau was outside the range of pressure of the instrumentation (>50 bar), the loading at the highest available pressure was considered as a suitable approximation. The three key performance indicators (KPIs) have then been compared side by side on both the powder and shaped samples.

UiO-66(Zr)

A visual inspection of the enthalpy curves on as-synthesised UiO-66(Zr) show it to be relatively homogenous, with flat profiles being common. This is typical of this MOF, which has a pore environment without high energy adsorption sites.⁽¹⁸⁾ Both CO₂ and CO show a higher enthalpy of adsorption at low loadings, as seen in Figure 5.6, which is likely due to their quadrupole and dipole interaction, respectively.

The KPI graphs in Figure 5.5 show very similar values for both initial Henry's constant and initial enthalpy of adsorption. It is therefore apparent that the shaping process did not change the interaction of the adsorbate with the MOF surface.

The maximum capacity graphs show a more interesting trend. When using small adsorbates such as N₂, CO₂ and CH₄, the shaped samples have a similar performance on a mass basis and, due to the densification process, better capacities on a volume basis. Starting with ethane, the maximum capacity difference starts to increase, with lower performance as molecule size increases. On hydrocarbons with a carbon number of 3 and 4, both mass basis and volume basis capacity are decreased compared to the original powder. This size exclusion effect could be explained by the coating of crystal surfaces with the alumina binder.

It could also be argued that instead of size exclusion, the effect is due to an overall decrease in pore volume, and that the isotherms of the low molecular weight gasses will diverge at higher pressures as the pores are filled. A counterargument for this hypothesis is that in the case of CO₂, the plateau is reached with no differences between the powder and the pellet as seen in Figure 5.6a.

Carbon monoxide is an apparent outlier to this trend, with a decreased maximum capacity and a small molecular size. However, when observing the isotherms directly (Figure 5.6b) it is obvious that the effect is likely to be due to experimental errors, considering the low amount adsorbed and the good overlap in the enthalpy curves.

Overall, the shaping performance of UiO-66(Zr) is reasonable, as long as only small adsorbates

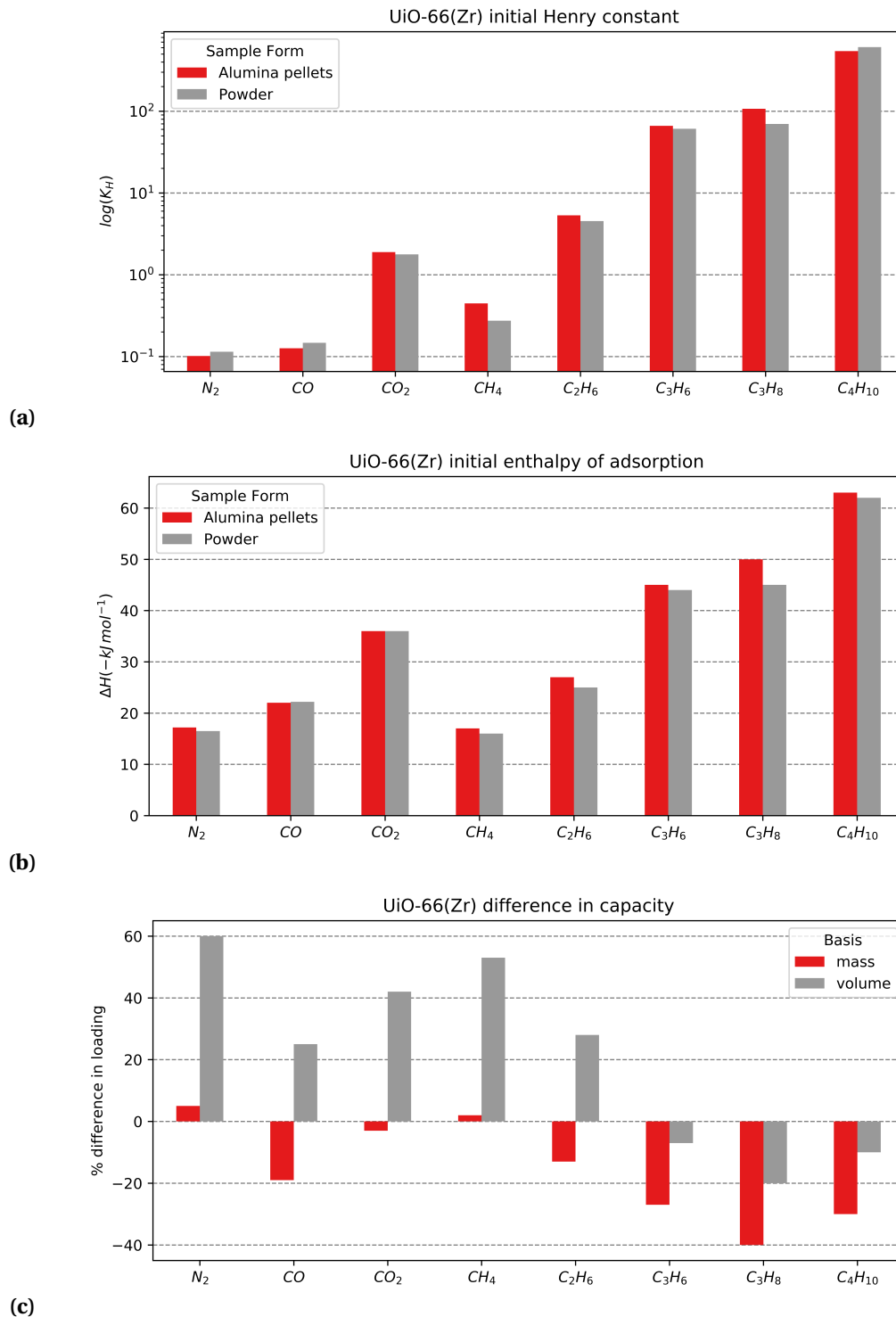
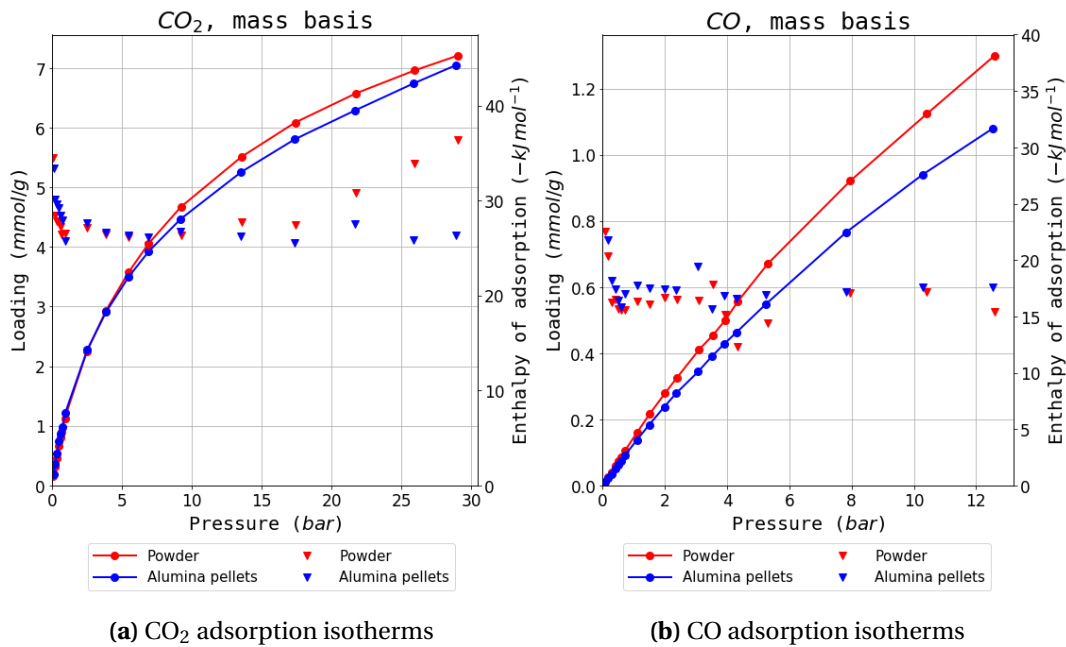


Figure 5.5.: KPIs extracted from the UiO-66(Zr) adsorption dataset with (a) logarithmic initial Henry constant (b) initial enthalpy of adsorption and (c) change in adsorption maximum capacity from the powder to the alumina shaped version on a mass and volume basis in red and grey respectively

**Figure 5.6.**: Selected isotherms from the $\text{UiO-66}(\text{Zr})$ dataset

are used.

MIL-100(Fe)

The enthalpy profiles on the MIL-100(Fe) powder are less homogenous than the ones on $\text{UiO-66}(\text{Zr})$. Some effects can be seen with probes which can interact with the partially reduced Fe(II) atom, such as carbon monoxide and propylene (Figure 5.8). Indeed, when comparing both the initial Henry constants and enthalpy of adsorption, for CO and C_3H_6 , these are higher than the values obtained on $\text{UiO-66}(\text{Zr})$. With initial enthalpy of adsorption for CO of around 45 kJ mol^{-1} , the value falls into the range of previous⁽²¹⁾ results for interactions with such Fe(II) CUS.

Comparing the powder and shaped variants, there are no apparent differences between the two. The only discrepancy, which can be seen on the nitrogen initial K_H follows as a result of an ill-fitting virial parameter, and can be assumed an error after observing the isotherm overlap directly. It could be theorised that by activation at a higher temperature (250°C), the percentage of iron trimers which would undergo reduction will increase and a further interaction could be observed. However, the activation temperature was chosen to allow comparisons with the PVA study⁽¹⁶⁾, where temperatures over 180°C would lead to the burn-off of the polymer binder.

The maximum loading differences (Figure 5.7c) of MIL-100(Fe) show a very similar behaviour. On all probes tested, a fixed capacity loss of between 10-20% can be seen on a mass basis. However, the increase in density afforded by the compression during pelletisation leads to a compensation in performance as can be seen directly when looking at isotherms on mass and volume material basis

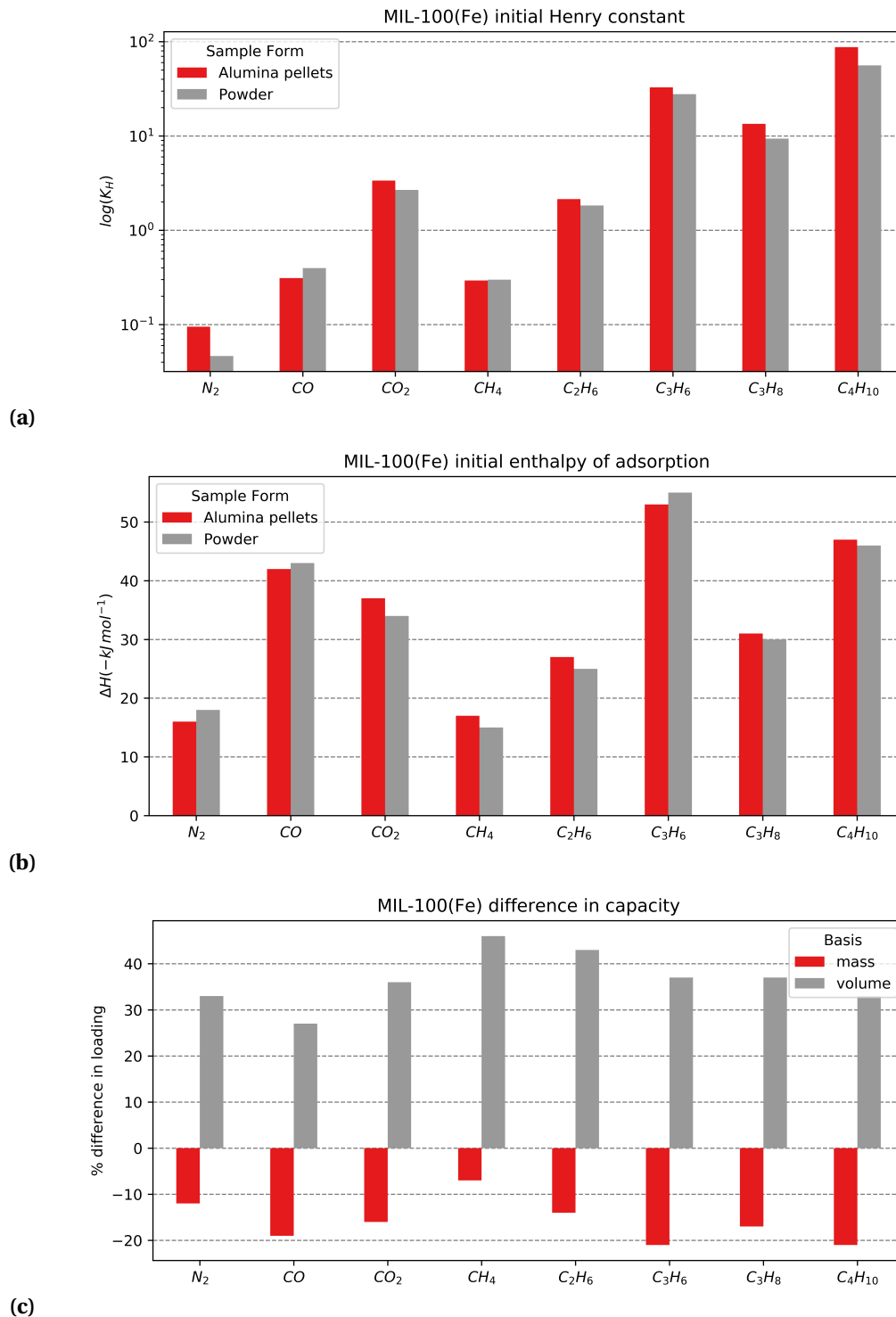


Figure 5.7.: KPIs extracted from the MIL-100(Fe) adsorption dataset with (a) logarithmic initial Henry constant (b) initial enthalpy of adsorption and (c) change in adsorption maximum capacity from the powder to the alumina shaped version on a mass and volume basis in red and grey respectively

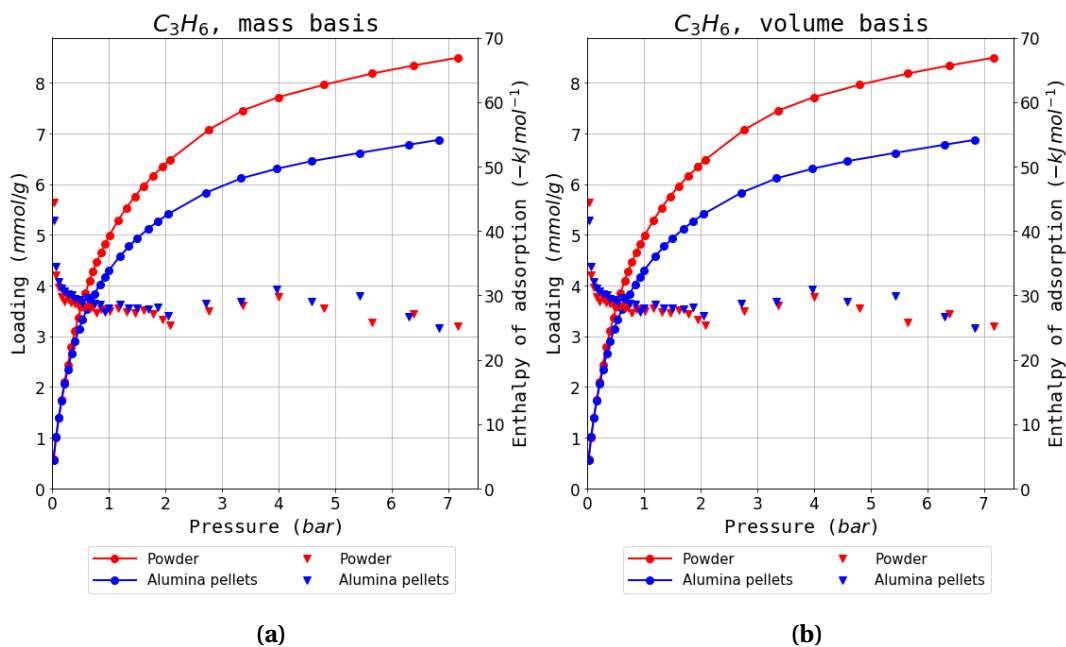


Figure 5.8: Propylene isotherms on MIL-100(Fe) on a (a) mass and (b) volume adsorbent basis.

in Figure 5.8a and Figure 5.8b respectively.

We can conclude that MIL-100(Fe) is almost unaffected by alumina shaping. A slight loss in maximum capacity on a mass basis is compensated by a pronounced densification, which is desirable in an industrial setting.

MIL-127(Fe)

The isotherms on the original powder form of MIL-127(Fe) should show similar behaviour as on MIL-100(Fe), due to the presence of the same iron trimesate moieties, although with a sharper uptake as a result of the smaller pores. Enthalpy profiles are also influenced by the similar interactions with the iron CUS leading to higher initial heats of adsorption on CO and C₃H₆. An overall increase in the enthalpy of adsorption at higher loadings is seen throughout the probe series, as seen for example on butane in Figure 5.10a. Due to the bimodal pore distribution in the MIL-127(Fe) structure, it is likely that adsorption first commences in the small (~0.6 nm) channels and then, at higher pressures, intrusion into the larger cage-type pores is possible through the ~0.3 nm narrow apertures. The confined cages have an increased interaction with the molecule which leads to the higher enthalpy values.

When comparing the powder and the pellet variant with respect to initial Henry's constant, a large difference in K_H on CO stands out. The value of the initial enthalpy of adsorption does not follow the same pattern. However, visual inspection of the enthalpy curve in Figure 5.10b shows that the energy of adsorption corresponding to interactions with the more active sites is maintained for a

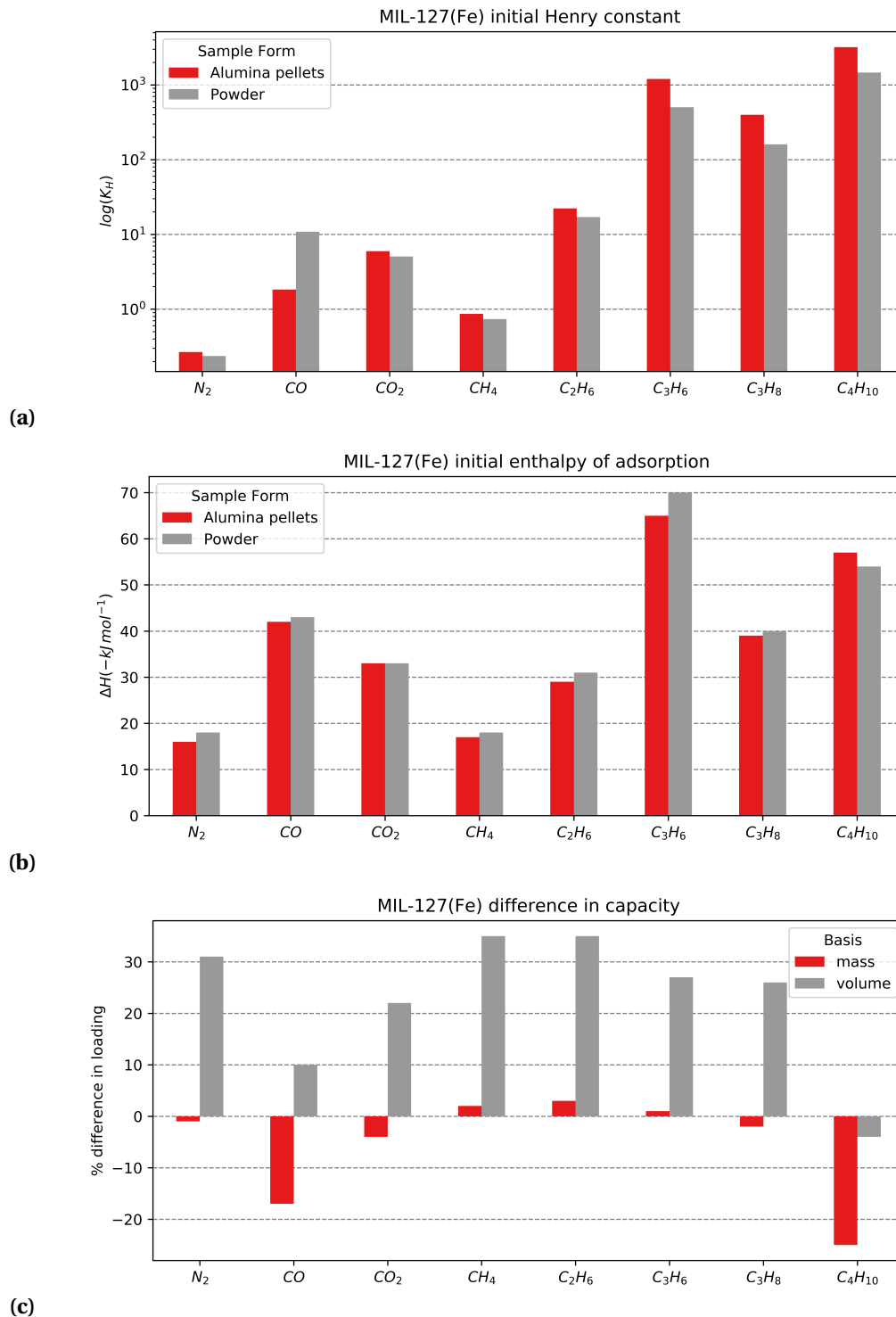


Figure 5.9.: KPIs extracted from the MIL-127(Fe) adsorption dataset with (a) logarithmic initial Henry constant (b) initial enthalpy of adsorption and (c) change in adsorption maximum capacity from the powder to the alumina shaped version on a mass and volume basis in red and grey respectively

larger percentage of the total coverage. This points to the higher preponderance of such sites in the powder variant. A similar offset can be seen in the propylene enthalpy at very low pressures, but this is not reflected in the shape of the isotherm. The weaker complexation strength and the larger size of the molecule likely limits the effect seen in the carbon monoxide isotherm. As for the underlying reason behind the isotherm divergence, it could be that the alumina binder acts as protection against the generation of iron (II) during thermal activation. No other differences are seen between the two forms on either Henry constant and initial enthalpy of adsorption.

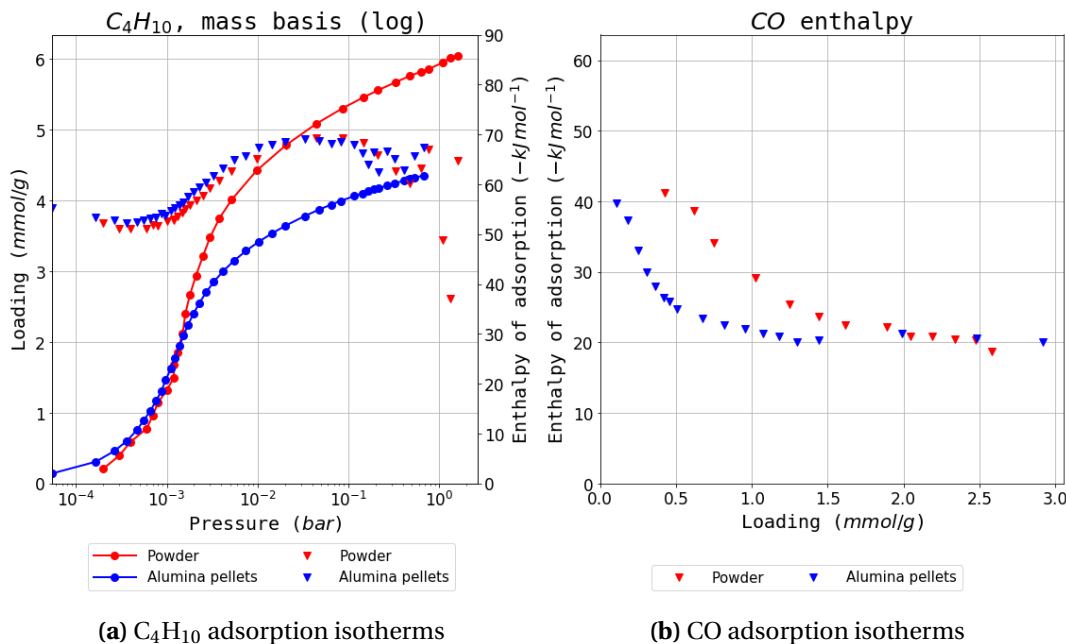


Figure 5.10: Selected isotherms from the MIL-127(Fe) dataset

The capacity comparison in Figure 5.9c paints an interesting picture. For most probes there is no change in maximum loading showing that there is no structure degradation or pore filling. Two outliers are apparent: carbon monoxide and butane. The decrease in capacity on CO can be explained through the aforementioned changes in active site prevalence. The drop in butane cannot be a consequence of the same effect as there is a perfect overlap in the enthalpy curves as seen in Figure 5.10a. Therefore it likely better explained through a size exclusion effect similar to UiO-66(Zr).

Overall, MIL-127(Fe) shows excellent performance when undergoing alumina shaping, with almost no capacity loss, as long as carbon monoxide or butane adsorption are required, where specific effects come into play.

5.4.4. Vapour adsorption

The effects of shaping with ρ -alumina are so far more subtle than the changes encountered when using PVA, as shown in the corresponding study.⁽¹⁶⁾ As such the characterisation was extended us-

ing adsorption of vapours at room temperature. The influence of the binder on hydrophobic character of the material may be of interest for tuning the properties of the beads. Here, water and methanol can serve as probes for small changes in surface properties. To this end, the same PVA samples which were used in the previous study were investigated alongside the MRA-shaped MOF.

Due to its surface charges, alumina is a hydrophilic substance, with a contact angle of 10°. It is expected that its addition may therefore increase the affinity of the resulting pellet towards water. On the other hand, the PVA binder is more hydrophobic, with a water contact angle of 51°. The medium affinity for water is due to the surface hydroxyl functionalisations, which can lead to hydrogen bonding.

Two indicators may highlight changes in material hydrophilicity: the slope of the isotherm in the low relative pressure region ($p/p^0 < 0.3$) and condensation steps in the isotherm. Adsorption at low pressures is representative of the initial interactions with the surface, as discussed in the previous section. The pressure at which condensation occurs in the pores of the material, underlined by a sharp increase in the isotherm, depends on the size of the pore but also on pore environment and guest-guest interactions. Finally, hysteresis in the adsorption isotherm may also be an indication of the nature of pores.

The measured isotherms on water and methanol can be found in Figure 5.11 and Figure 5.13 respectively. Initial Henry constants have been calculated for the isotherms using the initial point method, and are displayed in Figure 5.12.

UiO-66(Zr)

On the parent UiO-66(Zr), the water isotherm shows a slow uptake at the start, indicating a hydrophobic surface, and then shows a small step at $p/p^0 = 0.3$. While little is adsorbed on the MOF before this step, its presence at a low relative humidity is indicative of intrinsic defects in the framework.⁽²⁶⁾ Complete saturation takes place around $p/p^0 = 0.9$. A wide hysteresis curve can be seen, which does not fully close, even at low pressures. Both the saturation step and the condensation may be attributed to agglomeration of crystals and interparticle voids.

The methanol isotherm has the same features as the water one, with the condensation step shifted at a much lower partial pressure ($10^{-1} p/p^0$). It is likely that the organic component of methanol interacts with the hydrophobic surface, thus permitting pore filling at lower pressures. This is also evidenced through the higher Henry constant when compared to water.

When comparing the powder and the pellet variants, the general shape of the isotherm remains the same with both water and methanol. Initial interactions with the surface are also identical, as evidenced by the overlap in the low pressure region and through the calculated Henry constants. The isotherms begin to diverge after the condensation step, where the maximum loading evolves in the order MRA < powder < PVA for both vapours. This is a surprising trend, as both pellets have been

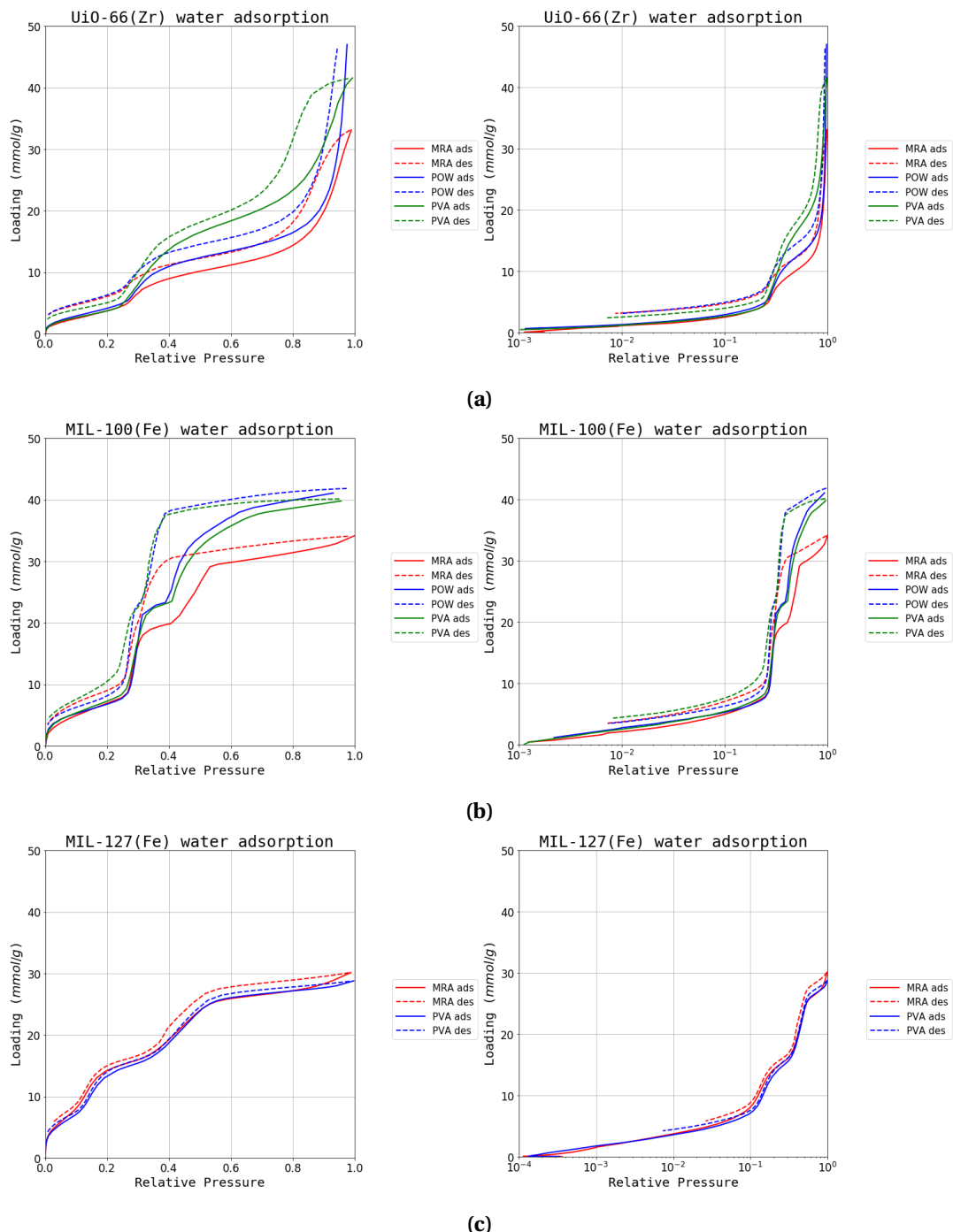


Figure 5.11.: Water adsorption isotherms (a) UiO-66(Zr), (b) MIL-100(Fe) and (c) MIL-127(Fe). The powder samples are in light blue, while the ρ -alumina and poly-vinyl alcohol samples are in red and dark blue respectively. Logarithmic graphs of the isotherms are on the right for clarity of the low pressure region.

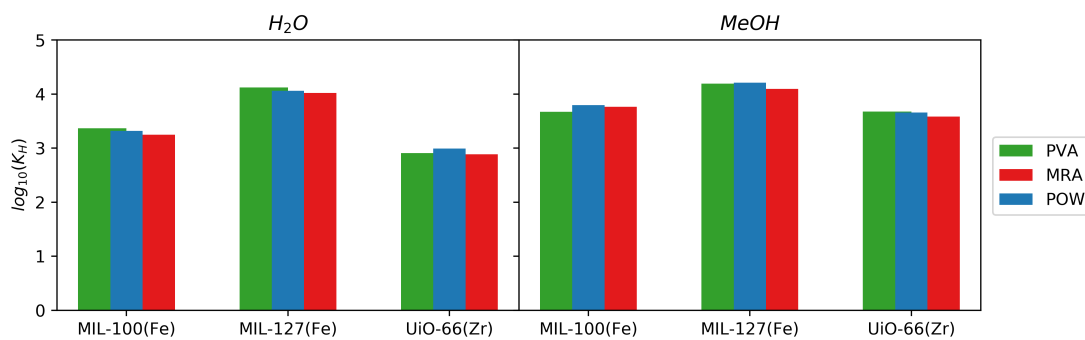


Figure 5.12.: Calculated initial Henry constant for the vapour adsorption isotherms in Figure 5.11 and Figure 5.13

shown to have lower capacities than the powder, stemming from material amorphization during granulation. The addition of hydrophilic alumina conforms to this hypothesis, and appears to have no impact on the initial interaction with the surface. On the other hand, polymer-shaped particles seem to have a higher maximum capacity than both powder and alumina pellets. It is unclear if this effect is due to a cooperative effect of hydrogen bonding with hydroxyl groups on the polymer chains or has another underlying cause.

MIL-100(Fe)

The water isotherm on the powder MIL-100(Fe) material show a more hydrophilic environment, with a higher initial uptake, and two condensation steps at $p/p^0 = 0.3$ and $p/p^0 = 0.5$. At low pressures, adsorption takes place on metal sites in the large cages, with clusters formed around these hydrophilic sites. The two steps correspond to the successive filling of the 2.5 nm and the 2.9 nm pores. The adsorption and desorption branches show a hysteresis loop formation, associated with the condensation in the largest mesoporous spherical pore.

The methanol isotherm on the same parent MOF still presents two condensation steps, which have been shifted at to lower pressure. There is no longer any hysteresis present, an indication that the critical pore radius for its formation is not attained when using methanol.

If comparing the powder isotherms with their shaped counterparts, no differences in features are visible. Initial Henry's constant is similar with all

MIL-127(Fe)

On the last MOF powder, the water isotherm shows a hydrophilic surface, with a highest initial slope out of the three materials studied. The isotherm has two condensation steps, a low relative humidity one at $0.15 p/p^0$, which corresponds to the filling of the hydrophilic pore, and a condensation step situated at $0.5 p/p^0$ inside the more hydrophobic micropore. No hysteresis is observed.

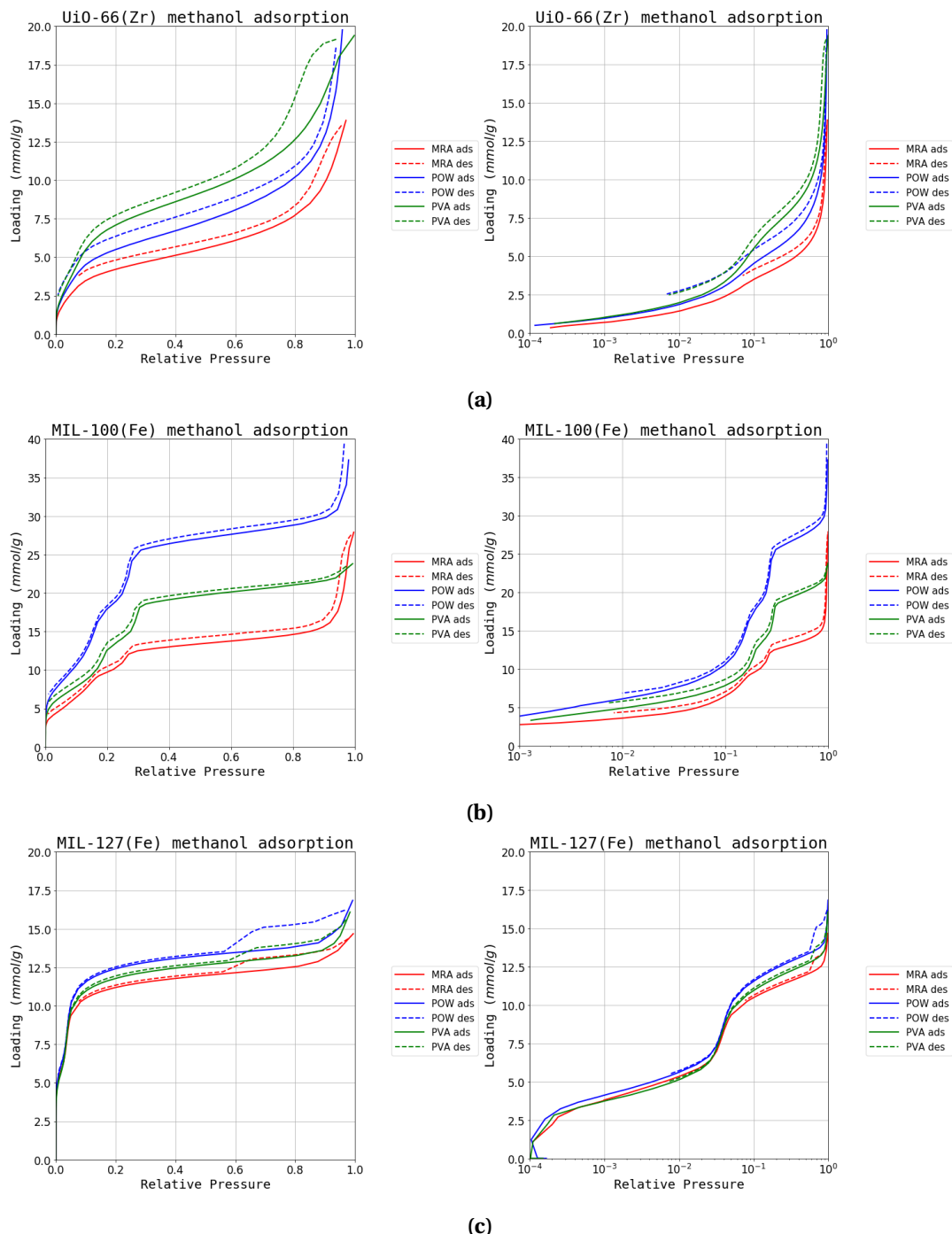


Figure 5.13.: Methanol adsorption isotherms (a) UiO-66(Zr), (b) MIL-100(Fe) and (c) MIL-127(Fe). The powder samples are in light blue, while the ρ -alumina (MRA) and poly-vinyl alcohol (PVA) samples are in red and dark blue respectively. Logarithmic graphs of the isotherms are on the right for clarity of the low pressure region.

As a striking difference from water behaviour, methanol adsorption leads to completely filled pores at below 0.15 relative pressure. By examining the logarithmic isotherms in Figure 5.13c a steep slope at low pressures is evident. It is likely that the larger size of the methanol molecule is much more affected by confinement in the hydrophilic pore, and leads to sudden micropore filling. The same effect, combined with the increased affinity for the organic part of the probe is likely responsible for shifting the secondary condensation step at lower pressures.

The similarities between the both variants of shaped pellets and the original powder confirms the previously observed suitability of this MOF towards the shaping process. The isotherms overlap almost fully, with a slight difference in maximum uptake in the order of powder > PVA > alumina.

5.5. Conclusion

It can be concluded that the process of alumina shaping does not, in general, have an impact on the surface chemistry of the three MOF materials. Interestingly, in regards to the changes in maximum capacity, each material has its own particular behaviour: UiO-66(Zr) has a higher loss in capacity with larger molecular probes, MIL-100(Fe) has a decrease of 10–20% across all gasses and MIL-127(Fe) matches loading on a mass basis except on CO and C₄H₁₀.

Water and methanol adsorption also further the hypothesis that the granulation process resulted in different effects on the MOF samples studied. The surface characteristics of neither pellet type appear changed from the the powder variant, judging by the overlapping low pressure areas of all isotherms. When compared to the parent material, the alumina shaping method reduces the crystallinity of the samples studied, leading to lower uptakes. On the other hand, the polymer shaped version is less prone to amorphization, with the total adsorbed volume actually increasing in the case of UiO-66(Zr).

The shaping also induces a densification which, in almost all cases, leads to a better performance on a volumetric basis. However, the influence on the mass transport effects of the alumina binder is not known and should be investigated further.

Overall, the process of alumina shaping is a promising method of preparing MOFs for gas-related applications in separation and storage, but care should be taken to not generalise the effects present on one material to another. It is also worth noting that, from an industrial point of view, alumina shaping holds promise as a method which does not cause the surface properties of the underlying material to change. Even if some loss of capacity is observed, the volumetric densification counter-balances this effect.

In the context of this thesis, the post-processing of adsorbent materials is shown to be highly relevant to their adsorption behaviour, generally negatively impacting properties such as pore volume and surface area.

Bibliography

- [1] Farid Akhtar, Linnéa Andersson, Steven Ogunwumi, Niklas Hedin, and Lennart Bergström. Structuring adsorbents and catalysts by processing of porous powders. *Journal of the European Ceramic Society*, 34(7):1643–1666, July 2014. ISSN 09552219. doi: 10.1016/j.jeurceramsoc.2014.01.008.
- [2] Douglas M. Ruthven, Shamsuzzaman Farooq, and Kent S. Knaebel. *Pressure Swing Adsorption*. VCH Publishers, New York, N.Y, 1994. ISBN 978-1-56081-517-4 978-3-527-89517-5.
- [3] Sharon Mitchell, Nina-Luisa Michels, Gerardo Majano, and Javier Pérez-Ramírez. Advanced visualization strategies bridge the multidimensional complexity of technical catalysts. *Current Opinion in Chemical Engineering*, 2(3):304–311, August 2013. ISSN 22113398. doi: 10.1016/j.coche.2013.04.005.
- [4] Douglas M. Ruthven. *Principles of Adsorption and Adsorption Processes*. Wiley, New York, 1984. ISBN 978-0-471-86606-0.
- [5] T. Ohji, M. Singh, J. A. Salem, Dongming Zhu, and American Ceramic Society, editors. *Advanced Processing and Manufacturing Technologies for Structural and Multifunctional Materials: A Collection of Papers Presented at the 31st International Conference on Advanced Ceramics and Composites, January 21-26, 2007, Daytona Beach, Florida*. Number v. 28, issue 7 in Ceramic engineering and science proceedings. Wiley-Interscience, Hoboken, N.J, 2008. ISBN 978-0-470-19638-0. OCLC: ocn154800301.
- [6] Teresa J. Bandosz, editor. *Activated Carbon Surfaces in Environmental Remediation*. Number 7 in Interface science and technology. Elsevier/AP, Amsterdam, 2006. ISBN 978-0-12-370536-5. OCLC: 255269962.
- [7] Gareth T. Whiting, Abhishek Dutta Chowdhury, Ramon Oord, Pasi Paalanen, and Bert M. Weckhuysen. The curious case of zeolite-clay/binder interactions and their consequences for catalyst preparation. *Faraday Discuss.*, 188:369–386, 2016. ISSN 1359-6640, 1364-5498. doi: 10.1039/C5FD00200A.
- [8] Nina-Luisa Michels, Sharon Mitchell, and Javier Pérez-Ramírez. Effects of Binders on the Performance of Shaped Hierarchical MFI Zeolites in Methanol-to-Hydrocarbons. *ACS Catalysis*, 4(8):2409–2417, August 2014. ISSN 2155-5435, 2155-5435. doi: 10.1021/cs500353b.
- [9] Stefan Kaskel, editor. *The Chemistry of Metal-Organic Frameworks: Synthesis, Characterization, and Applications*. Wiley-VCH Verlag GmbH & Co. KGaA, Weinheim, 2016. ISBN 978-3-527-33874-0 978-3-527-69305-4 978-3-527-69308-5 978-3-527-69306-1 978-3-527-69307-8.
- [10] Enrique V. Ramos-Fernandez, Mariana Garcia-Domingos, Jana Juan-Alcañiz, Jorge Gascon, and Freek Kapteijn. MOFs meet monoliths: Hierarchical structuring metal organic framework catalysts. *Applied Catalysis A: General*, 391(1-2):261–267, January 2011. ISSN 0926860X. doi: 10.1016/j.apcata.2010.05.019.
- [11] Sonia Aguado, Jerome Canivet, and David Farrusseng. Facile shaping of an imidazolate-based MOF on ceramic beads for adsorption and catalytic applications. *Chemical Communications*, 46(42):7999, 2010. ISSN 1359-7345, 1364-548X. doi: 10.1039/c0cc02045a.
- [12] D. Bazer-Bachi, L. Assié, V. Lecocq, B. Harbuzaru, and V. Falk. Towards industrial use of metal-organic framework: Impact of shaping on the MOF properties. *Powder Technology*, 255:52–59, March 2014. ISSN 00325910. doi: 10.1016/j.powtec.2013.09.013.
- [13] Tian Tian, Jose Velazquez-Garcia, Thomas D. Bennett, and David Fairen-Jimenez. Mechanically and chemically robust ZIF-8 monoliths with high volumetric adsorption capacity. *Journal of Materials Chemistry A*, 3(6):2999–3005, 2015. ISSN 2050-7488, 2050-7496. doi: 10.1039/C4TA05116E.
- [14] Rocio Semino, Naseem A. Ramsahye, Aziz Ghoufi, and Guillaume Maurin. Microscopic Model of the Metal–Organic Framework/Polymer Interface: A First Step toward Understanding the Compatibility in Mixed Matrix Membranes. *ACS Applied Materials & Interfaces*, 8(1):809–819, January 2016. ISSN 1944-8244, 1944-8252. doi: 10.1021/acsami.5b10150.
- [15] Takashi Kitao, Yuanyuan Zhang, Susumu Kitagawa, Bo Wang, and Takashi Uemura. Hybridization of MOFs and polymers. *Chemical Society Reviews*, 46(11):3108–3133, 2017. ISSN 0306-0012. doi: 10.1039/C7CS00041C.

- [16] Nicolas Chanut, Andrew D. Wiersum, U-Hwang Lee, Young Kyu Hwang, Florence Ragon, Hubert Chevreau, Sandrine Bourrelly, Bogdan Kuchta, Jong-San Chang, Christian Serre, and Philip L. Llewellyn. Observing the Effects of Shaping on Gas Adsorption in Metal-Organic Frameworks. *European Journal of Inorganic Chemistry*, 2016(27):4416–4423, September 2016. ISSN 14341948. doi: 10.1002/ejic.201600410.
- [17] Jasmina Hafizovic Cavka, Søren Jakobsen, Unni Olsbye, Nathalie Guillou, Carlo Lamberti, Silvia Bordiga, and Karl Petter Lillerud. A New Zirconium Inorganic Building Brick Forming Metal Organic Frameworks with Exceptional Stability. *Journal of the American Chemical Society*, 130(42):13850–13851, October 2008. ISSN 0002-7863. doi: 10.1021/ja8057953.
- [18] Andrew D. Wiersum, Estelle Soubeyrand-Lenoir, Qingyuan Yang, Beatrice Moulin, Vincent Guillerm, Mouna Ben Yahia, Sandrine Bourrelly, Alexandre Vimont, Stuart Miller, Christelle Vagner, Marco Daturi, Guillaume Clet, Christian Serre, Guillaume Maurin, and Philip L. Llewellyn. An Evaluation of UiO-66 for Gas-Based Applications. *Chemistry - An Asian Journal*, 6(12):3270–3280, December 2011. ISSN 18614728. doi: 10.1002/asia.201100201.
- [19] Patricia Horcajada, Suzy Surblé, Christian Serre, Do-Young Hong, You-Kyong Seo, Jong-San Chang, Jean-Marc Grenèche, Irene Margiolaki, and Gérard Férey. Synthesis and catalytic properties of MIL-100(Fe), an iron(III) carboxylate with large pores. *Chem. Commun.*, (27):2820–2822, 2007. ISSN 1359-7345, 1364-548X. doi: 10.1039/B704325B.
- [20] Qingyuan Yang, Sébastien Vaesen, Florence Ragon, Andrew D. Wiersum, Dong Wu, Ana Lago, Thomas Devic, Charlotte Martineau, Francis Taulelle, Philip L. Llewellyn, Hervé Jobic, Chongli Zhong, Christian Serre, Guy De Weireld, and Guillaume Maurin. A Water Stable Metal-Organic Framework with Optimal Features for CO₂ Capture. *Angewandte Chemie*, 125(39):10506–10510, September 2013. ISSN 00448249. doi: 10.1002/ange.201302682.
- [21] Ji Woong Yoon, You-Kyong Seo, Young Kyu Hwang, Jong-San Chang, Hervé Leclerc, Stefan Wuttke, Philippe Bazin, Alexandre Vimont, Marco Daturi, Emily Bloch, Philip L. Llewellyn, Christian Serre, Patricia Horcajada, Jean-Marc Grenèche, Alirio E. Rodrigues, and Gérard Férey. Controlled Reducibility of a Metal-Organic Framework with Coordinatively Unsaturated Sites for Preferential Gas Sorption. *Angewandte Chemie International Edition*, 49(34):5949–5952, August 2010. ISSN 14337851. doi: 10.1002/anie.201001230.
- [22] Yunling Liu, Jarrod F. Eubank, Amy J. Cairns, Juergen Eckert, Victor Ch. Kravtsov, Ryan Luebke, and Mohamed Ed-daoudi. Assembly of Metal-Organic Frameworks (MOFs) Based on Indium-Trimer Building Blocks: A Porous MOF with soc Topology and High Hydrogen Storage. *Angewandte Chemie International Edition*, 46(18):3278–3283, April 2007. ISSN 14337851, 15213773. doi: 10.1002/anie.200604306.
- [23] Hubert Chevreau, Anastasia Permyakova, Farid Nouar, Paul Fabry, Carine Livage, Florence Ragon, Alfonso Garcia-Marquez, Thomas Devic, Nathalie Steunou, Christian Serre, and Patricia Horcajada. Synthesis of the biocompatible and highly stable MIL-127(Fe): From large scale synthesis to particle size control. *CrystEngComm*, 18(22):4094–4101, 2016. ISSN 1466-8033. doi: 10.1039/C5CE01864A.
- [24] Nicolas Chanut, Sandrine Bourrelly, Bogdan Kuchta, Christian Serre, Jong-San Chang, Paul A. Wright, and Philip L. Llewellyn. Screening the Effect of Water Vapour on Gas Adsorption Performance: Application to CO₂ Capture from Flue Gas in Metal-Organic Frameworks. *ChemSusChem*, 10(7):1543–1553, April 2017. ISSN 18645631. doi: 10.1002/cssc.201601816.
- [25] Anil H. Valekar, Kyung-Ho Cho, U-Hwang Lee, Ji Sun Lee, Ji Woong Yoon, Young Kyu Hwang, Seung Gwan Lee, Sung June Cho, and Jong-San Chang. Shaping of porous metal-organic framework granules using mesoporous ρ -alumina as a binder. *RSC Advances*, 7(88):55767–55777, 2017. ISSN 2046-2069. doi: 10.1039/C7RA11764G.
- [26] Pritha Ghosh, Yamil J. Colón, and Randall Q. Snurr. Water adsorption in UiO-66: The importance of defects. *Chem. Commun.*, 50(77):11329–11331, 2014. ISSN 1359-7345, 1364-548X. doi: 10.1039/C4CC04945D.

6. Exploring intrinsic framework phenomena — adsorption induced phase changes

6.1. Introduction

Until this chapter, it has been assumed that the porous materials are static when adsorbing a gas. Differences in pore size, crystallinity or structure may exist, but these properties did not change as the host fluid enters the pores. In most cases this is a reasonable assumption. However, it is not universally applicable, as the forces and interactions exerted during adsorption may induce changes in solid itself.

Such effects in classic porous inorganic materials like zeolites, carbons and clays take the form of structural contraction and expansion, swelling or counterion displacement.⁽¹⁾ It is only recently that flexibility was discovered in coordination polymers, such as MOFs. A feature which arises from their comparatively weak coordination bonds or pliant organic components, it allows for a systematic deflection of bonds throughout the entire crystal lattice. As such, the term “soft porous crystals” defines porous solids that are both highly ordered and possess the ability to reversibly transform their structure upon external stimuli. Part of the so-called third generation of crystalline porous compounds, they represent some of the latest developments in the field of MOFs.

The unique properties of flexible materials can preclude their application in fields such as sensing, micromechanical devices and highly efficient gas storage. It is these perspectives that make their synthesis and design a key research interest. However, their flexible nature introduces new challenges in their characterisation, as factors such as temperature and thermal history⁽²⁾, crystal size^(3,4), external pressure^(5,6), structural defects⁽⁷⁾ and even adsorption kinetics play a role in their compliance. This type of variability goes beyond what has been insofar discussed in this thesis and it is here where a combined characterisation approach becomes essential in understanding the fundamental physics governing flexibility and prediction of adsorption behaviour.

Summary

After a brief introduction of the background of soft porous materials, this chapter will present the characterization of a novel flexible MOF (DUT-49) and its analogues. This material undergoes a sudden collapse of its pore network into a closed form state upon adsorption, resulting in the expulsion

of gas from its pores. This phenomena was coined “negative gas adsorption” (NGA). The text will focus on characterisation through calorimetric methods performed by Paul Iacomi, together with references of results obtained by collaborating groups, included in order obtain a complete story of the underlying mechanism behind NGA.

Contribution

The synthesis of all MOFs was performed by Simon Krause (TU Dresden), together with their initial characterization through nitrogen adsorption at 77 K. Ambient and low temperature calorimetry was carried out by Paul Iacomi. Computer simulations of adsorption isotherms, linker buckling and structural contraction are the result of work from Jack Evans and Prof. F.X Coudert. Mechanical compression experiments were performed in the group of Prof. Guillaume Maurin in Montpellier. Prof. Philip Llewellyn and Prof. Stefan Kaskel were instrumental in the analysis of the results obtained.

neutron
methods

6.2. Compliance in porous crystals

6.2.1. Examining the assumption of an inert adsorbent

Adsorption induced changes in porous media have been known to occur for over 90 years⁽⁸⁾, with both clays, coals and polymers undergoing swelling during gas or vapour uptake.⁽⁹⁾ However, the effect upon the macroscopic properties of the material is often negligibly small and of little consequence to industrial adsorption processes. Studies of this aspect of porous adsorbents have therefore been scarce in the large part of the 20th century, likewise influenced by lack of sufficiently accurate methods for characterising and modelling such occurrences.

In recent years, the advent of reference materials, highly sensitive methods such as synchrotron-grade light sources and *in silico* computational techniques such as DFT has put at our disposal the tools required to study these transformations. Together with the discovery of their role in natural and industrial processes e.g. the swelling of shale during natural gas extraction, maturation of concrete and the perspectives afforded by novel porous materials, these factors have generated much scientific interest in material compliance. As an example, the attractive option of combined carbon capture and methane recovery implemented through pumping of carbon dioxide into reservoirs is prohibited by swelling-induced loss of porosity and well blocking.⁽⁹⁾

In-depth studies⁽¹⁰⁾ have revealed that most porous materials posses some small degree of compliance, with *in-situ* dilatometry going so far as to obtain pore size distributions from accurate volume changes.⁽¹¹⁾ Most flexible processes can be likened to continuous order transitions. It is, however, the discovery of large scale flexibility in MOFs such as MIL-53 and linker-controlled gate opening like in ZIF-8, where the transformation between the different framework states occurs suddenly at precise points in the loading curve, which has shown that compliance may also take the

form of a first-order transition. Such types of transformations are desirable⁽¹²⁾ due to their highly specific response. The possible dependence of flexibility on other stimuli, such as light, mechanical pressure, temperature or magnetic fields may allow for precise tuning of structural changes. As such, it is reasonable to state that the mobility of the solid phase can no longer be ignored.

6.2.2. Flexibility in metal organic frameworks

Since the highlight of compliance in porous coordination polymers in the report of Kitagawa et al.⁽¹²⁾, much progress has been made in the synthesis and understanding of this phenomenon. An exhaustive review of MOF flexibility is outside the scope of this thesis, with the field progressing rapidly enough to generate a wealth of critical literature.^(13–19) Some of the known types of structural flexibility encountered in MOFs will be briefly discussed, with a summary available in Figure 6.1.

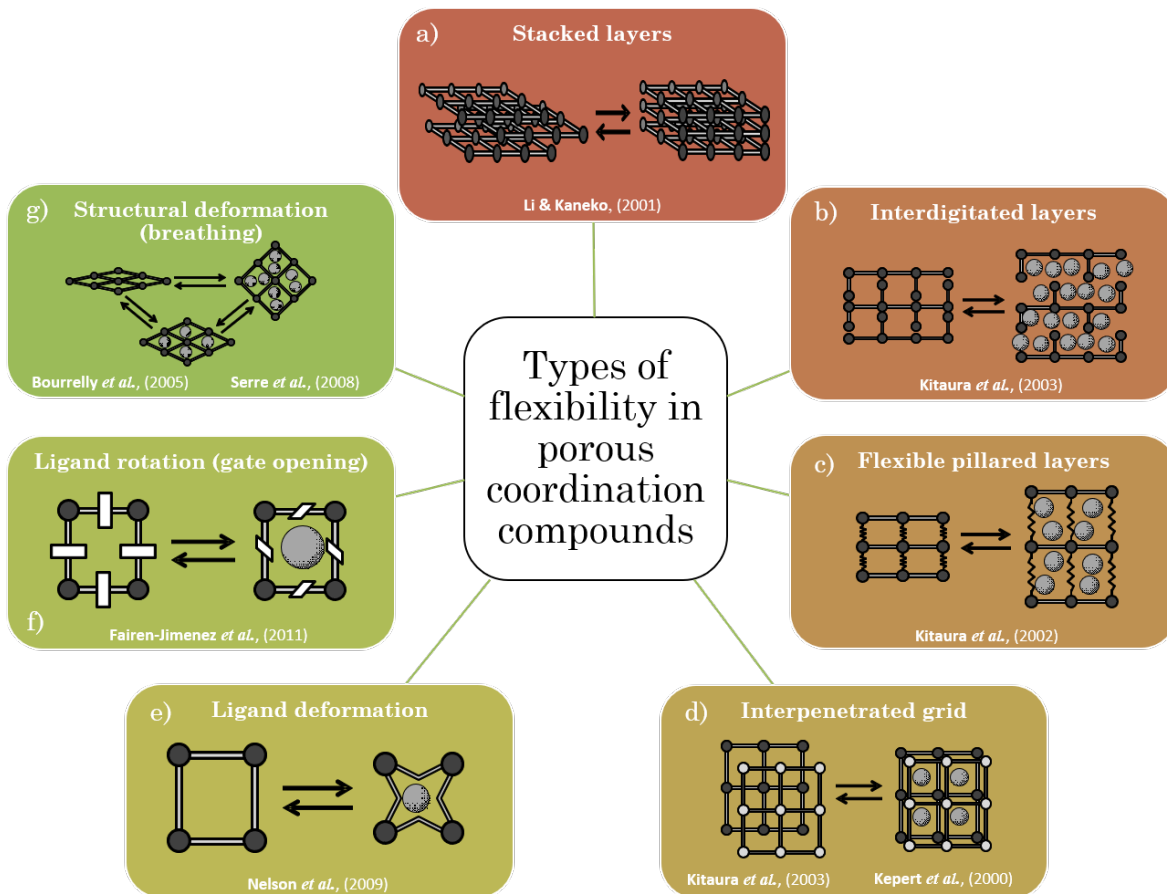


Figure 6.1.: A (non-exhaustive) visual summary of the types of flexibility documented in MOFs, as detailed in (a) Li and Kaneko⁽²⁰⁾ (b) Kitaura et al.⁽²¹⁾ (c) Kitaura et al.⁽²²⁾ (d) Kitaura et al.⁽²¹⁾, Kepert et al.⁽²³⁾ (e) Nelson et al.⁽²⁴⁾ (f) Fairen-Jimenez et al.⁽²⁵⁾ (g) Bourrelly et al.⁽²⁶⁾, Serre et al.⁽²⁷⁾

Since MOFs, like clays and graphite, can form discrete two-dimensional sheets, bound together by weak Van-der-Waals, $\pi - \pi$ interactions or hydrogen bonds, adsorbed molecules may force these

layers apart by intercalation. The concept is taken further in the pillared layer approach, where the sheets are connected by tertiary linkers instead of weak attractions. With the judicious choice of linker, these can act as springs, allowing pore expansion while maintaining structural integrity.

As briefly mentioned in chapter 4, a large void space in the unit cells allows secondary networks to grow throughout the MOF, effectively creating an intercalated structure.^(21,23) These secondary grids are independent of the primary framework and are displaced upon guest adsorption.⁽²⁸⁾ This internal translation may also be associated with a tilting of the linker⁽²⁹⁾, combining intercalation with structural-deformation type flexibility.

The origin of flexibility may be purely due to the linker itself. Organic bonds are inherently labile, as seen in polymer chains, since unsaturated connections in the linker may bend if the strain on the organic strut overcomes its tensile strength. Increasing the linker length often induces this type of flexibility, for example in the IRMOF isoreticular series of materials.⁽²⁴⁾ Even an unsaturated bond may be induced by a photon with a suitable energy to undergo an analogue of a *cis-trans* transition. The deformation may also lead to expansion and therefore of framework swelling, as encountered in MIL-88 and its derivatives.⁽³⁰⁾

MOFs can also have structural flexibility which does not require any volume changes in the unit cell. The rotation of linkers can act as gating for different guests, allowing entry of probes larger than the window size would suggest or preferential adsorption of a gas which has the right property to act as a “key” from a mixture.⁽³¹⁾ The former effect is common in zeolitic imidazole frameworks (ZIFs).⁽²⁵⁾

The discovery of the so-called “breathing” type of structural deformation^(26,27,32) in the MIL-53 and MIL-47 family of materials has revealed step-like transformations in its unit cell size and metastable intermediaries with an open pore (*op*), closed pore (*cp*) and narrow/intermediate states (*np/ ip*). No other family of flexible MOFs has, to date, generated more scientific interest. This is likely due to the relative stability of the material, combined with its ability to undergo massive and reversible structural deflections, while retaining its crystallinity. The relatively simple structure and large capability for functionalisation, either through ligand modification or exchange of the metal node (with variants of MIL-53 synthesised for Cr, Fe, Al, Sc, Ga or In), allowed for its use as an archetypal material for the study of flexible behaviour. More recently, similar materials, like DUT-8(M) (M=Ni, Co, Cu, Zn) which allow the the impact of the metal⁽³³⁾ on compliance to be evidenced have emerged.

6.2.3. Describing and inducing MOF compliance

The mechanistic phenomena during adsorption can be seen as an overlap⁽³⁴⁾ of several competing effects: a sub-monolayer contraction⁽³⁵⁾ resulting from micropore bridging or surface stresses, followed by a monotonic expansion with the gradual decrease of the solid-fluid interface energy also

known as the Bangham effect.⁽³⁶⁾ Such behaviour is highly dependent of pore size, geometry and anisotropy, with condensation in macropores a further complex source of strain.^(37–39) The degree of adsorption induced changes in a framework is generally a function of its porosity, with very high surface area materials such as aerogels capable of undergoing up to 30% deformation.⁽⁴⁰⁾ In MOFs, the adsorption stresses are no different than in other materials. However, the ability of the porous network to undergo displacements is much higher, since its rigidity is in between that of “hard” adsorbents such as zeolites/silica and purely organic polymers (although porous covalent frameworks can also achieve self-support and porosity).

Finding a suitable model that would predict both the adsorption induced stress and the resulting structural changes from strain has so far remained a challenge. A thermodynamic-based method which has been successfully applied to breathing MOFs is that of Neimark et al.⁽⁴¹⁾. This model assumes that the deformation strain is fully determined due to surface stress, calculated from the grand thermodynamical of a rigid analogue of the pore. It has been used to explain the existence domains of MIL-53(Al)⁽⁴²⁾, in conjunction with an osmotic thermodynamic description of the framework itself.⁽⁴³⁾ For mesoporous materials, the stress-strain model has been extended by Gor and Neimark⁽³⁴⁾ through the Derjaguin–Broekhoff–de Boer (DBdB) theory⁽⁴⁴⁾ and applied to predict the resulting strain in mesoporous silica. Nevertheless a complete theory of adsorption-deformation which can fully predict the changes in the measured enthalpy of adsorption and the mechanistic behaviour of MOFs has remained elusive.

The most promising characteristics of flexible MOFs are the ability to control the compliance through external means which are detached from guest loading, which would dramatically expand their potential applications. Pure mechanical pressure on a flexible material is often enough to induce transitions. First observed on ZIFs, through pressure induced phase change^(45,46) and latter applied to breathing MOFs using mercury porosimetry^(47,48), it shows a direct relationship between the bulk modulus of a MOF and its flexible behaviour. Entropic control through temperature-induced switching has been shown to be possible in MIL-53 by Liu et al.⁽²⁾, explained as a change in the range of metastability of its pore forms.⁽⁴²⁾ More precise external control may be possible if molecules which have the ability to switch their state when exposed to suitable wavelengths are used as linkers. In this case light irradiation may be used to force the transition.⁽⁴⁹⁾ Magnetic field dependent switching can also be theorised, although has not been so far encountered. One of the least understood factors that changes the flexible behaviour of porous crystals is the effect of particle size. It is clear that the thermodynamical potential of the crystal surface has a profound influence on its compliance, as shown on the large shift of the gate-opening pressure of ZIF-8.⁽³⁾ However, a rigorous model of the contribution of the surface on breathing has yet to be developed in our knowledge. Finally, the presence of structural defects likely impacts the framework flexibility, as highlighted by Bennett et al.⁽⁷⁾ in a recent article, although currently few studies have focused on this subject.

6.2.4. Consequences and applications of flexible MOFs

The study of flexible MOFs is motivated from both a desire for fundamental understanding of compliance and from the potential applications of such systems. The use of soft porous crystals in sensing and gas storage and separation is evident, although applications in catalysis, electrochemistry and drug delivery have also been alluded to by recent studies.

The usefulness of adsorption induced flexibility for sensors or actuators has been recognised, initially by nature itself, with humidity induced swelling acting to open pine cones.⁽⁵⁰⁾ More recently, similar sensing devices based on adsorption strain in mesoporous silica have been developed such as a flexing silica-polymer membrane⁽⁵¹⁾ or deformation of a nano sized cantilever⁽⁵²⁾ which show promise for use in micromechanical systems.

From a gas storage and separation point of view, changes in the adsorbent structure may yield crucial process improvements. Pressure swing adsorption (PSA) is heavily dependent on the working capacity of the adsorbent used, or the difference between loading at the operation pressure and at the regeneration pressure. In this case, an S-shaped isotherm, with the vertical part of the slope in the aforementioned pressure range would lead to high process efficiency gains by eliminating material “dead volume adsorbed”.⁽¹³⁾ In a temperature swing process (TSA), where the regeneration is performed through heating of the adsorbent bed, the key parameter is the integral enthalpy of adsorption, a measure of the energy requirements for the process. As a part of the chemical potential of the adsorbed phase is used by the mechanical contraction of the material, flexible adsorbents have the advantage of intrinsic thermal management, reducing the energy cost.⁽⁵³⁾ Both effects are equally applicable to the storage of pure gasses, increasing the storage capacity and minimizing the energetic requirement of recovery. Entrapment of guest molecules inside a gated pore might lend itself to temperature controlled storage and release of gasses⁽⁵⁴⁾, or “sealing” of a target gas inside the structure once adsorption has taken place. It is also possible that by using external mechanical pressure to control flexibility, the adsorption behaviour of porous materials may be tuned, as suggested by the work of Chanut⁽⁶⁾ on MIL-53.

Catalytic applications of flexible MOFs could be envisaged where the switching behaviour can bring into contact active sites or hold reactants in place until complete reaction has taken place. A recent study by Souto et al.⁽⁵⁵⁾, has shown that the redox potential of the sulphur bond in a tetrathiafulvalene breathing MOF is dependent on its dihedral angle in different pore states. This raises the possibility of tunability of the oxidation potential of flexible framework. Finally flexible MOFs constructed of biocompatible materials could be used as drug delivery methods^(56,57) if release of the encapsulated molecule is triggered through a structural transition.

6.2.5. Unique flexible behaviour of DUT-49

It is clear that one of the most desirable kinds of flexibility is one that can be likened to a Heaviside step function, where switching occurs between two or more material states at well defined pressure. However, not many MOFs synthesised to date follow this type of behaviour. It is why the surprising compliance of DUT-49, a highly porous structure, has generated interest in the MOF community.

In the initial paper of Stoeck et al.⁽⁵⁸⁾, the synthesis of DUT-49 through a super-molecular approach is described, with the goal of generating a highly porous material. The MOF is built through the secondary building unit or SBU approach, where the crystallographic vertices of the structure are metal organic polyhedra (MOP), in this case 12-connected cuboctahedra based on copper paddlewheels, which are then connected by a tetratopic carboxilate linker. The resulting MOF forms a face centered cubic (**fcu**) net if the MOP are considered as nodes and a trimodal pore size distribution: the 1.2 nm MOP, a 1.8 nm tetrahedron and a very large 2.6 nm octahedron. The material has a high nitrogen accessible surface area (of more than 5000 m²/g) and accessible volume (84.7%).

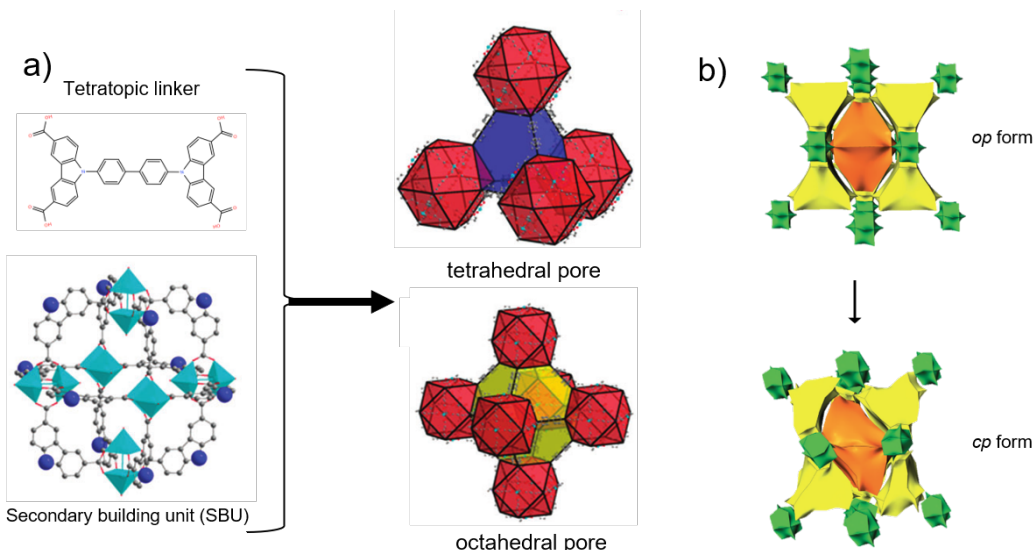


Figure 6.2: (a) The tetratopic linker and secondary copper paddlewheel building unit used to synthesise DUT-49, and the resulting structure and generated pores.⁽⁵⁸⁾ (b) Two possible phases of the material, with the open to closed pore transition.⁽⁵⁹⁾

In the original study, the MOF did not show any flexible behaviour. However, it was later found by Krause et al.⁽⁵⁹⁾ that when adsorbing CH₄ at 111 K, a sharp step occurs in the isotherm, corresponding to an *op/cp* transition. More interestingly, the step is accompanied by an expulsion of the adsorbed gas from the interior of the pores, increasing the pressure in the experiment cell. This type of pressure-amplifying transition has been coined negative gas adsorption (NGA) and was found to occur with other adsorbates at different temperatures such as C₄H₁₀ at 303 K or Xe at 195 K, which allowed study of the transition at ambient temperature and through ¹²⁹Xe NMR spectroscopy.⁽⁶⁰⁾

The origin of this phenomenon has been elucidated by Evans et al.⁽⁶¹⁾ where it has been shown to emerge due to a buckling of the central strut of the tetratopic linker under compressive stress induced by adsorption, similar to the failure of a metal column under critical load. The *op* and *cp* phase stability depends on the adsorbate loading of the material, with the *op* form being energetically favoured at zero and high loadings. At intermediate pore filling, the *cp* state is stabilized by the fluid molecules and becomes energetically favoured. At this point, the *op* phase enters a metastable regime and can contract if the energy barrier between the two states is overcome. As the transition from the *cp* to the *op* state requires an activation energy, re-opening of the structure is only possible through complete structure loading. If the system is in its *cp* state during adsorbate removal, the structure undergoes complete structural collapse.

However, questions still remain about the driving forces behind the transition itself, such as the contribution of guest-host interactions, as well as the temperature range and adsorbates where it is possible. The rational design of such materials is also put into question, where framework parameters such as linker length, functionalisation and composition may be used to tune the pressure and extent of NGA. It is here where the adsorption methodology introduced in chapter 2 combined with *in-situ* calorimetry as presented in chapter 3 can be used to shed light on the energetic background of NGA in DUT-49.

6.3. Materials and characterisation methods

6.3.1. Materials

Several DUT materials have been synthesised in order to study the effect of different parameters on the switching behaviour. From the point of view of the criterion of interest, the materials can be divided into the following categories:

- Series dedicated to studying the influence of isoreticular design through variation of linker length in the order of theoretical increasing porosity: DUT-48, DUT-46, DUT-49, DUT-50, DUT-151/DUT-152. These materials are designed with a linker of increasing size by using differently structured phenyl rings. A corresponding increase in porosity is expected, however, starting from a 4-linear phenyl chain (DUT-151), the internal voids are large enough to allow for a secondary interpenetrated network to develop. An attempt to prevent this by grafting bulky naphthalene rings was made in the synthesis of DUT-152, but the resulting structure was still found to be interpenetrated.
- Series assessing the impact of steric hindrance of the central linker bond on NGA, in the order of connectivity: DUT-49, DUT-149, DUT-148, DUT-147. The rationale behind this approach is to improve the tensile strength of the strut by the addition of sterically hindering side connections.

- Series investigating the effect of heterocycles on compliant behaviour, using thiophene as replacement for the benzene rings, in the order of increasing linker size: DUT-170, DUT-171, DUT-172, DUT-173. If interactions with the framework plays a role in NGA, the addition of potentially stronger host-guest sites.
- Series aiming to possess a progressively more labile central strut through the use of different degrees of saturation, in order of central bond hybridization: DUT-160, DUT-161, DUT-163. It was found that the removal of solvent from DUT-162 could not be performed without structure collapse. The softness of the saturated backbone lends itself to an unstable *op* state.
- Series of increasing crystallite size to study the effect of the crystal surface to volume ratio on NGA. Different sizes of DUT-49 were synthesised either through the addition of a acid modulator for obtaining large crystals or through the addition of a base to inhibit crystal growth. A series of 4 DUT-49 was received, of 800 nm, 1 µm, 4 µm and 10 µm average size respectively.

The material name, together with the central part of the linker, which was modified to change the flexible behaviour of the framework, is presented in Table 6.1.

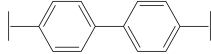
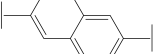
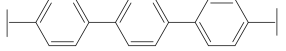
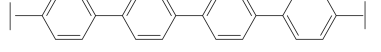
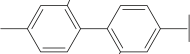
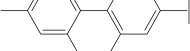
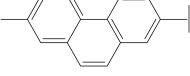
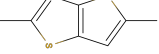
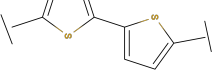
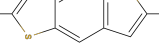
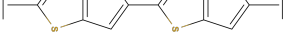
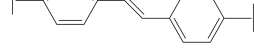
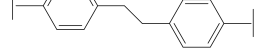
Need
data
from
simon
on these
materi-
als

6.3.2. Characterisation methods

In order to examine the energetic components of both adsorption and NGA, the combined manometry and calorimetry setup first presented in chapter 3 was used. Ambient temperature calorimetry was conducted at 303 K with probes such as butane, propane and propylene using the step-by-step gas introduction method. The exact procedure for such an experiment can be found in section A.10 of Appendix A.

For low temperatures (77 K), a high resolution continuous introduction method was employed, together with a home-made calorimetric system first described in the work of Rouquerol et al.⁽⁶²⁾. To summarize, the adsorbate is placed in a J-shaped custom designed glass cell which is then sealed with an oxyacetylene torch prior to evacuation and sample activation. Borosilicate glass is selected as the material of choice to prevent any thermal expansion induced leaks. The cell is then introduced into a LN₂-filled dewar, through the bottom of the differential calorimeter. Good thermal equilibrium between the cell and surrounding thermopile is ensured using by using a helium blanket in the calorimetric enclosure, kept under positive pressure through a continuous low flow. The connection to the gas dosing system is made through a Swagelock VCR 1/4" stainless steel connection. High leak resistance and gas purity is assured by the single use copper joint metal-to-metal interlock. Pressure is measured through the use of a double gauge assembly, a sensitive low pressure gauge (up to 2 kPa) and an ambient pressure gauge (up to 120 kPa). A sonic nozzle is used to control the flow of adsorbate into the reference volume and the cell. A separate calibration step is performed at the start of each experiment to determine the adsorbate flowrate and the dead volume

Table 6.1.: Flexible materials analogous to DUT-49

Name	Linker center	Study	Observations
DUT-49		Original material	<p>Multiple crystal sizes</p> <ul style="list-style-type: none"> • DUT-49(o)-0.8 μm • DUT-49(s)-1.0 μm • DUT-49(m)-4.0 μm • DUT-49(l)-10.0 μm
DUT-48		Linker size	—
DUT-46		Linker size	—
DUT-50		Linker size	—
DUT-151		Linker size	Interpenetrated
DUT-152		Linker size	Interpenetrated
DUT-149		Functionalization	—
DUT-148		Functionalization	—
DUT-147		Functionalization	—
DUT-170		Heterocycle	—
DUT-171		Heterocycle	—
DUT-172		Heterocycle	Not measured
DUT-173		Heterocycle	Not measured
DUT-160		Strut saturation	—
DUT-161		Strut saturation	Not measured
DUT-162		Strut saturation	No stable <i>op</i> state

before the entrance to the cell. An experiment takes between 1–4 days depending on the flowrate used. A picture of the different components of the setup can be seen in Figure 6.3.

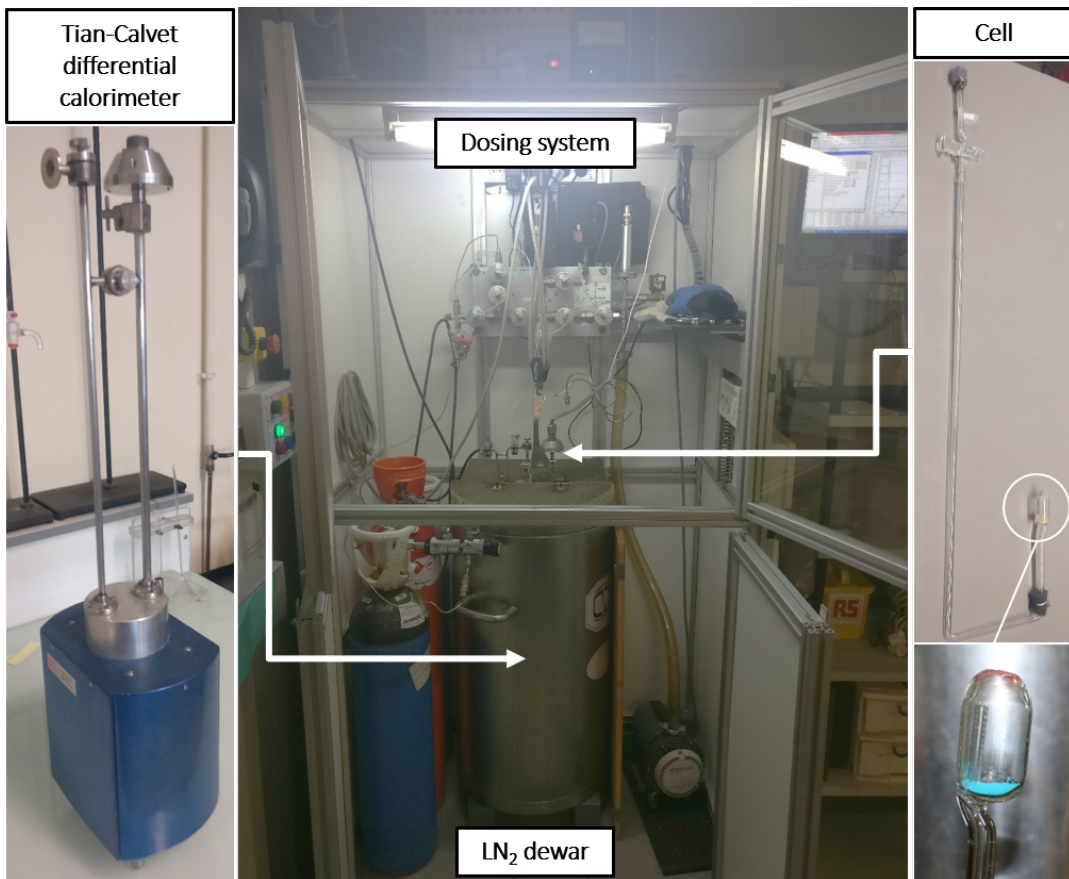


Figure 6.3.: The low temperature calorimetry setup

Extreme care has to be taken during sample preparation, as all materials studied are sensitive to heat and water vapour, which attack the Cu paddlewheel and lead to material degradation. To prevent any decomposition, the samples were stored under an inert argon atmosphere in a glovebox. The loading of ambient temperature cells was performed inside the glovebox while filling and sealing of low temperature glass cells was done in an argon flow. After sample cell preparation, the materials are activated under dynamic vacuum at 120 °C.

It is worth noting that if the sample undergoes an *op/cp* phase transition during the experiment and cannot be reopened with the application of high pressure, as is the case for butane at 303 K, the material cannot be reused. Any attempt to activate it under vacuum leads to structural breakdown of the unstable *cp* phase. Since a limited amount of sample is available, this played a large role in data acquisition, with several isotherms only recorded once.

6.4. Results and discussion

The first part of this section will present the characteristics of the NGA step in DUT-49 as recorded by ambient calorimetry, and what a cursory examination of the isotherm and enthalpy curves at 303 K can reveal about the energetics of the system and the stability of the two phases.

The following subsection contains the results of the studies on DUT-49 analogues, highlighting the effects that linker elongation and functionalization have on the adsorption behaviour and NGA extent at ambient temperature.

Finally, an in-depth study of the DUT-49 NGA mechanism is performed, employing a variety of gas probes (N_2 , Ar, O_2 , CO) at low temperature. The time-resolved data obtained through continuous adsorbate introduction sheds light on the influence of the host-guest and guest-guest interactions on transition mechanics, the energetic barrier of the transition state and on system kinetics. A comparison with non-flexible analogues allows an assessment of the role of the pore filling mechanism on the structural transition to be made.

6.4.1. The structural transition leading to NGA in DUT-49

In the time-resolved pressure and calorimetry signal recorded when performing butane adsorption at 303 K, the NGA step is clearly visible as the pressure in the cell suddenly increases after a dosing point. An example can be seen in Figure 6.4, next to a regular dosing step. A short time after the adsorbate is introduced in the measurement cell, the material contracts. The calorimeter signal is positive, therefore the overall process is still exothermic — even though desorption and structural transition, both endothermic processes, are taking place.

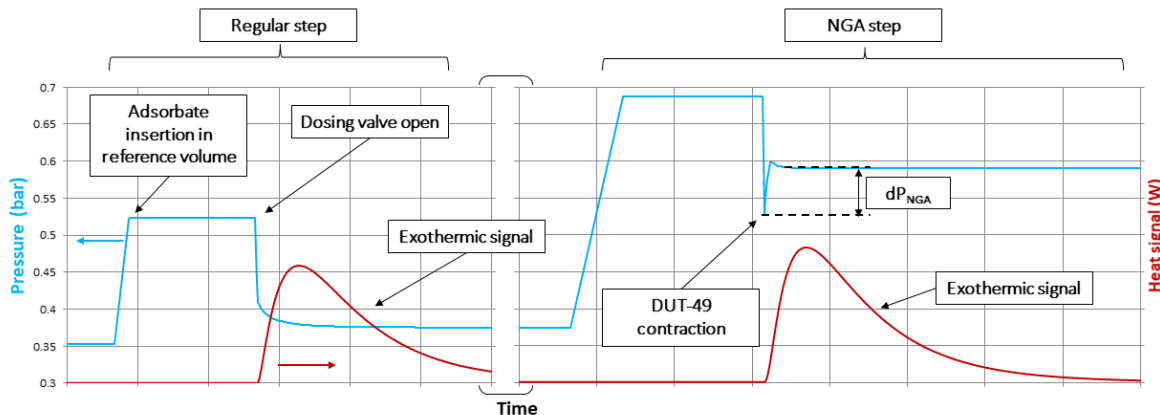
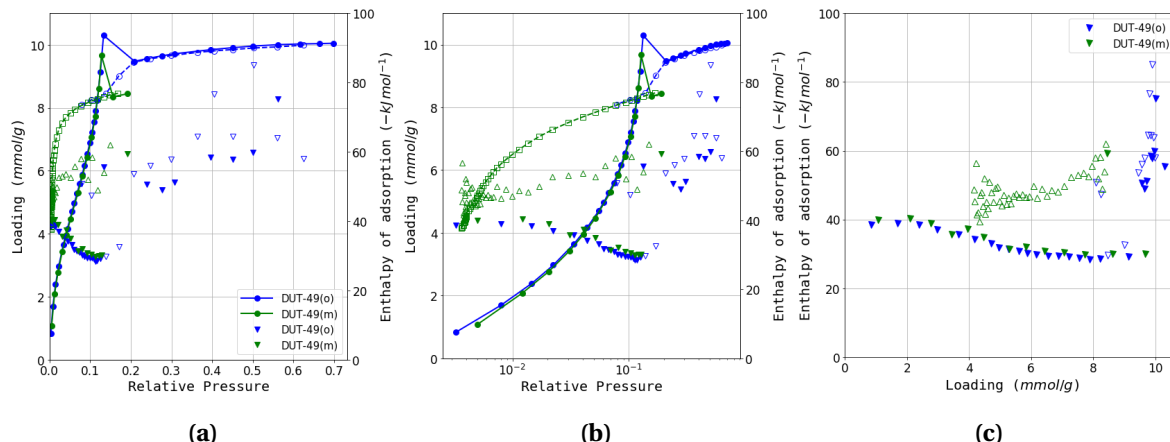


Figure 6.4.: The pressure and calorimeter signal from butane adsorption on DUT-49, highlighting a typical step (left) and the observed NGA step (right)

The signals are then processed to yield the combined isotherm and differential heat of adsorption. Figure 6.5 shows two isotherms recorded on different DUT-49 samples. Several observations

can be made. First, a clear transition takes place around $0.15 p/p_0$. This corresponds to the *op/cp* transition which *decreases* the amount adsorbed per gram of material. After NGA, the material is in its *cp* form, where it remains throughout the remainder of the measurement. Unlike in the methane experiments performed at 111 K, the structure does not re-open. A secondary transition to the *op* form is expected at higher pressures, close to the saturation pressure of the adsorbate. However, this pressure range could not be reached within the experimental conditions.



Need simulated isotherms from Simon

Figure 6.5.: Butane adsorption experiments on two samples of DUT-49, DUT-49(o) and DUT-49(m) shown as (a) regular isotherms (b) logarithmic isotherms and (c) enthalpy as a function of pressure.

Due to the steep knee in the adsorption/desorption branch of the *cp* form, a complete desorption branch cannot be obtained, with the minimum attained loading of 4 mmol. As such, framework collapse is not seen in the experiments. Another shortcoming is that the isotherm and energy landscape of the *op* form in its metastable region is inaccessible, since by definition the material will undergo a transition in this pressure range.

A key feature visible in the two recorded isotherms is that, while adsorption on the open pore form fully overlaps between the two experiments, both the location and extent of NGA differ slightly. In the DUT-49(o) isotherm, a smaller NGA step occurs, with the resulting structural contraction apparently unable to achieve a complete closing of the pores. Upon desorption, a secondary step occurs in the same $0.15 - 0.2 p/p_0$ pressure range, after which the material is fully in its *cp* state, as evidenced by the overlap with the DUT-49(m) isotherm. The reason behind the dissimilar behaviour is the contribution of crystal size to the energy barrier of transition. A thorough analysis can be found in the paper published by Krause et al.⁽⁴⁾ where it is shown that a high surface to volume ratio has a negative impact on NGA, with smaller crystallites unable to achieve a complete contraction, instead accessing an intermediate or *ip*, with the “*a*” lattice parameter 5–7% smaller than the *op* phase rather than 24% in the *cp* phase.

The enthalpy curves in Figure 6.5c, paint a picture of the energetic landscape of both phases. First it should be noted that the differential enthalpy of the NGA step itself does not appear on the

graph as it is a negative value. This is not because the transition step is endothermic, as proven in Figure 6.4. However, as the net change in adsorbed amount between the two points where the transition occurs is negative, the calculated enthalpy *per mol of gas adsorbed* takes the same sign.

In the adsorption branch, the initial enthalpy of adsorption can be observed to be around 38 kJ mol^{-1} to 40 kJ mol^{-1} . This value is relatively low for a copper-based MOF⁽⁶³⁾ and suggest that the interaction of the pore wall with the adsorbate is relatively low. After 2 mmol g^{-1} , the enthalpy curve slopes downwards until a local minima around 30 kJ mol^{-1} before NGA. This is the multilayer adsorption region, where the field gradient of the pore wall decreases and guest-guest interactions dominate. The enthalpy calculated for the desorption curve is essentially the differential enthalpy of adsorption on the *cp* form. A large difference, in the range of 10 kJ mol^{-1} to 20 kJ mol^{-1} , exists between the enthalpy of adsorption in the two states. This can be attributed to the microporous nature of the *cp* form, with the smaller pore walls increasing the interaction of the framework backbone with an adsorbate molecule. The energy required to drive the transition and generate the observed thermal effect can be accounted for by the increased total interactions of remaining adsorbed molecules with the *cp* state of the framework. A more in-depth analysis of the NGA energetics will be presented in subsection 6.4.3.

A brief analysis of measurement uncertainty

In order to assess whether results obtained through calorimetry are within acceptable accuracy, uncertainty calculations have been carried out. The method used here is laid out by the International Organisation for Standardisation (ISO) in the Guide to the expression of Uncertainty in Measurements (GUM). The method is fully detailed in Appendix C, and consists of an identification of all variables used in the calculation of the final result, and estimation of the uncertainty in the final value as a function of the uncertainty in each such variable. The result is multiplied by a factor of confidence, which has been chosen as 95% in the figures presented in Figure 6.6.

The use of the manometric method for isotherm measurement entails a cumulative error in the pressure measurement that leads to an increase in uncertainty with each measured point. It can be seen in Figure 6.6a that in spite of the margin of error, there is perfect overlap between the two measured isotherms in the adsorption branch and in the desorption branch. It is reasonable to assume that the error is therefore much smaller than the calculation would suggest.

The uncertainty in the differential enthalpy of adsorption (Figure 6.6b) is a function of Δn , the amount adsorbed in each step, as well as pressure, with the same cumulative error applicable. The former variable accounts for the large uncertainty in flat sections of the isotherm where almost no adsorption takes place, while the latter results in the spread seen at the end of the desorption curves. However, when observing $\Delta_{ads} h$ as a function of loading in Figure 6.6c, the uncertainty is confined to high values on the x axis, with a clear separation of isotherm branches.

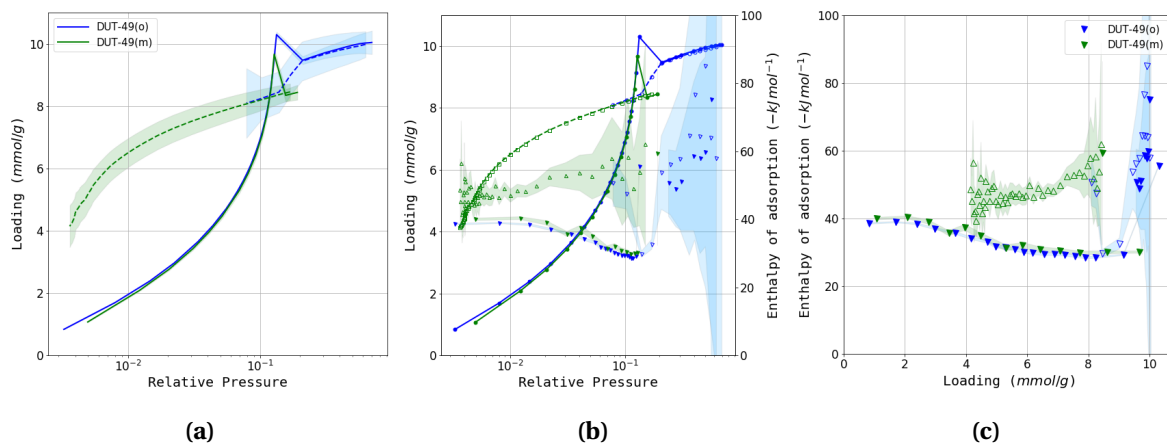


Figure 6.6: Estimated errors at a 95% confidence range for (a) loading as a function of pressure, (b) differential enthalpy as a function of pressure (c) differential enthalpy as a function of loading.

As the display of uncertainty ranges clutter the isotherm graphs and makes it hard to distinguish features, the remainder of this chapter will only display them if the error range is significant.

6.4.2. Impact of framework structure on transition mechanics

While the discovery of the NGA transition in DUT-49 was a result of serendipity, it opens the door to a rational design approach to modify the extent and the location of the phenomenon. In principle, there are several avenues that could be taken in order to tune the contraction mechanics.

- Changing the range of metastability of the open pore state.
- Decreasing the porosity of the closed pore state.
- Increasing the capacity of the open pore form.

These factors are bound to be tightly interlinked, with a slight alteration in one possibly leading a shift in all. For example, the addition of a stabilizing group which would increase the tensile strength of the linker is also likely to decrease the porosity of the entire system.

There are a range of physicochemical modifications available to tune the properties of the framework, many already employed in the MIL-53 and MIL-47 family of flexible MOFs. Through functionalisation or modification of the linker, the strength of the guest-guest and guest-host interactions is affected, as evidenced by the different gate opening behaviour with nitrogen and water on several functionalised versions on MIL-53.⁽⁶⁴⁾ In the case of DUT-49, moieties grafted to the central strut or changes in the linker backbone are also likely to affect its buckling behaviour. While the use of a different metal as the node has succeeded in changing the mechanical response of MIL-53⁽⁶⁵⁾, this approach is likely to have less impact on DUT-49, as the mechanism of contraction is due to linker flexibility. A common rational design methodology is the so-called isoreticular design, where topo-

logically isomorphic MOFs are synthesised through progressive elongation of the linker. Another path to controlling flexibility is manipulation of crystal size, as it has already been shown by Krause et al.⁽⁴⁾. Finally, structural defects, of which a description was given in chapter 4, are another degree of freedom to consider for NGA tunability. Approaches such as mixed linkers synthesis and vacancy defects may allow for fine-grain influence of framework stiffness.

Behaviour of isoreticular materials

The series of materials DUT-48, DUT-46, DUT-49, DUT-50 and DUT-151/DUT-152 was synthesised with the aim of studying the effect of linker elongation on the NGA step. It was found that the tetra-phenyl chain in DUT-151 increased the pore size to the threshold where a secondary net can form in the intracrystal voids, resulting in two identical interpenetrated frameworks. An attempt to introduce a bulky side-functionalisation in DUT-152 resulted in a similarly interpenetrated material. Figure 6.7 shows the butane adsorption dataset recorded on the non-interpenetrated versions.

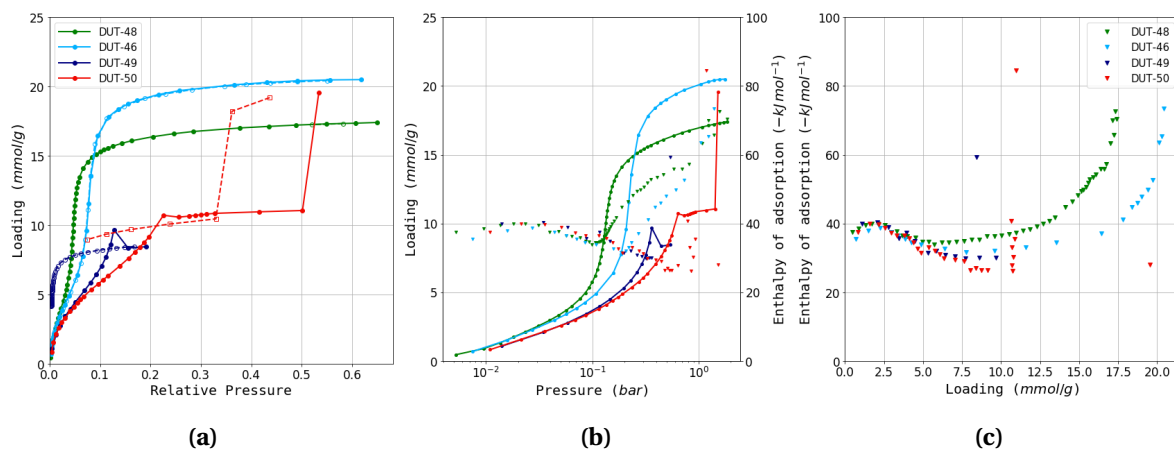


Figure 6.7: (a) Experimental adsorption isotherms for DUT-48, DUT-46, DUT-49 and DUT-50. Enthalpy points are omitted for clarity. (b) A logarithmic plot of isotherms and enthalpy curves, to highlight the low pressure region. (c) Differential enthalpy of adsorption as a function of loading.

Indeed, the results follow a predictable trend. First, it is worth noting that, as seen in Figure 6.7a, only DUT-49 and DUT-50 undergo an *op/cp* transition. This confirms that a shorter linker imparts the resulting MOF with a more stable backbone, raising the strain required in order to collapse the framework. The desorption branch of the non-flexible materials completely overlaps the adsorption branch in both isotherm and enthalpy, further confirming the small error in measurement (available in ??). With an increase of linker size, a larger pore volume and consequently a higher amount of butane can be adsorbed in the open pore form. The increase in pore size is also responsible for a shift in the partial pressure corresponding to the condensation or pore filling step.

In DUT-50, the structure is seen to re-open around $0.5 p/p_0$, although the pressure is not high enough to completely transition to the *op* form. The collapse to the closed phase in the desorption

branch achieves a lower plateau than in the adsorption branch, suggesting an incomplete *op/cp* transition as seen in one of the isotherms on DUT-49 in the previous section.

One surprising finding is that the enthalpy curves (Figure 6.7c) present a near identical behaviour and differential enthalpy of adsorption in the low pressure region, characterized by a slight increase up to 40 kJ mol^{-1} followed by a drop-off. The adsorption mechanism and surface characteristics are therefore *common* to all four materials. The shift of the enthalpies of adsorption to lower values at higher loadings from DUT-46 to 50 is expected, with the increase in pore size leading to a progressive decrease of the contribution of dispersion interactions with the guest, which could also be referred to as a confinement effect. The steep uptake in the isotherm is indicative of a cooperative adsorption mechanism similar to a fluid condensation, accompanied by an increase in the contribution of guest-guest interactions to $\Delta_{ads}\dot{h}$.

As neither DUT-48 and DUT-46 show any phase transition with butane at this temperature, the question arises whether their frameworks can still undergo a structural contraction. A combined simulation and mechanical pressure study was performed on DUT-48 in parallel to the microcalorimetry experiments, which can be found in the paper published in collaboration with the TU Dresden, Chimie ParisTech and ICGM groups.⁽⁶⁶⁾ In brief, DFT optimisations of a single linker molecule under increasing stress show that buckling of the molecule is still possible, albeit at a much higher stress. Constant volume (N, V, T) molecular dynamics simulations of the evolution of the system free energy with decreasing unit cell volume have shown that, while a *cp* phase for DUT-48 exists, the increased tensile strength of the central backbone leads to an increase in both the free energy of this state and the activation energy required to enter it compared to DUT-49. To prove that structural transition can still take place, mercury intrusion experiments are carried out on both DUT-48 and DUT-49. The intrusion/extrusion curves on both materials show that an *op/cp* transition takes place, although with a much higher external pressure in the case of DUT-48 (65 MPa vs. 35 MPa). A similar approach on all other materials in this series reveals a very clear trend in both energy of the *cp* form and pressure required for the transition.

The interpenetrated materials DUT-151 and DUT-152 show a very different isotherm shape and enthalpy curve, as presented in Figure 6.8. In their case, the adsorption behaviour is very complex, with multiple transitions and hysteresis loops visible. However, several trends can still be rationalized. The total pore volume of DUT-152 is lower than that of DUT-151, as the bulkier central strut lowers the available space. Both materials show steeper adsorption curve at low pressures, due to the increased interactions of the adsorbate molecules with the doubled framework net. This is reflected in the differential adsorption enthalpy in the same region, with both DUT-151 and 152 displaying a higher enthalpy (45 kJ mol^{-1} to 50 kJ mol^{-1} as opposed to 40 kJ mol^{-1} for DUT-49). The smaller pore size of DUT-152 also leads to a shift in the adsorption isotherm to lower pressures and an increased enthalpy of adsorption at higher loadings. Finally, a total of three hysteresis loops are visible on DUT-152 associated with apparent transitions, highlighting several accessible intermediate pore states in its structure. These transitions are also found in the enthalpy curve, a result of

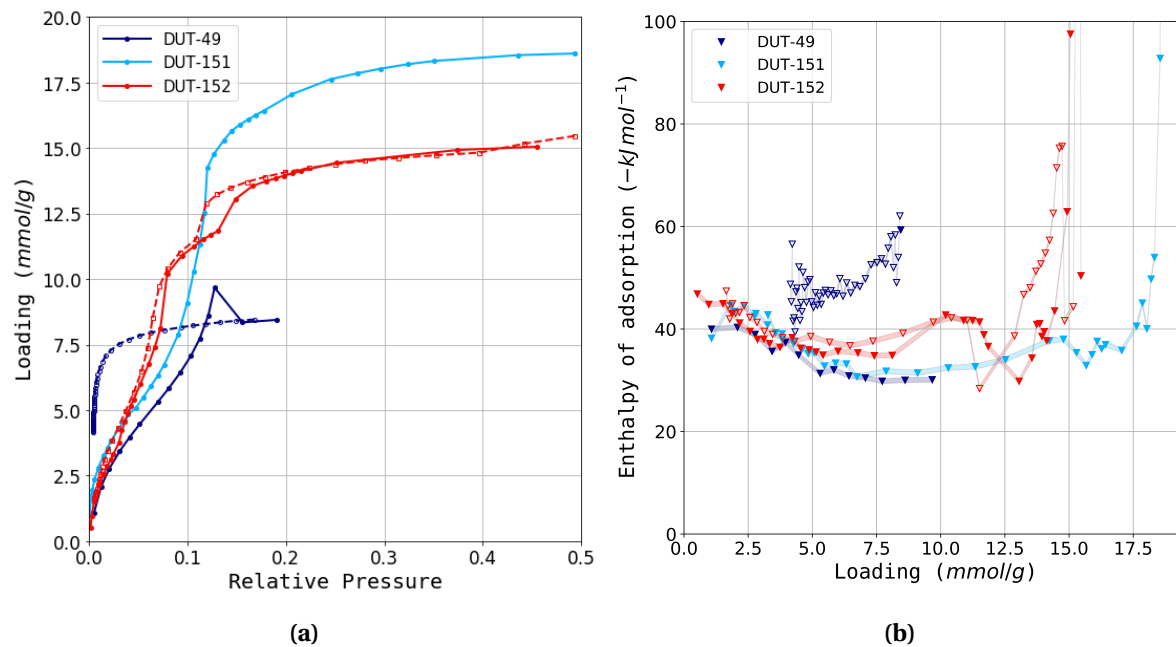


Figure 6.8: The (a) isotherms and (b) enthalpy curves of the interpenetrated materials DUT-151 and DUT-152 as compared to DUT-49. Shaded regions are guides for the eye rather than uncertainty domains.

different energetic contributions of the contraction/expansion. In order to elucidate such a complex interplay of factors more powerful methods such as *in-situ* PXRD are required to monitor the change of structural parameters during adsorption. While interesting, it should be pointed out that all transitions on DUT-151 and 152 seem to be continuous phase changes, with no potential for an NGA-type contraction.

Behaviour of “reinforced” linker analogues

A series of DUT-49 analogues, DUT-149, DUT-148 and DUT-147, with progressively connected central additions was created in order to observe the effect of linker strengthening on the structural transition. DUT-149 has two methyl groups in the ortho position relative to the central bond. DUT-148 has the same carbon number, but connects the two methyl groups with a single bond. Finally DUT-147 has a fully aromatic structure, with delocalised double bonds on each side of the original phenyl ring. The resulting isotherm and enthalpy curve are shown in Figure 6.9.

An unexpected trend emerges from the measured isotherms. DUT-149 does not show an NGA step, with adsorption taking place entirely on the *op* form of the material. In this regard it is an almost perfect non-flexible variant of DUT-49, with near-complete overlap of both its isotherm and enthalpy curves. A minute shift to lower pressure can be seen in the isotherm, as the methyl groups introduce a slight decrease in the large octahedral and medium tetrahedral pore size. Counterintuitively, the next material in the series, DUT-148, undergoes structural contraction in the same

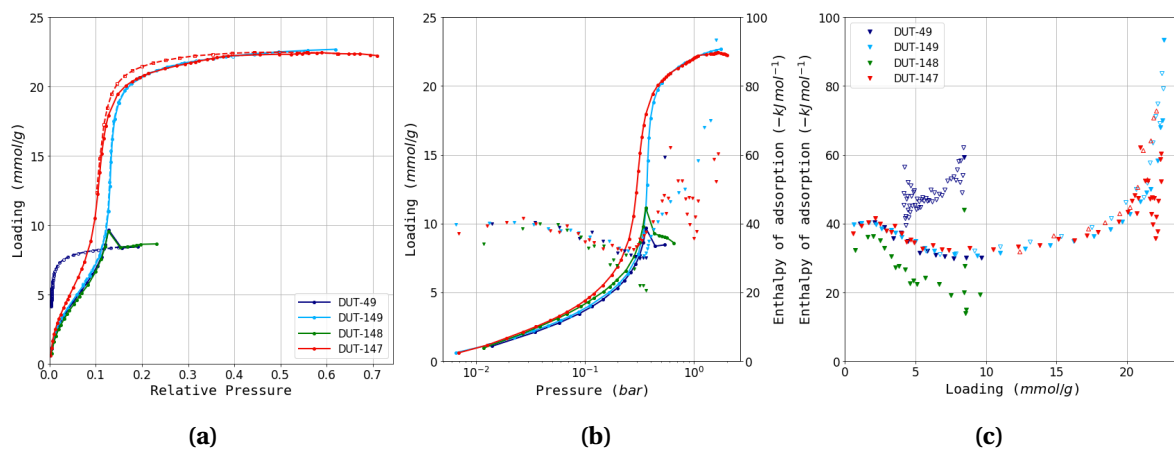


Figure 6.9: (a) Experimental adsorption isotherms for DUT-49, DUT-149, DUT-148 and DUT-147. Enthalpy points are omitted for clarity. (b) A logarithmic plot of isotherms and enthalpy curves, to highlight the low pressure region. (c) Differential enthalpy of adsorption as a function of loading.

manner as DUT-49, retaining the NGA transition despite its increased connectivity. Finally, DUT-147 is stiffer and maintains its *op* state throughout adsorption. A wide hysteresis appears in the desorption branch, which may be an indication of subtle structural effects such as a rotation of the central part of the linker.

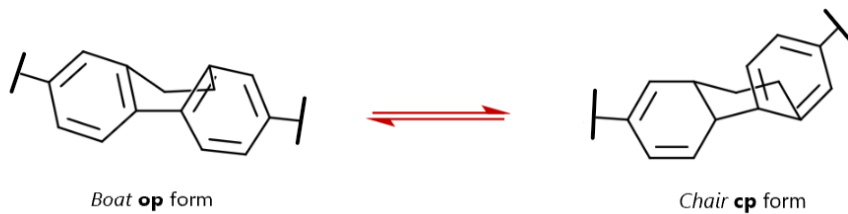


Figure 6.10: A possible mechanism for a conformer stabilised *op/cp* transition for DUT-148.

The different behaviour these analogues may have two possible causes: a change in the stability of the *cp* phase or a difference in the strain necessary to induce ligand buckling. Both parameters are influenced by the introduced functionalisations. In the case of DUT-147 the central phenyl-phenyl bond has been strengthened, resulting in an increased strain required to induce the transition and a structural failure likely taking place in the phenyl-nitrogen bonds rather than the central strut. For DUT-148 and DUT-149 the source of the counterintuitive trend is less clear-cut. In DUT-149, the methyl groups are sterically hindered, which results in the likely adoption of the lowest energy state, with the two phenyl rings at a 180° angle with each other and 90° degree with the terminal ligand planes. This steric hindrance may increase the required strain to enter the elastic buckling regime. Conversely, the single bond in DUT-148 restricts the alkyl chain to a single side of the bond and may actually lower the energetic barrier for the existence of the *cp* form, through the stabilisation afforded by a chair-like 6-ring conformer, a possible variant of which can be seen in Figure 6.10.

DFT optimisations, as those performed on the previous isoreticular linkers are recommended to shed light on the buckling behaviour.

Behaviour of heterocyclic DUT-49 analogues

Using a thiophene-substituted aromatic linker may introduce additional guest-host interactions due to the resulting heterogeneous pore surface. Additionally, the change in geometry allows for new flexibility modes. The butane isotherms measured on these materials are summarized in Figure 6.11.

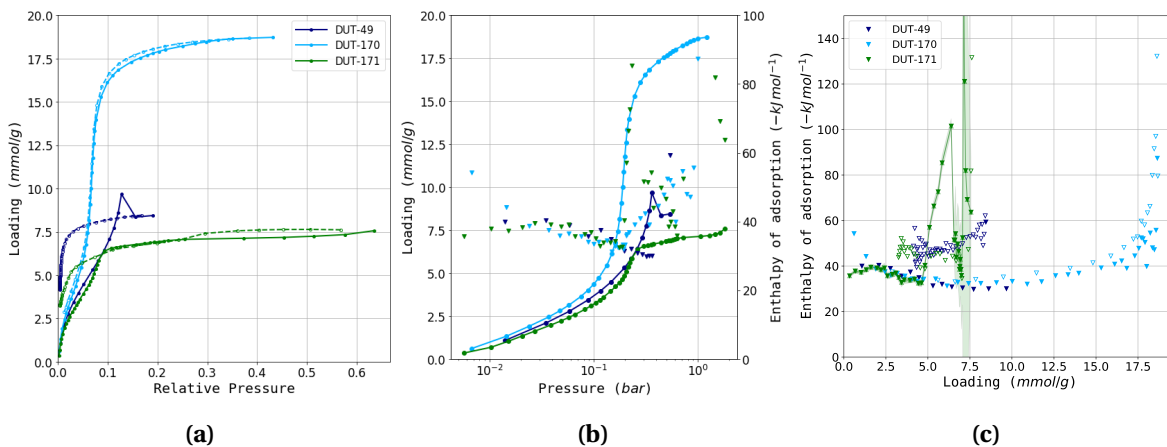


Figure 6.11.: (a) Experimental adsorption isotherms for DUT-49 and heterocyclic analogues DUT-170 and DUT-171. Enthalpy points are omitted for clarity. (b) A logarithmic plot of isotherms and enthalpy curves to highlight the low pressure region. (c) Differential enthalpy of adsorption as a function of loading, highlighting the adsorption branch and error range of DUT-171.

DUT-170, which has a linker with a similar structure and length as the naphtyl-derived DUT-48 is expected to remain non-flexible. This is seen to be the case, with the two isotherms similar in regard to total amount adsorbed and pore filling pressure. The isotherm of DUT-171 does show a structural transition, but without any observed NGA. A slight hysteresis can be seen, likely due to partial structure re-opening before the beginning of the desorption branch. Instead of NGA, the enthalpy curve reveals a significant departure from the baseline as the slope of the isotherm changes slowly in a manner indicative of continuous contraction to a *cp* form. The resulting phase has enthalpies of desorption in the same range as DUT-49*cp*. This type of continuous phase change may suggest a different ligand deformation mechanism, without a sudden buckling and more akin to an elastic bending regime, perhaps due to the starting zig-zag shape of the linker.

Finally, the low pressure region of the enthalpy curve for DUT-170 shows a higher differential enthalpy of adsorption. However, a repeat of the experiment found that instead of a specific interaction of the heterocycle with the guest, this anomaly is due to poor thermal equilibration of the sample cell before the start of data recording in that particular measurement.

Behaviour of elongated central strut materials

The final series of synthesised materials comprise DUT-160, 161 and 162, materials with a triple, double and single bond inserted between the central phenyl rings. In particular the behaviour of DUT-161 could prove interesting, as the linker may exist in either a *trans* or *cis* isomer. Unfortunately, DUT-162 cannot be obtained in a desolvated open pore form, as it immediately collapses upon supercritical activation. Furthermore, the yield of DUT-160 and 161 was so low that not enough material was available for an experiment with DUT-161, and resulted in large errors in the enthalpy curve of DUT-160. The recorded isotherms are presented in Figure 6.12.

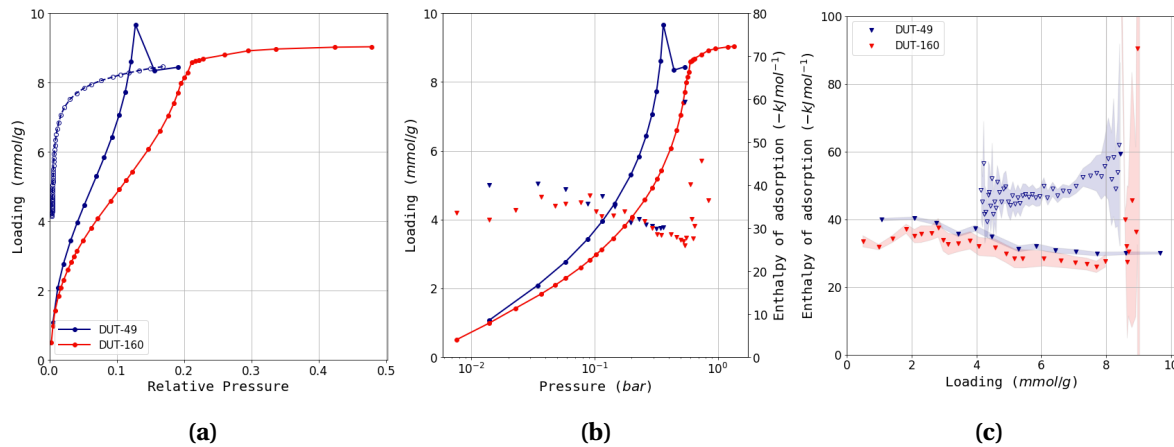


Figure 6.12.: (a) Experimental adsorption isotherms for DUT-49 and DUT-160. Enthalpy points are omitted for clarity. (b) A logarithmic plot of isotherms and enthalpy curves, to highlight the low pressure region. (c) Differential enthalpy of adsorption as a function of loading together with the uncertainty range for each measurement.

From its isotherm slope change in Figure 6.12a, DUT-160 can be seen to undergo a sharp transition at $0.2 p/p_0$, without NGA. The isotherm is very similar to the one measured on DUT-50, whose linker is comparable in length, pointing to a similar buckling behaviour. The lack of NGA is likely due to a lower energetic barrier between the *op* and *cp* state. The enthalpy curve of both DUT-160 and 50 has the same shape, although the differential enthalpy of adsorption on DUT-160 is lower across the entire loading range, a consequence of the larger uncertainty in the measurement.

Overview of NGA tuning through different methods

This extensive study of different DUT-49 derivatives demonstrates the large range of options available for tuning structural transitions in the prototypical NGA material. Both linker shortening and functionalisation lead to increased framework stiffness, in an analogue fashion to increasing the structural integrity of a pillar. This approach might allow for the design of materials which would only undergo an *op/cp* transition with desired adsorbates and temperature ranges, or limit structural collapse to mechanical pressure. The porosity limit at which net interpenetration begins to

occur is found around the length of the DUT-151 linker, or 4 phenyl rings between terminal moieties, a process which does not completely suppress flexibility. More importantly, more fundamental changes to the type of flexibility, such as a continuous “breathing” phase transition, or light-induced switchability might be induced with careful choice of linker, as seen in DUT-171 and suspected in DUT-161, respectively.

6.4.3. An in-depth analysis of the NGA mechanism

As it has been shown in the previous section, there are several avenues to achieve tuning of NGA in the DUT-49 framework. However, a fundamental understanding of the factors and energetics of the process itself may lend itself to prediction of when the phenomenon occurs without experimental input, and even lead to the rational design of similar materials.

To this end, the adsorption of multiple probes was investigated at 77 K with *in situ* continuous low temperature microcalorimetry, in order to observe the influence of the guest on the mechanism of adsorption and NGA. To obtain a baseline of adsorption in the *op* phase, a non-flexible alternative is used. DUT-149 is the most similar material out of all previously studied analogues, as it has the same linker length and nearly identical pore size and surface area.

Four gas probes were used, chosen as they have a non-trivial saturation pressure at this temperature: Ar, N₂, CO and O₂. Argon, as a noble gas, has a completely spherical molecule, which does not have any specific host-guest or guest-guest interactions. Nitrogen is commonly used as the probe in material characterisation, and carries a weak quadrupole. Carbon monoxide has been used as it often forms coordination bonds through electron donation, as well as being a weak dipole and quadrupole. Finally oxygen has a weaker quadrupolar moment than nitrogen, and can interact with the surface in a similar way. It is worth noting that both argon and carbon monoxide are below their freezing point at this temperature. A table with relevant properties of the probes used at the experimental conditions can be found in section G.1.

Results and initial observations

A large dataset was gathered on these materials as experiments were performed with different amounts of sample, different gas introduction flowrates, as well as repeats with identical conditions to ensure that factors such as equilibrium or diffusion do not play a role in the results. No desorption isotherms can be recorded using this method, with leads to an inability to obtain an enthalpy curve corresponding to the *cp* form at low pressure. A list of experiments, as well as all isotherms and enthalpy curves measured can be found in Appendix G.

Selected isotherms and corresponding enthalpy curves for both DUT-49 and DUT-149 are shown in Figure 6.13 for N₂ and CO and in Figure 6.14 for Ar and O₂. A cursory observation of the isotherms reveals that the DUT-149 framework is not as stiff as previously assumed. A clear NGA step can be

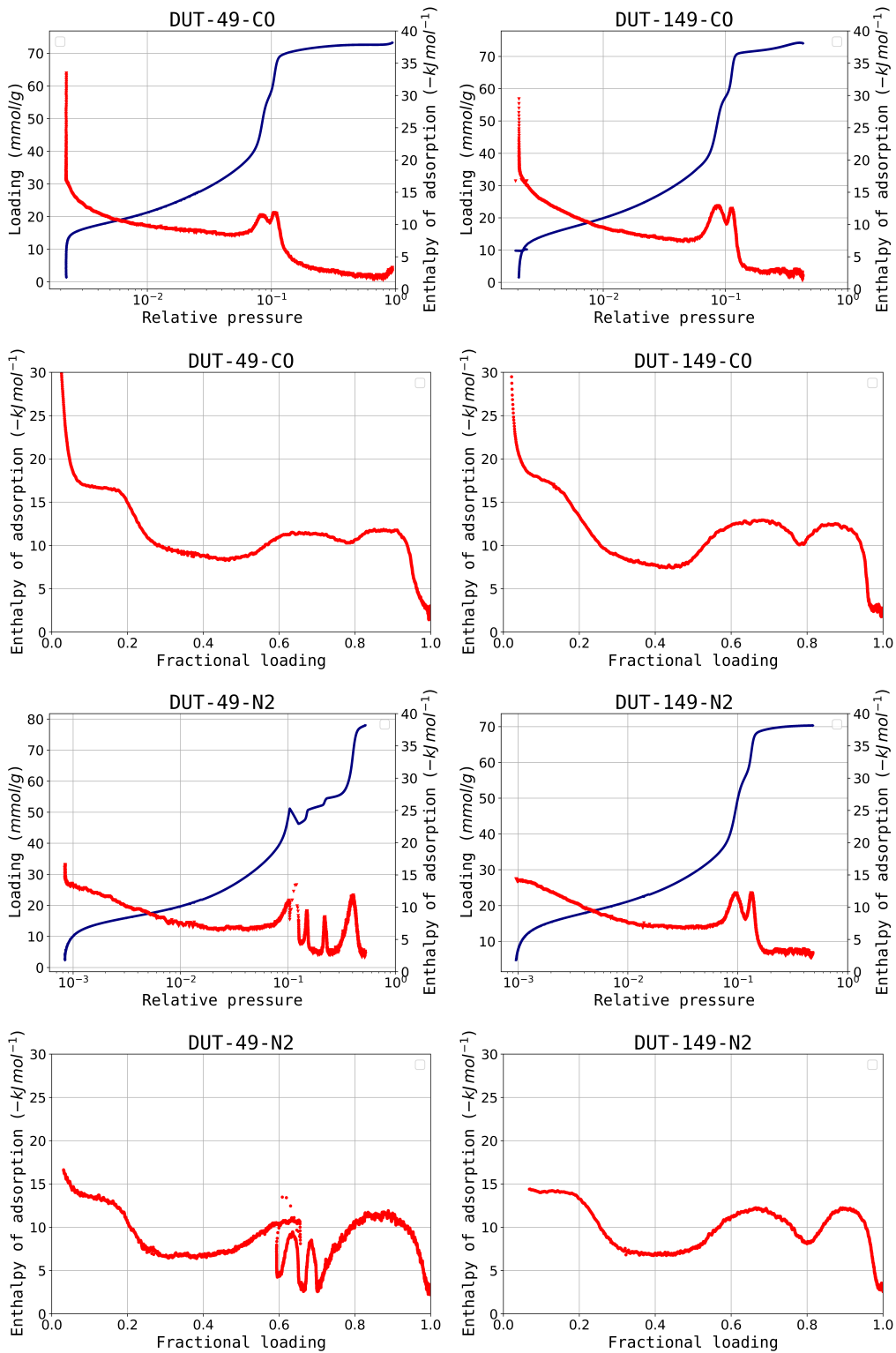


Figure 6.13.: Carbon monoxide (top) and nitrogen (bottom) isotherms and enthalpy curves measured on DUT-49 (left) and DUT-149 (right).

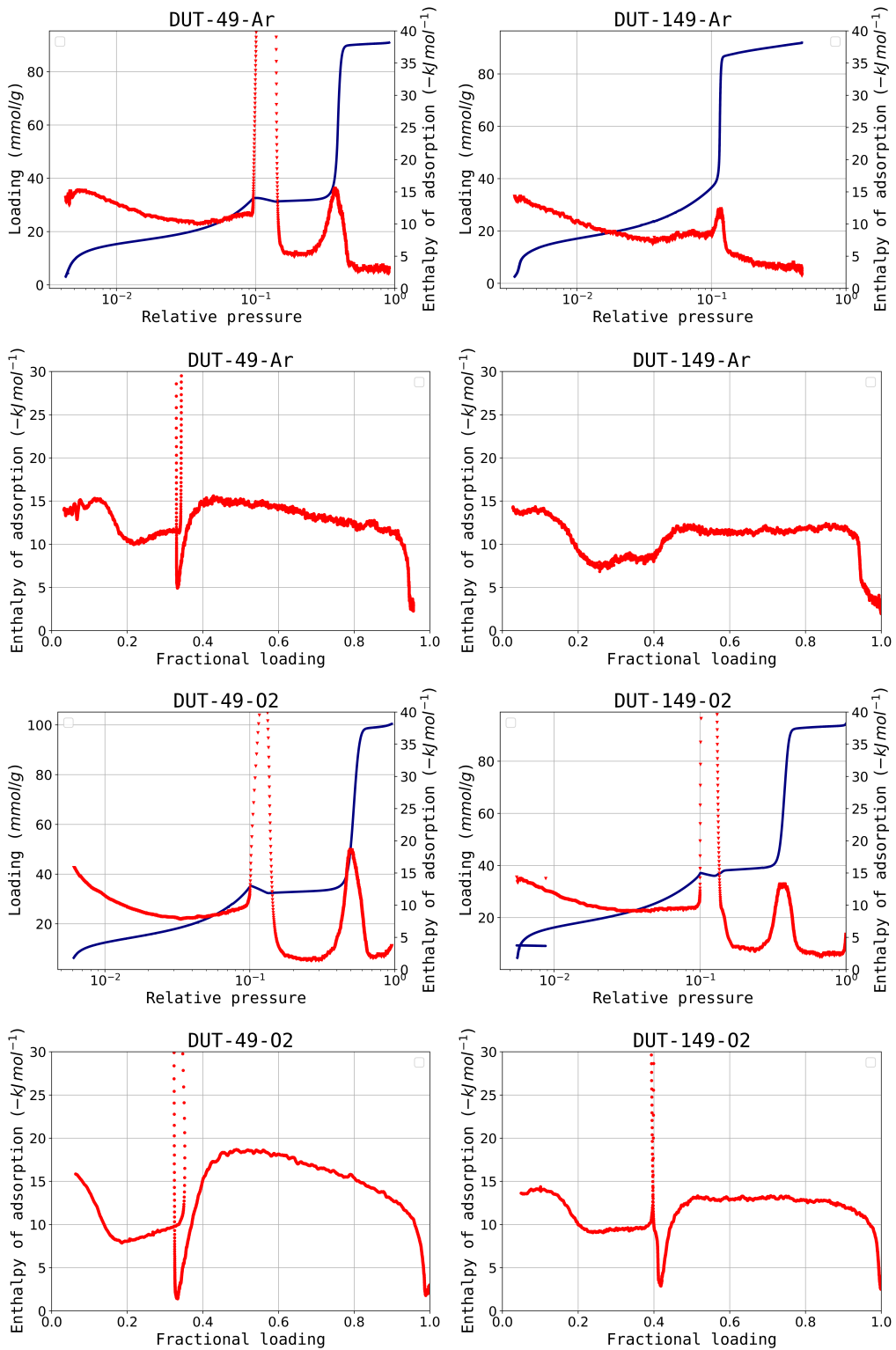


Figure 6.14. Argon (top) and oxygen (bottom) isotherms and enthalpy curves measured on DUT-49 (left) and DUT-149 (right).

found in the oxygen isotherm, suggesting that adsorption of this probe is capable of overcoming the higher energy barrier of linker buckling in this methyl functionalised version. If comparing the isotherms measured on the two materials, they are seen to be nearly identical until structural contraction. The total amount adsorbed after pore re-opening is also in a 2% range with all probes. The assumption that the mechanism of adsorption in DUT-49 can be likened to its functionalised version holds in this case.

Another surprising behaviour can be seen in the nitrogen isotherm on DUT-49. While an NGA discontinuity is still present, structural re-opening takes place in several distinct steps, each accompanied by a sharp peak in the enthalpy curve. This behaviour is in agreement with the study published by Krause et al.⁽⁴⁾ on the evolution of the contraction step with variation of crystallite size. In their paper, the increase of average crystal dimensions is seen to change the material from non-flexible to a progressively better defined NGA transition. *In situ* PXRD shows that between complete structural stiffness and a purely *op/cp* phase transition, several intermediate pore forms can be accessed. It can therefore be theorised that nitrogen adsorption takes place near the lower limit of favourable transition energetics, where particulate surface effects can have a high influence on the stability domain of the open pore form.

Talk
about
CO

Physical state of the adsorbate in the material pores

As two of the four gas probes are below their respective freezing point at experimental conditions, a question arises about the state of the adsorbate in the pores of the material. While a structuring of the fluid similar to a solid phase is possible inside the pores of various adsorbents⁽⁶⁷⁾, it is often that the adsorbed phase is more similar to a liquid, even at low temperatures.

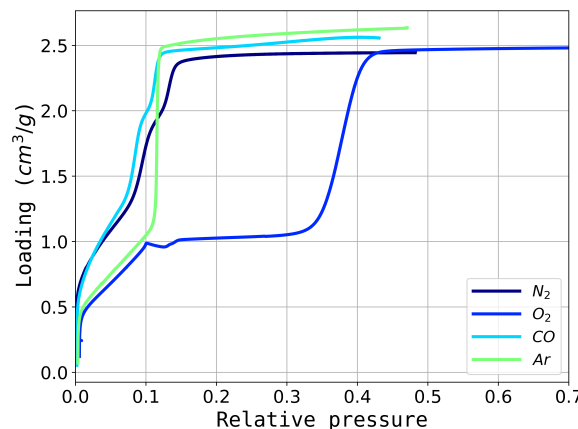


Figure 6.15.: Volumetric adsorption isotherms of all probe gasses on DUT-149. The density of the adsorbate was obtained assuming from the liquid density at the corresponding temperature. It is assumed that the structure re-opening after oxygen adsorption is complete.

A simple method to check whether the phase of all measured probes is close to a liquid state, as-

suming that the accessible void space is identical with all probes, is to convert measured isotherms to a fluid volume basis and compare the total pore volume as determined with each fluid. The density used for this conversion is the liquid density of the saturated liquid as calculated using the REFPROP equation of state at the isotherm temperature. Figure 6.15 plots isotherms measured on DUT-149 transformed using this method. All isotherms reach a plateau at around $2.5 \text{ cm}^3/\text{g}$, confirming that the fluid in the pores can be considered in a liquid state.

Specific guest-host interactions

A common feature to almost all measured isotherms on the DUT-49 systems is the equivalent adsorption mechanism before structural transition takes place. Indeed if enthalpy curves recorded with different adsorbates at different temperatures below the critical point of the fluid are compared at low loading, they may be mistaken for the same datapoints shifted to various enthalpy values. In adsorption in the *op* state, this “typical” enthalpy curve first increases to a local maxima, followed by a gentle downward slope. The pore filling step (or steps) are accompanied by an increase in $\Delta_{ads}\dot{h}$, an indication of high guest-guest interactions. It is in this pore filling step where the structural contraction occurs. This prototypical enthalpy profile of the *op* phase is also seen on most DUT-49 analogues in subsection 6.4.2, suggesting that it is a consequence of the topology of this structure. These features suggest that specific interactions with the framework are generally low. The only exception to this case are adsorbates which can interact with the Cu paddlewheel, either through adduct formation, electron donation or π backbonding interactions.

Such effects are noticeable in the CO adsorption isotherms, as the initial measured differential enthalpy of adsorption is around 40 kJ mol^{-1} , consistent with the formation of Cu(II)…CO adducts as seen in similar paddlewheel based MOF such as HKUST-1.⁽⁶⁸⁾ Indeed, a visual examination of the carbon monoxide saturated DUT-149 at 77 K (Figure 6.16b) shows a pronounced colour shift and suggests a change in the coordination sphere of the copper atoms. As the sample is brought to ambient temperature, the cyan colour disappears, attesting that there is no strong coordination bond, such as is typical in more stable Cu(I)…CO coordination compounds.

A separate study on the possible interaction of π bond containing unsaturated hydrocarbons was performed using ambient temperature calorimetry. Propane and propylene isotherms and enthalpy curves were recorded on the shorter linker, non-flexible DUT-48. Figure 6.16a reveals that there is indeed a larger enthalpy of adsorption at low loadings when propylene is used as the probe gas, with the curves overlapping after the initial region. The difference of around 20 kJ mol^{-1} between the two initial enthalpies of adsorption is consistent to what has been predicted and recorded on the copper center in HKUST-1⁽⁶⁹⁾, and can be explained through the formation of a partial dative bond between the propylene π orbital and the Cu²⁺ cation.

In both the case of CO and C₃H₆, the stronger interactions occur only at fractional loadings lower than 0.1, before the occurrence of NGA. The enthalpy of adsorption after this region take values

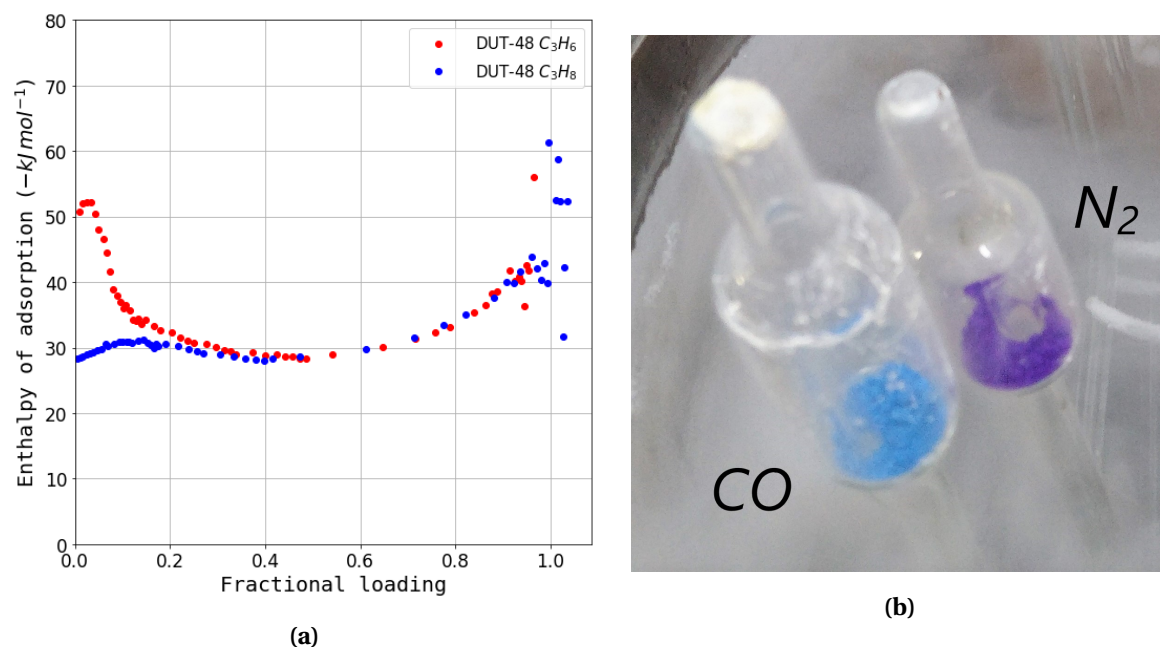


Figure 6.16.: (a) Enthalpy curves of propane and propylene on DUT-48 as a function of fractional loading, with higher enthalpy of adsorption of the unsaturated hydrocarbon at low loading as an indication of π -Cu interactions. (b) Photo of DUT-149 cells filled with CO and N_2 at 77 K. Note the colour change of the CO-filled cell as evidence of the formation of Cu(II)…CO adducts.

which are close to those of similar probes (CO-N_2 , C_3H_6 - C_3H_8). This is further evidence that, while specific guest-host interactions may exist, they play little to no role in the mechanism of contraction.

Pore filling mechanism of the *op* phase

If focusing on the pore filling behaviour of DUT-149, two types of mechanisms can be seen. While the initial part of the isotherm (below $0.1 p/p_0$) is typical of BET-type multilayer adsorption with a possible micropore filling step at very low pressure, the large framework pores are seen to be filled in either a single or two-step process. Both nitrogen and carbon monoxide have two distinct filling steps, corresponding to the octahedral and tetrahedral pores, respectively. The two steps are accompanied by identical peaks in the enthalpy curve. This points to a highly similar filling process for both pores, with cooperative adsorption dominating the pore filling mechanism rather than guest-host effects. The argon isotherm, similar to the behaviour of butane at 303 K, shows a very sharp single-step process, which can be likened to condensation in a mesopore. As the two pores in the DUT-49/149 framework are interconnected through windows of $\approx 1 \text{ nm}$, pore filling in one type of pore can induce filling in the adjacent pore of a larger size. The sudden transition to the fluid phase can further be understood if considering the MOF pores are nearly in the mesoscale range. Adsorption in such pores can be characterised through the formation of a vapour-like spinodal if the pore size is within a “critical hysteresis radius”⁽⁷⁰⁾, a metastable state which subsequently undergoes a

phase change when nucleation occurs. Unfortunately, the presence of a hysteresis curve cannot be confirmed, as no desorption isotherms can be obtained through the continuous method.

For a better understanding of the pore filling mechanism, adsorption in DUT-49 was studied through *in situ* neutron powder diffraction (NPD) during adsorption of deuterated methane CD₄ at 111 K, and complemented through grand canonical monte carlo (GCMC) simulations of the same system. Refinement of the NPD patterns allowed the distribution of the adsorbed CD₄ in a structural unit cell to be obtained, which was further analysed using a radial distribution function to determine how the filling of each pore as a function of pressure occurs. Results show that adsorption first takes place inside the SBU, on the copper open metal sites. Figure 6.17 reveals how the filling of each pore contributes to the overall isotherm. As expected, the SBU pore is completely filled at very low pressures and corresponds to the initial “knee” in the adsorption isotherm. Gradual pore filling then takes place until a condensation step which leads to complete filling of all pores. This step coincides with the structural transition associated with NGA and is likely a driver for the contraction.

Relating adsorption conditions to structural contraction

As continuous adsorption introduction is a time-resolved technique, the signal obtained during the structural contraction step can be examined for clues about the energetics of transition. An example of peaks obtained during the NGA step can be observed in Figure 6.18. It is immediately obvious that the nitrogen transition is actually endothermic, unlike the signal obtained during the argon and oxygen experiments.

As the system contraction is responsible for a pressure increase in the unit cell, transition of any crystallite is likely to be a trigger of a cascade effect, where local increases in guest partial pressure induce collapse of neighbouring particles. As such, deconvolution of the calorimeter peaks during the NGA is a nearly impossible task, since minute factors such as diffusion effects, cell geometry, sample amount or flowrate can drastically change the shape of the evolved signal. However, integrating the heat recorded throughout the NGA step should give an independent value of such substeps as it represents the total heat of the transition. The average values of the observed energetics of NGA presented in Figure 6.18 paints an interesting picture regarding the influence of the adsorbate. The stress induced by the probe gas differs with its physical nature. A good indication of guest-guest interactions at a particular temperature is the enthalpy of vaporisation (ΔH_{vap}) of a saturated liquid. Indeed, the magnitude of the transition energy appears to be related to this value,

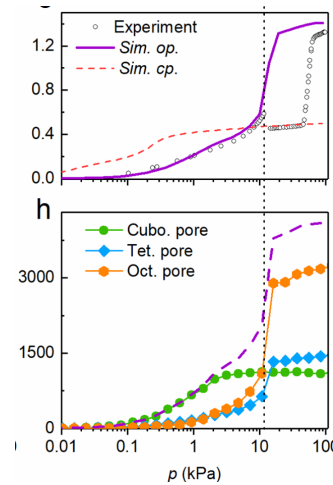


Figure 6.17.: A dissection of the CD₄ isotherm at 111 K in components of adsorption in each type of pore.

need
data
from Si-
mon for
figure...

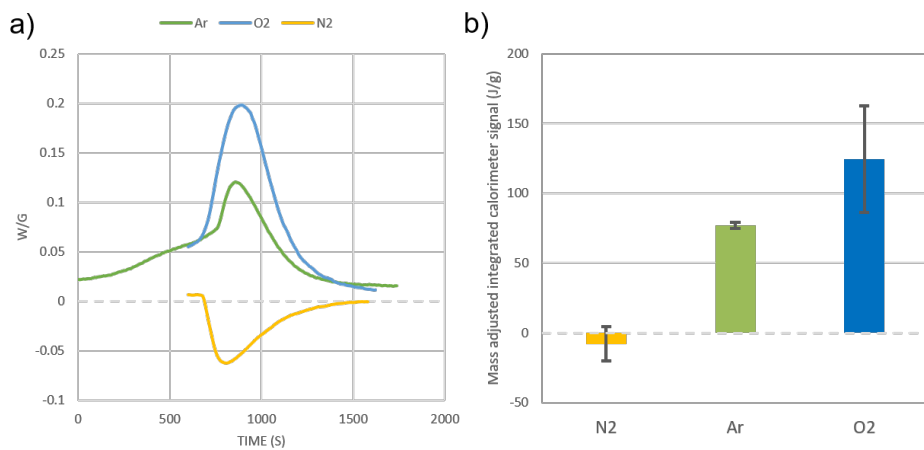


Figure 6.18: (a) An example of three recorded signals during structural contraction on DUT-49 with nitrogen, argon and oxygen. (b) Integrated calorimetric heat signal from nitrogen, argon and oxygen experiments. Error bars represent one standard deviation from the dataset mean.

as oxygen which has the highest ΔH_{vap} out of all probes used also capable of inducing transition in stiffer frameworks. By plotting the enthalpy of vaporisation for different adsorbates and adjusting it by assuming the energetic barrier is purely entropic, a remarkable correlation with the existence windows of NGA extending up to ambient temperature and with different probes can be found, as seen in Figure 6.19. This empiric model can seemingly predict the energetic limit for a favourable transition, and is likely a reflection of the true energetics of the system in the subset of cases where the assumption of pure guest-guest interaction overcoming an entropic barrier holds. However, carbon monoxide is seen to deviate from the predicted behaviour and exhibit no NGA at 77 K. It is likely that the increased interactions with the framework metal sites account for a larger energy barrier.

It is also worth noting that an inverse relationship exists between the exothermicity of the transition step and the amount of fluid ejected from the structure pores during the NGA step, with nitrogen experiments generating the highest Δn_{NGA} even if the transition to a *cp* state is incomplete. As the energy required for the expulsion of the material from the pores can be thought of as the enthalpy of desorption of the same amount from the closed pore, this component should be considered if attempting to calculate the energy difference between the two states. Repeating continuous microcalorimetry experiments at a different temperature, such as in an argon bath at 87 K, would allow for the temperature dependence of the adsorbate influence to be recorded. It is highly likely that NGA would be completely suppressed in the case of nitrogen and perhaps argon on DUT-49.

Effect of cycling on DUT-49 transition

By increasing the partial pressure of any of the low temperature calorimetry probes over $\approx 0.8 p/p_0$, a re-opening of the structure can be observed. If the sample is exposed to vacuum while at 77 K,

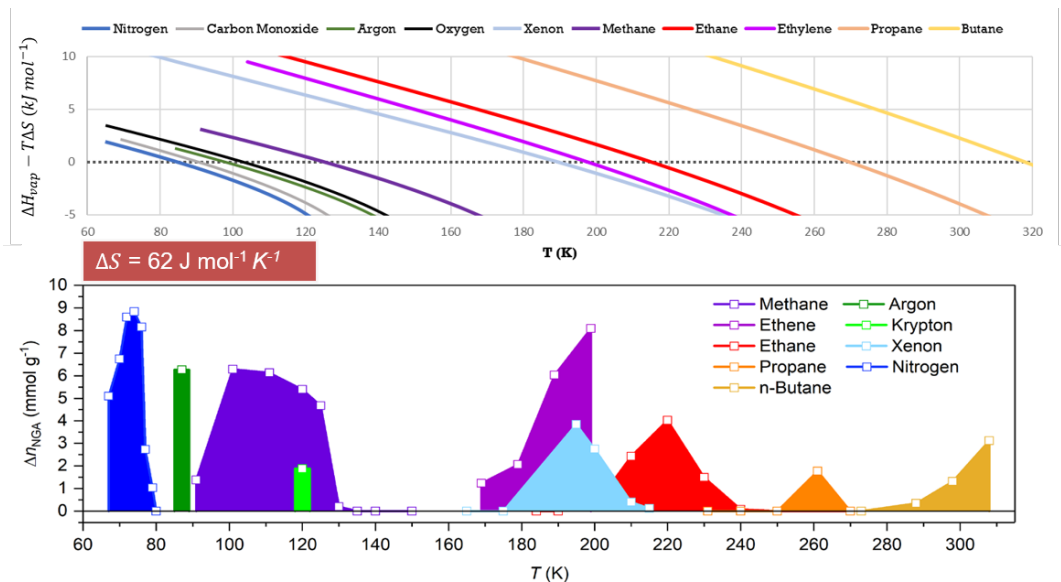


Figure 6.19.: A surface obtained by subtracting an entropic contribution from the enthalpy of vaporisation of several common adsorbates (top) compared to the magnitude and existence region of NGA measured on DUT-49 with various adsorbates.

it collapses to the *cp* phase during desorption and undergoes a structural breakdown due to the instability of this form. However, if the temperature is raised above the adsorbate critical point while maintaining the sample at saturation pressure, the material can be kept in the *op* phase. No NGA has been observed with supercritical adsorbates, which is why the material is normally activated through this method.

Repeating nitrogen adsorption on a DUT-49 sample which has been cycled in this manner reveals a different kind of isotherm, as seen in Figure 6.20. While the initial part of the isotherms is fully overlapped, the second experiment does not have an NGA step. A structural transition still occurs, signalled by the small peak in the enthalpy curve at the end of the peak corresponding to the filling of the medium pore. However, instead of a sudden contraction, the transition becomes a continuous process. The two progressive smaller re-opening steps still exist, at similar partial pressure and with comparable differential enthalpy of adsorption. Further cycling of this cell has shown only isotherms of this kind. This effect is not seen on cycling with other adsorbents, with the NGA transition fully developed in each cycle.

A possible explanation can be found if recalling the effect of crystal size on nitrogen induced NGA.⁽⁴⁾ It is likely that the sample exists as a mixture of different crystallite sizes, some large enough to be capable of an NGA-type transition while smaller ones only contract to an intermediate pore state (or even remain in the *op* state). The cycling may introduce large scale defects such as dislocations or grain boundaries, effectively reducing the average crystal size and increasing the percentage of material which cannot undergo complete contraction. Experimental evidence for the coexistence of both the *cp* and *op* phases after the transition pressure can be found in the ^{129}Xe

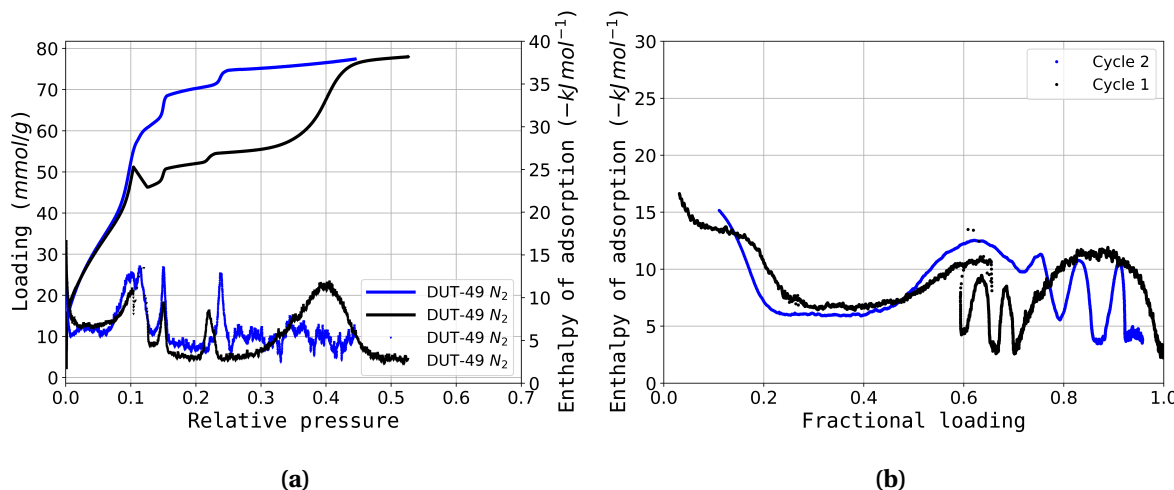


Figure 6.20.: Isotherms (a) and (b) enthalpy curves of nitrogen on cycled DUT-49. The first cycle is in black and the second cycle is in blue.

NMR study performed by Schaber et al.⁽⁶⁰⁾. In their paper, the chemical shift of ¹²⁹Xe is monitored during adsorption at 200 K. The resulting peaks can be attributed to the two phases of the material and a small open pore signal is seen to be present concomitantly with the closed pore form. This kind of behaviour further stresses the contribution of surface potentials on the occurrence of NGA.

Overview of the mechanism of contraction in DUT-49

From a structural perspective, two requirements are highlighted for NGA to occur. First, the free energy surface as a function of loading and unit cell volume must have two local minima, corresponding to the two phases of the framework. An inversion of the overall stability of the two phases must occur as the guest is loaded, which will place the system in a metastable state. While the transition is energetically favoured, the activation barrier between the two forms must be overcome, and the contraction becomes kinetically controlled. The stability of the two phases depends on the combined contribution of the framework together with the stabilisation effect of the adsorbed molecules, which can also be represented as the difference in *integral* enthalpy of adsorption between the *op* and *cp* states. On the other hand, the energy barrier between the two states can be traced to the buckling limit of the linker.

6.5. Conclusion

In this chapter, an extensive study of the unique phase transitions in the flexible framework of DUT-49 and its analogues was performed through combined adsorption and microcalorimetry. The results offer insight into the mechanism of phase transition and the influence of structural modi-

fications on the contraction step, as well as corroborate the ongoing multi-pronged approach to understand this type of transition.

An exploration of several approaches for tuning the NGA step through synthesis is explored using adsorption microcalorimetry has revealed several interesting findings regarding what linker properties can influence the barrier to structural transition and stability of the two phases. These can be generally summarised as follows.

- Stiffening of the central linker can be achieved through linker shortening or side functionalisation, usually accompanied by a reduction in total pore volume. Structural contraction may still take place through adsorption in conditions of strong guest-guest interactions or through mechanical pressure.
- Lengthening of the linker can increase porosity, but is only effective before framework interpenetration occurs, after which complete structural contraction is prevented.
- Different linker hinging systems may change the mechanism of contraction, but a ligand backbone with deformable bonds is essential for phase transition.

Extending the characterisation through microcalorimetry at 77 K with other probes allowed an in-depth exploration of the guest-host and guest-guest interactions in the DUT-49 system. First, it is confirmed that at the experimental conditions, the adsorbates can be assumed to be in a liquid state in the pores. DUT-149 is selected as a non-flexible analogue, which allows for complete adsorption curves on the *op* state of the framework to be recorded, except during oxygen adsorption, when the increased energy barrier induced through linker functionalisation is also overcome. The enthalpy curves of all the probes used are seen to be similar in the low pressure region. Even in adsorbates which interact strongly with the copper atoms in the MOP, such as carbon monoxide and π -bond containing hydrocarbons, the increased interactions with the framework affect only the initial 10% of all adsorbed guests. Together with the location of NGA in the secondary pore filling step, guest-guest interactions are determined to be the dominant contribution to the transition mechanism. The pore filling process itself is likened to a condensation step, which is confirmed through *in situ* powder neutron diffraction results. The probes used reveal the lower limits of the DUT-49 and DUT-149 phase transitions at 77 K with nitrogen and oxygen, respectively. The calorimetric signal during the NGA step is seen to be an indication of the energy required or generated during contraction. The emerging trend of $N_2 < Ar < O_2$ can then be related to the strength of temperature and probe dependence of NGA through the enthalpy of vaporisation of the fluid.

However, many questions and research opportunities still remain about the system as a whole. From an adsorption standpoint, a rigorous theoretical model of the influence of the adsorbed phase on the forces acting on the framework is still lacking at the current time. From a material point of view, the particular molecular properties that can affect the activation barrier between the two phases without decreasing the stability of the closed pore from have only been subject of a cursory examination. Furthermore, the influence of crystal size and surface on the barrier of transition is yet

to be quantified. The use of a copper paddlewheel leads to instability to humidity and it is currently not known if the metal has an influence on transition mechanics. Finally, tantalising applications, unique to such systems can be envisaged, like micromechanical switches or pressure amplifiers.

Beyond the properties of this particular framework, it is shown that the assumption of a static porous solid during adsorption can often diverge significantly from the behaviour of a real system. In particular with soft materials such as MOFs, flexibility may introduce unexpected and counter-intuitive phenomena which can only be elucidated through the use of the use of complementary techniques such as *in situ* microcalorimetry, NMR, electron and neutron diffraction and advanced *in silico* simulations.

Bibliography

- [1] François-Xavier Coudert and Daniela Kohen. Molecular Insight into CO₂ “Trapdoor” Adsorption in Zeolite Na-RHO. *Chemistry of Materials*, 29(7):2724–2730, April 2017. ISSN 0897-4756, 1520-5002. doi: 10.1021/acs.chemmater.6b03837.
- [2] Yun Liu, Jae-Hyuk Her, Anne Dailly, Anibal J. Ramirez-Cuesta, Dan A. Neumann, and Craig M. Brown. Reversible Structural Transition in MIL-53 with Large Temperature Hysteresis. *Journal of the American Chemical Society*, 130(35):11813–11818, September 2008. ISSN 0002-7863, 1520-5126. doi: 10.1021/ja803669w.
- [3] Chen Zhang, Jason A. Gee, David S. Sholl, and Ryan P. Lively. Crystal-Size-Dependent Structural Transitions in Nanoporous Crystals: Adsorption-Induced Transitions in ZIF-8. *The Journal of Physical Chemistry C*, 118(35):20727–20733, September 2014. ISSN 1932-7447, 1932-7455. doi: 10.1021/jp5081466.
- [4] Simon Krause, Volodymyr Bon, Irena Senkovska, Daniel M. Többens, Dirk Wallacher, Renjith S. Pillai, Guillaume Maurin, and Stefan Kaskel. The effect of crystallite size on pressure amplification in switchable porous solids. *Nature Communications*, 9(1), December 2018. ISSN 2041-1723. doi: 10.1038/s41467-018-03979-2.
- [5] Masashi Ito, Hirotomo Nishihara, Kentaro Yamamoto, Hiroyuki Itoi, Hideki Tanaka, Akira Maki, Minoru T. Miyahara, Seung Jae Yang, Chong Rae Park, and Takashi Kyotani. Reversible Pore Size Control of Elastic Microporous Material by Mechanical Force. *Chemistry - A European Journal*, 19(39):13009–13016, September 2013. ISSN 09476539. doi: 10.1002/chem.201301806.
- [6] Nicolas Chanut. *Using External Factors to Improve Gas Adsorption in Nanoporous Materials: Control of Humidity and Mechanical Pressure*. PhD thesis, Aix-Marseille, December 2016.
- [7] Thomas D. Bennett, Anthony K. Cheetham, Alain H. Fuchs, and François-Xavier Coudert. Interplay between defects, disorder and flexibility in metal-organic frameworks. *Nature Chemistry*, 9(1):11–16, December 2016. ISSN 1755-4330. doi: 10.1038/nchem.2691.
- [8] J. W. McBain and John Ferguson. On the Nature of the Influence of Humidity Changes upon the Composition of Building Materials. *The Journal of Physical Chemistry*, 31(4):564–590, January 1927. ISSN 0092-7325, 1541-5740. doi: 10.1021/j150274a010.
- [9] Gennady Y. Gor, Patrick Huber, and Noam Bernstein. Adsorption-induced deformation of nanoporous materials—A review. *Applied Physics Reviews*, 4(1):011303, March 2017. ISSN 1931-9401. doi: 10.1063/1.4975001.
- [10] B. P. Bering, O. K. Krasil’nikova, A. I. Sarakhov, V. V. Serpinskii, and M. M. Dubinin. Alteration of zeolite granule dimensions under krypton adsorption. *Bulletin of the Academy of Sciences of the USSR Division of Chemical Science*, 26(11):2258–2261, November 1977. ISSN 0568-5230, 1573-9171. doi: 10.1007/BF00958705.
- [11] G Reichenauer and G.W Scherer. Extracting the pore size distribution of compliant materials from nitrogen adsorption. *Colloids and Surfaces A: Physicochemical and Engineering Aspects*, 187-188:41–50, August 2001. ISSN 09277757. doi: 10.1016/S0927-7757(01)00619-7.
- [12] Susumu Kitagawa, Ryo Kitaura, and Shin-ichiro Noro. Functional Porous Coordination Polymers. *Angewandte Chemie International Edition*, 43(18):2334–2375, April 2004. ISSN 1433-7851, 1521-3773. doi: 10.1002/anie.200300610.
- [13] A. Schneemann, V. Bon, I. Schwedler, I. Senkovska, S. Kaskel, and R. A. Fischer. Flexible metal-organic frameworks. *Chem. Soc. Rev.*, 43(16):6062–6096, May 2014. ISSN 0306-0012, 1460-4744. doi: 10.1039/C4CS00101J.
- [14] Gérard Férey. Hybrid porous solids: Past, present, future. *Chem. Soc. Rev.*, 37(1):191–214, 2008. ISSN 0306-0012, 1460-4744. doi: 10.1039/B618320B.
- [15] Jian-Rong Li, Julian Sculley, and Hong-Cai Zhou. Metal–Organic Frameworks for Separations. *Chemical Reviews*, 112(2):869–932, February 2012. ISSN 0009-2665. doi: 10.1021/cr200190s.
- [16] Ritesh Haldar, Nivedita Sikdar, and Tapas Kumar Maji. Interpenetration in coordination polymers: Structural diversities toward porous functional materials. *Materials Today*, 18(2):97–116, March 2015. ISSN 13697021. doi: 10.1016/j.mattod.2014.10.038.

- [17] Ivo Stassen, Nicholas Burtch, Alec Talin, Paolo Falcaro, Mark Allendorf, and Rob Ameloot. An updated roadmap for the integration of metal-organic frameworks with electronic devices and chemical sensors. *Chemical Society Reviews*, 46(11):3185–3241, 2017. ISSN 0306-0012. doi: 10.1039/C7CS00122C.
- [18] L. Vanduyfhuys, S. M. J. Rogge, J. Wieme, S. Vandenbrande, G. Maurin, M. Waroquier, and V. Van Speybroeck. Thermodynamic insight into stimuli-responsive behaviour of soft porous crystals. *Nature Communications*, 9(1), December 2018. ISSN 2041-1723. doi: 10.1038/s41467-017-02666-y.
- [19] Christopher R. Murdock, Brianna C. Hughes, Zheng Lu, and David M. Jenkins. Approaches for synthesizing breathing MOFs by exploiting dimensional rigidity. *Coordination Chemistry Reviews*, 258-259:119–136, January 2014. ISSN 00108545. doi: 10.1016/j.ccr.2013.09.006.
- [20] Di Li and Katsumi Kaneko. Hydrogen bond-regulated microporous nature of copper complex-assembled microcrystals. *Chemical Physics Letters*, 335(1-2):50–56, February 2001. ISSN 00092614. doi: 10.1016/S0009-2614(00)01419-6.
- [21] Ryo Kitaura, Kenji Seki, George Akiyama, and Susumu Kitagawa. Porous Coordination-Polymer Crystals with Gated Channels Specific for Supercritical Gases. *Angewandte Chemie International Edition*, 42(4):428–431, January 2003. ISSN 14337851, 15213773. doi: 10.1002/anie.200390130.
- [22] Ryo Kitaura, Kentaro Fujimoto, Shin-ichiro Noro, Mitsuru Kondo, and Susumu Kitagawa. A Pillared-Layer Coordination Polymer Network Displaying Hysteretic Sorption: $[\text{Cu}_2(\text{pzdc})_2(\text{dpyg})]_n$ (pzdc= Pyrazine-2,3-dicarboxylate; dpyg=1,2-Di(4-pyridyl)glycol). *Angewandte Chemie*, 114(1):141–143, January 2002. ISSN 0044-8249, 1521-3757. doi: 10.1002/1521-3757(20020104)114:1<141::AID-ANGE141>3.0.CO;2-D.
- [23] C. J. Kepert, T. J. Prior, and M. J. Rosseinsky. A Versatile Family of Interconvertible Microporous Chiral Molecular Frameworks: The First Example of Ligand Control of Network Chirality. *Journal of the American Chemical Society*, 122(21):5158–5168, May 2000. ISSN 0002-7863, 1520-5126. doi: 10.1021/ja993814s.
- [24] Andrew P. Nelson, Omar K. Farha, Karen L. Mulfort, and Joseph T. Hupp. Supercritical Processing as a Route to High Internal Surface Areas and Permanent Microporosity in Metal-Organic Framework Materials. *Journal of the American Chemical Society*, 131(2):458–460, January 2009. ISSN 0002-7863, 1520-5126. doi: 10.1021/ja808853q.
- [25] D. Fairen-Jimenez, S. A. Moggach, M. T. Wharmby, P. A. Wright, S. Parsons, and T. Düren. Opening the Gate: Framework Flexibility in ZIF-8 Explored by Experiments and Simulations. *Journal of the American Chemical Society*, 133(23):8900–8902, June 2011. ISSN 0002-7863, 1520-5126. doi: 10.1021/ja202154j.
- [26] Sandrine Bourrelly, Philip L. Llewellyn, Christian Serre, Franck Millange, Thierry Loiseau, and Gérard Férey. Different Adsorption Behaviors of Methane and Carbon Dioxide in the Isotypic Nanoporous Metal Terephthalates MIL-53 and MIL-47. *Journal of the American Chemical Society*, 127(39):13519–13521, October 2005. ISSN 0002-7863. doi: 10.1021/ja054668v.
- [27] C. Serre, S. Bourrelly, A. Vimont, N. A. Ramsahye, G. Maurin, P. L. Llewellyn, M. Daturi, Y. Filinchuk, O. Leynaud, P. Barnes, and G. Férey. An Explanation for the Very Large Breathing Effect of a Metal-Organic Framework during CO₂ Adsorption. *Advanced Materials*, 19(17):2246–2251, September 2007. ISSN 09359648, 15214095. doi: 10.1002/adma.200602645.
- [28] Tapas Kumar Maji, Ryotaro Matsuda, and Susumu Kitagawa. A flexible interpenetrating coordination framework with a bimodal porous functionality. *Nature Materials*, 6(2):142–148, February 2007. ISSN 1476-1122, 1476-4660. doi: 10.1038/nmat1827.
- [29] Y. Sakata, S. Furukawa, M. Kondo, K. Hirai, N. Horike, Y. Takashima, H. Uehara, N. Louvain, M. Meilikhov, T. Tsuruoka, S. Isoda, W. Kosaka, O. Sakata, and S. Kitagawa. Shape-Memory Nanopores Induced in Coordination Frameworks by Crystal Downsizing. *Science*, 339(6116):193–196, January 2013. ISSN 0036-8075, 1095-9203. doi: 10.1126/science.1231451.
- [30] Mingyan Ma, Angélique Bétard, Irene Weber, Noura Saad Al-Hokbany, Roland A. Fischer, and Nils Metzler-Nolte. Iron-Based Metal-Organic Frameworks MIL-88B and NH₂-MIL-88B: High Quality Microwave Synthesis and Solvent-Induced Lattice “Breathing”. *Crystal Growth & Design*, 13(6):2286–2291, June 2013. ISSN 1528-7483, 1528-7505. doi: 10.1021/cg301738p.

- [31] Joobeam Seo, Ryotaro Matsuda, Hirotoshi Sakamoto, Charlotte Bonneau, and Susumu Kitagawa. A Pillared-Layer Coordination Polymer with a Rotatable Pillar Acting as a Molecular Gate for Guest Molecules. *Journal of the American Chemical Society*, 131(35):12792–12800, September 2009. ISSN 0002-7863, 1520-5126. doi: 10.1021/ja904363b.
- [32] Thierry Loiseau, Christian Serre, Clarisse Huguenard, Gerhard Fink, Francis Taulelle, Marc Henry, Thierry Bataille, and Gérard Férey. A Rationale for the Large Breathing of the Porous Aluminum Terephthalate (MIL-53) Upon Hydration. *Chemistry - A European Journal*, 10(6):1373–1382, March 2004. ISSN 0947-6539, 1521-3765. doi: 10.1002/chem.200305413.
- [33] Nicole Klein, Herbert C. Hoffmann, Amandine Cadiou, Juergen Getzschmann, Martin R. Lohe, Silvia Paasch, Thomas Heydenreich, Karim Adil, Irena Senkovska, Eike Brunner, and Stefan Kaskel. Structural flexibility and intrinsic dynamics in the M₂(2,6-ndc)₂(dabco) (M = Ni, Cu, Co, Zn) metal-organic frameworks. *Journal of Materials Chemistry*, 22(20):10303, 2012. ISSN 0959-9428, 1364-5501. doi: 10.1039/c2jm15601f.
- [34] Gennady Yu. Gor and Alexander V. Neimark. Adsorption-Induced Deformation of Mesoporous Solids. *Langmuir*, 26(16):13021–13027, August 2010. ISSN 0743-7463, 1520-5827. doi: 10.1021/la1019247.
- [35] J.R. Dacey and M.J.B. Evans. Volume changes in saran charcoal caused by the adsorption of water, methanol and benzene vapours. *Carbon*, 9(5):579–585, October 1971. ISSN 00086223. doi: 10.1016/0008-6223(71)90079-0.
- [36] D. H. Bangham and Nazim Fakhoury. The Expansion of Charcoal accompanying Sorption of Gases and Vapours. *Nature*, 122(3079):681–682, November 1928. ISSN 0028-0836, 1476-4687. doi: 10.1038/122681b0.
- [37] G. Dolino, D. Bellet, and C. Faivre. Adsorption strains in porous silicon. *Physical Review B*, 54(24):17919–17929, December 1996. ISSN 0163-1829, 1095-3795. doi: 10.1103/PhysRevB.54.17919.
- [38] C. H. Amberg and R. McIntosh. A STUDY OF ADSORPTION HYSTERESIS BY MEANS OF LENGTH CHANGES OF A ROD OF POROUS GLASS. *Canadian Journal of Chemistry*, 30(12):1012–1032, December 1952. ISSN 0008-4042, 1480-3291. doi: 10.1139/v52-121.
- [39] Gerrit Günther, Johannes Prass, Oskar Paris, and Martin Schoen. Novel Insights into Nanopore Deformation Caused by Capillary Condensation. *Physical Review Letters*, 101(8), August 2008. ISSN 0031-9007, 1079-7114. doi: 10.1103/PhysRevLett.101.086104.
- [40] G Reichenauer and G.W Scherer. Nitrogen sorption in aerogels. *Journal of Non-Crystalline Solids*, 285(1-3):167–174, June 2001. ISSN 00223093. doi: 10.1016/S0022-3093(01)00449-5.
- [41] Alexander V. Neimark, François-Xavier Coudert, Anne Boutin, and Alain H. Fuchs. Stress-Based Model for the Breathing of Metal-Organic Frameworks. *The Journal of Physical Chemistry Letters*, 1(1):445–449, January 2010. ISSN 1948-7185. doi: 10.1021/jz9003087.
- [42] Anne Boutin, François-Xavier Coudert, Marie-Anne Springuel-Huet, Alexander V. Neimark, Gérard Férey, and Alain H. Fuchs. The Behavior of Flexible MIL-53(Al) upon CH₄ and CO₂ Adsorption. *The Journal of Physical Chemistry C*, 114(50):22237–22244, December 2010. ISSN 1932-7447, 1932-7455. doi: 10.1021/jp108710h.
- [43] François-Xavier Coudert, Marie Jeffroy, Alain H. Fuchs, Anne Boutin, and Caroline Mellot-Draznieks. Thermodynamics of Guest-Induced Structural Transitions in Hybrid Organic-Inorganic Frameworks. *Journal of the American Chemical Society*, 130(43):14294–14302, October 2008. ISSN 0002-7863, 1520-5126. doi: 10.1021/ja805129c.
- [44] J Broekhoff. Studies on pore systems in catalysts IX. Calculation of pore distributions from the adsorption branch of nitrogen sorption isotherms in the case of open cylindrical pores A. Fundamental equations. *Journal of Catalysis*, 9(1):8–14, September 1967. ISSN 00219517. doi: 10.1016/0021-9517(67)90174-1.
- [45] Karena W. Chapman, Dorina F. Sava, Gregory J. Halder, Peter J. Chupas, and Tina M. Nenoff. Trapping Guests within a Nanoporous Metal-Organic Framework through Pressure-Induced Amorphization. *Journal of the American Chemical Society*, 133(46):18583–18585, November 2011. ISSN 0002-7863, 1520-5126. doi: 10.1021/ja2085096.
- [46] Jin Chong Tan and Anthony K. Cheetham. Mechanical properties of hybrid inorganic-organic framework materials: Establishing fundamental structure-property relationships. *Chemical Society Reviews*, 40(2):1059, 2011. ISSN 0306-0012, 1460-4744. doi: 10.1039/c0cs00163e.
- [47] Isabelle Beurroies, Mohammed Boulhout, Philip L. Llewellyn, Bogdan Kuchta, Gérard Férey, Christian Serre, and

- Renaud Denoyel. Using Pressure to Provoke the Structural Transition of Metal–Organic Frameworks. *Angewandte Chemie International Edition*, 49(41):7526–7529, August 2010. ISSN 14337851. doi: 10.1002/anie.201003048.
- [48] Pascal G. Yot, Qintian Ma, Julien Haines, Qingyuan Yang, Aziz Ghoufi, Thomas Devic, Christian Serre, Vladimir Dmitriev, Gérard Férey, Chongli Zhong, and Guillaume Maurin. Large breathing of the MOF MIL-47(VIV) under mechanical pressure: A joint experimental–modelling exploration. *Chemical Science*, 3(4):1100, 2012. ISSN 2041-6520, 2041-6539. doi: 10.1039/c2sc00745b.
- [49] Richelle Lyndon, Kristina Konstas, Bradley P. Ladewig, Peter D. Southon, Prof Cameron J. Kepert, and Matthew R. Hill. Dynamic Photo-Switching in Metal–Organic Frameworks as a Route to Low-Energy Carbon Dioxide Capture and Release. *Angewandte Chemie*, 125(13):3783–3786, March 2013. ISSN 00448249. doi: 10.1002/ange.201206359.
- [50] Colin Dawson, Julian F. V. Vincent, and Anne-Marie Rocca. How pine cones open. *Nature*, 390:668, December 1997.
- [51] Mickael Boudot, Hervé Elettro, and David Gross. Converting Water Adsorption and Capillary Condensation in Usable Forces with Simple Porous Inorganic Thin Films. *ACS Nano*, 10(11):10031–10040, November 2016. ISSN 1936-0851, 1936-086X. doi: 10.1021/acsnano.6b04648.
- [52] Christian Ganser, Gerhard Fritz-Popovski, Roland Morak, Parvin Sharifi, Benedetta Marmiroli, Barbara Sartori, Heinz Amenitsch, Thomas Griesser, Christian Teichert, and Oskar Paris. Cantilever bending based on humidity-actuated mesoporous silica/silicon bilayers. *Beilstein Journal of Nanotechnology*, 7:637–644, April 2016. ISSN 2190-4286. doi: 10.3762/bjnano.7.56.
- [53] Jarad A. Mason, Julia Oktawiec, Mercedes K. Taylor, Matthew R. Hudson, Julien Rodriguez, Jonathan E. Bachman, Miguel I. Gonzalez, Antonio Cervellino, Antonietta Guagliardi, Craig M. Brown, Philip L. Llewellyn, Norberto Masciocchi, and Jeffrey R. Long. Methane storage in flexible metal–organic frameworks with intrinsic thermal management. *Nature*, 527(7578):357–361, October 2015. ISSN 0028-0836, 1476-4687. doi: 10.1038/nature15732.
- [54] Hana Bunzen, Felicitas Kolbe, Andreas Kalytta-Mewes, German Sastre, Eike Brunner, and Dirk Volkmer. Achieving Large Volumetric Gas Storage Capacity in Metal–Organic Frameworks by Kinetic Trapping: A Case Study of Xenon Loading in MFU-4. *Journal of the American Chemical Society*, 140(32):10191–10197, August 2018. ISSN 0002-7863, 1520-5126. doi: 10.1021/jacs.8b04582.
- [55] Manuel Souto, Jorge Romero, Joaquín Calbo, Iñigo J. Vitónica-Yrezábal, José L. Zafra, Juan Casado, Enrique Ortí, Aron Walsh, and Guillermo Mínguez Espallargas. Breathing-Dependent Redox Activity in a Tetrathiafulvalene-Based Metal–Organic Framework. *Journal of the American Chemical Society*, August 2018. ISSN 0002-7863, 1520-5126. doi: 10.1021/jacs.8b05890.
- [56] A. C. McKinlay, J. F. Eubank, S. Wuttke, B. Xiao, P. S. Wheatley, P. Bazin, J.-C. Lavalle, M. Daturi, A. Vimont, G. De Weireld, P. Horcajada, C. Serre, and R. E. Morris. Nitric Oxide Adsorption and Delivery in Flexible MIL-88(Fe) Metal–Organic Frameworks. *Chemistry of Materials*, 25(9):1592–1599, May 2013. ISSN 0897-4756, 1520-5002. doi: 10.1021/cm304037x.
- [57] Patricia Horcajada, Christian Serre, Guillaume Maurin, Naseem A. Ramsahye, Francisco Balas, María Vallet-Regí, Muriel Sebban, Francis Taulelle, and Gérard Férey. Flexible Porous Metal–Organic Frameworks for a Controlled Drug Delivery. *Journal of the American Chemical Society*, 130(21):6774–6780, May 2008. ISSN 0002-7863, 1520-5126. doi: 10.1021/ja710973k.
- [58] Ulrich Stoeck, Simon Krause, Volodymyr Bon, Irena Senkovska, and Stefan Kaskel. A highly porous metal–organic framework, constructed from a cuboctahedral super-molecular building block, with exceptionally high methane uptake. *Chemical Communications*, 48(88):10841, 2012. ISSN 1359-7345. doi: 10.1039/c2cc34840c.
- [59] Simon Krause, Volodymyr Bon, Irena Senkovska, Ulrich Stoeck, Dirk Wallacher, Daniel M. Többens, Stefan Zander, Renjith S. Pillai, Guillaume Maurin, François-Xavier Coudert, and Stefan Kaskel. A pressure-amplifying framework material with negative gas adsorption transitions. *Nature*, 532(7599):348–352, April 2016. ISSN 0028-0836. doi: 10.1038/nature17430.
- [60] Jana Schaber, Simon Krause, Silvia Paasch, Irena Senkovska, Volodymyr Bon, Daniel M. Többens, Dirk Wallacher, Stefan Kaskel, and Eike Brunner. In Situ Monitoring of Unique Switching Transitions in the Pressure-Amplifying

- Flexible Framework Material DUT-49 by High-Pressure ^{129}Xe NMR Spectroscopy. *The Journal of Physical Chemistry C*, 121(9):5195–5200, March 2017. ISSN 1932-7447, 1932-7455. doi: 10.1021/acs.jpcc.7b01204.
- [61] Jack D. Evans, Lydéric Bocquet, and François-Xavier Coudert. Origins of Negative Gas Adsorption. *Chem*, 1 (6):873–886, December 2016. ISSN 24519294. doi: 10.1016/j.chempr.2016.11.004.
- [62] Jean Rouquerol, Stanislas Partyka, and Françoise Rouquerol. Calorimetric evidence for a bidimensional phase change in the monolayer of nitrogen or argon adsorbed on graphite at 77 K. *Journal of the Chemical Society, Faraday Transactions 1: Physical Chemistry in Condensed Phases*, 73:306, 1977. ISSN 0300-9599. doi: 10.1039/f19777300306.
- [63] Marcus Lange, Merten Kobalz, Jens Bergmann, Daniel Lässig, Jörg Lincke, Jens Möllmer, Andreas Möller, Jörg Hofmann, Harald Krautscheid, Reiner Staudt, and Roger Gläser. Structural flexibility of a copper-based metal–organic framework: Sorption of C_4 -hydrocarbons and in situ XRD. *J. Mater. Chem. A*, 2(21):8075–8085, 2014. ISSN 2050-7488, 2050-7496. doi: 10.1039/C3TA15331B.
- [64] Shyam Biswas, Tim Ahnfeldt, and Norbert Stock. New Functionalized Flexible Al-MIL-53-X ($\text{X} = \text{-Cl}, \text{-Br}, \text{-CH}_3, \text{-NO}_2, \text{-}(\text{OH})_2$) Solids: Syntheses, Characterization, Sorption, and Breathing Behavior. *Inorganic Chemistry*, 50(19): 9518–9526, October 2011. ISSN 0020-1669, 1520-510X. doi: 10.1021/ic201219g.
- [65] Pascal G. Yot, Ke Yang, Vincent Guillerm, Florence Ragon, Vladimir Dmitriev, Paraskevas Parisiades, Erik Elkaïm, Thomas Devic, Patricia Horcajada, Christian Serre, Norbert Stock, John P. S. Mowat, Paul A. Wright, Gérard Férey, and Guillaume Maurin. Impact of the Metal Centre and Functionalization on the Mechanical Behaviour of MIL-53 Metal–Organic Frameworks: Impact of the Metal Centre and Functionalization on the Mechanical Behaviour of MIL-53 Metal–Organic Frameworks. *European Journal of Inorganic Chemistry*, 2016(27):4424–4429, September 2016. ISSN 14341948. doi: 10.1002/ejic.201600263.
- [66] Simon Krause, Jack D. Evans, Volodymyr Bon, Irena Senkovska, Sebastian Ehrling, Ulrich Stoeck, Pascal G. Yot, Paul Iacomi, Philip Llewellyn, Guillaume Maurin, François-Xavier Coudert, and Stefan Kaskel. Adsorption Contraction Mechanics: Understanding Breathing Energetics in Isoreticular Metal–Organic Frameworks. *The Journal of Physical Chemistry C*, August 2018. ISSN 1932-7447, 1932-7455. doi: 10.1021/acs.jpcc.8b04549.
- [67] P. L. Llewellyn, J. P. Coulomb, Y. Grillet, J. Patarin, H. Lauter, H. Reichert, and J. Rouquerol. Adsorption by MFI-type zeolites examined by isothermal microcalorimetry and neutron diffraction. 1. Argon, krypton, and methane. *Langmuir*, 9(7):1846–1851, July 1993. ISSN 0743-7463, 1520-5827. doi: 10.1021/la00031a036.
- [68] C. Prestipino, L. Regli, J. G. Vitillo, F. Bonino, A. Damin, C. Lamberti, A. Zecchina, P. L. Solari, K. O. Kongshaug, and S. Bordiga. Local Structure of Framework Cu(II) in HKUST-1 Metallorganic Framework: Spectroscopic Characterization upon Activation and Interaction with Adsorbates. *Chemistry of Materials*, 18(5):1337–1346, March 2006. ISSN 0897-4756, 1520-5002. doi: 10.1021/cm052191g.
- [69] Miroslav Rubeš, Andrew D. Wiersum, Philip L. Llewellyn, Lukáš Grajciar, Ota Bludský, Petr Nachtigall, Miroslav Rubes, Andrew D. Wiersum, Philip L. Llewellyn, Lukáš Grajciar, Ota Bludský, and Petr Nachtigall. Adsorption of propane and propylene on CuBTC metal–organic framework: Combined theoretical and experimental investigation. *Journal of Physical Chemistry C*, 117(21):11159–11167, May 2013. ISSN 19327447. doi: 10.1021/jp401600v.
- [70] Tatsumasa Hiratsuka, Hideki Tanaka, and Minoru T. Miyahara. Critical energy barrier for capillary condensation in mesopores: Hysteresis and reversibility. *The Journal of Chemical Physics*, 144(16):164705, April 2016. ISSN 0021-9606, 1089-7690. doi: 10.1063/1.4947243.

7. Conclusions

A. Common characterisation techniques

A.1. Thermogravimetry

Thermogravimetry (TGA) is a standard laboratory technique where the weight of a sample is monitored while ambient temperature is controlled. Changes in sample mass can be correlated to physical events, such as adsorption, desorption, sample decomposition or oxidation, depending on temperature and its rate of change.

TGA experiments are carried out on approximately 15 mg of sample with a TA Instruments Q500 up to 800 °C. The sample is placed on a platinum crucible and sealed in a temperature controlled oven, under a total gas flow of $100 \text{ cm}^3 \text{ min}^{-1}$. Experiments can use a blanket of either air or argon. The temperature ramp can be specified directly and should be chosen to ensure that the sample is in equilibrium with the oven temperature and no thermal conductivity effects come into play. Alternatively, a dynamic “Hi-Res” mode can be used which allows for automatic cessation of heating rate while the sample undergoes mass loss.

The main purpose of thermogravimetry as used in this thesis is the determination of sample decomposition temperature, to ensure that thermal activation prior to adsorption is complete and that all guest molecules have been removed without loss of structure. To this end, experiments are performed under an inert atmosphere (argon), and the sample activation temperature is chosen as 50 °C to 100 °C lower than the sample decomposition temperature.

A.2. Bulk density determination

Bulk density is a useful metric for the industrial use of adsorbent materials, as their volume plays a critical role in equipment sizing.

Bulk density is determined by weighing 1.5 ml empty glass vessels and settling the MOFs inside. Powder materials are then added in small increments and settled through vibration between each addition. The full vessel is finally weighed, which allowed the bulk density to be determined. The same cell is used in all experiments, with cleaning through sonication between each experiment.

A.3. Skeletal density determination

True density or skeletal density is determined through gas pycnometry in a MicrotracBEL BELSORP-max apparatus. Helium is chosen as the fluid of choice as it is assumed to be non-adsorbing.

The volume of a glass sample cell (V_c) is precisely measured through dosing of the reference volume with helium up to (p_1), then opening the valve connecting the two and allowing the gas to expand up to (p_2). Afterwards approximately 50 mg of sample are weighed and inserted in a glass sample cell. After sample activation using the supplied electric heater to ensure no solvent residue is left in the pores, the same procedure is repeated to determine the volume of the cell and the adsorbent. With the volume of the sample determined, the density can be calculated by:

$$V_s = V_c + \frac{V_r}{1 - \frac{p_1}{p_2}} \quad (\text{A.1})$$

A.4. Nitrogen physisorption at 77 K

Nitrogen adsorption experiments are carried out on a Micromeritics Triflex apparatus. Approximately 60 mg of sample are used for each measurement. Empty glass cells are weighed and filled with the samples, which are then activated in a Micromeritics Smart VacPrep up to their respective activation temperature under vacuum and then back-filled with an inert atmosphere. After sample activation, the cells are re-weighed to determine the precise sample mass. The cells are covered with a porous mantle which allows for a constant temperature gradient during measurement by wicking liquid nitrogen around the cell. Finally, the cells are immersed in a liquid nitrogen bath and the adsorption isotherm is recorded using the volumetric method. A separate cell is used to condense the adsorptive throughout the measurement for accurate determination of its saturation pressure.

A.5. Vapour physisorption at 298 K

Vapour adsorption isotherms throughout this work are measured using a MicrotracBEL BELSORP-max apparatus in vapour mode. Glass cells are first weighed and then filled with about 50 mg of sample. The vials are then heated under vacuum up to the activation temperature of the material and re-weighed in order to measure the exact sample mass without adsorbed guests. The cells are then immersed in a mineral oil bath kept at 298 K. To ensure that the cold point of the system occurs in the material and to prevent condensation on cell walls, the reference volume, dead space and vapour source are temperature controlled through an insulated enclosure.

A.6. Gravimetric isotherms

The gravimetric isotherms in this thesis are obtained using a commercial Rubotherm GmbH balance. Approximately 1 g of dried sample is used for these experiments. Samples are activated in situ by heating under vacuum. The gas is introduced using a step-by-step method, and equilibrium is assumed to have been reached when the variation of weight remained below 30 µg over a 15 min interval. The volume of the sample is determined from a blank experiment with helium as the non-adsorbing gas and used in combination with the gas density measured by the Rubotherm balance to compensate for buoyancy.

A.7. High throughput isotherm measurement

A high-throughput gas adsorption apparatus is presented for the evaluation of adsorbents of interest in gas storage and separation applications. This instrument is capable of measuring complete adsorption isotherms up to 50 bar on six samples in parallel using as little as 60 mg of material. Multiple adsorption cycles can be carried out and four gases can be used sequentially, giving as many as 24 adsorption isotherms in 24 h.⁽¹⁾

A.8. Powder X-ray diffraction

A.9. Nuclear magnetic resonance

A.10. Adsorption manometry and calorimetry at 303 K

Bibliography

- [1] Andrew D. Wiersum, Christophe Giovannangeli, Dominique Vincent, Emily Bloch, Helge Reinsch, Norbert Stock, Ji Sun Lee, Jong-San Chang, and Philip L. Llewellyn. Experimental Screening of Porous Materials for High Pressure Gas Adsorption and Evaluation in Gas Separations: Application to MOFs (MIL-100 and CAU-10). *ACS Combinatorial Science*, 15(2):111–119, February 2013. ISSN 2156-8952. doi: 10.1021/co300128w.

B. Synthesis method of referenced materials

B.1. Takeda 5A reference carbon

The Takeda 5A carbon was purchased directly from the Takeda corporation. It is a highly microporous material shaped as spheres with an average diameter of 1 mm. The sample was activated at 250 °C under secondary vacuum (5 mbar) before any measurements.

B.2. MCM-41 mesoporous silica

MCM-41 (Mobil Composition of Matter No. 41) is a mesoporous silica (SiO_2) material with a narrow pore distribution. First synthesised by the Mobil Oil Corporation, it is produced through templated synthesis using micelle-forming surfactants. The material referenced in this thesis was purchased from Sigma-Aldrich. The activation procedure consists of heating at 250 °C under secondary vacuum (5 mbar).

B.3. Zr fumarate MOF

The synthesis of the Zr fumarate was performed in Peter Behren's group in Hannover, through modulated synthesis. This MOF can only be synthesised through the addition of a modulator, in this case fumaric acid, to the ongoing reactor, as detailed in the original publication.⁽¹⁾

The procedure goes as follows: ZrCl_4 (0.517 mmol, 1 eq) and fumaric acid (1.550 mmol, 3 eq) are dissolved in 20 mL N,N-dimethylformamide (DMF) and placed in a 100 mL glass flask at room temperature. 20 equivalents of formic acid were added. The glass flasks were Teflon-capped and heated in an oven at 120 °C for 24 h. After cooling, the white precipitate was washed with 10 mL DMF and 10 mL ethanol, respectively. The washing process was carried out by centrifugation and redispersion of the white powder, which was then dried at room temperature over night

B.4. UiO-66(Zr) for defect study

The UiO-66(Zr) sample preparation was adapted from Shearer et al.⁽²⁾ as follows: ZrCl₄ (1.55 g, 6.65 mmol), an excess of terephthalic acid (BDC) (1.68 g, 10.11 mmol), HCl 37 % solution (0.2 mL, 3.25 mmol) and N,N'-dimethylformamide (DMF) (200 mL, 2.58 mol) were added to a 250 mL pressure resistant Schott bottle. The mixture was stirred for 10 min, followed by incubation in a convection oven at 130 °C for 24 h. The resulting white precipitate was washed with fresh DMF (3 × 50 mL) followed by ethanol (3 × 50 mL) over the course of 48 h and dried at 60 °C. After drying, the sample was activated on a vacuum oven by heating at 200 °C under vacuum for 12 h. The yield was 78 % white microcrystalline powder. Before the experiment, the sample was calcined at 200 °C under vacuum (5 mbar) to remove any residual solvents from the framework.

B.5. UiO-66(Zr) for shaping study

The scaled-up synthesis of UiO-66(Zr) was carried out in a 5 L glass reactor (Reactor Master, Syrris, equipped with a reflux condenser and a Teflon-lined mechanical stirrer) according to a previously reported method.⁽³⁾ In short, 462 g (2.8 mol) of H₂BDC (98%) was initially dissolved in 2.5 L of dimethyl formamide (DMF, 2.36 kg, 32.3 mol) at room temperature. Then, 896 g (2.8 mol) of ZrOCl₂ · 8H₂O (98%) and 465 mL of 37% HCl (548 g, 15 mol) were added to the mixture. The molar ratio of the final ZrOCl₂ · 8H₂O/H₂BDC/DMF/HCl mixture was 1 : 1 : 11.6 : 5.4. The reaction mixture was vigorously stirred to obtain a homogeneous gel. The mixture was then heated to 423 K at a rate of 1 Kmin⁻¹ and maintained at this temperature for 6 h in the reactor without stirring, leading to a crystalline UiO-66(Zr) solid. The resulting product (510 g) was recovered from the slurry by filtration, redispersed in 7 L of DMF at 333 K for 6 h under stirring, and recovered by filtration. The same procedure was repeated twice, using methanol (MeOH) instead of DMF. The solid product was finally dried at 373 K overnight.

B.6. MIL-100(Fe) for shaping study

The synthesis of the MOF for the shaping study was done at the KRICT institute using a previously published method.⁽⁴⁾ To synthesise the MIL-100(Fe) material Fe(NO₃)₃ was completely dissolved in water. Then, trimesic acid (BTC) was added to the solution; the resulting mixture was stirred at room temperature for 1h. The final composition was Fe(NO₃)₃ · 9H₂O:0.67 BTC:*n*H₂O (*x*= 55–280). The reactant mixture was heated at 433 K for 12 h using a Teflon-lined pressure vessel. The synthesized solid was filtered and washed with deionized (DI) water. Further washing was carried out with DI water and ethanol at 343 K for 3 h and purified with a 38 mM NH₄F solution at 343 K for 3 h. The solid was finally dried overnight at less than 373 K in air.

B.7. MIL-127(Fe) for shaping study

MIL-127(Fe) was synthesized by reaction of $\text{Fe}(\text{ClO}_4)_3 \cdot 6\text{H}_2\text{O}$ (3.27 g, 9.2 mmol) and $\text{C}_{16}\text{N}_2\text{O}_8\text{H}_6$ (3.3 g) in DMF (415 mL) and hydrofluoric acid (5 M, 2.7 mL) at 423 K in a Teflon flask. The obtained orange crystals were placed in DMF (100 mL) and stirred at ambient temperature for 5 h. The final product was kept at 375 K overnight. MIL-127(Fe) was synthesized by reaction of $\text{Fe}(\text{ClO}_4)_3 \cdot 6\text{H}_2\text{O}$ (3.27 g, 9.2 mmol) and $\text{C}_{16}\text{N}_2\text{O}_8\text{H}_6$ (3.3 g) in DMF (415 mL) and hydrofluoric acid (5 M, 2.7 mL) at 423 K in a Teflon flask. The obtained orange crystals were placed in DMF (100 mL) and stirred at ambient temperature for 5 h. The final product was kept at 375 K overnight.

Bibliography

- [1] Gesa Wißmann, Andreas Schaate, Sebastian Lilienthal, Imke Bremer, Andreas M. Schneider, and Peter Behrens. Modulated synthesis of Zr-fumarate MOF. *Microporous and Mesoporous Materials*, 152:64–70, April 2012. ISSN 13871811. doi: 10.1016/j.micromeso.2011.12.010.
- [2] Greig C. Shearer, Sachin Chavan, Jayashree Ethiraj, Jenny G. Vitillo, Stian Svelle, Unni Olsbye, Carlo Lamberti, Silvia Bordiga, and Karl Petter Lillerud. Tuned to Perfection: Ironing Out the Defects in Metal–Organic Framework UiO-66. *Chemistry of Materials*, 26(14):4068–4071, July 2014. ISSN 0897-4756, 1520-5002. doi: 10.1021/cm501859p.
- [3] Florence Ragon, Patricia Horcajada, Hubert Chevreau, Young Kyu Hwang, U-Hwang Lee, Stuart R. Miller, Thomas Devic, Jong-San Chang, and Christian Serre. In Situ Energy-Dispersive X-ray Diffraction for the Synthesis Optimization and Scale-up of the Porous Zirconium Terephthalate UiO-66. *Inorganic Chemistry*, 53(5):2491–2500, March 2014. ISSN 0020-1669, 1520-510X. doi: 10.1021/ic402514n.
- [4] Felix Jeremias, Stefan K. Henninger, and Christoph Janiak. Ambient pressure synthesis of MIL-100(Fe) MOF from homogeneous solution using a redox pathway. *Dalton Transactions*, 45(20):8637–8644, 2016. ISSN 1477-9226, 1477-9234. doi: 10.1039/C6DT01179A.

C. Calculation of uncertainty in adsorption measurements

To obtain the experimental errors, the procedure described in the Guide to the Expression of Uncertainty in Measurement.⁽¹⁾ was used. The quantity, enthalpy or pressure, is first was expressed as a function $f(y)$ of other physical measured quantities through a functional relationship (Equation C.1).

$$f(y) = f(N_1, N_2 \cdots N_i) \quad (\text{C.1})$$

The standard uncertainty $u_c(y)$ is then calculated on the basis of Equation C.2, where $u_i(x_i)$ is the standard uncertainty in each input quantity.

$$u_c(y) = \sqrt{\sum_{i=1}^N \left(\frac{\partial f(y)}{\partial x_i} u_i x_i \right)^2} \quad (\text{C.2})$$

Here it is assumed that the input quantities are independent and uncorrelated. The error margins a_i for each quantity were taken from manufacturer specifications of the equipment used for recording. They were then divided by a value k_i chosen to cover the expected variance in that quantity, as each variable is assumed to be characterized by a probability distribution. The error introduced by the equation of state used (NIST REFPROP⁽²⁾) were assumed to be minor compared to the error introduced by the physical quantities, with the same to be said regarding the error in the calorimetric heat signal, which represents less than 1% of the error in enthalpy. Finally, the expanded uncertainty was calculated by choosing a suitable coverage factor of 1.645, corresponding to a 95% confidence interval.

Bibliography

- [1] Evaluation of measurement data — Guide to the expression of uncertainty in measurement. Technical Report 100:2008, JCGM, 2008.
- [2] Eric Lemmon. NIST Reference Fluid Thermodynamic and Transport Properties Database: Version 9.0, NIST Standard Reference Database 23, 1989.

D. Appendix for chapter 3

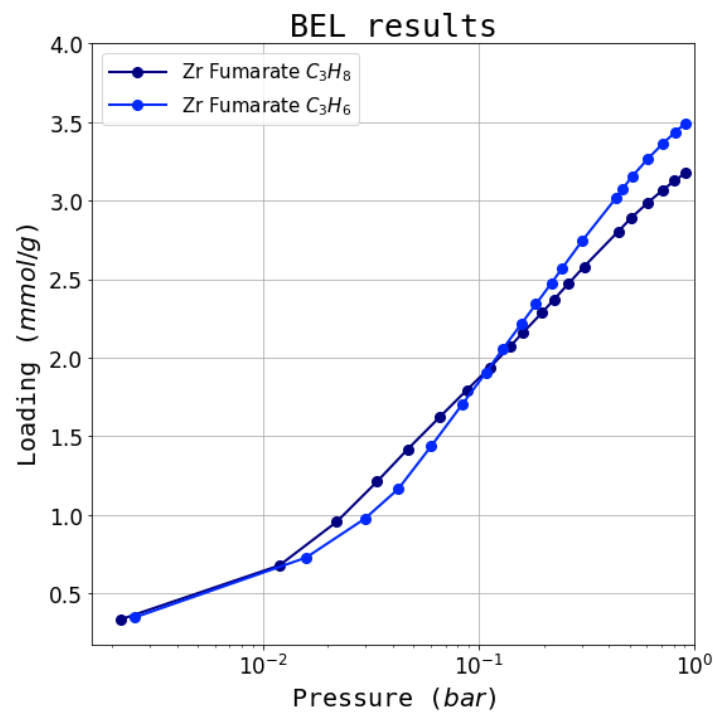


Figure D.1.: Propane and propylene isotherms recorded on Zr Fumarate in a commercial volumetric apparatus (BEL Mini).

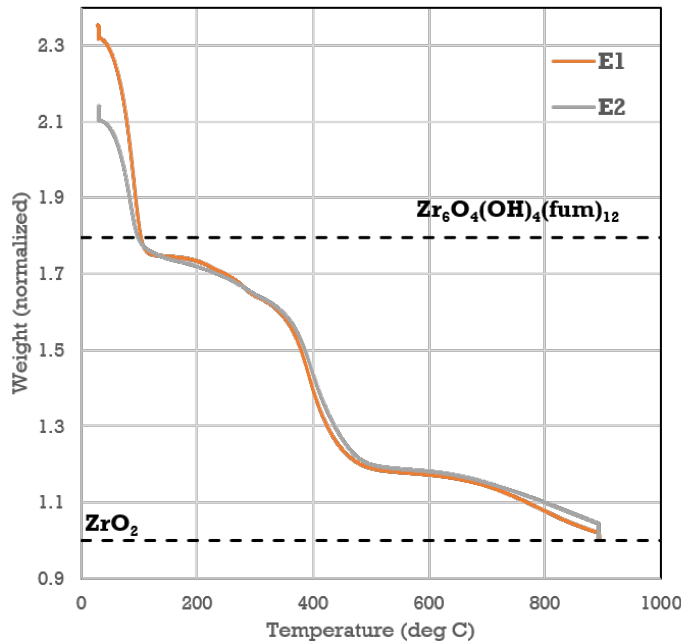


Figure D.2.: Thermogravimetric experiments highlighting the presence of defects in the Zr Fumarate structure.

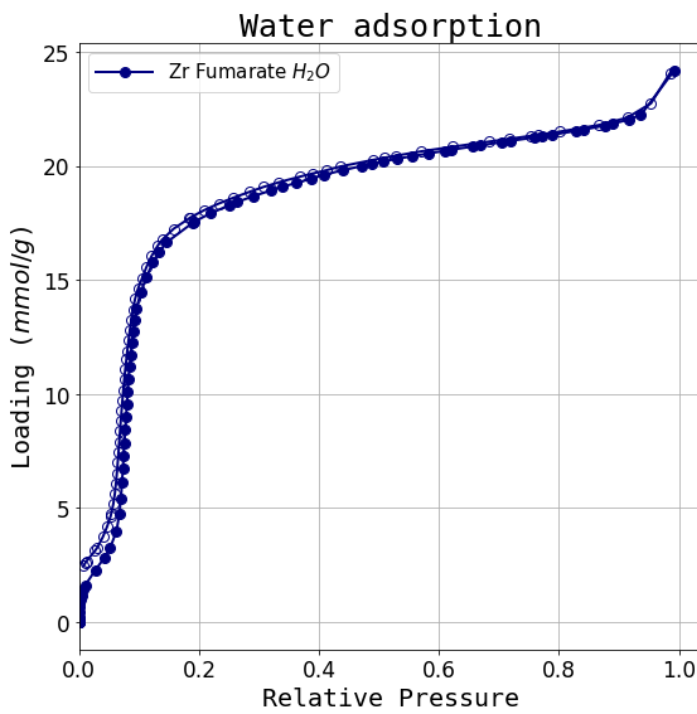


Figure D.3.: Water isotherm recorded on Zr Fumarate. The steep adsorption curve at below $0.2 p/p_0$ is an indication of defects in the MOF structure.⁽¹⁾

Bibliography

- [1] Jongwon Choi, Li-Chiang Lin, and Jeffrey C. Grossman. Role of Structural Defects in the Water Adsorption Properties of MOF-801. *The Journal of Physical Chemistry C*, 122(10):5545–5552, March 2018. ISSN 1932-7447, 1932-7455. doi: 10.1021/acs.jpcc.8b00014.

E. Appendix for chapter 4

E.1. Acid and solvent properties

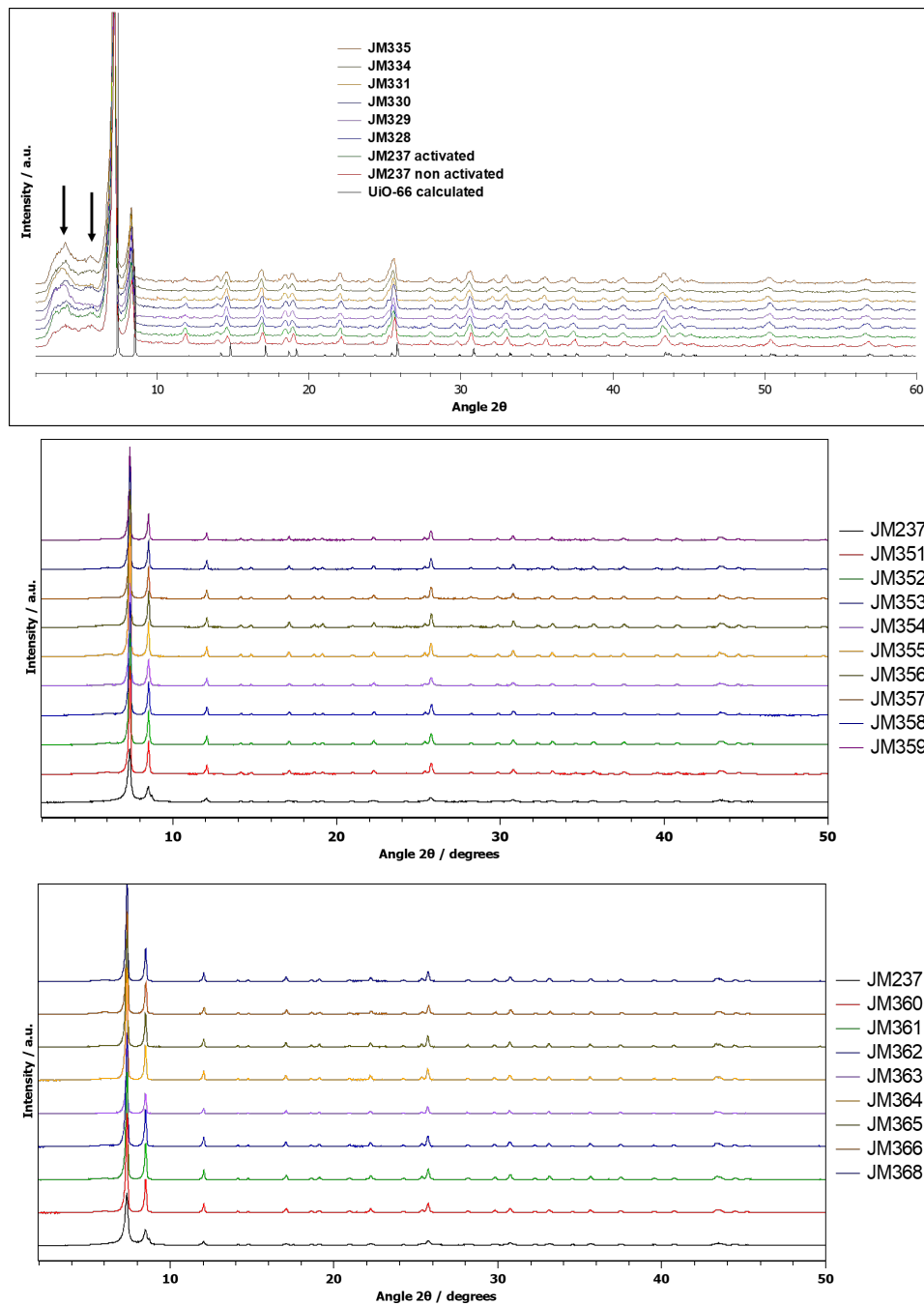
Table E.1.: Solvent properties

Solvent	Polarity relative to water	Boiling point °C	Viscosity cP, at 20 °C	Acidity pKa
DMF	0.386	65	0.92	base of formic acid
DMSO	0.444	100	1.99	35
EtOH	0.762	153	0.54	15.5
H ₂ O	1.000	189	0.89	14

Table E.2.: Leaching acid properties

Acid	pKa	Solubility (g/100g) at 25 °C			
		H ₂ O	MeOH	DMF	DMSO
formic	3.75	miscible	miscible	miscible	miscible
acetic	4.45	miscible	miscible	miscible	miscible
trifluoroacetic	0.3	miscible	miscible	miscible	miscible
benzoic	4.19	0.24 ⁽¹⁾	77 ⁽¹⁾	149 ⁽¹⁾	162 ⁽¹⁾

E.2. Powder diffraction patterns



E.3. TGA curves

E.3.1. DMF leached samples

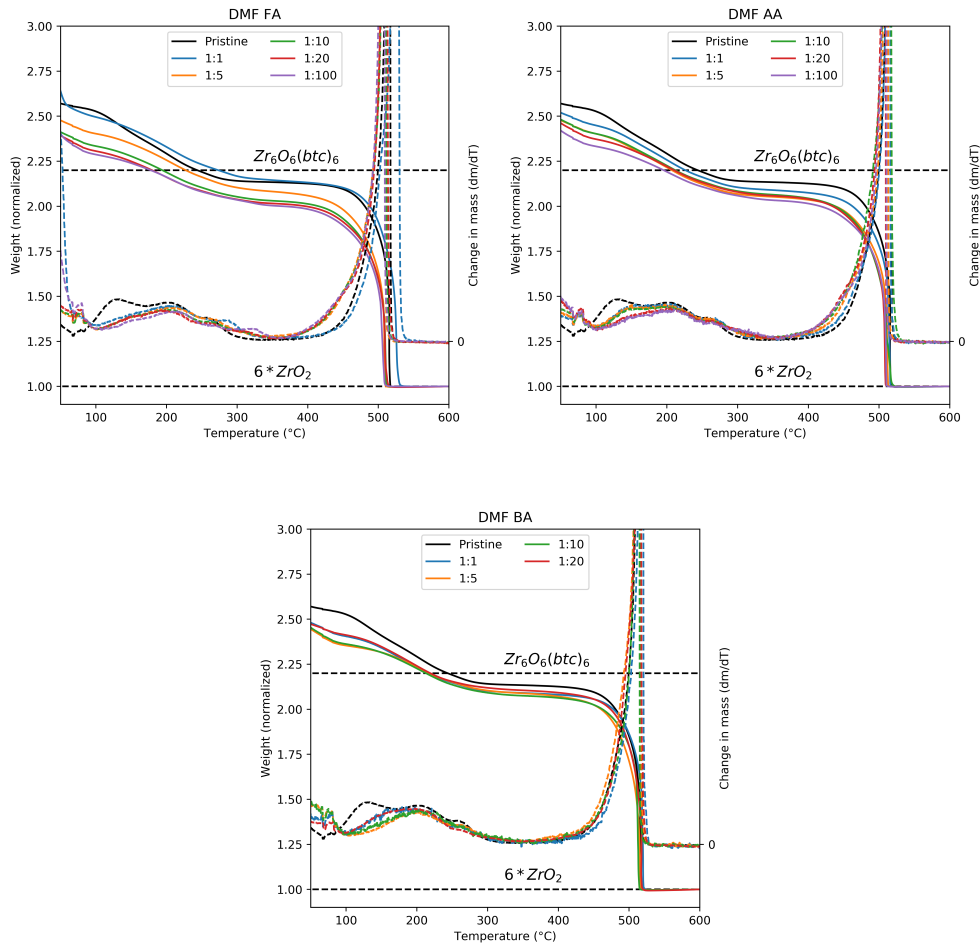


Figure E.1.: TGA curves for samples leached in DMF

E.3.2. Water leached samples

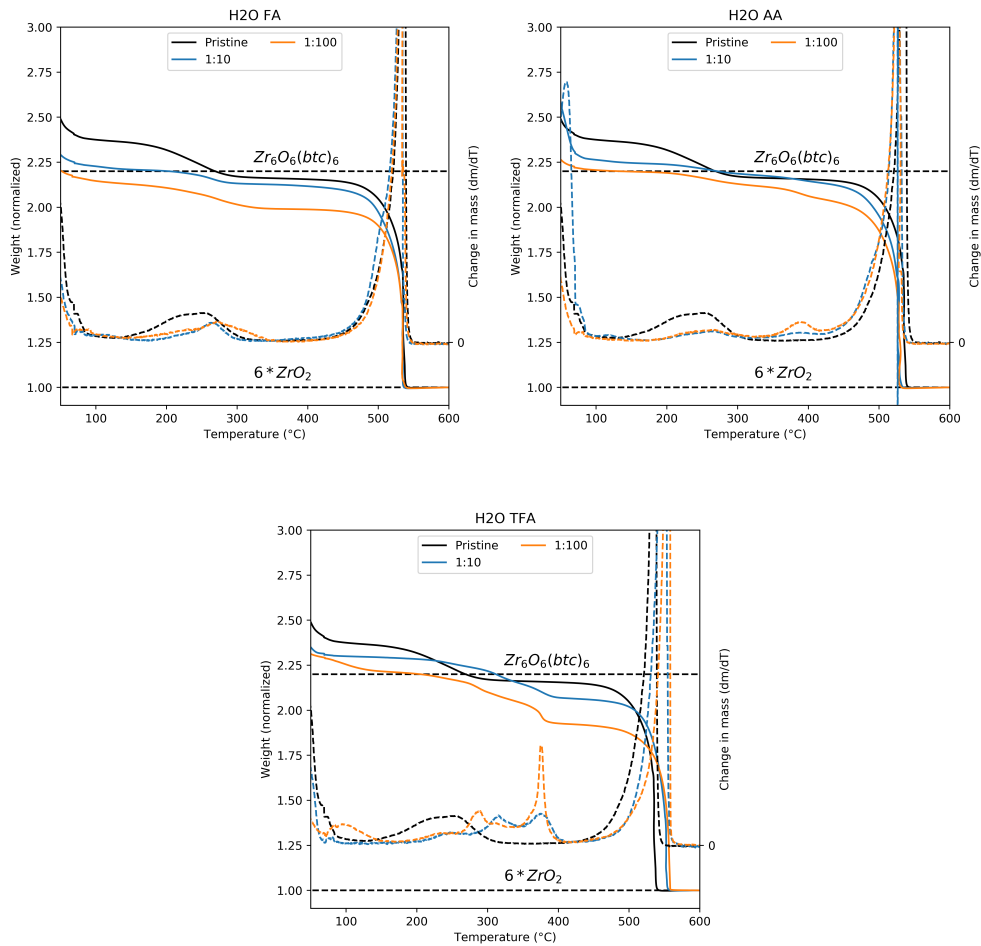


Figure E.2.: TGA curves for samples leached in H₂O

E.3.3. Methanol leached samples

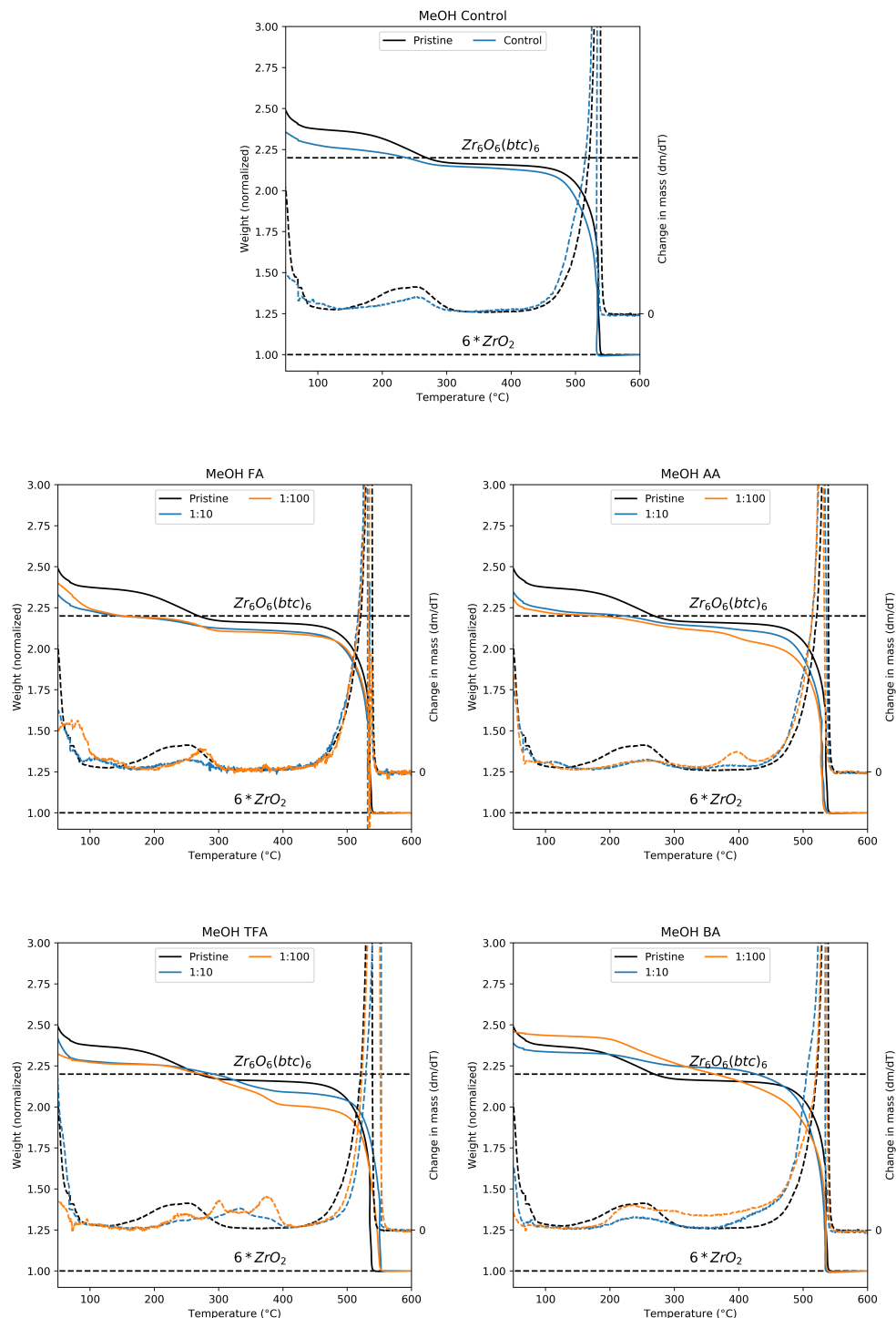


Figure E.3.: TGA curves for samples leached in MeOH

E.3.4. DMSO leached samples

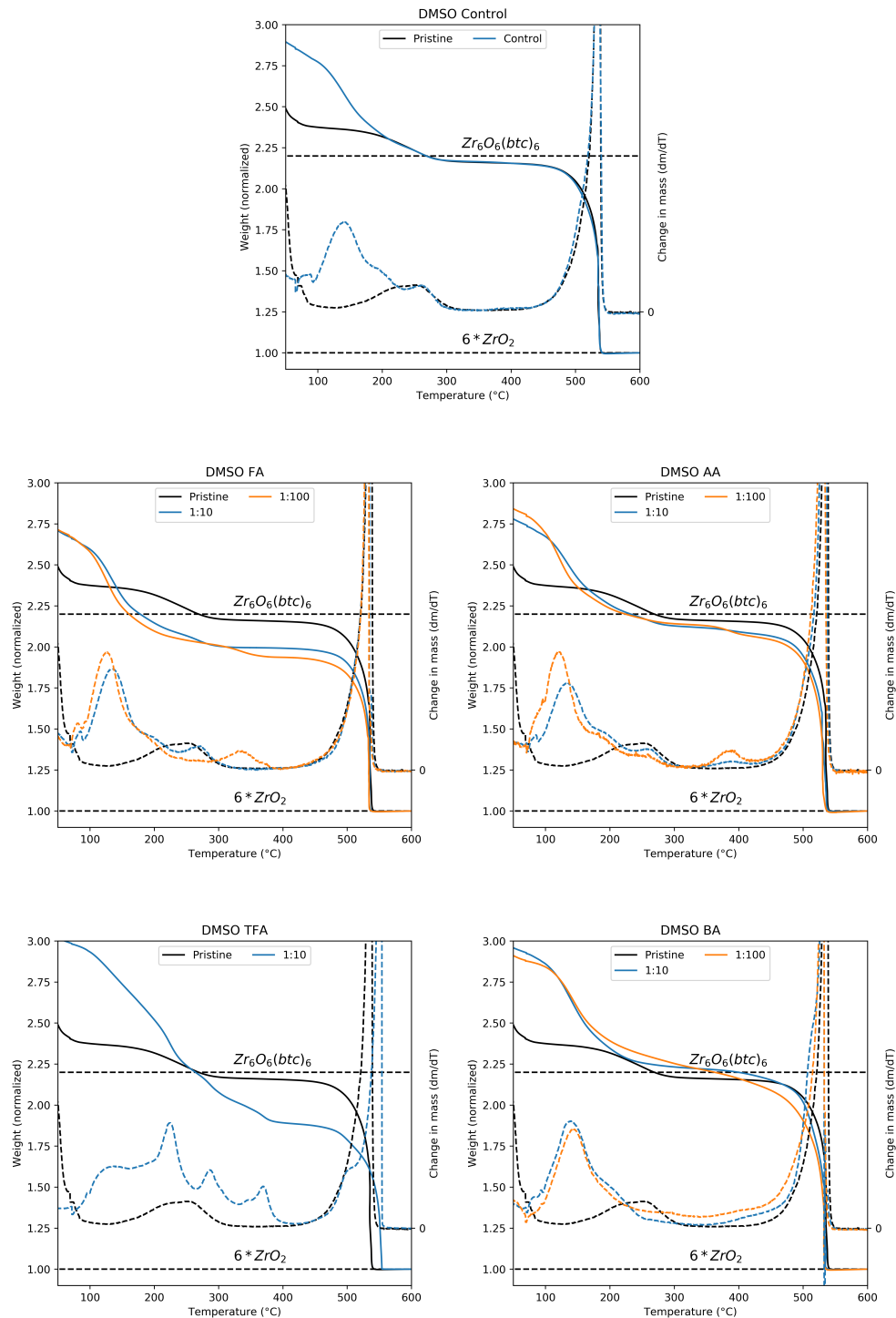


Figure E.4.: TGA curves for samples leached in DMSO

E.3.5. High resolution curves

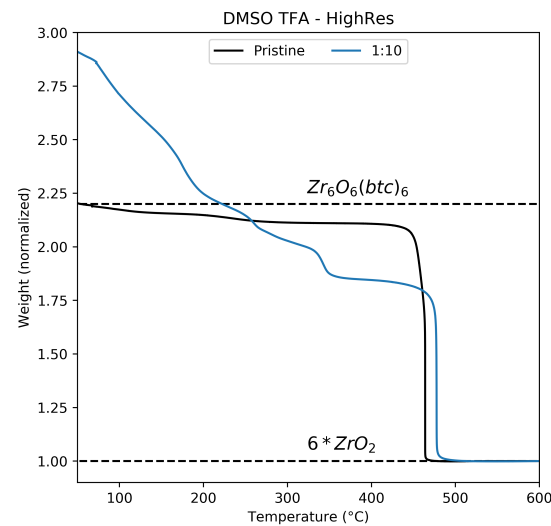


Figure E.5.: High resolution TGA curves for a DMSO/TFA leached sample

E.4. Nitrogen sorption isotherms

E.4.1. DMF leached samples

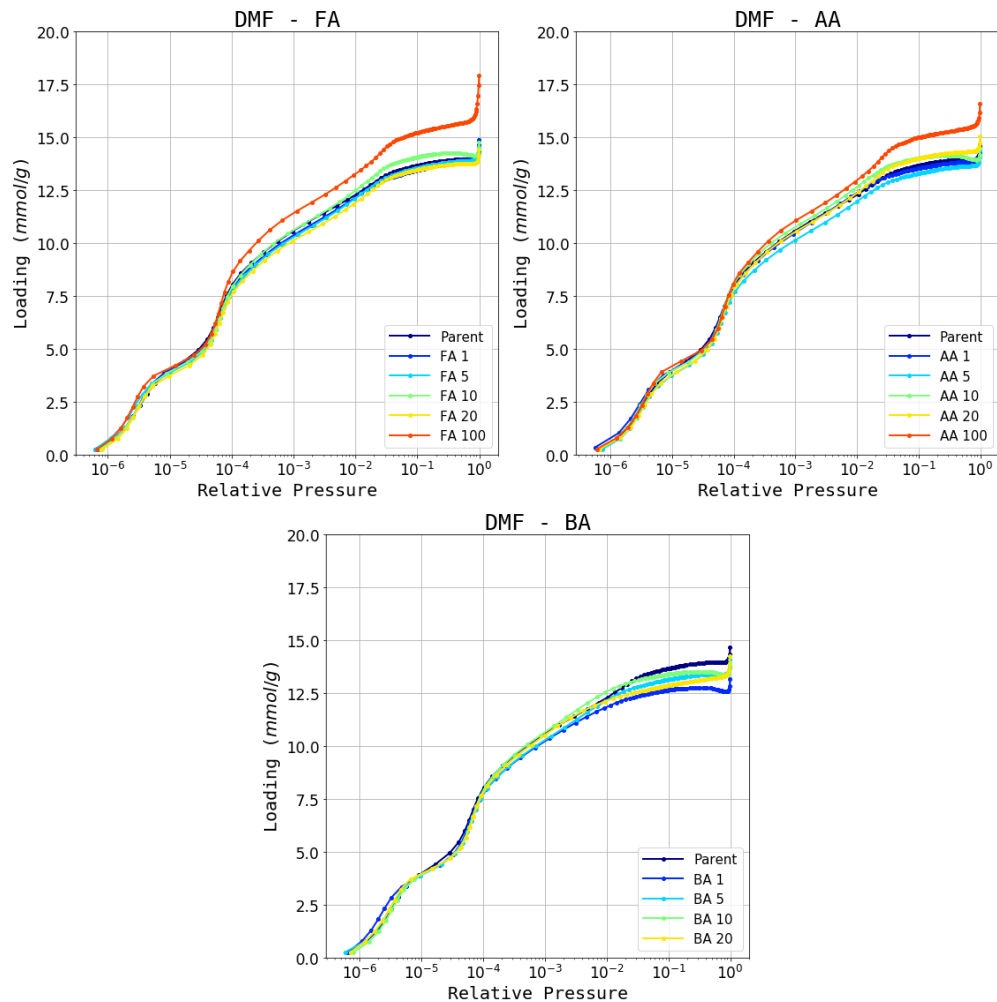


Figure E.6.: DMF isotherm dataset activated at 200 °C

E.4.2. H₂O leached samples

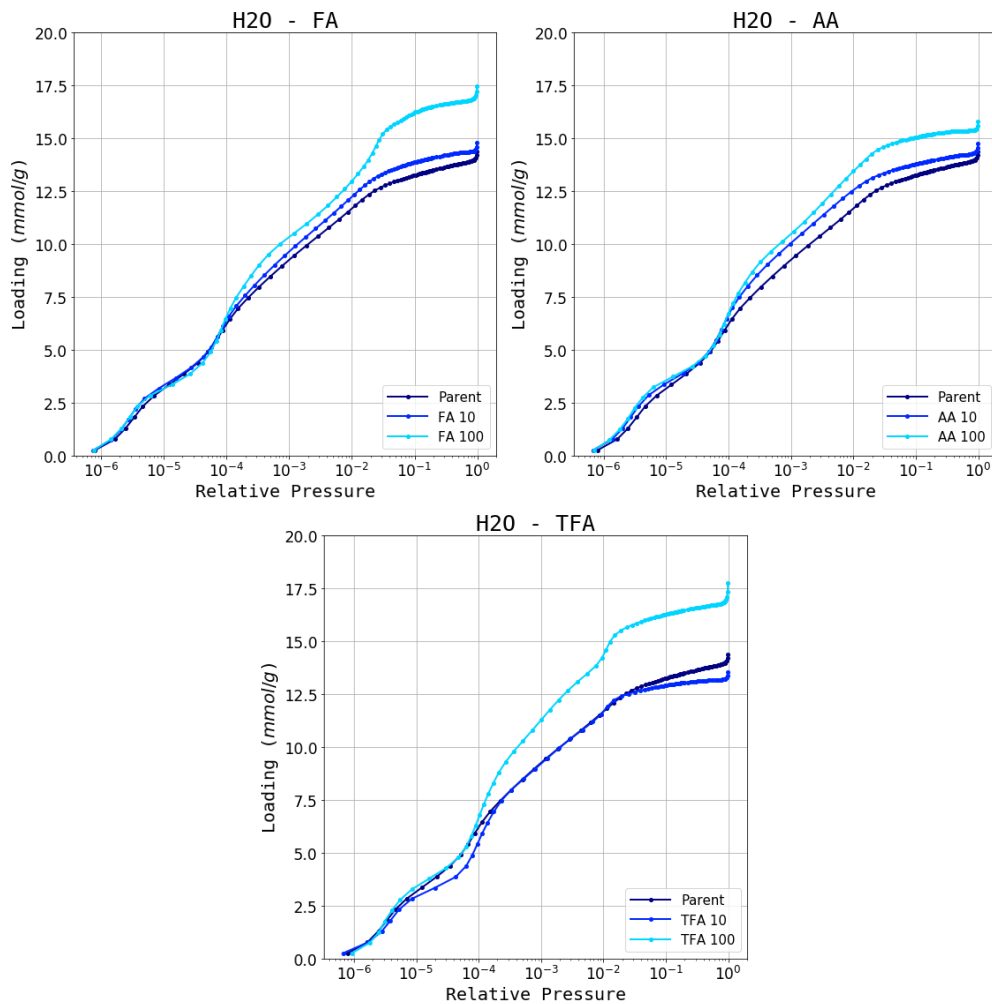


Figure E.7.: H₂O isotherm dataset activated at 200 °C

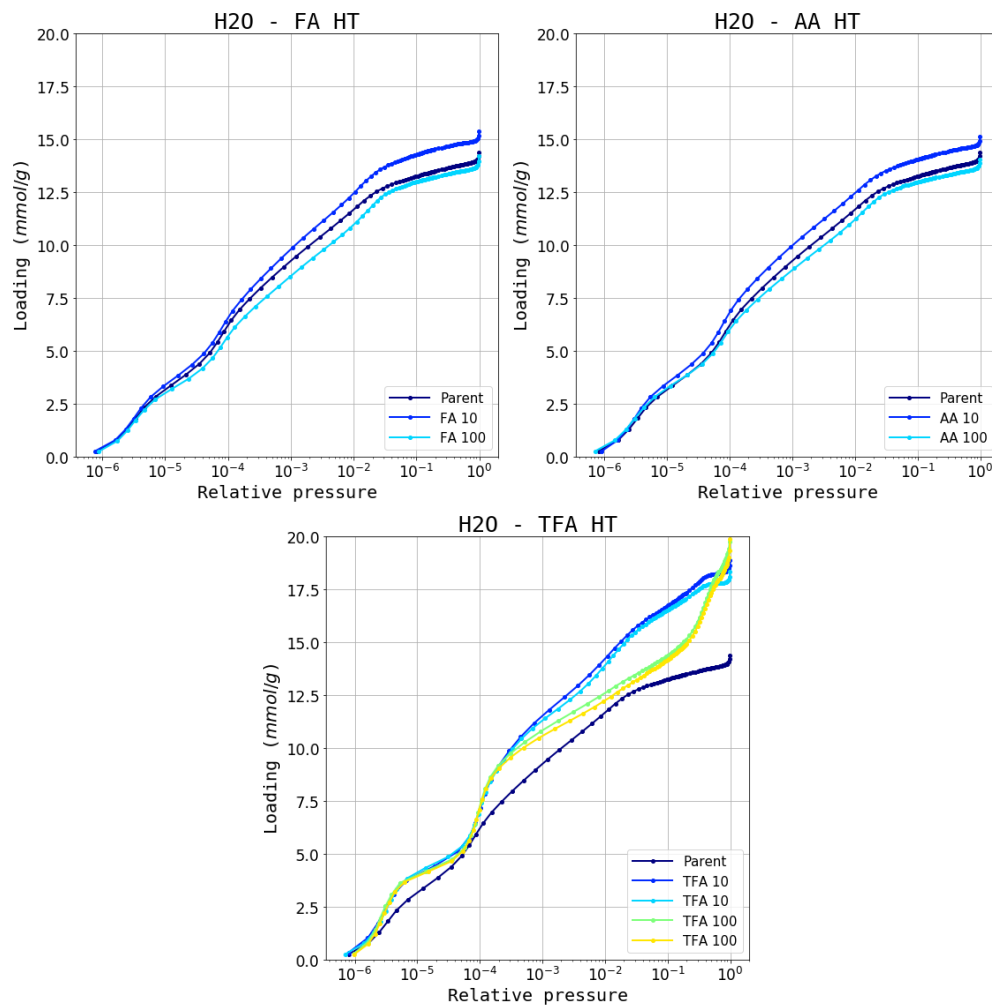


Figure E.8.: H_2O isotherm dataset activated at 320°C

E.4.3. MeOH leached samples

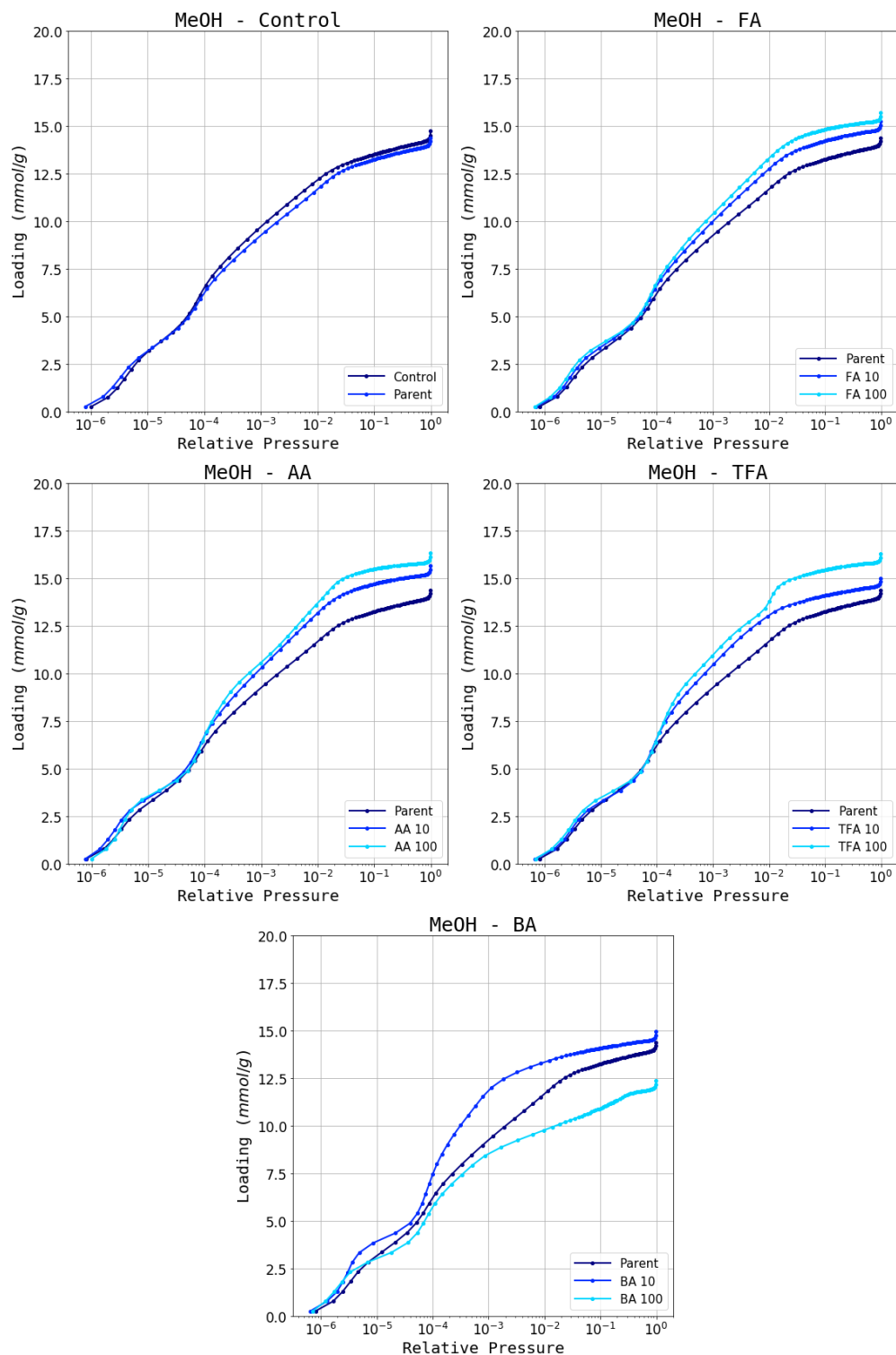
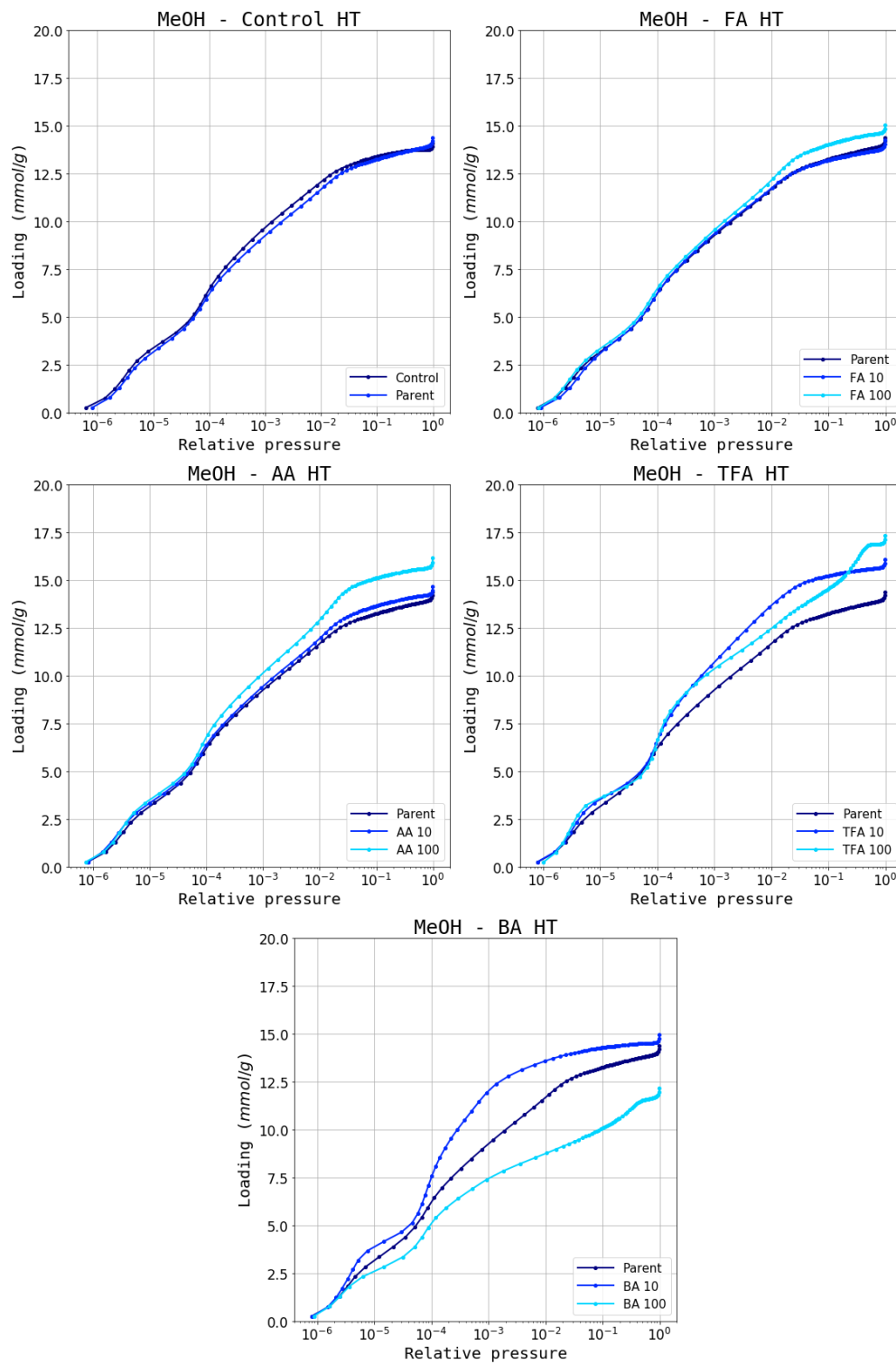


Figure E.9.: MeOH isotherm dataset activated at 200 °C

**Figure E.10.:** MeOH isotherm dataset activated at 320 °C

E.4.4. DMSO leached samples

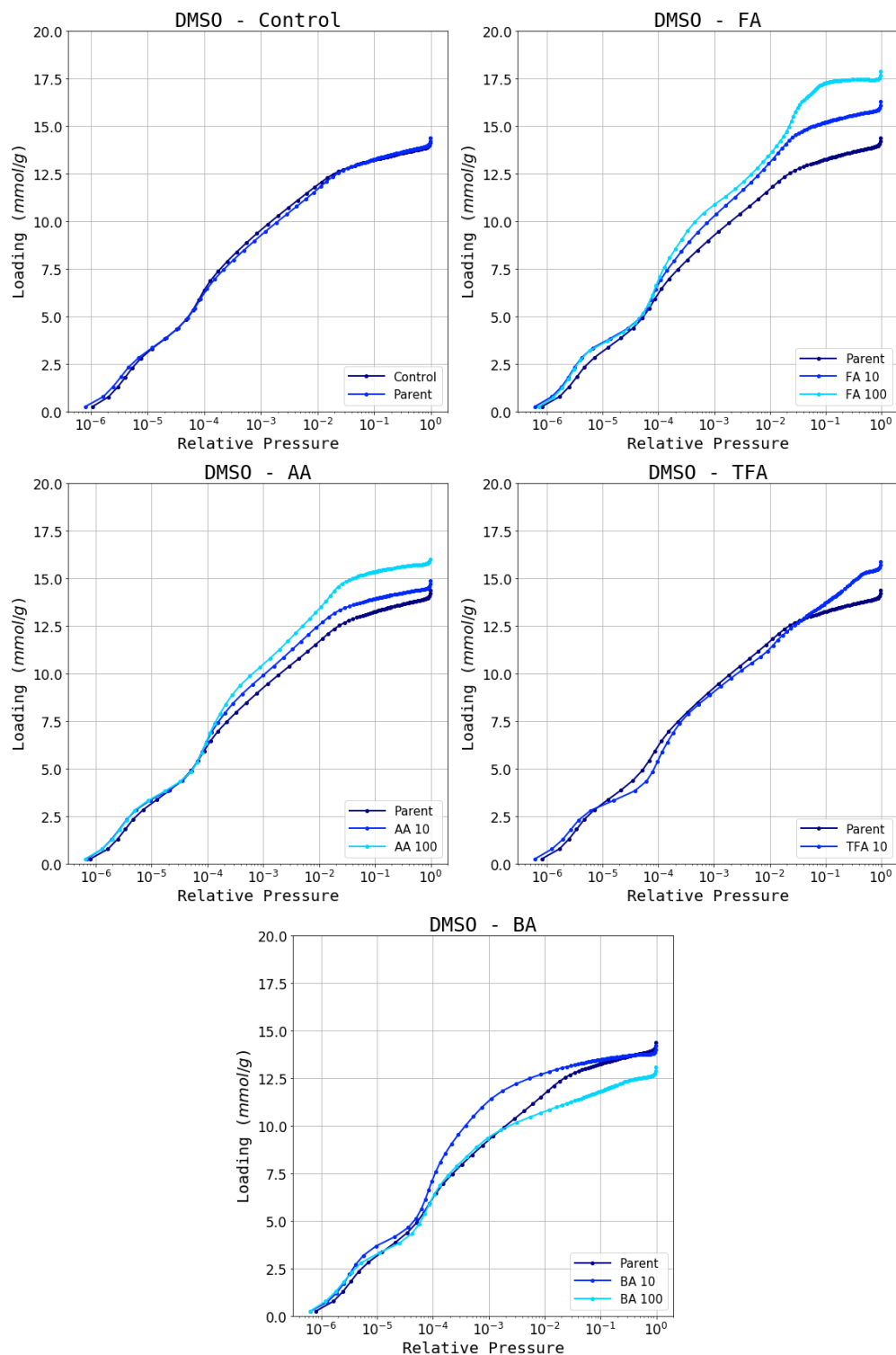
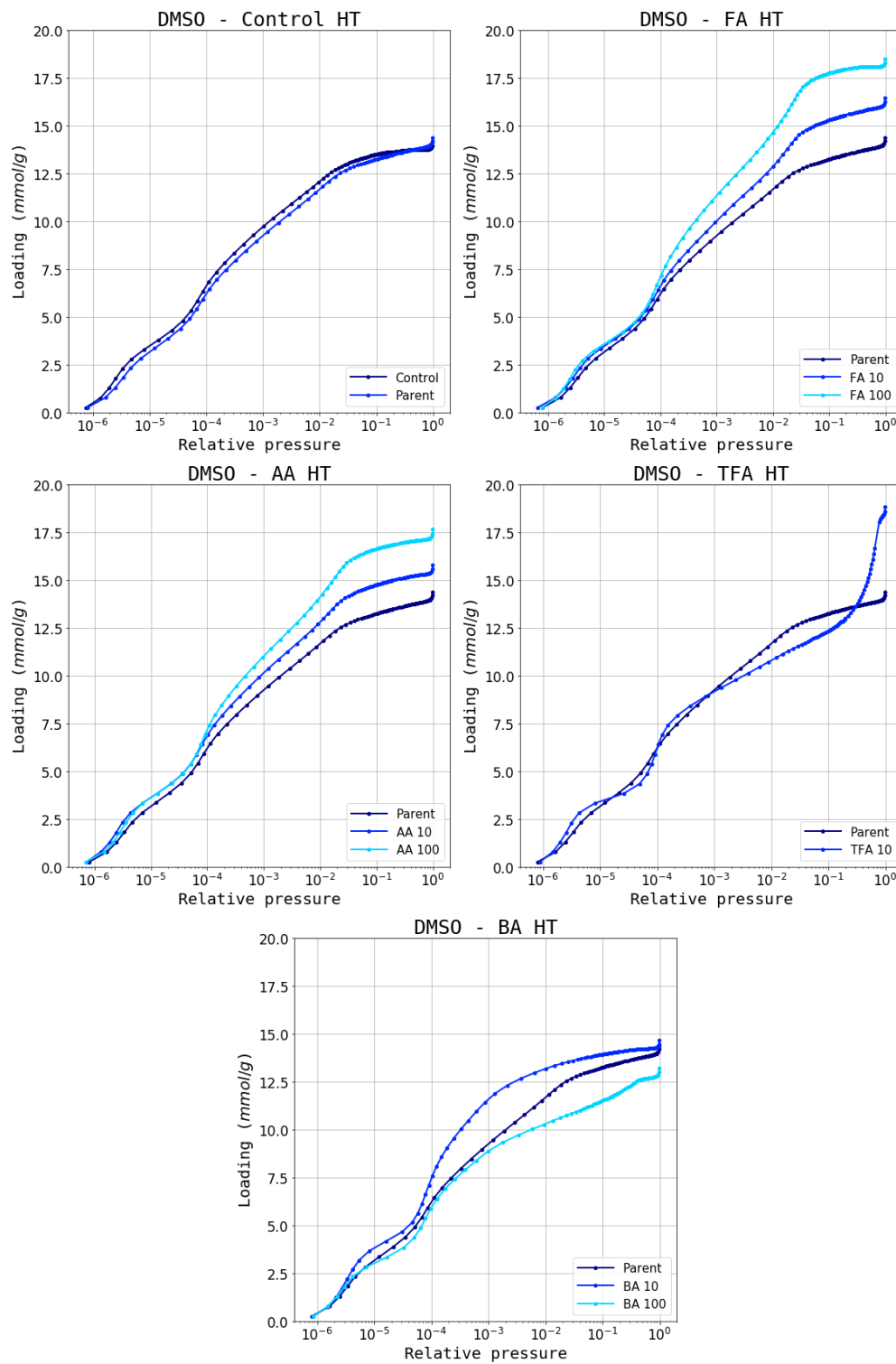
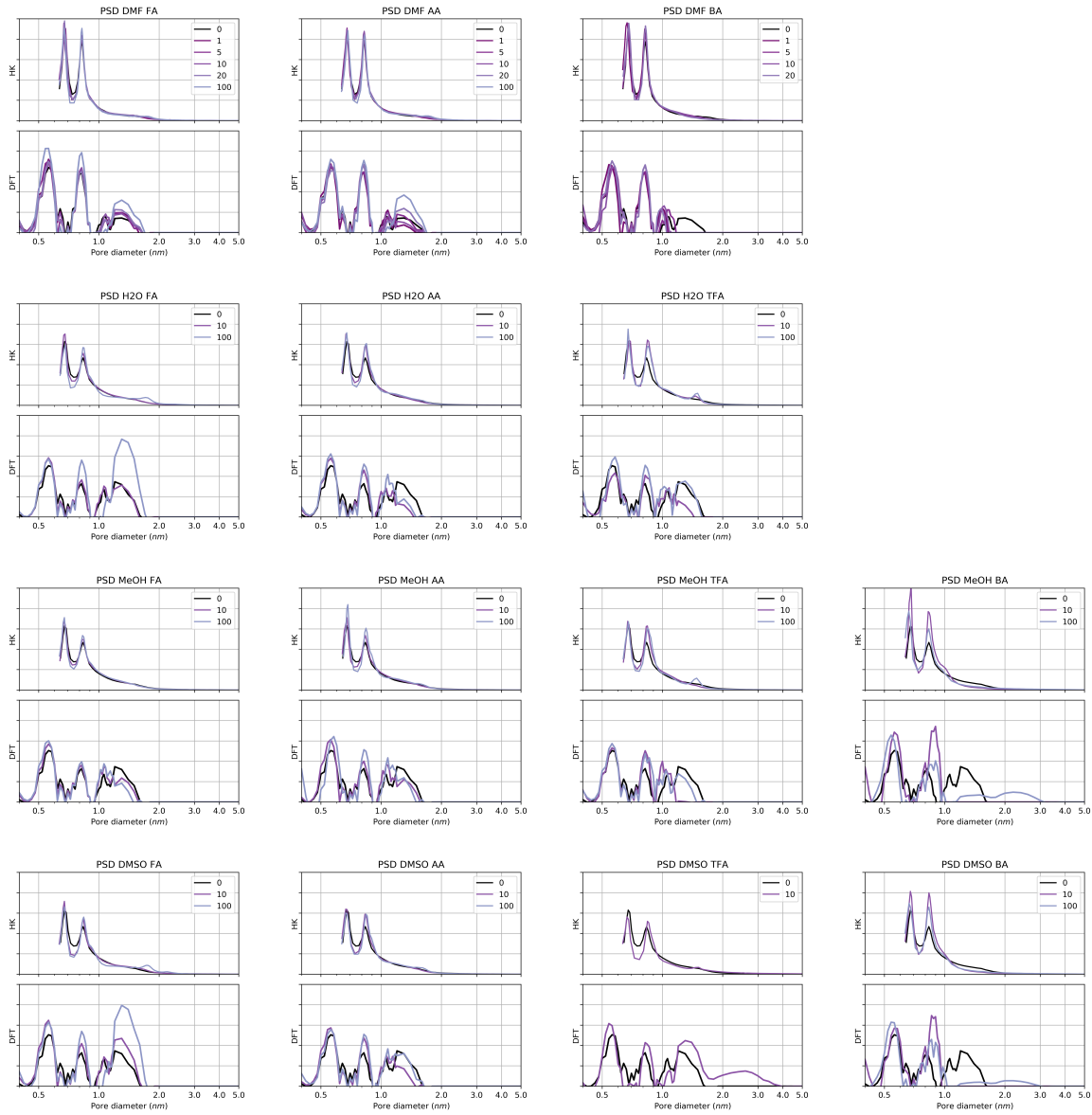


Figure E.11.: DMSO isotherm dataset activated at 200 °C

**Figure E.12.:** DMSO isotherm dataset activated at 320 °C

E.5. Characterisation



Bibliography

- [1] William E. Acree. IUPAC-NIST Solubility Data Series. 99. Solubility of Benzoic Acid and Substituted Benzoic Acids in Both Neat Organic Solvents and Organic Solvent Mixtures. *Journal of Physical and Chemical Reference Data*, 42(3): 033103, September 2013. ISSN 0047-2689, 1529-7845. doi: 10.1063/1.4816161.

F. Appendix for chapter 5

F.1. Calorimetry dataset UiO-66(Zr)

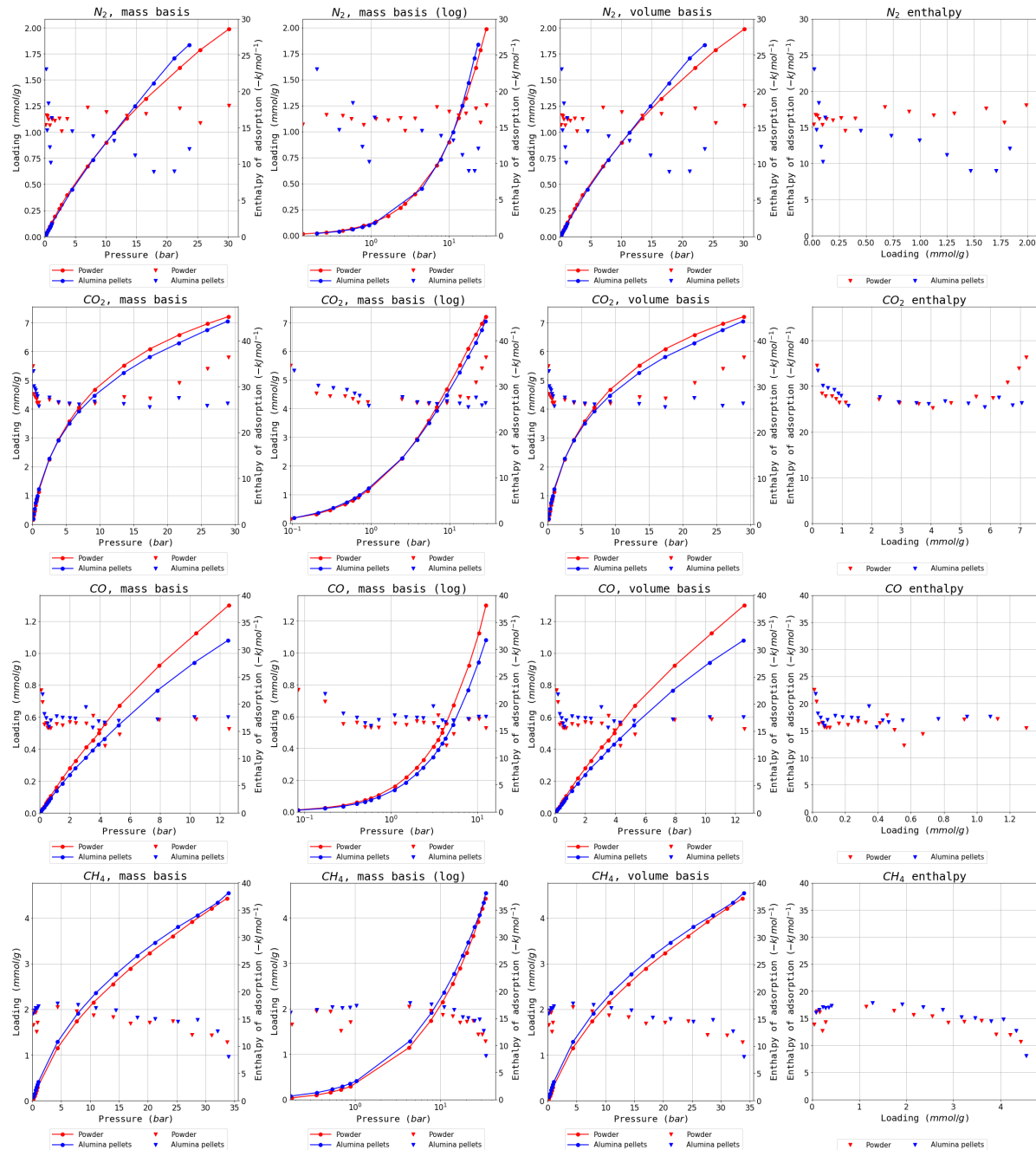


Figure F.1.: Complete isotherm and enthalpy dataset for UiO-66(Zr)

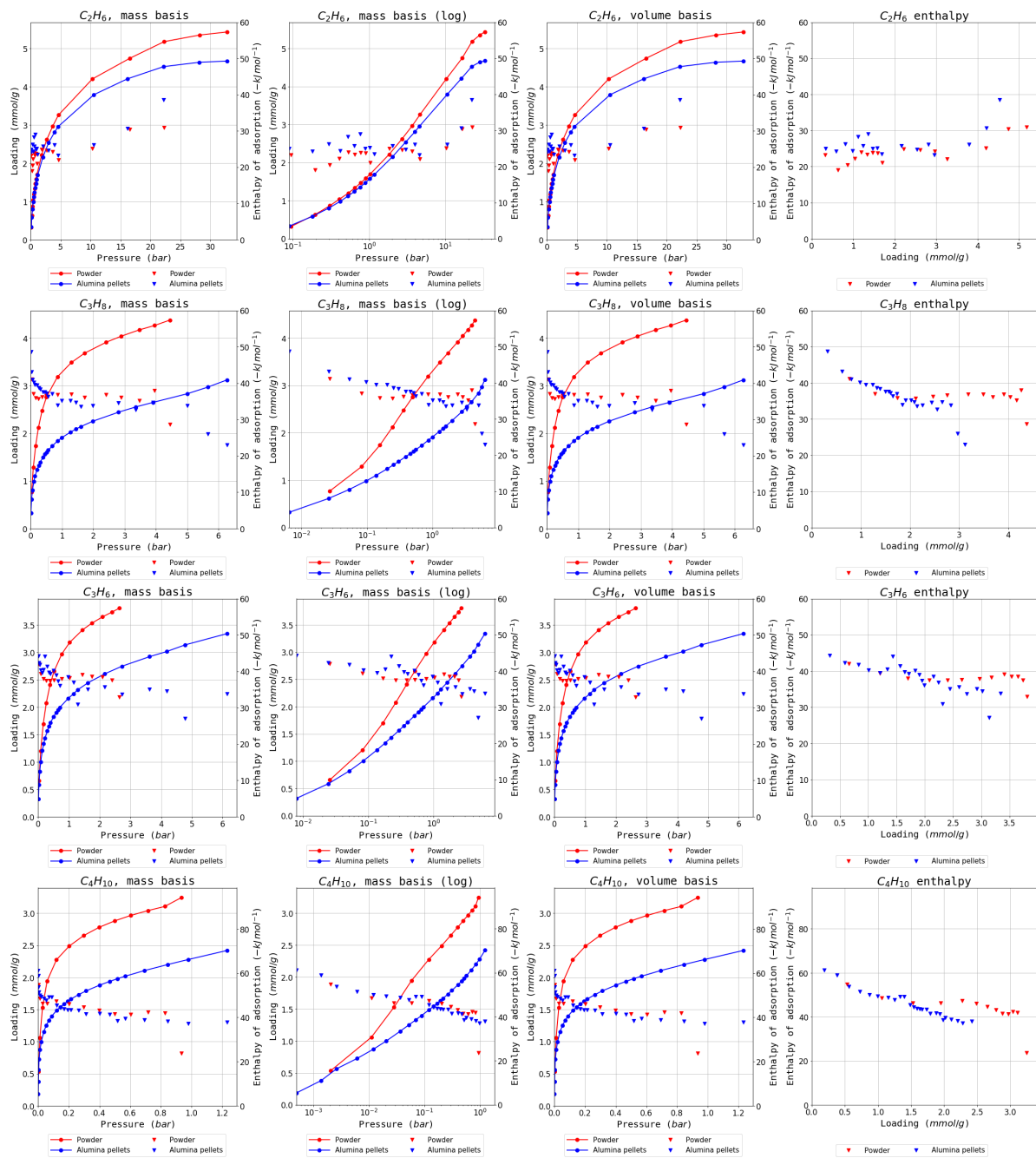


Figure F.2.: Complete isotherm and enthalpy dataset for UiO-66(Zr)

E.2. Calorimetry MIL-100(Fe)

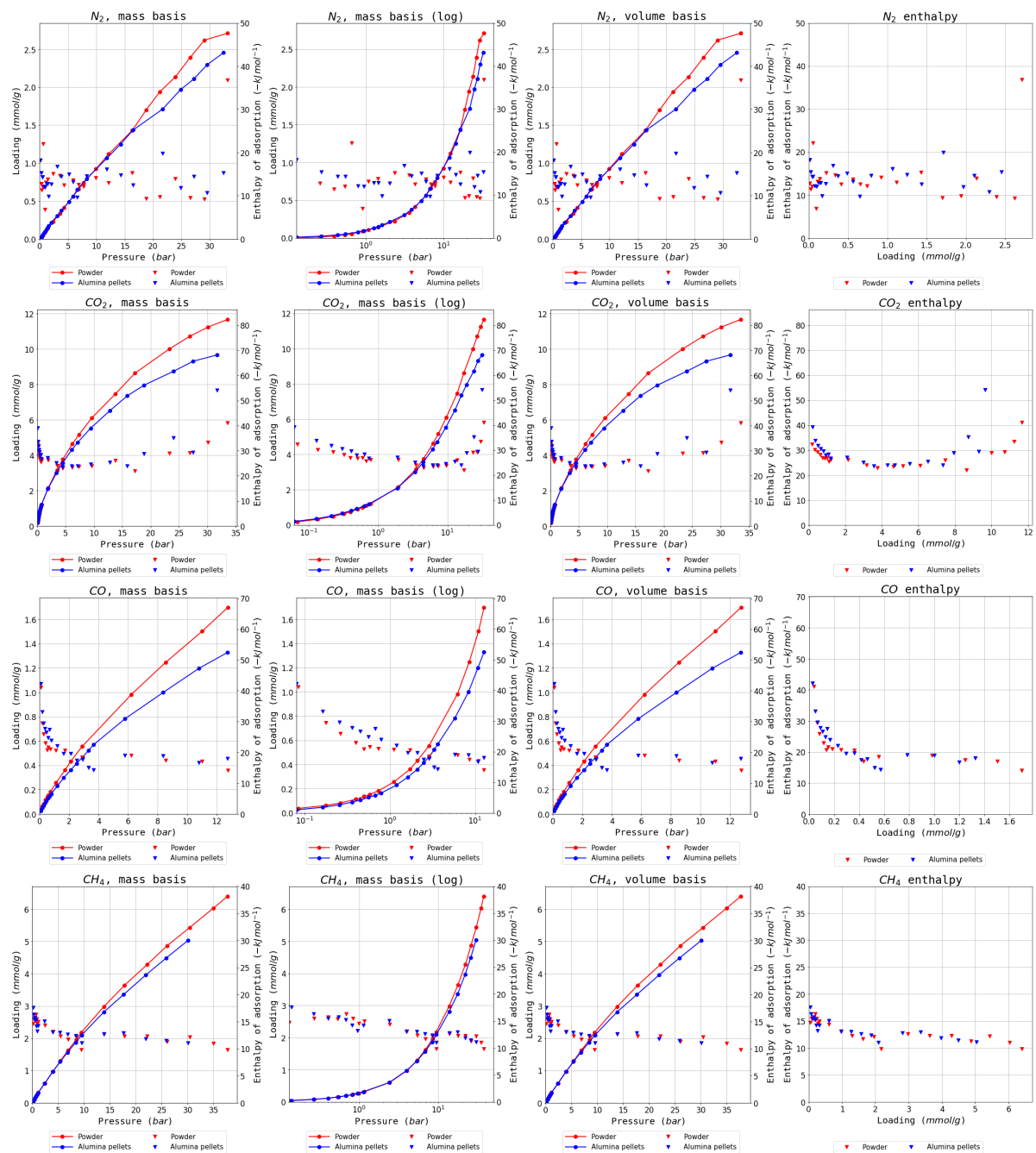


Figure E.3.: Complete isotherm and enthalpy dataset for MIL-100(Fe)

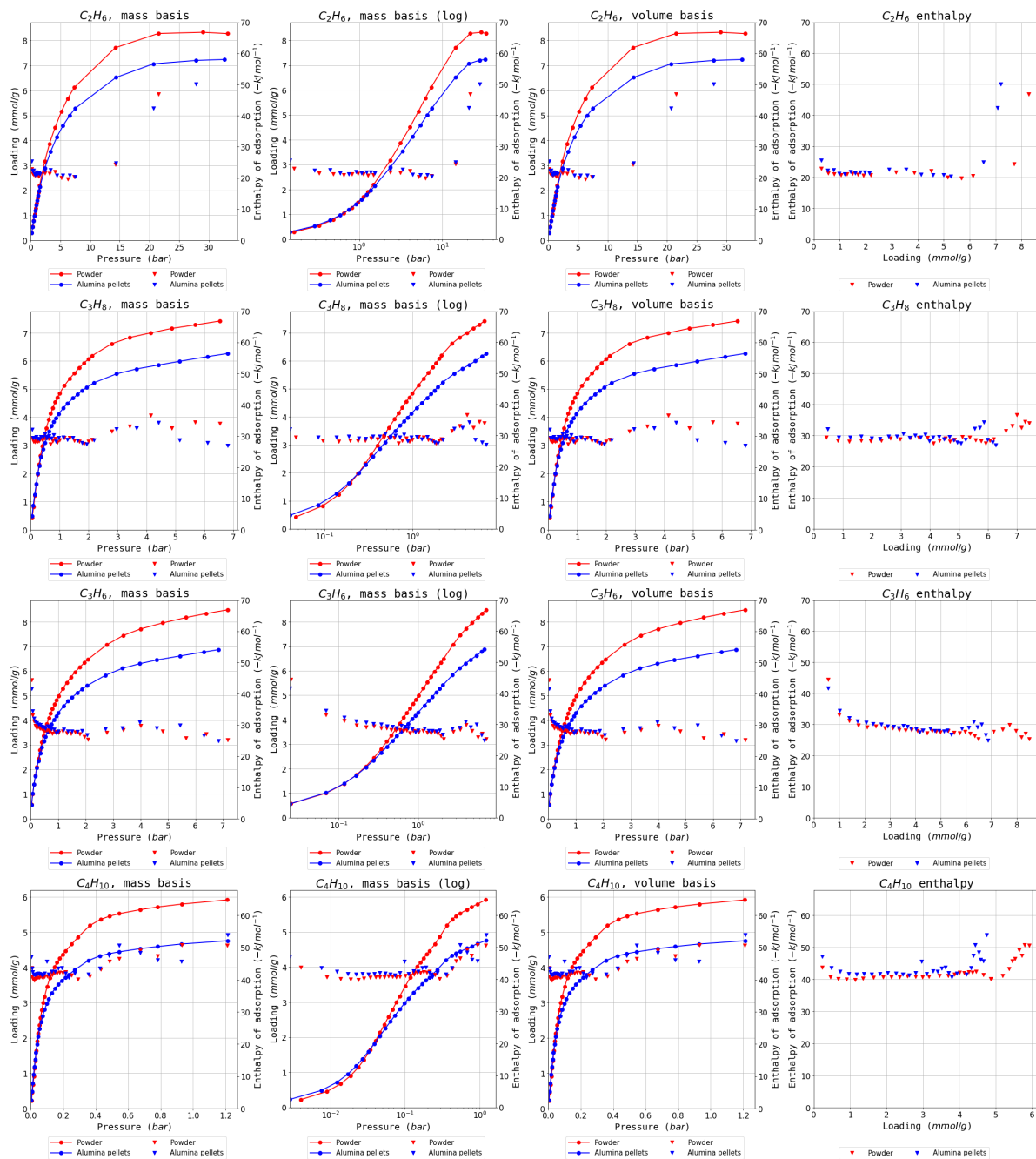


Figure F.4.: Complete isotherm and enthalpy dataset for MIL-100(Fe)

E.3. Calorimetry MIL-127(Fe)

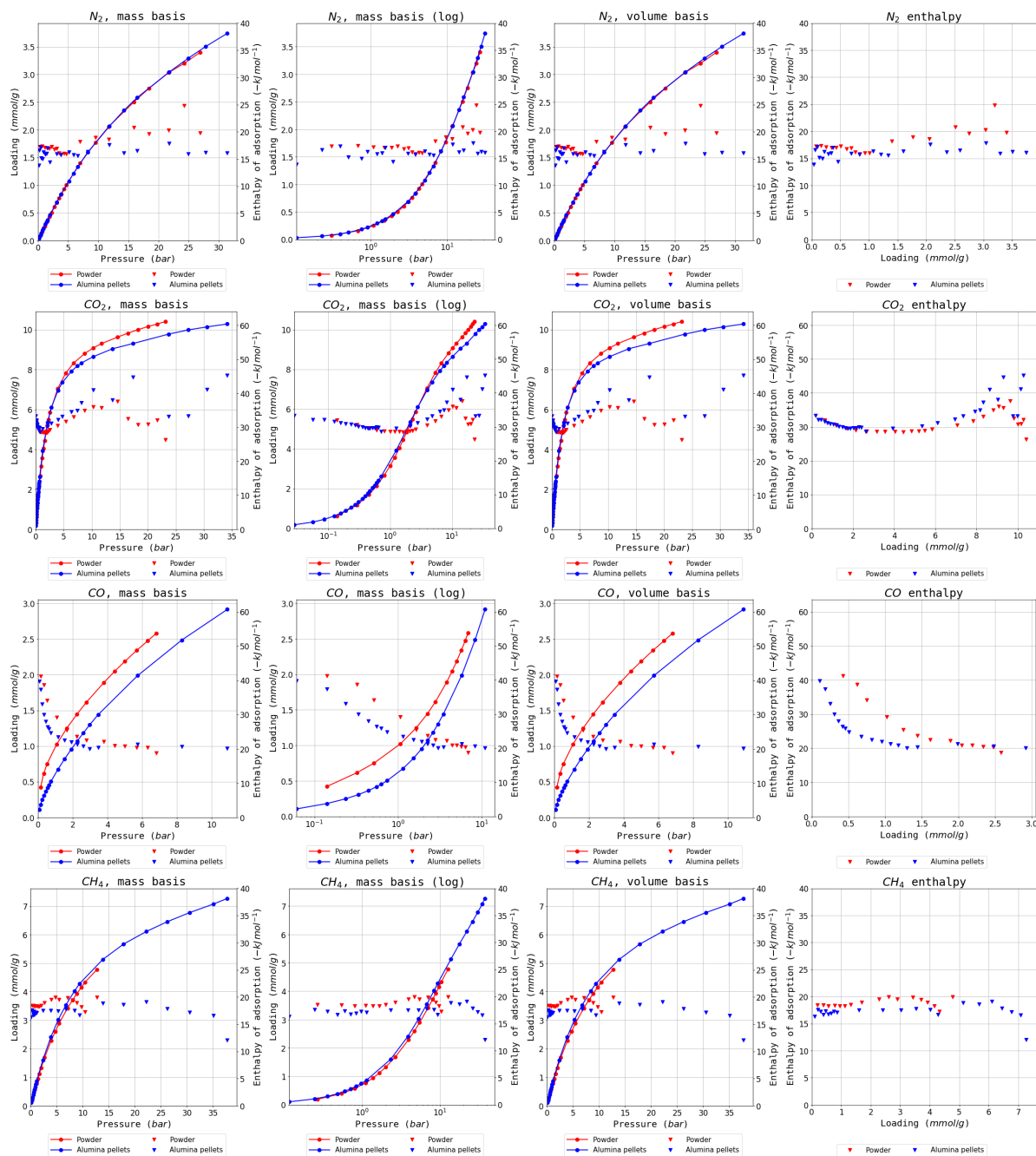


Figure E.5.: Complete isotherm and enthalpy dataset for MIL-127(Fe)

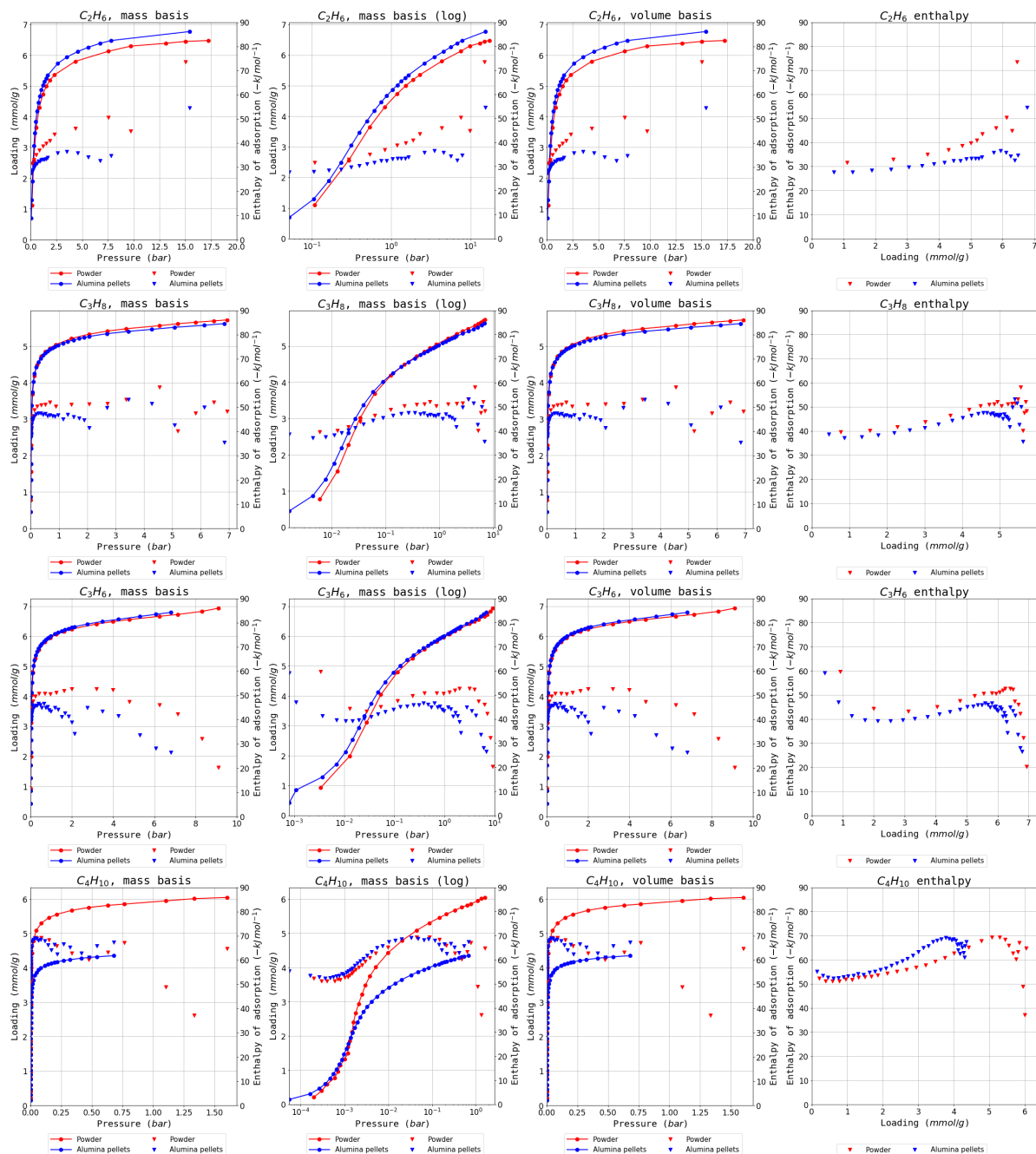


Figure F.6.: Complete isotherm and enthalpy dataset for MIL-127(Fe)

G. Appendix for chapter 6

G.1. Table of properties for low temperature probes

Table G.1.: Properties of probe gasses used at 77 K.

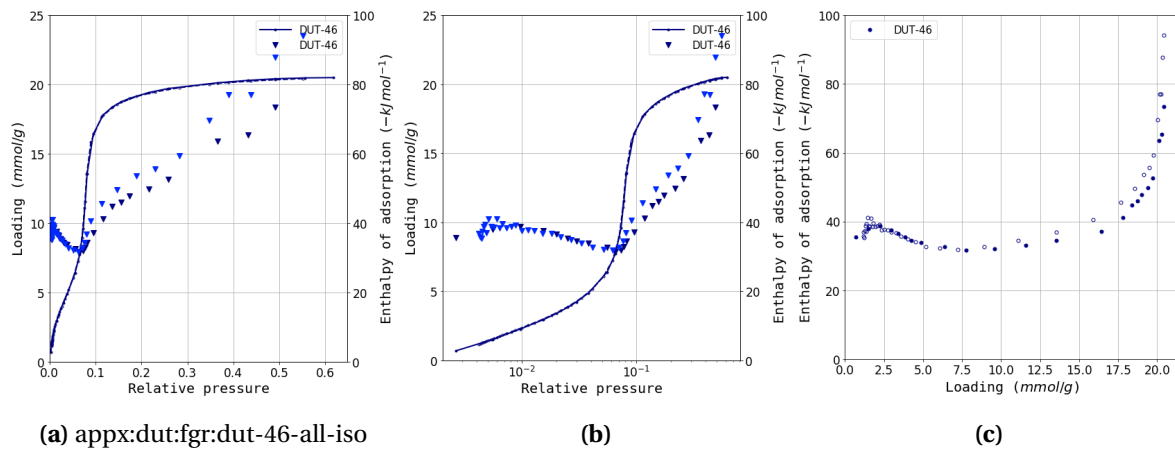
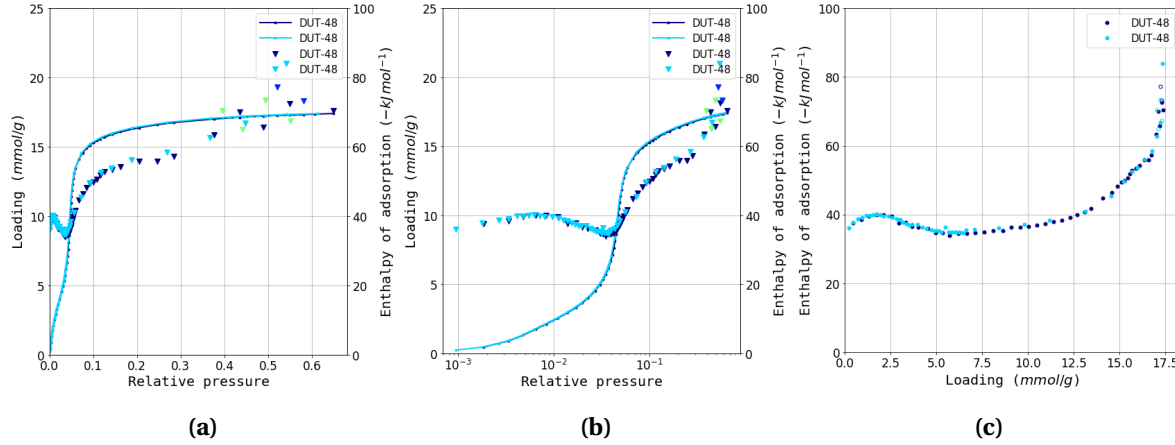
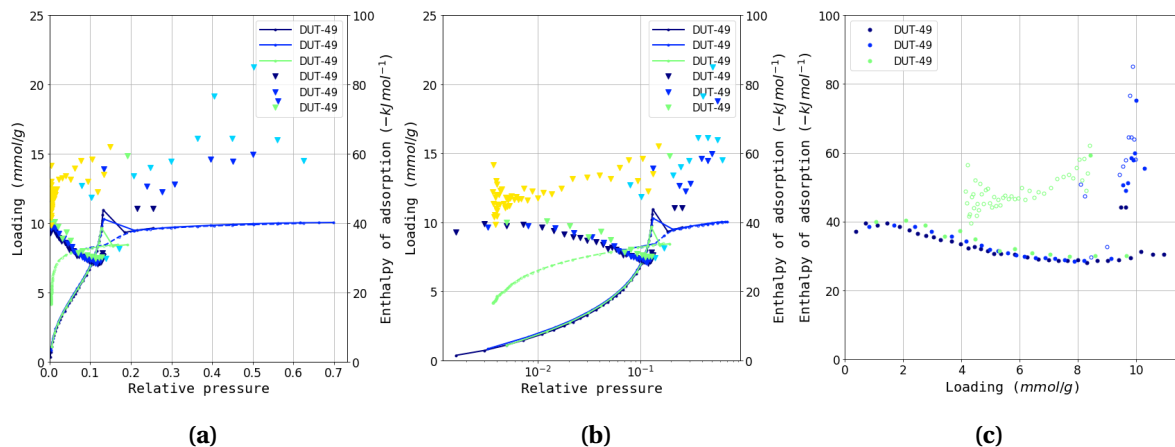
Probe	Ar	CO	N ₂	O ₂
molar mass g mol ⁻¹	39.948	28.010	28.0134	31.999
cross-sectional area nm	0.138	0.168	0.162	0.141
polarizability 10 ⁻³ nm ³	1.63	1.95	1.76	1.59
dipole moment 10 ⁻³⁰ C m	0.0	0.39	0.0	0.0
quadrupole moment 10 ⁻⁴⁰ C m ²	0.0	-12.3	-5.0	1.3
enthalpy of vaporisation*	6.49	6.03	5.58	7.18
liquid density g/cm ³	1.393	0.811	0.806	1.203
solid density g/cm ³	1.623	0.924	0.945	1.300
critical point T K	150.86	132.91	126.20	154.57
triple point point T K	83.78	68.14	63.15	54.35

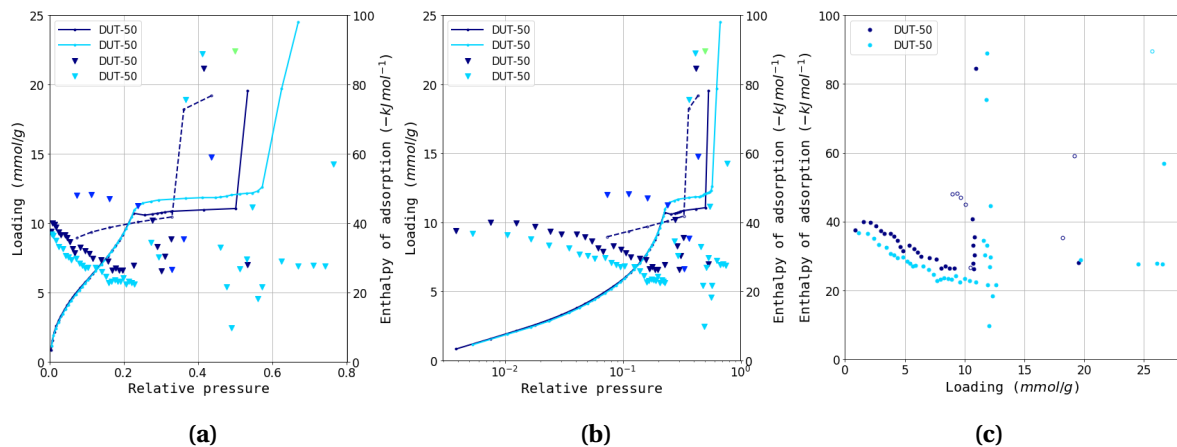
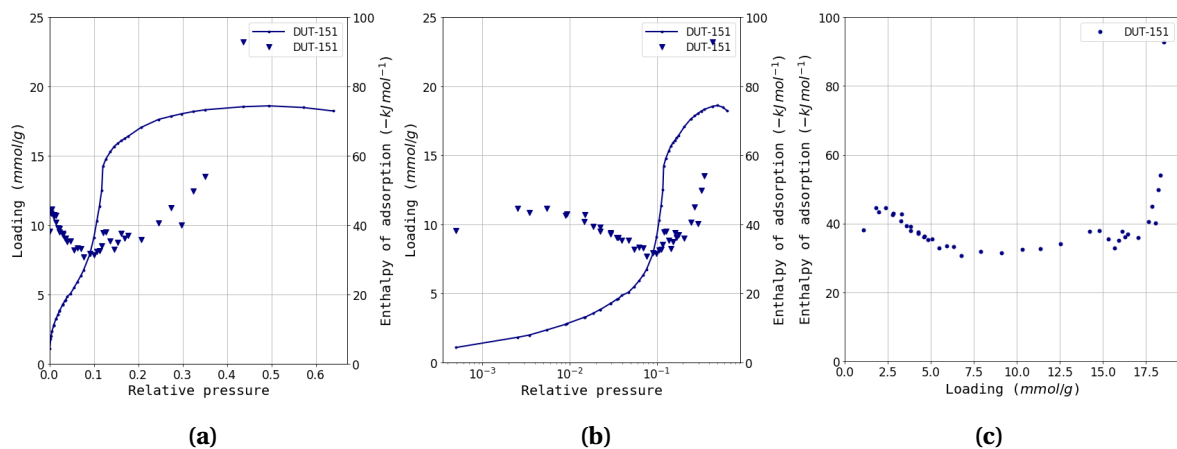
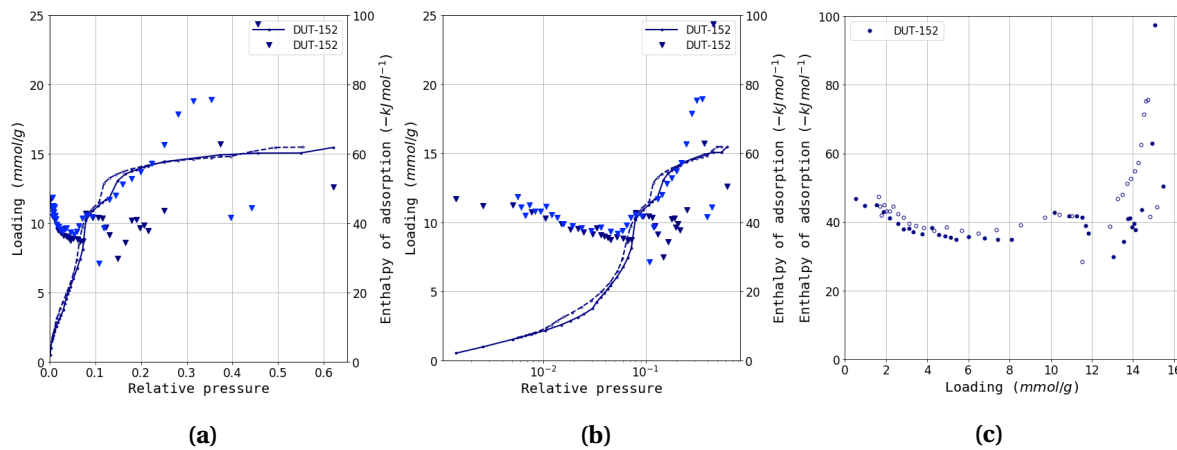
* from a liquid state

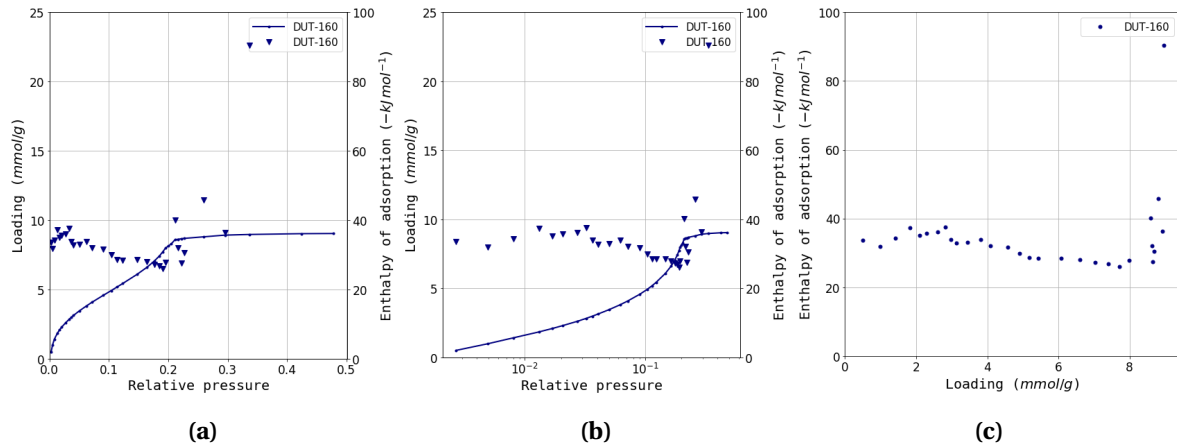
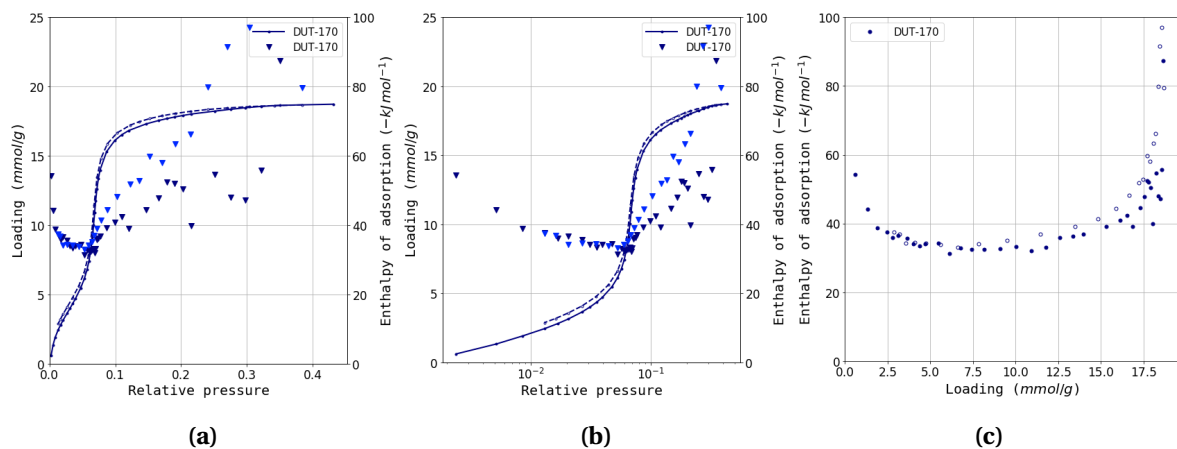
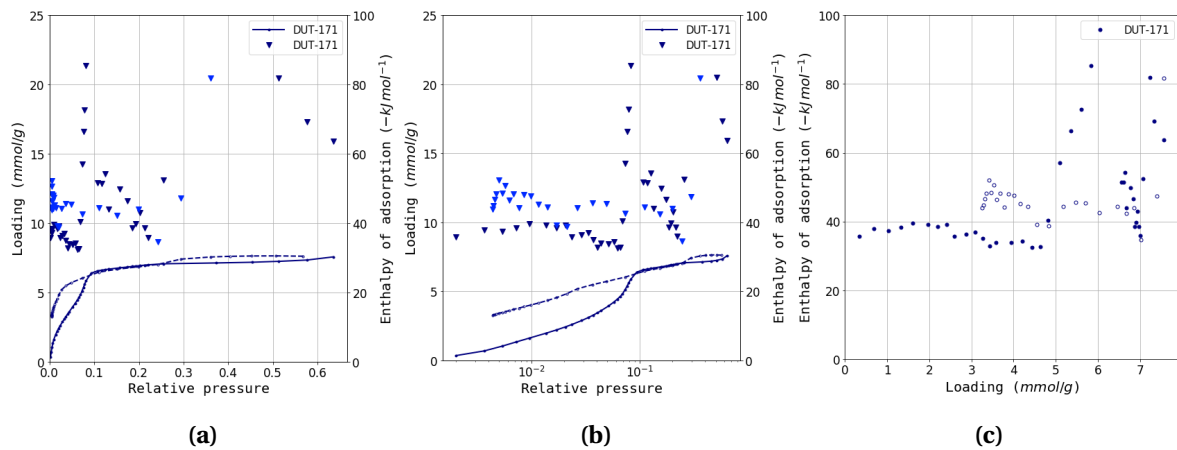
G.2. Ambient temperature calorimetry experiments

Table G.2.: Summary of ambient temperature calorimetry experiments performed at 77 K. Probe used is butane unless explicitly stated.

Material	Conditions	Observations
<i>C = cell, E = experiment, m = mass (mg)</i>		
DUT-46	C1, E1, $m \approx 35$	non-flexible
DUT-46	C1, E2	non-flexible
DUT-48	C1, E1, $m \approx 10$	non-flexible
DUT-48	C1, E2	non-flexible
DUT-48	C₃H₈ , C1, E3	no observed interactions
DUT-48	C₃H₆ , C1, E4	increased enthalpy at low loading
DUT-48	CO , C1, E5	no observed interactions
DUT-49(o)	C1, E1, $m \approx 97$	NGA
DUT-49(o)	C1, E2	sample decomposed
DUT-49(m)	C2, E1, $m \approx 42$	NGA
DUT-49(m)	C3, E1, $m \approx 38$	NGA
DUT-49(m)	C4, E1, $m \approx 18$	NGA
DUT-50	C1, E1, $m \approx 24$	NGA
DUT-50	C1, E2	sample decomposed
DUT-50	C2, E1, $m \approx 6$	NGA
DUT-147	C1, E1, $m \approx 18$	non-flexible
DUT-148	C1, E1, $m \approx 10$	NGA
DUT-149	C1, E1, $m \approx 45$	non-flexible
DUT-149	C1, E2, $m \approx 45$	non-flexible
DUT-151	C1, E1, $m \approx 15$	complex transitions
DUT-151	C1, E2	complex transitions
DUT-152	C1, E1, $m \approx 30$	complex transitions
DUT-160	C1, E1, $m \approx 22$	NGA
DUT-170	C1, E1, $m \approx 23$	non-flexible, low sensitivity
DUT-170	C1, E2	non-flexible
DUT-171	C1, E1, $m \approx 35$	continuous transition

**Figure G.1.:** DUT-46 (a) isotherms, (b) logarithmic isotherms and (c) enthalpy curves.**Figure G.2.:** DUT-48 (a) isotherms, (b) logarithmic isotherms and (c) enthalpy curves.**Figure G.3.:** DUT-49 (a) isotherms, (b) logarithmic isotherms and (c) enthalpy curves.

**Figure G.4.:** DUT-50 (a) isotherms, (b) logarithmic isotherms and (c) enthalpy curves.**Figure G.5.:** DUT-151 (a) isotherms, (b) logarithmic isotherms and (c) enthalpy curves.**Figure G.6.:** DUT-152 (a) isotherms, (b) logarithmic isotherms and (c) enthalpy curves.

**Figure G.7.:** DUT-160 (a) isotherms, (b) logarithmic isotherms and (c) enthalpy curves.**Figure G.8.:** DUT-170 (a) isotherms, (b) logarithmic isotherms and (c) enthalpy curves.**Figure G.9.:** DUT-171 (a) isotherms, (b) logarithmic isotherms and (c) enthalpy curves.

G.3. Low temperature calorimetry experiments

Table G.3.: Summary of low temperature calorimetry experiments. Conditions are identical for subsequent experiments unless explicitly stated.

Material	Probe	Conditions	Observations
<i>C = cell, E = experiment, HF/LF = high/low flowrate, m = mass (mg)</i>			
DUT-49(o)	Ar	C1, E1, LF, $m \approx 180$	NGA
DUT-49(o)	Ar	C2, E1, LF, $m \approx 20$	NGA
DUT-49(o)	O ₂	C3, E1, LF, $m \approx 20$	NGA
DUT-49(o)	N ₂	C4, E1, LF, $m \approx 10$	NGA, additional transitions
DUT-49(o)	N ₂	C5, E1, LF, $m \approx 5$	NGA, additional transitions
DUT-49(o)	N ₂	C5, E2, LF	no NGA, additional transitions
DUT-49(o)	N ₂	C5, E3, LF	no NGA, additional transitions
DUT-49(o)	O ₂	C5, E4, LF	NGA
DUT-49(m)	CO	C6, E1, HF, $m \approx 20$	no NGA
DUT-49(m)	N ₂	C6, E2, HF	NGA, additional transitions
DUT-49(m)	CO	C7, E1, HF, $m \approx 20$	no NGA
DUT-49(m)	Ar	C7, E2, HF	NGA
DUT-149	N ₂	C1, E1, LF, $m \approx 10$	no NGA
DUT-149	N ₂	E2, HF	no NGA
DUT-149	Ar	E3, LF	no NGA
DUT-149	Ar	E4, HF	no NGA
DUT-149	CO	E5, LF	no NGA
DUT-149	CO	E6, LF	no NGA
DUT-149	CO	E7, HF	no NGA
DUT-149	O ₂	E8, LF	NGA
DUT-149	O ₂	E9, HF	NGA
DUT-48	Ar	C1, E1, LF, $m \approx 5$	no NGA
DUT-48	Ar	E2, LF	no NGA
DUT-48	CH ₄	E3, LF	no NGA, low sensitivity
DUT-148	O ₂	C1, E1, HF, $m \approx 10$	NGA
DUT-148	O ₂	E2, LF	NGA
DUT-148	N ₂	E3, HF	no NGA
DUT-148	N ₂	E4, LF	no NGA

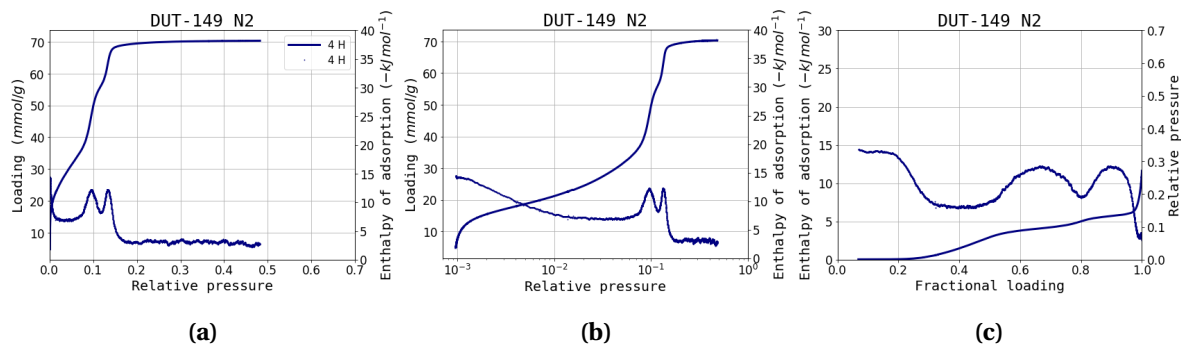


Figure G.10.: DUT-149 (a) isotherms, (b) logarithmic isotherms and (c) enthalpy curves for N2.

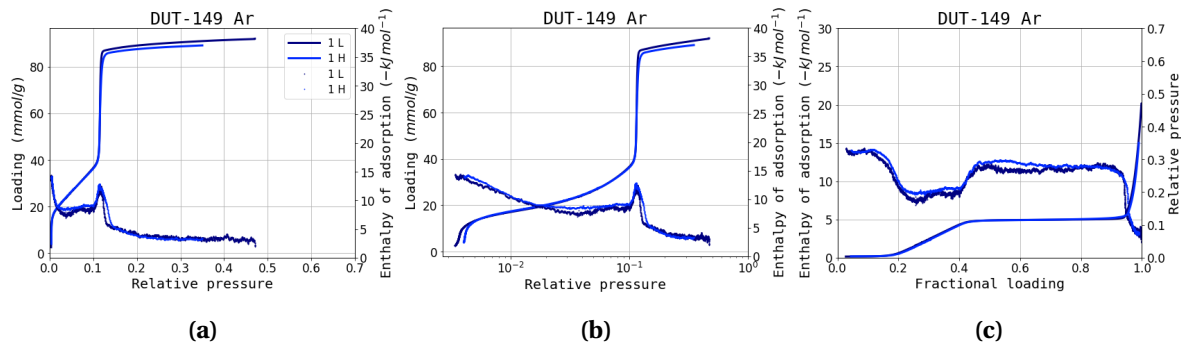


Figure G.11.: DUT-149 (a) isotherms, (b) logarithmic isotherms and (c) enthalpy curves for Ar.

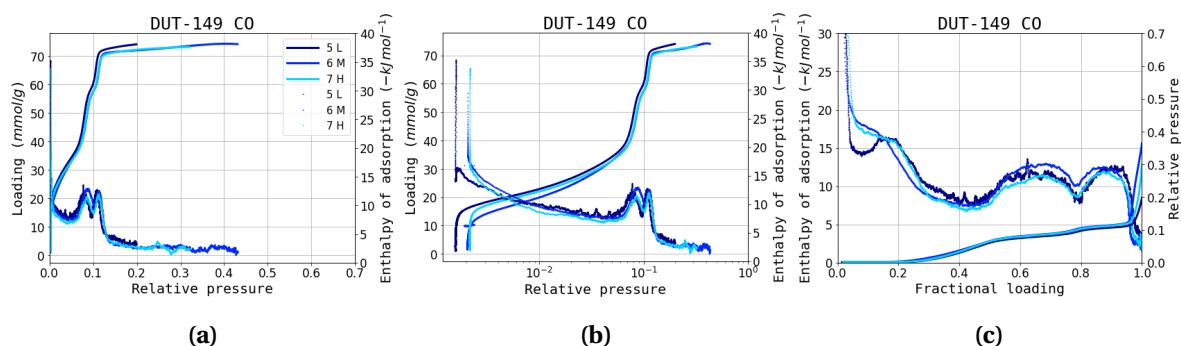


Figure G.12.: DUT-149 (a) isotherms, (b) logarithmic isotherms and (c) enthalpy curves for CO.

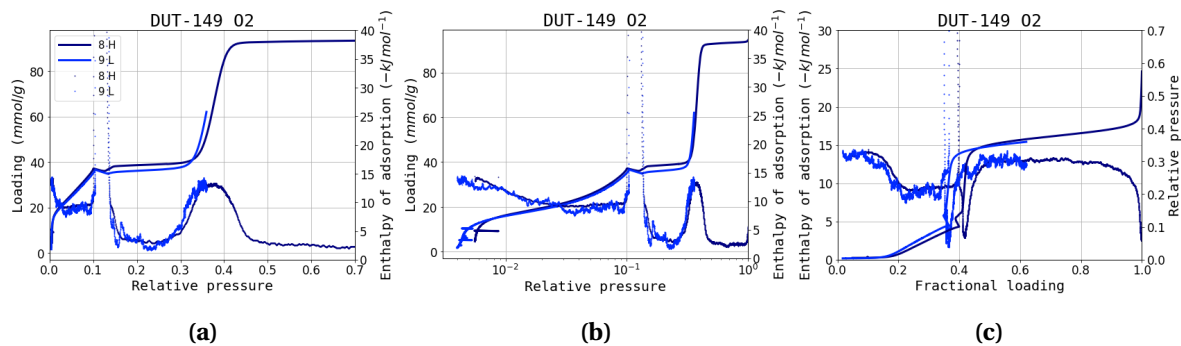


Figure G.13.: DUT-149 (a) isotherms, (b) logarithmic isotherms and (c) enthalpy curves for O₂.

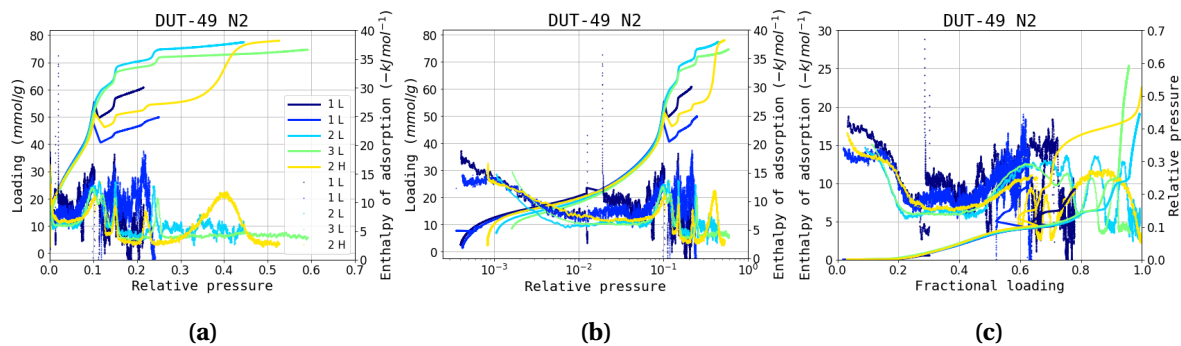


Figure G.14.: DUT-49 (a) isotherms, (b) logarithmic isotherms and (c) enthalpy curves for N₂.

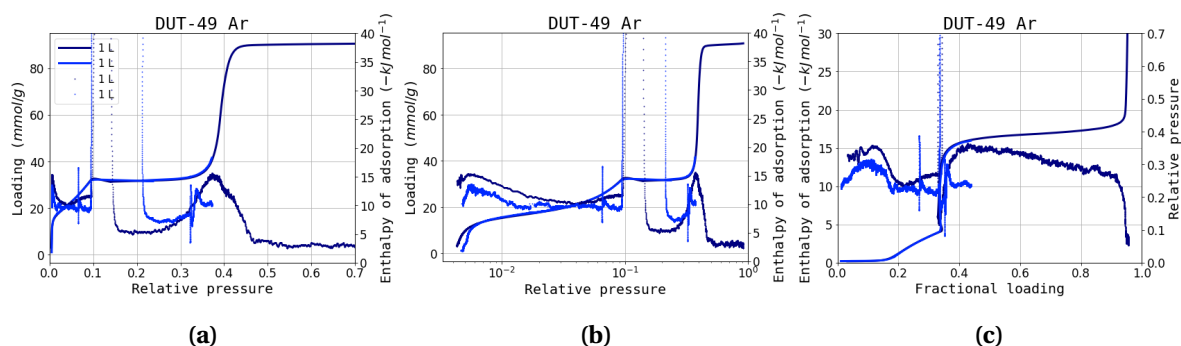


Figure G.15.: DUT-49 (a) isotherms, (b) logarithmic isotherms and (c) enthalpy curves for Ar.

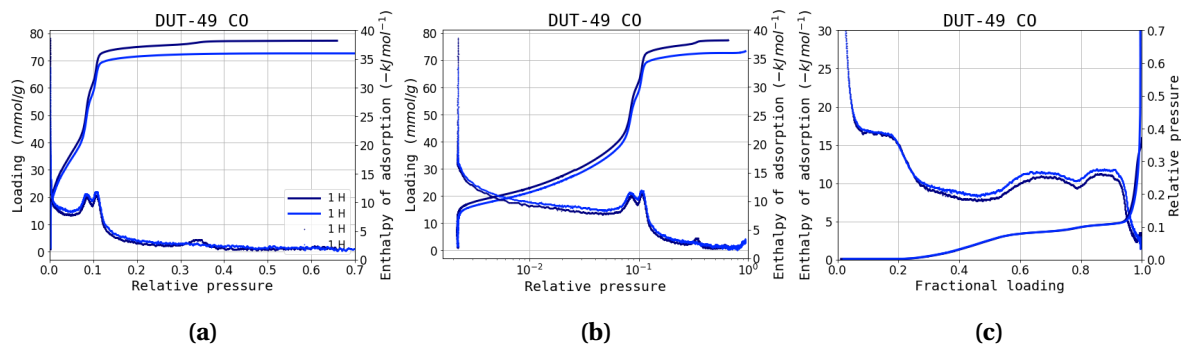


Figure G.16.: DUT-49 (a) isotherms, (b) logarithmic isotherms and (c) enthalpy curves for CO.

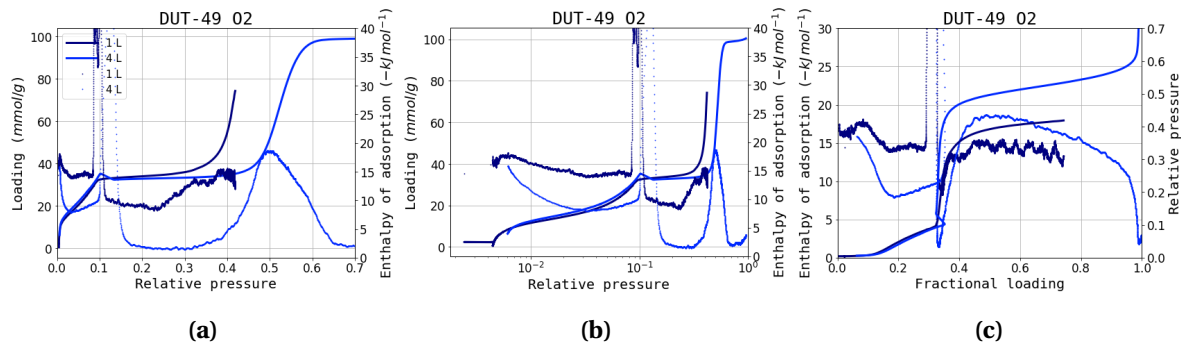


Figure G.17.: DUT-49 (a) isotherms, (b) logarithmic isotherms and (c) enthalpy curves for O₂.

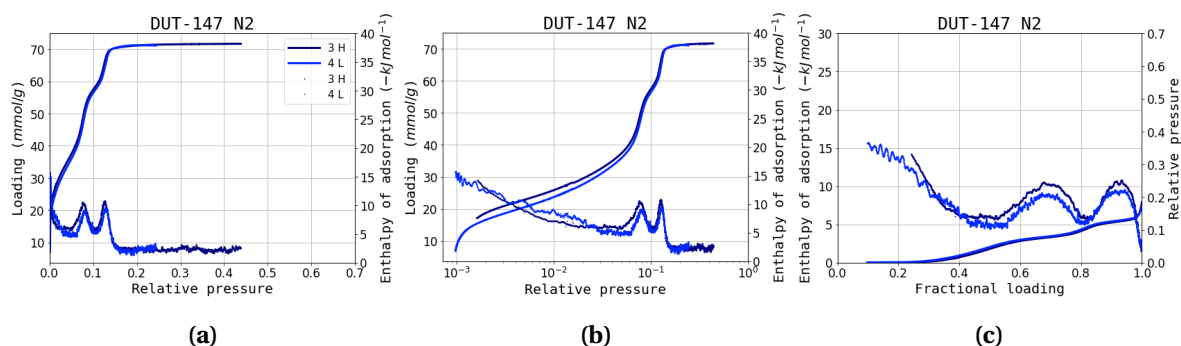


Figure G.18.: DUT-147 (a) isotherms, (b) logarithmic isotherms and (c) enthalpy curves for N₂.

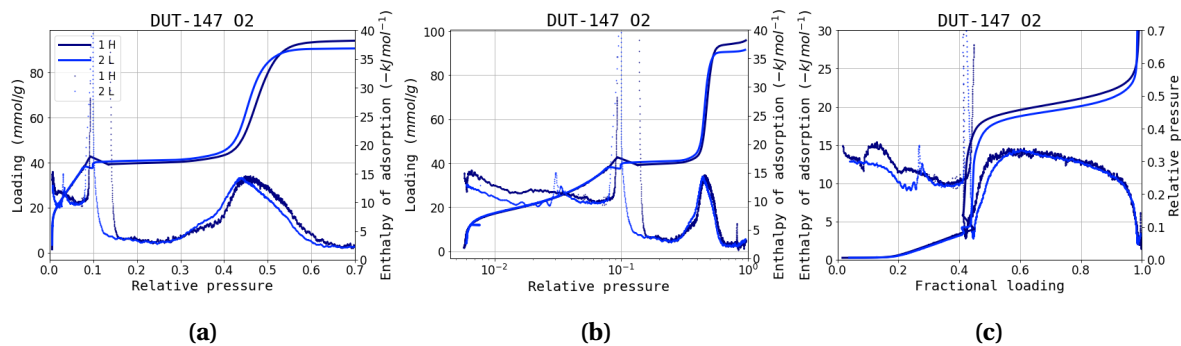


Figure G.19.: DUT-147 (a) isotherms, (b) logarithmic isotherms and (c) enthalpy curves for O₂.

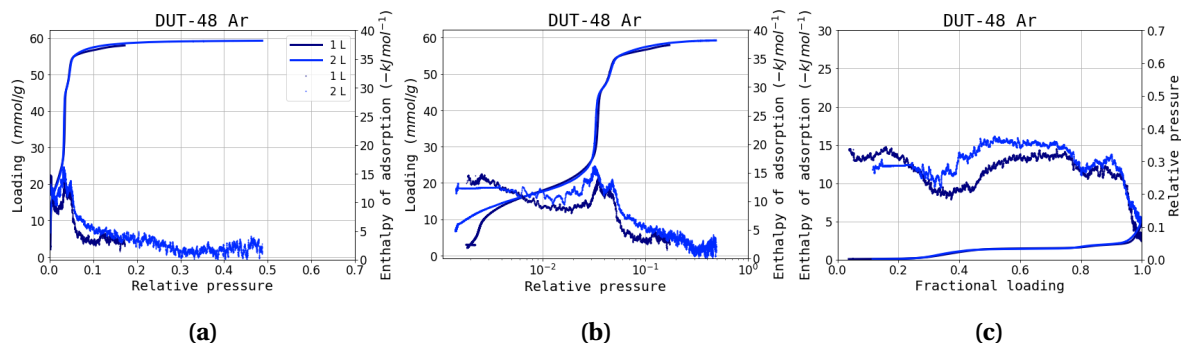


Figure G.20.: DUT-48 (a) isotherms, (b) logarithmic isotherms and (c) enthalpy curves for Ar.

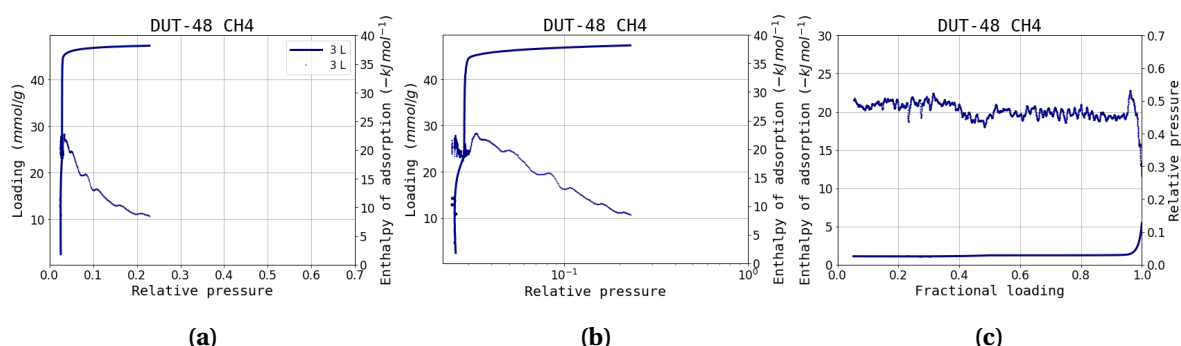


Figure G.21.: DUT-48 (a) isotherms, (b) logarithmic isotherms and (c) enthalpy curves for CH₄.